



# UNIVERSITAT DE BARCELONA

## Laser direct-writing for microfabrication

Camilo Florian Baron

**ADVERTIMENT.** La consulta d'aquesta tesi queda condicionada a l'acceptació de les següents condicions d'ús: La difusió d'aquesta tesi per mitjà del servei TDX ([www.tdx.cat](http://www.tdx.cat)) i a través del Dipòsit Digital de la UB ([diposit.ub.edu](http://diposit.ub.edu)) ha estat autoritzada pels titulars dels drets de propietat intel·lectual únicament per a usos privats emmarcats en activitats d'investigació i docència. No s'autoritza la seva reproducció amb finalitats de lucre ni la seva difusió i posada a disposició des d'un lloc aliè al servei TDX ni al Dipòsit Digital de la UB. No s'autoritza la presentació del seu contingut en una finestra o marc aliè a TDX o al Dipòsit Digital de la UB (framing). Aquesta reserva de drets afecta tant al resum de presentació de la tesi com als seus continguts. En la utilització o cita de parts de la tesi és obligat indicar el nom de la persona autora.

**ADVERTENCIA.** La consulta de esta tesis queda condicionada a la aceptación de las siguientes condiciones de uso: La difusión de esta tesis por medio del servicio TDR ([www.tdx.cat](http://www.tdx.cat)) y a través del Repositorio Digital de la UB ([diposit.ub.edu](http://diposit.ub.edu)) ha sido autorizada por los titulares de los derechos de propiedad intelectual únicamente para usos privados enmarcados en actividades de investigación y docencia. No se autoriza su reproducción con finalidades de lucro ni su difusión y puesta a disposición desde un sitio ajeno al servicio TDR o al Repositorio Digital de la UB. No se autoriza la presentación de su contenido en una ventana o marco ajeno a TDR o al Repositorio Digital de la UB (framing). Esta reserva de derechos afecta tanto al resumen de presentación de la tesis como a sus contenidos. En la utilización o cita de partes de la tesis es obligado indicar el nombre de la persona autora.

**WARNING.** On having consulted this thesis you're accepting the following use conditions: Spreading this thesis by the TDX ([www.tdx.cat](http://www.tdx.cat)) service and by the UB Digital Repository ([diposit.ub.edu](http://diposit.ub.edu)) has been authorized by the titular of the intellectual property rights only for private uses placed in investigation and teaching activities. Reproduction with lucrative aims is not authorized nor its spreading and availability from a site foreign to the TDX service or to the UB Digital Repository. Introducing its content in a window or frame foreign to the TDX service or to the UB Digital Repository is not authorized (framing). Those rights affect to the presentation summary of the thesis as well as to its contents. In the using or citation of parts of the thesis it's obliged to indicate the name of the author.

# Laser direct-writing for microfabrication

Camilo Florian Baron



UNIVERSITAT<sup>DE</sup>  
BARCELONA

Barcelona, Spain

June 2016







UNIVERSITAT DE  
BARCELONA

Departament de Física Aplicada  
Martí i Franquès 1, 08028 Barcelona

# **Laser direct-writing for microfabrication**

**Camilo Florian Baron**

**Nanosciences Doctorate Program**

**Thesis Advisors: Pere Serra Coromina; Juan Marcos Fernández Pradas**

**Tutor: Pere Serra Coromina**

A thesis presented to the Physics Faculty  
to obtain the degree of Doctor

Barcelona, June 2016



The present work has been developed in the Departament de Física Aplicada of the Universitat de Barcelona, in the frame of a research program funded by Ministerio de Ciencia e Innovación (Projects MAT2010-15905 and CSD2008-00023), Ministerio de Economía y Competitividad (Project TEC2014-54544-C2-1-P), Fondo Europeo de Desarrollo Regional (FEDER), the European Commission (Project DigiPRINT, FP7 ERA-NET OLAE+, RDNET12-2-0002), and thanks to the scholarship Ajuts per a la contractació de personal investigador novell FI-DGR2013, from the Agència de Gestió d'Ajuts Universitaris i de Recerca (AGAUR) de la Generalitat de Catalunya.



*A mi familia*



# Acknowledgements

Este espacio está reservado para aquellas personas que han contribuido de alguna forma durante mi doctorado y mi formación en general. La mejor analogía sería un proyecto de Verkami: todos hemos hecho alguna aportación y al final aquí tenemos nuestra recompensa.

Para empezar, quiero agradecer de forma especial al *Dr. Pere Serra*, quien me acogió en el grupo de investigación en el cuál desarrollé todo mi trabajo de Máster y Doctorado. Él, junto con el *Dr. Juan Marcos Fernández*, fueron los directores de mi tesis de doctorado y quienes me acompañaron incansablemente en todas las etapas de este proceso. Tengo que decir que he contado con mucha suerte al poder trabajar con ellos, ya que no solamente son unos excelentes profesores de los que he aprendido cómo investigar, sino que también han cumplido una parte paternal al escuchar y ayudar a resolver muchas preocupaciones sobre el futuro. Gracias por corregir escritos cuyas correcciones parecían no tener fin, por enseñarme todo lo que aprendí durante el tiempo que compartimos y sobre todo, por haber sido mis primeros instructores de esquí.

Conocer a mis directores no habría sido posible sin la ayuda del profesor *Dr. José Luis Morenza*. Quiero agradecerle por las indicaciones durante mi proceso de llegada a Barcelona e incorporación a la universidad y por estar siempre atento ante todas las eventualidades burocráticas que se presentaron.

A més a més, vaig conèixer el *Dr. Martí Duocastella*, amb qui vaig tenir l'oportunitat de compartir l'últim any del doctorat i aprendre d'ell durant l'estada al seu grup de recerca a l'Istituto Italiano di Tecnologia. El seu gust per la investigació és contagiós i la seva forma de treballar, un exemple a seguir.

Mi estancia en la universidad ha sido enriquecedora, gracias a los profesores y demás miembros del Departament de Física Aplicada. En particular, quiero men-



cionar a los profesores *Dr. Arturo Lousa* y *Dr. Joan Esteve*, con los que compartí comidas, conversaciones, cafés, salidas a patinar y 'pulpadas'. Espero que sigan siendo así de cercanos con los estudiantes. En mi opinión, es gracias a ellos que se ha construido la identidad de nuestro departamento. Por otro lado, *Jordi Solà* y *Maite Fraile* han sido los responsables de atender y tramitar incontables problemas burocráticos. Sin ustedes, es difícil imaginar un departamento funcional, gracias por toda su amabilidad, paciencia y eficiencia.

En el grupo de investigación tuve la oportunidad de conocer diversas personas que con el pasar del tiempo se hicieron mis amigos: *Francesc*, sens dubte un 'influencer' molt important durant la meva estada a Barcelona: introductor del català al meu món, de l'estima pel bon menjar i de tot un estil de pensament. *Leyre*, a quien aprecio mucho pese a sus preferencias cafeteras, tengo que decir que has sido una amiga incondicional y en muchos casos, un ejemplo a seguir. M'alegro de tenir amics com vosaltres que vau acompanyar-me en moltes fases d'aquest procés, sobretot escoltant les queixes i preocupacions. *Adrian*, thanks for all the funny stories, beers, coffees, and all the English lessons we had. *Pol*, el més petit del grup, segurament ens trobarem en un futur proper i parlarem de las idees que desenvoluparàs, gràcies per totes les bromes espontànies i per sempre crear moments graciosos al despatx. *Noemí*, per tota l'ajuda i els consells rebuts durant el màster i el començament del doctorat, i especialment per mantenir el contacte malgrat la distància. *Sandra*, quien tuvo paciencia infinita al explicarme el funcionamiento de los instrumentos del laboratorio justo al llegar al grupo.

Fuera de la universidad, aunque de cierta forma en relación con ella, he conocido personas que han sido importantes y que me han acompañado en esta travesía. Por ejemplo, *Mariángeles* compartió conmigo buenos y malos momentos y al mismo tiempo me enseñó a ver el mundo desde una perspectiva más optimista. Gracias por enseñarme cómo exteriorizar el anti-chef que llevo dentro. También, mis amigos *Marcela* y *Frank* deben llevarse un agradecimiento enorme ya que me han contagiado con su alegría cuantizada en 'breves' cafés y han estado pendientes en muchas de las etapas del doctorado. *João*, el meu company de les classes de català amb qui vaig tenir converses molt interessants. El vincle d'amistat que s'ha creat romandrà malgrat la distància.

---

Por supuesto, todo esto no habría sido posible sin una idea inicial. De esta parte se encargó el profesor *Orlando Organista*, uno de los que me enseñaron a aprender y me motivaron para seguir en el mundo académico. Tengo que reconocer todo el esfuerzo que hizo no solamente durante nuestras clases en la Universidad Pedagógica Nacional de Bogotá, sino también el tiempo personal que invirtió en nosotros. De ese nosotros formábamos parte *David Duque*, *Milton Linares* y *Harvey Suárez* a quienes considero 'los precursores' del sueño de estudiar fuera de Colombia, ellos eran mi equipo, con los que compartí muchos años de mi vida en Colombia y con los que incluso ahora mantengo una amistad que recuerda aquellos días prácticamente sin importar la distancia. Además de ellos, *Mónica Valencia* ha sido una de las mecenas más grades de todo el proyecto. Sin ella hubiese sido imposible. Debo agradecerle que me garantizara las condiciones iniciales necesarias que me llevaron a Barcelona, también por las largas llamadas y los correos express de 3 páginas y sobretodo, por encontrar siempre un espacio en su maleta para traerme obsequios en paquetes gigantes desde Colombia.

Mi último año en Barcelona fue especialmente interesante. No solamente aprendí cosas nuevas en mi grupo, en el lab y en el despacho organizando la tesis, sino que también tuve la oportunidad de visitar otros países, vivir un tiempo en ellos, aprender nuevas costumbres y conocer personas cuya forma de pensar se ha convertido en mi referente personal. Una de las cosas más especiales de este año fue poder conocer a *Mingjiao*. Me considero afortunado de haberte conocido y de compartir contigo una historia de la que aún nos queda mucho por escribir. 茗娇, 我爱你.

Finalmente, el turno de la familia. Primero quiero mencionar a mi tío *Néstor*, por su ayuda y su paciencia en la preparación de los documentos de mi viaje. También él fue uno de los que me ayudó de forma incondicional al venir a estudiar a Barcelona. Debo decir que en general, mi familia 'grande' jugó un papel muy importante ya que logró garantizar la estabilidad que necesitaba con todos los mensajes de ánimo y los incontables momentos en los que estuvieron pendientes de mi familia 'pequeña'. Por supuesto, mi hermana *Alejandra* se lleva una mención especial, ya que ha sido mi motivación y la persona por la que me esfuerzo incluso cuando pienso que no puedo más. Gracias por escucharme y soportarme, por tus cartas, mensajes, muñecos y llamadas. Una mala noticia: somos hermanos, itendrás que seguir haciéndolo! *Jairo*, que ha sido una persona que me ha estado enseñando

habilidades técnicas incluso desde antes de empezar el colegio, gracias por todas las horas de 'cacharreo' con la moto, todos mis trabajos y arreglos en casa que han hecho de mi todo un experimentador, por estar pendiente de mi hermana y mi mamá y por siempre tener las palabras y los consejos adecuados. A mi papá, por todo el apoyo tanto en Colombia como en España, por siempre mostrarse positivo sin importar lo gris del panorama y por escuchar cuando lo necesitaba. Por último, a mi Mamá. Gracias por aprender a lidiar con estos ~8500 km que nos separan, por las incontables horas de Skype, los consejos, por madrugar y trasnochar, por todos los dulces detalles y sobretodo por ser la mejor mamá del mundo.

# Contents

<b>Outline</b>	<b>vii</b>
<b>1 Introduction</b>	<b>1</b>
1.1 Microfabrication . . . . .	1
1.2 Laser ablation of transparent materials . . . . .	4
1.3 Laser-induced forward transfer . . . . .	10
<b>2 Experimental</b>	<b>15</b>
<b>3 Subtractive laser direct-writing</b>	<b>27</b>
3.1 Z-scan focusing technique . . . . .	27
3.2 Surface ablation of polymethyl-methacrylate . . . . .	31
<b>4 Additive laser direct-writing</b>	<b>37</b>
4.1 High speed printing . . . . .	37
4.2 Line printing . . . . .	40
4.3 Microlenses fabrication . . . . .	42
<b>5 Combined approaches</b>	<b>47</b>
5.1 Nanopatterning with liquid microlenses . . . . .	47
5.2 Line printing in fluidic guides . . . . .	50
<b>6 Conclusions</b>	<b>53</b>
<b>Bibliography</b>	<b>57</b>
<b>Included Publications</b>	<b>69</b>
Subtractive laser direct-writing . . . . .	69
Paper 1 . . . . .	69
Paper 2 . . . . .	77
Paper 3 . . . . .	85

---

Paper 4 . . . . .	93
Paper 5 . . . . .	105
Additive laser direct-writing . . . . .	113
Paper 6 . . . . .	113
Paper 7 . . . . .	121
Paper 8 . . . . .	129
Combined approaches . . . . .	153
Paper 9 . . . . .	153
Paper 10 . . . . .	165
<b>Resum en Català</b>	<b>173</b>
<b>Conclusions en Català</b>	<b>181</b>
<b>Curriculum Vitae</b>	<b>185</b>

# Outline

Digital manufacturing constitutes a real industrial revolution that is transforming the production processes from the early stages of research and development to mass production and marketing. The biggest difference in comparison with old fabrication methods is the possibility to perform design changes using only mouse clicks instead of modifying an already fabricated prototype, resulting in faster, cheaper and more efficient fabrication processes [1].

In order to make it possible, scientists and engineers continuously face new challenges to respond the current production demands. For example, new technologies enabling the production of printed electronic devices on flexible substrates compatible with roll-to-roll processing methods are required. This would result in cheaper fabrication costs than the traditional batch processing of silicon wafers. Such fabrication methods comprise a series of processing steps which are applied to the substrates while they are moving on rolls in the fabrication line. Therefore, it is desired that the new technologies can work at high speeds allowing at the same time the production of miniaturized features. Indeed, miniaturization constitutes a key aspect in areas such prominent as electronics [2], pharmaceuticals [3] and chemical-biological sensing [4,5], to name a few. The most immediate challenge is the creation of new direct-write techniques or the adaptation of the existing ones that allow processing those flexible substrates massively with high accuracy and at high speeds.

Lasers are a versatile tool that can meet the demands of flexibility, speed, resolution and compatibility with roll-to-roll processing of digital manufacturing [6–10]. At the time of its invention in 1960 by T.H. Mainman [11], the laser was the answer without a question since there were no clear applications in mind for such a device. Ironically, lasers are ubiquitous today and can be found in areas such diverse as industrial manufacturing, medicine, telecommunications and science [12]. The main advantages of laser radiation rely in its unique properties: high directionality,

coherence and monochromaticity. The combination of such properties allows generating high intensities that can be focused into extremely small volumes, which makes lasers an ideal tool for the processing of materials at the micro- and nano-scale, not only as a subtractive technique but also as an additive one.

Laser ablation is the best known subtractive technique and it consists in the irradiation of a material with a focused laser beam. The absorbed energy typically produces the vaporization of a tiny fraction of material that results in the formation of a crater on the irradiated area [13]. The working principle is similar to the work that a sculptor performs on a piece of marble using a hammer and a chisel to transform it into a sculpture. In general, the main challenge in micromachining is to pursue the smallest possible feature. In the case of laser ablation this is often limited by heat transfer [14]. This challenge can be overcome by the use of ultra-short laser pulses, which can deliver all the pulse energy to the material in a period of time shorter than the lattice thermal relaxation time, reducing drastically the unwanted heat dissipation beyond the irradiated zone [15]. On the other hand, many applications require that ablation occurs only at the materials surface. This is not a problem when the material is opaque to the laser wavelength; however, in the case of transparent materials it constitutes a serious challenge since it is necessary to develop new strategies that allow controlling the position where the energy is delivered to ensure that ablation really occurs in the surface without modifying the bulk material.

Lasers can also be used as additive tools. In a similar way as we can construct structures with Lego pieces, lasers can enable the deposit of tiny amounts of material pixel by pixel that through superposition they allow the formation of 2D and 3D structures. Laser-induced forward transfer is a technique that allows the transfer of materials in both solid and liquid state with high spatial resolution [16–20]. This is achieved through the focusing of a pulsed laser beam on a donor film of the material of interest, so that the absorption of the laser pulse energy results in the propulsion of a tiny fraction of the irradiated material towards an acceptor substrate placed conveniently close, producing in this way a printed pixel. Through the overlap of consecutive pixels any pattern can be printed. In particular, the printing of liquids allows working with a substantially broad range of materials: metallic nanoparticle solutions, semiconductors, dielectrics and even biological samples. In this case, the printed pixels correspond to sessile droplets, which once dried leave

the material of interest deposited on the acceptor substrate. The printing of individual droplets has been largely studied through the analysis of the influence of the main process parameters on the morphology of the deposited droplets. Besides, the mechanisms responsible for the ejection of liquid have been investigated in detail, revealing the particular jetting dynamics that gives place to the formation of the printed droplets [21–23]. However, some challenges still remain. Among them we can find key aspects such as the particular printing dynamics encountered during the high speed printing of liquids, or the problem of printing uniform, continuous and stable lines with high spatial resolution.

The objective of this thesis is to propose and implement feasible solutions to some of the challenges that are associated with both the subtractive and additive laser based techniques presented above. On one side, we study the laser ablation of transparent polymers using femtosecond laser pulses with the aim of reaching spatial resolutions that overcome the diffraction limit, and at the same time solving the problem of the required precise focusing of the laser beam on the materials surface. On the other side, we study the LIFT transfer dynamics during the high speed printing of liquids, and we propose alternative printing strategies to solve the inherent quality defects usually encountered during the formation of printed lines. Finally, a couple of approaches which combine both subtractive and additive techniques are also investigated.

This thesis is presented as a compilation of papers that have been published during the development of the doctorate in the frame of the PhD program in Nanosciences at the Departament de Física Aplicada of the Universitat de Barcelona. It is structured in five main chapters as follows:

**Introduction:** In this chapter the state of the art on laser-based microfabrication techniques is presented, giving special attention to the surface laser ablation of transparent materials and the recent advances in the LIFT of liquids.

**Experimental:** A description of the femtosecond and nanosecond laser systems as well as the fast acquisition imaging system used during the experiments is presented in this chapter. A few considerations about issues related with Gaussian beams are also included.



**Subtractive laser direct-writing:** In this chapter, the results corresponding to our investigation on femtosecond laser ablation are presented. A precise focusing method to perform laser ablation with high spatial resolution on the surface of a transparent material is developed, characterized and implemented.

**Additive laser direct-writing:** In this chapter, the results on the LIFT of liquids are presented, including an analysis of the jetting dynamics presented during the simultaneous printing of droplets, as well as an efficient printing approach for the fabrication of continuous lines. Finally, a new application of LIFT as a technique for the fabrication of microlenses is presented.

**Combined approaches:** The final block of results is included in this chapter. It comprises two different approaches that are a combination of both subtractive and additive techniques. On one side, we implement LIFT for the fabrication of liquid microlenses used for the surface nanopatterning of materials. On the other side, we create fluidic guides by laser ablation for the printing of high quality continuous lines.

**Conclusions:** The last section presents the general conclusions of the presented results as well as the main achievements of the thesis.

The developed work has resulted in 10 research papers, out of which 9 have already been published in different scientific journals. Only these 9 papers have to be considered for the evaluation of the thesis:

#### **Group 1: Subtractive laser direct-write**

**Paper 1** - J.M. Fernández-Pradas, C. Florian, F. Caballero-Lucas, J.L. Morenza, P. Serra. "Femtosecond laser ablation of polymethyl-methacrylate with high focusing control," *Applied Surface Science* **278** 185-189 (2013).

Impact factor JDR 2013: 2.538 - (Q1).

**Paper 2** - C. Florian, F. Caballero-Lucas, J.M. Fernández-Pradas, J.L. Morenza, P. Serra. "Surface ablation of transparent polymers with femtosecond laser pulses," *Applied Surface Science* **302** 226-230 (2014).

Impact factor JDR 2014: 2.711 - (Q1).

**Paper 3** - F. Caballero-Lucas, C. Florian, J.M. Fernández-Pradas, J.L. Morenza, P. Serra. "Beam waist position study for surface modification of polymethyl-methacrylate with femtosecond laser pulses," *Applied Surface Science* **374** 353-358 (2016).  
Impact factor JDR 2014: 2.711 - (Q1).

**Paper 4** - C. Florian, F. Caballero-Lucas, J.M. Fernández-Pradas, S. Bosch, J.L. Morenza, P. Serra. "Femtosecond laser surface ablation of polymethyl-methacrylate with position control through z-scan," *Journal of Physics D: Applied Physics* **48** 335302 (2015).  
Impact factor JDR 2014: 2.721 - (Q1).

**Paper 5** - F. Caballero-Lucas, C. Florian, J.M. Fernández-Pradas, J.L. Morenza, P. Serra. "Precise surface modification of polymethyl-methacrylate with near-infrared femtosecond laser," *Applied Surface Science* **336** 170-175 (2015).  
Impact factor JDR 2014: 2.711 - (Q1).

## **Group 2: Additive laser direct-write**

**Paper 6** - A. Patrascioiu, C. Florian, J.M. Fernández-Pradas, J.L. Morenza, G. Hennig, P. Delaporte, P. Serra. "Interaction between jets during laser-induced forward transfer," *Applied Physics Letters* **105** 014101/1-5 (2014).  
Impact factor JDR 2014: 3.302 - (Q1).

**Paper 7** - C. Florian, F. Caballero-Lucas, J.M. Fernández-Pradas, R. Artigas, S. Ogier, D. Karnakis, P. Serra. "Conductive silver ink printing through the laser-induced forward transfer technique," *Applied Surface Science* **336** 304-308 (2015).  
Impact factor JDR 2014: 2.711 - (Q1).

For the sake of completeness, an additional paper is also presented, but since it has not been accepted for publication yet, it has not to be considered for evaluation:

**Paper 8** C. Florian, S. Piazza, A. Diaspro, P. Serra, M. Duocastella. "Direct laser printing of tailored polymeric microlenses," *Submitted to: ACS Materials and Interfaces*.

**Group 3: Combined approaches**

**Paper 9** - M. Duocastella, C. Florian, P. Serra, A. Diaspro. "Sub-wavelength laser nanopatterning using droplet lenses," *Scientific Reports* **5** 16199/1-9 (2015).

Impact factor JDR 2014: 5.578 - (Q1).

**Paper 10** - C. Florian, F. Caballero-Lucas, J.M. Fernández-Pradas, S. Ogier, L. Winchester, D. Karnakis, R. Artigas, P. Serra. "Printing of silver conductive lines through laser-induced forward transfer," *Applied Surface Science* **374** 265-270 (2016).

Impact factor JDR 2014: 2.711 - (Q1).

# 1 Introduction

In this chapter we present a general overview of the current available approaches for the microprocessing of materials. In particular, we dedicate special attention to laser based techniques such as laser ablation and laser-induced forward transfer (LIFT). The chapter is divided in three different sections. The first part comprises an overview of the different techniques for the processing of materials in the microscale. The second one is focused on laser ablation techniques, specially the modification of transparent materials using ultrashort laser pulses. Finally, the last part includes the state of the art of the LIFT technique for liquids printing.

## 1.1. Microfabrication

Nowadays, the fabrication of devices evolves towards the miniaturization of the different components with the main objective of fabricating compact, efficient and outperforming products. As a consequence, the different fabrication techniques have to be adapted to provide the required spatial resolutions in the every time smaller scales. Examples of this miniaturization trend can be found in electronics [2], chemistry [4,24], medicine [3] and biology [5] among many other areas.

We can classify the microprocessing techniques in two groups: mask-based and direct-write. In the first group we include the techniques that implement a mask or a master in order to replicate the pre-fabricated pattern in the material of interest. Among them, we can find photolithography [25], hot-embossing [26], micro-moulding [27] and micro-contact printing [28,29]. All of them implement a mask or mold that generally has been fabricated using photolithographic methods. Thus, the best known and widespread is photolithography itself. This technique is currently used for the fabrication of integrated circuits and the micro- and nano-processing of diverse materials. Figure 1.1 shows a basic scheme of the process. Basically, UV light is used to promote the selective polymerization of a photoresist that is placed on top of the material of interest. In the case of a silicon wafer, for

example, the surface is coated with a thin layer of a photoresist material. Then, the previously prepared mask that contains the pattern is placed within the optical path, shadowing some of the incoming UV light. The image of the mask is projected through optics that finally reproduce the image (generally demagnified) onto the surface of the photoresist. The combination of deep ultraviolet lasers and high numerical aperture objectives allows reaching extremely high spatial resolutions, in some cases only limited by diffraction.

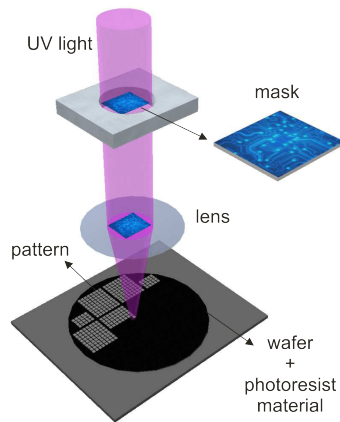


**Figure 1.1:** Schematic diagram of a basic photolithographic process.

Once the UV light selectively polymerizes the photoresist, the sample is exposed to an etching treatment to remove the unwanted part of the photoresist. Generally, the part that remains on the substrate is the irradiated one; however, in some applications the process is the opposite. This process produces the desired modification of the substrate either by chemical or by plasma etching. Once the photoresist is no longer needed, it is removed from the sample by using chemical removers, leaving the image of the mask engraved on the surface of the wafer. This technique offers the possibility of processing batches of identical samples with outperforming reproducibility. However, the main drawback is that each design requires a separate mask which fabrication is complex, time consuming and expensive.

In contrast, direct write methods are mask free techniques that require fewer fabrication steps and constitute a cheaper and faster alternative to mask based methods [8, 30]. Besides, and most important, they are specially suited when the

fabrication processes demand a fast transition between the design and the fabricated product. In this group of techniques we can include ink-jet printing [31], laser micromachining [13], and more sophisticated techniques such as focused ion beam [32] and two photon polymerization [33]. Among them, ink-jet printing, the most widespread direct-write technique, consists in the deposition of liquid droplets onto a substrate through a nozzle. The droplets are generated through the onset of high pressures in the liquid that lead to the formation of a jet, which rupture produces a flying droplet that is deposited on the receptor substrate placed nearby. Typically, the generation of the droplet can be performed following two different mechanisms: continuous ink-jet printing (CIJ) and drop-on-demand (DOD) ink-jet printing, as it can be observed in Figure 1.2.

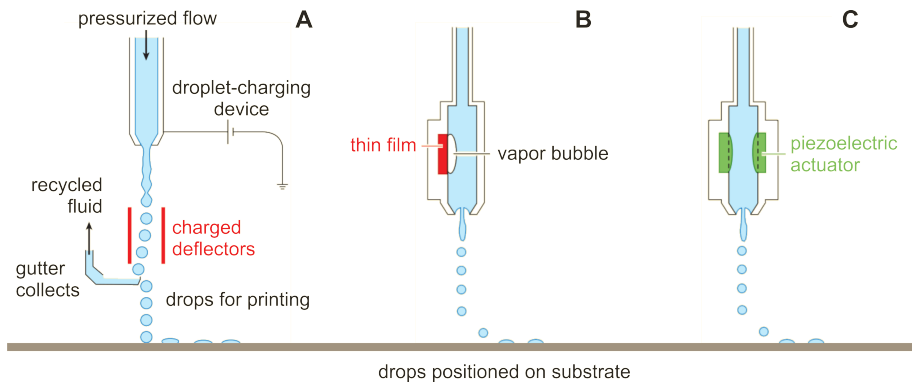


**Figure 1.2:** Schematic diagram showing the principles of operation of ink-jet printing. (A) Continuous ink-jet printing (CIJ). Drop-on-demand (DOD) ink-jet printing generated by (B) a thermally generated pulse, and (C) a piezoelectric actuator. (Figure adapted from [31]).

CIJ printing, generates droplets continuously, even when printing is not required. The generation of the droplets is produced by a constant pressurized flow that is applied to the liquid inside the printed head. As a consequence, the liquid is ejected through the nozzle as small droplets which are deflected by an electric field that deviates the unwanted droplets to a gutter, which receives the unused liquid and recycles it, depending on the application. The droplet diameter routinely achieved by this principle of operation is approximately  $100\ \mu\text{m}$  [31]. DOD generates droplets only when they are required by the action of a thermally-induced pressure pulse or by a piezoelectric actuator. The created disturbance in the liquid allows the formation of a jet which rupture follows the formation of a droplet. The typical droplet

diameter using this principle of operation typically ranges from 50 to 70  $\mu\text{m}$ . Using this operation principle it is possible to print complex functional materials with high spatial resolution [34].

Unfortunately, despite that ink-jet printing is the most widespread additive technique allowing to print with high spatial resolution, some drawbacks arise concerning the liquids compatible with this technique. Typically, the window of viscosities ranges between 1 and 50 mPa.s [35]. In order to work with different viscosity liquids, it is required a customization of the ink or the engineering of the printing head [35,36]. Moreover, nozzle clogging issues can be present when working with complex rheology liquids, when the inks dry and block the head output, or when the size of the particles are around an order of magnitude smaller than the nozzle diameter or larger [37].

## 1.2. Laser ablation of transparent materials

The advent of lasers resulted in an unnumbered amount of applications that range from consumer goods as telecommunications, music players and printers to more specialized implementations such as industrial processing of materials as well as medical and biological applications [12]. The modification of a wide variety of materials with high spatial resolution can be performed with laser radiation, since lasers can produce high intensity and almost monochromatic beams that can be focused in exceptionally small volumes. The operation principle is simple: when the material of interest is irradiated by energetic enough laser radiation, a tiny fraction of material around the irradiated area is vaporized.

The absorption process can proceed through linear and non-linear mechanisms, depending on the material, the laser wavelength and the intensity. In most laser ablation situations, laser radiation is generally absorbed following linear processes, with the pulse energy being coupled to free electrons or to phonons in the material, depending on the laser wavelength. The photon absorption, in the first case, can take place by promoting an electron from a lower energy band to a higher energy band (interband absorption), or from a low energy level to a high energy level inside the same energy band (intraband absorption). Metals can absorb radiation of virtually any wavelength promoting intraband electronic transitions. In the case of semiconductor materials, in order to promote ablation, the incident laser radiation

must overcome the energy band gap to produce the excitation of electrons from the valence to the conduction band. For dielectric materials, the photon absorption process is the same, but with larger band gaps involved. The only laser wavelengths that can be effective to ablate wide band gap dielectrics following linear electronic transitions are ultraviolet lasers, which photons have enough energy to overcome the band gap; alternatively CO<sub>2</sub> lasers, with a wavelength of 10.6  $\mu\text{m}$ , in the far infrared, can be also used, but in this case absorption takes place through radiation coupling to phonons [38].

An efficient alternative to produce ablation in transparent dielectric materials is the use of focused ultra short laser pulses, since they can enable non-linear absorption mechanisms such as multiphoton absorption and quantum tunnelling in combination with avalanche ionization. Multiphoton absorption is produced when more than one photon couples to an electron in a single absorption event so that the total absorbed energy results larger than the energy band gap, while during quantum tunnelling the incoming electric field alters the Coulomb potential well so that an electron is liberated to the conduction band through tunnelling across the potential barrier (Figure 1.3). It is important to note that these absorption mechanisms just generate the seed electrons necessary for the onset of optical breakdown, which will finally take place through free-carrier absorption followed by avalanche ionization.

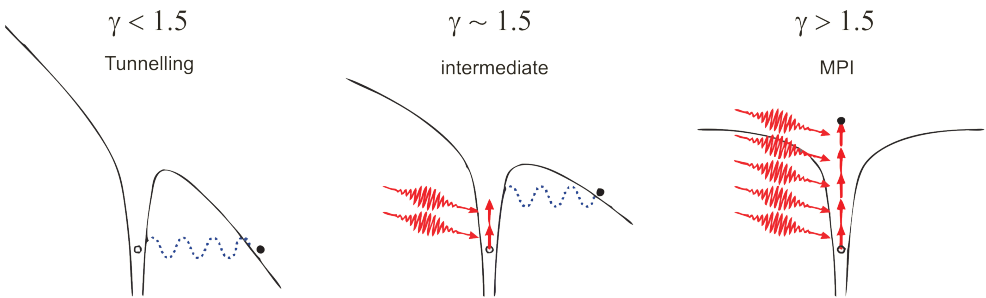


**Figure 1.3:** Schematic diagram of photoionization for different values of the Keldysh parameter. Image taken from [39].

In order to identify the predominant primary absorption process, it is possible to calculate the Keldysh parameter  $\gamma$ :



$$\gamma = \frac{\omega}{e} \sqrt{\frac{m_e c n \epsilon_0 E_g}{I}}, \quad (1.1)$$

where  $\omega$  is the laser frequency,  $I$  is the laser intensity at the focus,  $m_e$  is the effective electron mass,  $e$  is the fundamental electron charge,  $c$  is the speed of light,  $n$  is the refractive index of the irradiated material,  $\epsilon_0$  is the permittivity of free space, and  $E_g$  is the energy of the band gap. If  $\gamma < 1.5$  the tunnelling effect dominates, while if  $\gamma > 1.5$  the predominant process is multiphoton absorption; for  $\gamma \sim 1.5$ , electrons are promoted to the conduction band through a combination of both processes, as it can be visualized in Figure 1.3 [39].

Once there are enough seed electrons in the conduction band, optical breakdown takes place through the absorption of the remaining photons in the laser pulse by the newly generated free electrons in the conduction band, followed by avalanche ionization (Figure 1.4). During avalanche ionization, the seed electrons absorb the energy of incoming photons moving to a higher energy state inside the conduction band. The excess in the energy of the electron is transferred to another electron in the valence band that is impact-ionized to the conduction band, resulting in two excited electrons. The process can be repeated as long as the electric field of the incoming laser radiation is present, producing the avalanche effect.

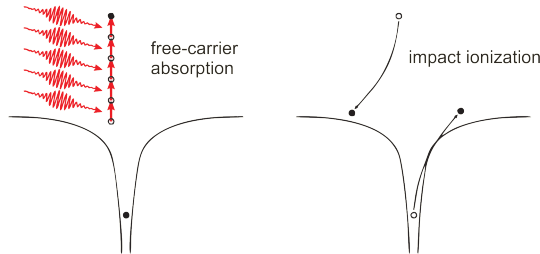


**Figure 1.4:** Schematic diagram of avalanche ionization. Image taken from [39].

## Laser induced damage in transparent materials

The absorption mechanisms described above can induce permanent damage on transparent materials with visible and near-infrared photons by using ultrashort

laser pulses. In those cases, the absorption per unit length ( $dI/dz$ ) depends non-linearly on the optical intensity ( $I$ ) of the incoming laser radiation. At different wavelengths, different numbers of photons ( $n$ ) are absorbed by multiphoton absorption to ionize the electrons in the irradiated material (Figure 1.5).

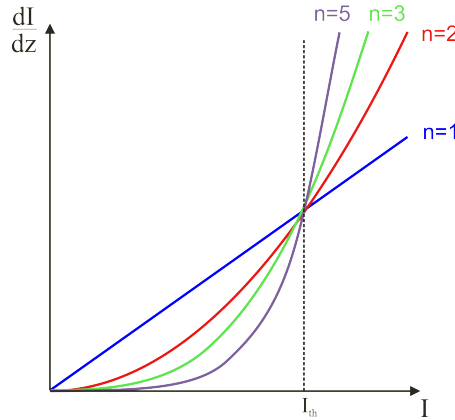


**Figure 1.5:** Schematic plot of the absorption per unit length ( $dI/dz$ ) vs the intensity ( $I$ ) for different number of photons  $n$ . The dotted line corresponds to the trend in a hypothetical process with  $n \rightarrow \infty$  that would indicate a defined intensity threshold  $I_{th}$  for absorption [40].

If only one photon ( $n = 1$ ) is needed to overcome the bandgap, the material will absorb the laser energy linearly so that it is not possible to determine a well defined radiation absorption threshold (though it is to determine a damage threshold). In non-linear absorption, however, the absorbed intensity per unit length follows a potential relationship with intensity ( $dI/dz = k(n)I^n$ ), where the power  $n$  corresponds to the number of photons required to promote absorption from the valence to the conduction band. This trend for non-linear processes indicates that the absorption at low intensities is lower than the linear case, and at higher intensities, the absorption is even higher. Figure 1.5 shows that as the number of photons increases, this difference is more noticeable. If the number of photons  $n \rightarrow \infty$ , the curve approaches a situation with a well defined threshold for absorption ( $I_{th}$ ). This effect finally results in much more confined radiation effects in the laser treatment of materials with ultrashort laser pulses than in treatments undergoing linear absorption, as sketched in Figure 1.6.

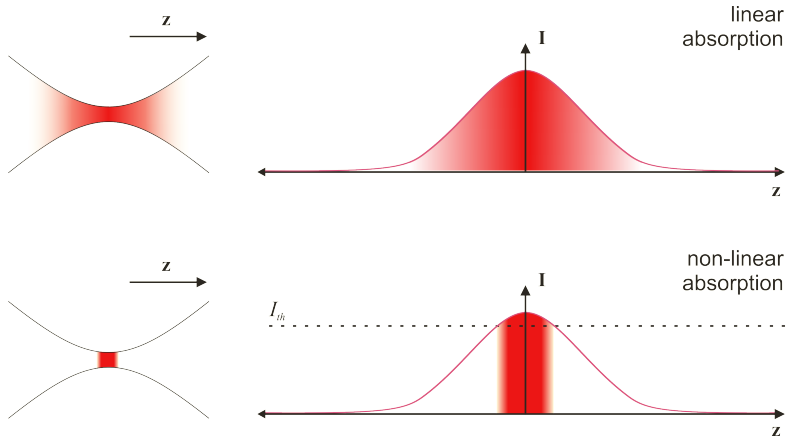


**Figure 1.6:** Confinement of absorption and damage along the intensity profile of a focused laser beam due to intensity threshold for linear and non-linear absorption. Image adapted from [40].

Once a material is irradiated with a high enough intensity pulse, it increases dramatically the electron density in the conduction band that generates further absorption through avalanche ionization, leading to the formation of an electron plasma in that band. If the electronic plasma reaches a critical density, the material absorbs the rest of the laser pulse through free carrier absorption. The outcome of this process is a very hot electron plasma which develops in a much shorter time than the typical recombination time for most materials [41,42]. The energy transfer from the hot electron plasma to the lattice of the material is the responsible for the permanent damage in the material. The heat affected zone, ultimately responsible for the definition and resolution of the modified laser areas, is therefore drastically reduced using ultrashort laser pulses. This makes ultrashort laser pulses an ideal tool for the processing of transparent materials with exceptionally high spatial resolutions (Figure 1.7).

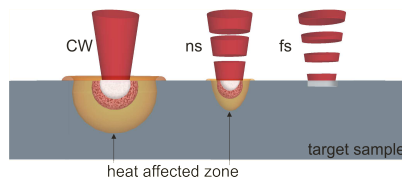


**Figure 1.7:** Schematic representation of laser ablation through CW, ns and fs laser radiation.

## Surface ablation of transparent materials

In view of the advantages that lasers with ultrashort pulses offer, they can be used for processing transparent materials with high spatial resolution. Moreover, the extremely reduced thermal dissipation make them an ideal tool for the processing of sensitive materials, such as polymers [43, 44] and biological materials [45], without compromising the functionality of the material beyond the irradiated zone.

The most widespread applications with transparent materials consist in the localized modification of the refractive index in the bulk material. Because of the high intensity at the focus, the energy is non-linearly absorbed there, increasing the temperature in a small volume around the focus and producing the rapid melting and re-solidification of the material. If the laser beam is scanned along the material, the outcome is the production of a guide. Thus, it is possible to create any desired 3D structure in the bulk that can be used for the production of optical waveguides [46], data storage devices [47, 48], and integrated fluidic channels when there is vaporization in the irradiated zone [49]. On the other hand, some applications demand the functionalization of the surface on transparent samples. The best known applications are surface microfluidic channels for lab-on-a-chip devices [50], miniaturized biological sensors [51], bioimplants [52] and microlenses [53].

In contrast to bulk microfabrication, surface ablation requires a high control on the position where the energy is delivered to the material. Slight variations of the position near the surface could produce bulk absorption or no absorption at all. Therefore, one of the challenges consists in developing methods for the controlled focusing of the laser beam in order to produce the surface ablation of transparent materials with high spatial resolution. Current methods include trial and error experiments [54], active [55] and passive [56] confocal positioning, all of which require complex setups and/or time consuming procedures. For instance, in the case of active confocal positioning it can only be implemented along one direction in the XY plane, and the passive confocal positioning requires a trial and error process to find the position of the surface on the target sample. Therefore, devising methods for the accurate positioning of the laser beam waist to produce surface ablation remains a true challenge in the microstructuring of transparent materials with ultrashort pulsed lasers.

### 1.3. Laser-induced forward transfer

Laser-induced forward transfer (LIFT) is an additive technique that allows the printing of materials on demand. The principle of operation consists in the transfer of material from a donor substrate that contains a coating of the material of interest, towards another substrate (receptor<sup>1</sup>) placed conveniently close, as it is shown in Figure 1.8. Depending on the focusing conditions and the parameters associated with the laser radiation, it is possible to control the amount of material that is extracted from the donor and thus the dimensions of the transferred pixels.

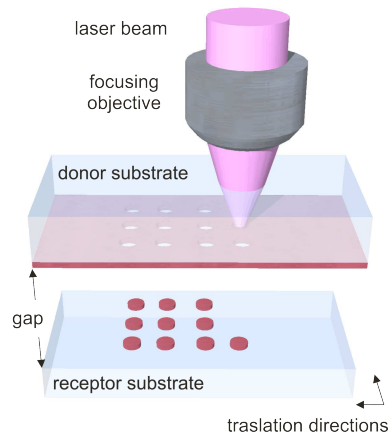


**Figure 1.8:** Principle of operation of the LIFT technique.

LIFT was devised as a deposition technique for the transfer of dried inks as early as 1970 [57]. However that work fell into oblivion and the technique was rediscovered by Bohandy's group in 1986; they used a thin solid layer of copper as a donor material to be deposited on a silicon receptor substrate first in vacuum conditions to minimize the material oxidation [6] and later in air [16].

Materials transfer in LIFT can be triggered following different mechanisms depending mainly on the laser fluence. For low fluences (Figure 1.9A) the propelling of the material can be activated by a vapor pocket generated in the interface between the transparent substrate and the donor film. The vapor can be generated either by evaporation of the donor material or by gas desorption by donor surface

<sup>1</sup>We have used the term 'receptor', but in the literature it is commonly used 'acceptor', 'receiving' or 'target substrate' as well.

defects [58]. The material can also be propelled by thermal expansion after laser heating, producing a bouncing effect on the transparent substrate which propels the solid layer towards the receptor substrate [59]. At fluences that allow the melting of the donor film, the material can be ejected as a droplet after a tiny fraction of the film is molten under the action of the laser pulse [60] (Figure 1.9B). For higher fluences, the ejected material is emitted through a combination of both evaporation and melting, creating a hybrid mechanism that involves the creation of a high pressure vapor pocket that propels the melted material [16, 61]. This mechanism is considered to be the one responsible for transfer in most of the reported works on LIFT with solid materials (Figure 1.9C). Finally, when the laser fluences are even higher (Figure 1.9D), the irradiated material is completely vaporized and deposited on the material through recondensation of the vapor [62, 63].

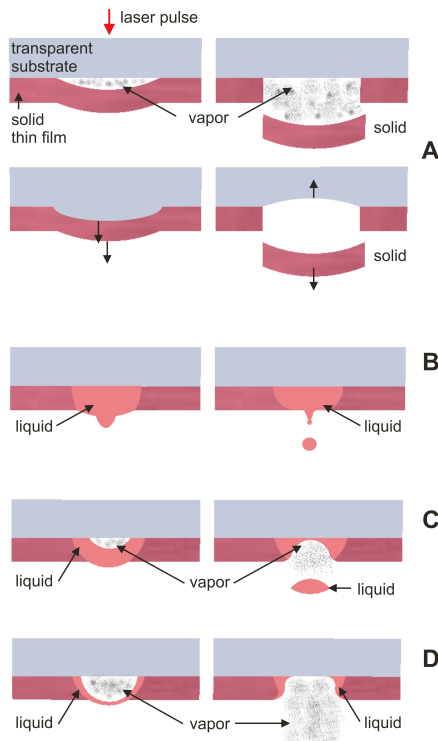


**Figure 1.9:** Possible transfer mechanisms in the LIFT of solid films. Image adapted from [64].

The LIFT of solid films allowed the printing of metals [65–67], semiconductors [68] and dielectrics [69–71] using laser pulses of different durations with almost all the available laser wavelengths (from ultraviolet to infrared). Nevertheless, despite the wide applicability of the LIFT to print solid materials, it has to be stated that the process presents some shortcomings regarding the quality of the transferred features and the processes required for the preparation of the donor thin film. Besides, the phase transition of the material during the transfer process can seriously alter the properties of the initially solid material, which makes the LIFT of solids a non-viable technique for the deposition of many complex materials. The printing of complex materials with no alterations of their functionality was therefore a big challenge for several applications where LIFT could be the fabrication technique of choice. The first group that demonstrated the transfer of complex materials was the Naval Research Laboratory [7]. The idea consisted in carrying out transfer from liquid donor films.

### **LIFT of liquids**

In this approach, the donor layer is an ink that contains the material of interest in either suspension or solution. The printing mechanism is similar to the one of the LIFT of solids: the laser energy is absorbed in a small region of the donor leading to the formation of a micron-sized vapor pocket which expansion propels the material towards another substrate, enabling the formation of droplets in the surface of the receptor substrate in a similar way as in ink-jet printing. The further drying of the liquid carrier leads to the formation of pixels adhered onto the receptor substrate. One of the requirements for this approach to work is that the donor layer should absorb the incoming laser radiation. In order to deposit liquid or solid materials that are transparent, the idea evolved towards the use of an intermediate layer that essentially absorbs the incoming laser radiation to enable the ejection of the material [72–78].

In general, the studies that have been carried out to print different materials with LIFT using liquids have been aimed to report the feasibility to transfer several kind of materials without modifying its functional properties. For instance, it has been reported the transfer of biological molecules [18, 79–82], materials for tissue engineering [83, 84], and the transfer of thermally, mechanically and electrically sensitive materials [76, 85–88]. All of these studies analyse also the influence of the

printing parameters on the morphology of the deposited material. One of the main parameters to study is the laser pulse energy<sup>2</sup> (Figure 1.10), aimed to control the droplet diameter and the deposited volume [21, 89–91]. Parameters related with the focusing conditions [21], liquids rehology [92], gap between donor-receptor substrates and pulse duration were also studied [93–95].

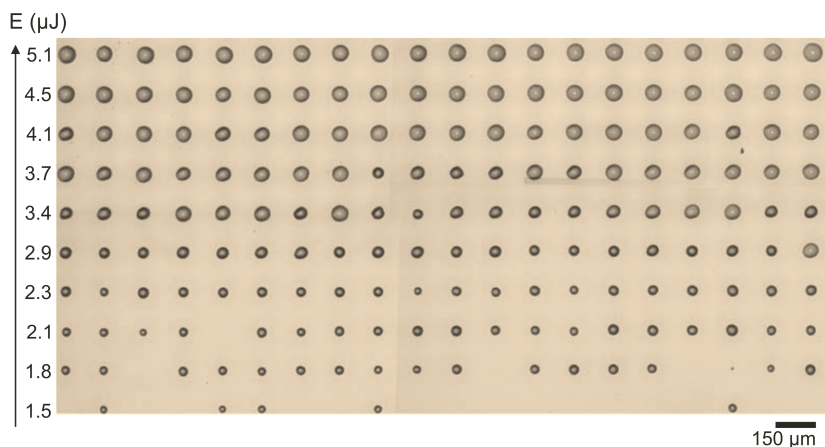


**Figure 1.10:** Circular droplets printed at different laser pulse energies using a donor liquid layer of a 0.05 mg/mL rabbit IgG solution where the solvent was a mixture of phosphate buffered saline powder at 60% (v/v) and glycerol at 40% (v/v). Image adapted from [18].

Time-resolved imaging techniques were used to record the transfer dynamics during the LIFT of liquids [22, 23, 77, 96, 97]. The typical dynamics of a transfer event is depicted in Figure 1.11. A single laser pulse is absorbed at the interface between the donor substrate and the donor film, located in the top of the images in the figure. This generates a cavitation bubble in the donor film that expands, leading to the formation of a jet which elongates until it contacts the receptor substrate, gradually feeding the growing droplet until it breaks leaving the sessile droplet conveniently deposited.

The potential applications of the transfer of different functional materials have addressed the studies on the LIFT technique towards the devising of suitable printing methods for the creation of complex structures. The possibility to shape the printed pixels into a functional structure becomes of high interest for the fab-

<sup>2</sup>Or better, the fluence, energy per unit area on the sample.



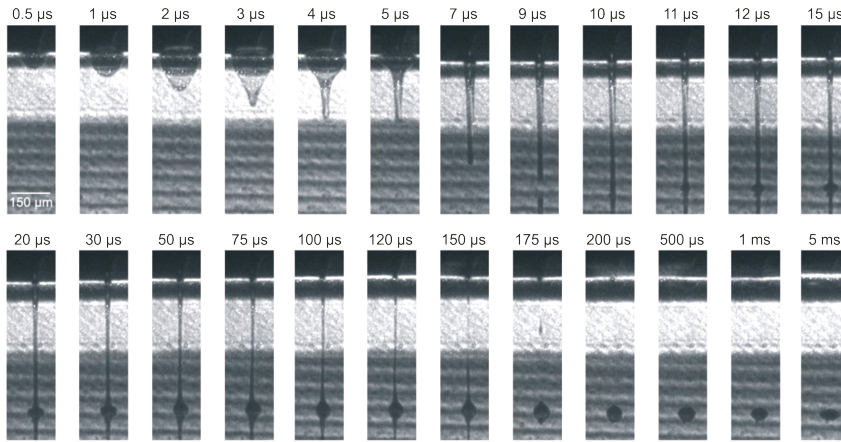


**Figure 1.11:** Time-resolved images of liquid ejection and sessile droplet formation through LIFT at different delay times with respect to the laser pulse. The donor substrate is placed in the top of the images. The laser pulse impinges from the top and the absorbed energy propels the liquid towards a receptor substrate placed in the bottom. Image adapted from [77].

rication of electronic components and interconnects in microelectronic devices [17, 98, 99]. Thus, the group of the Naval Research Laboratory have developed a procedure for the printing of pastes that allows the printing of a complete piece of material that conserves the shape of the incoming laser beam; this approach, however, is not free from drawbacks, like the difficulty of achieving the right rheology for the paste, or the short gaps required to print in a controlled way. [100, 101]. Most approaches, therefore, focus the attention on the printing of overlapping droplets at different separation distances using conductive materials in the form of nanoparticle suspensions, with the aim of forming customized 2D patterns [102–105]. However, the printing of continuous lines with high finishing quality often remains a true challenge; on one side, defects such as splashing and scalloping decrease the quality of the printed lines. On the other side, the onset of instabilities on the printed line usually leads to the formation of bulging, which compromises not only the appearance, but also the functionality of the printed features. Besides, the current demands for the fabrication of electronic devices through digital manufacturing at high speeds have triggered an unexplored area of research for the LIFT of liquids: printing at high speeds. All these aspects require further extensive investigation; this work aims at contributing to that task.

## 2 Experimental

A general description of the experimental setups implemented during the developing of this thesis work is presented in this chapter. The chapter is divided into three sections. The first one includes a description of the laser sources. The second section includes a description of the direct-write setups, including the time-resolved imaging system. Finally, some considerations about issues related with Gaussian beams are included in the third section.

### Laser sources

#### Femtosecond laser

The laser source was from Amplitude Systems, in particular the model s-Pulse. The active medium was a crystal of potassium, yttrium and tungsten doped with ytterbium, Yb:KYW. The output nominal laser wavelength was 1027 nm and the nominal duration of the pulses was 450 fs. The laser can work at repetition rates up to 10 kHz. A scheme of the system is presented in Figure 2.1.

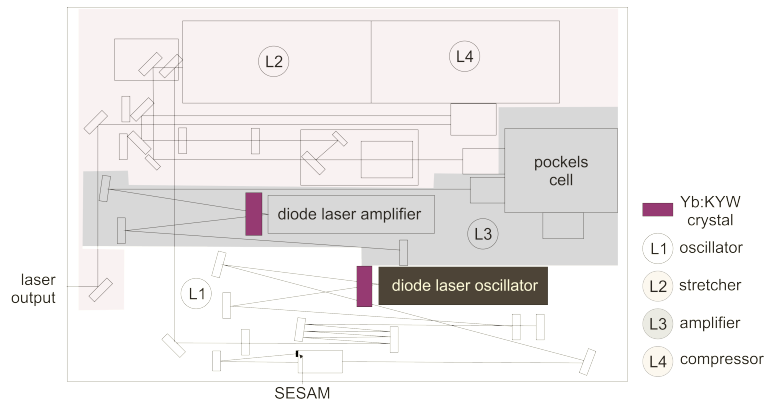


**Figure 2.1:** Scheme of the implemented Amplitude Systems femtosecond laser.

At the output of the laser, the measured beam intensity distribution corresponds to a Gaussian beam with a nominal quality factor  $M^2$  of  $1.4^1$ , and 5 mm diameter measured at  $1/e^2$  of the Gaussian maximum, as it can be observed in the intensity profile shown in Figure 2.2. The pulsed output beam is generated along four different steps: first, a low intensity femtosecond pulse is generated in a mode-locked laser oscillator, producing pulses with energies between 10 and 20 nJ (L1), then the pulse is stretched in (L2) to be subsequently amplified in (L3), to finally undergo a compression in (L4) leading to the high energy femtosecond laser pulse with output energy up to 100  $\mu$ J.

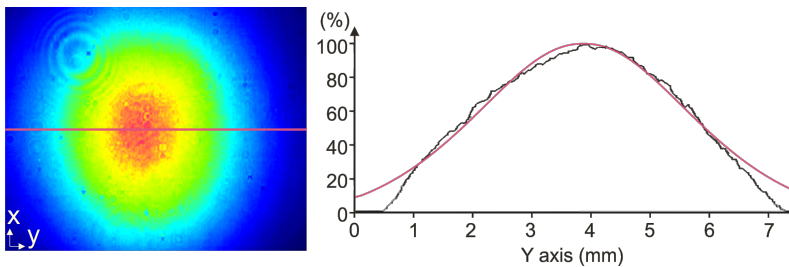


**Figure 2.2:** Image of the beam intensity distribution at the output of the femtosecond laser. The profile corresponds to a cross-section of the beam intensity along the Y axis in the position indicated by the line on the image.

## Nanosecond laser

The nanosecond laser was from Spectron Laser Systems, in particular the model Mini-Q SLMQIT-20. The active medium was a crystal of Nd:YAG with output laser wavelength of 1064 nm and nominal pulse duration of 10 ns. The operation frequency for this laser was from 0.5 to 20 Hz.

Pulsing is achieved by an active Q-switch system that comprises a Pockels cell with a polariser placed inside the resonant cavity. When the Pockels cell is activated, it changes the polarization of the radiation inside the cavity and allows the system to perform the laser effect. Out of the resonant cavity, there were two crystals of potassium dihydrogen phosphate (KDP) that doubled and tripled the frequency allowing the generation of pulses with 533 and 355 nm wavelengths.

<sup>1</sup>Described later in this section.

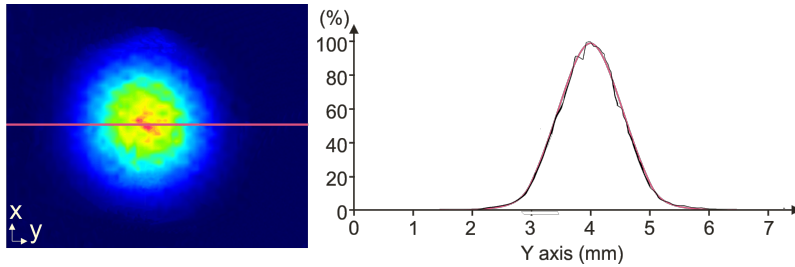


**Figure 2.3:** Image of the beam intensity distribution at the output of the nanosecond laser. The profile corresponds to a cross-section of the beam intensity along the Y axis in the position indicated by the line on the image.

The experiments in this work were performed only with the 355 nm wavelength. The measured beam intensity distribution corresponds to a nearly Gaussian beam with a diameter of 2 mm measured at  $1/e^2$  of the Gaussian maximum, as it can be observed in the intensity profile shown in Figure 2.3. A set of motorized polarisers allowed controlling the laser pulse energy from 1 nJ to 1 mJ.

## Laser direct-write setups

All the following elements have been mounted in its great majority during the development of the present PhD thesis. The optimization of the setups and the computer integration of the different translation stages via LabView programs were performed in parallel to the experiments.

The experimental setups described in the following sections were mounted on an optical bench (Melles Griot, 250 cm long, 125 cm wide) that comprised a triple-plate construction, with internal dampers and four air-suspended legs that formed the support system. It provided a steady, rigid and almost vibration-free working surface. The upper plate of the table disposed M6 mounting holes to enable an excellent fixation of the different elements. The rest of the elements are briefly described in the papers, such as the implemented materials, sample preparation and specific experimental parameters.

## Ablation setup

The ablation experiments presented in Papers 1 to 5 were all performed using the setup composed of the elements illustrated in Figure 2.4. The femtosecond laser radiation passes through a set of two polarisers (P1 and P3) and a half-wave plate ( $\lambda/2$ ) that allows the control of the laser pulse energy. Then, a first beam splitter Bs1 (60T/40R) divides the laser beam in two paths; the transmitted beam allows the measurement of the laser energy with an energy detector<sup>2</sup> (D1), and the reflected beam is directed towards a dichroic mirror (DM) that reflects the infrared (1027 nm) and transmits the visible light to have in situ visualization of the ongoing process by a CCD camera (JAI Protec 07013400) placed coaxially to the laser beam. A microscope objective (M Plan Apo 50 $\times$  and 0.55 NA) focuses the radiation on the sample. In some experiments, the reflected energy was measured by a second energy detector (D2, PD10-PJ-C from Ophir Optronics) that captures the reflected radiation from a second beam splitter Bs2 (10T/90R) collected with a lens (L). Reflectance and transmittance measurements were performed simultaneously with a multi-channel laser power/energy meter (Pulsar 4, from Ophir Optronics).

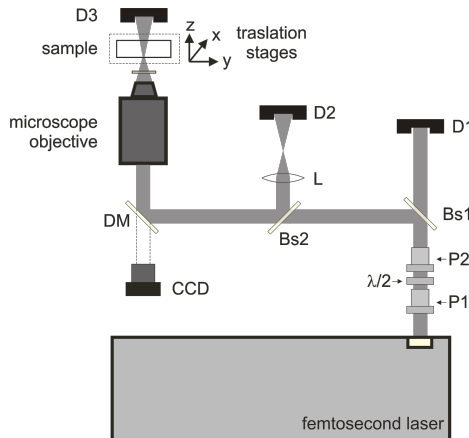


**Figure 2.4:** Sketch of the laser ablation system. P1 and P2: polarisers.  $\lambda/2$ : half-wave plate. Bs: Beam splitters. DM: dichroic mirror. D1 and D2: energy detectors.

Computer-controlled XYZ translation stages (Prior Scientific Systems, Pro Scan<sup>TM</sup> III) allow the translation of the sample with respect to the laser beam. The travel

<sup>2</sup>Depending on the energy range, the implemented detectors could vary: PD10-SH from 1 nJ to 10  $\mu$ J, PD10-V2 from 2 nJ to 20  $\mu$ J and PE10-C from 1  $\mu$ J up to 10 mJ, all from Ophir Optronics.

range of the XY motors is 100 mm with minimum incremental steps of  $0.01 \mu\text{m}$ , and for the Z motor the range is 40 mm with minimum incremental steps of  $0.5 \mu\text{m}$ . The maximum translation speed is 1 mm/s in the XY axis and 2.5 mm/s in the Z axis. Besides, the translation stage is furnished with a sample holder that allows the modification of the tilting level of the sample with respect to the laser beam axis by means of three integrated micro-screws.

## Hybrid setup

The experiments presented in Papers 7 to 9 were all performed using the setup composed of the elements illustrated in Figure 2.5. This is denominated a hybrid setup since it was used to perform experiments of laser ablation, and just by placing properly a donor-receptor system, it was used as a LIFT printing system as well.

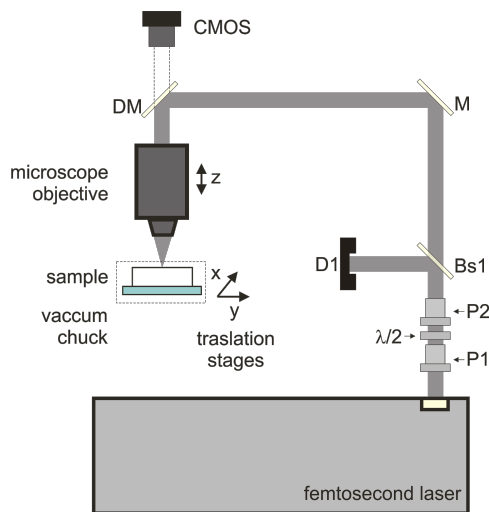


**Figure 2.5:** Sketch of the LIFT hybrid printing system. P1 and P2: polarisers.  $\lambda/2$ : half-wave plate. Bs: Beam splitters. M: mirrors. DM: dichroic mirror. D1: energy detector.

In this setup, the output laser radiation passes through a set of two polarisers (P1 and P3) and a half-wave plate ( $\lambda/2$ ). Then, a first beam splitter (Bs1, 60T/40R) divides the laser beam in two paths; the reflected beam allows the measurement of the laser energy with an energy detector (D1), and the transmitted beam is directed with mirrors (M) towards a dichroic mirror (DM) that reflects the infrared (1027 nm) and transmits the visible light to have in situ visualization of the ongo-

ing process by a CMOS camera (Thorlabs DCC1645C) placed coaxially to the laser beam. A microscope objective (Mitutoyo M Plan Apo 50 $\times$  and 0.55 NA) focuses the radiation on the sample.

In this case, computer-controlled XYZ translation stages from Physik Instrumente incorporate three stages (M-414 High-Load Precision Stage) that allow the translation of the sample in the XY plane. In order to change the focalization of the energy, the position of the microscope objective is controlled independently of the XY stages by the use of a Z axis stage. The travel range of all the stages is 100 mm with minimum incremental steps of 0.5  $\mu\text{m}$  and maximum translation speed of 100 mm/s. In order to ensure the steadiness of the sample, a vacuum chuck coupled to a low vacuum system is placed on the XY translation stages.

## LIFT setup

The printing experiment presented in Paper 6 was performed using the setup composed of the elements illustrated in Figure 2.6. The nanosecond laser radiation passes through a set of polarisers to control the energy. Then, it passes through an acousto-optical modulator (Neos Technology, model N35085-10-350) that selects at will one of the outgoing laser pulses, acting as a beam shutter. The beam gets diffracted after passing through the modulator. A properly placed diaphragm (D) selects the first order of diffraction, while the other orders are blocked. Then, the light is directed by a mirror (M) towards a beam splitter (Bs1, 50T/50R) and a set of two mirrors that enable the production of two quasi-identical beams with similar optical paths. The inter-beam separation is finely adjusted using the tuning knob of one of the mirrors of the optical system. A second beam splitter (Bs2, 50T/50R) directs the two beams to a microscope objective (Thorlabs, 15 $\times$ , 0.32 NA, LMU-15X-351) to be simultaneously focused on the sample, conserving the pre-established inter-beam separation.

The translation stage used in this setup was composed of three computer-controlled XYZ motorized translation stages (Physik Instrumente, model M-126) controlled by Apollo MS85E drivers. The travel range of each motor stage was 25 mm, with minimum incremental steps of 25 nm and maximum translation speed of 15 mm/s. This setup was integrated with the following time-resolved imaging setup that allowed acquiring side-view images of the liquid transfer process.

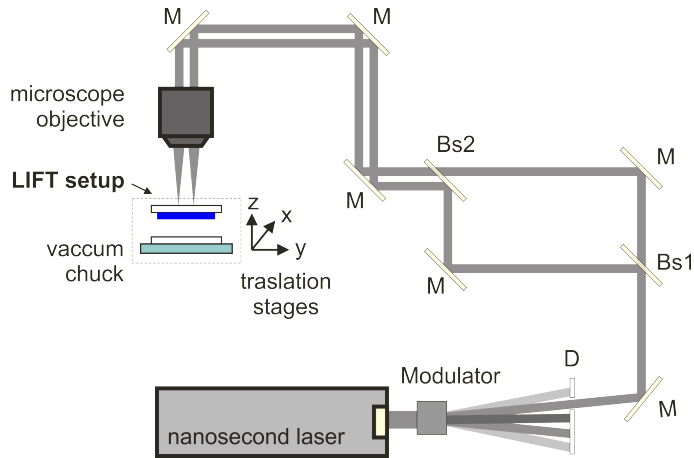


**Figure 2.6:** Sketch of the LIFT printing system. D: Diaphragm. M: mirrors. Bs: Beam splitters.

### Time-resolved imaging setup

The printing of liquids through LIFT occurs in a very short time scale. The visualization of the printing process requires a dedicated imaging system that allows acquiring images at such time scales. Therefore, a stroboscopic system able to take side-view snapshot images of the liquid transfer process was implemented. Each image corresponded to a unique transfer event; since the printing process under the same printing parameters produces a similar outcome, it is possible to reconstruct a stop action movie that allows the visualization of the entire process through the superposition of pictures obtained at different delays respect to the laser pulse. In Figure 2.7 we present a sketch of the implemented setup.

The imaging setup comprised a home-made illuminating source consisting in a red LED (Thorlabs, LED630E, 639 nm) controlled by an electronic driver (Picolas LDP-V 10 70) that allowed setting pulse widths to 100 ns. The outgoing light was then coupled to a condenser lens system composed of two plano-convex lenses (L1 and L2) that illuminated the donor/receptor gap in the LIFT setup. On the other side, a 2 Mp CCD camera (Diagnostic Instruments Inc., Insight IN 1800) coupled to a microscope objective (Thorlabs, 15 $\times$ , 0.32 NA, LMU-15X-351) followed by a teleobjective with a focal length of 100 mm were placed at grazing incidence respect to the donor film. An additional infrared absorber was placed after the



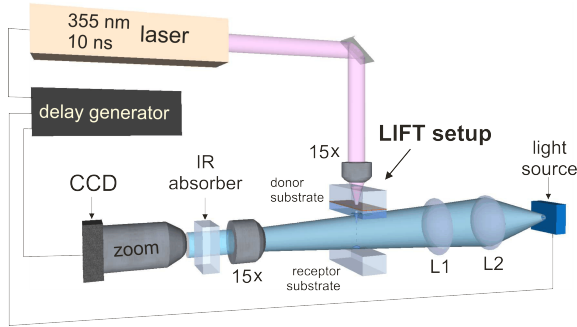


**Figure 2.7:** Sketch of the fast acquisition imaging system.

microscope objective in order to suppress the bright spot from the 1027 nm radiation of the laser pulse. This system acquired shadowgraphy images of the transfer events. The laser pulse, the LED light pulse and the aperture of the camera were triggered through a delay generator (Stanford Research Systems, DG 645) which sets both the duration of the LED pulse and its delay respect to the laser pulse.

## Gaussian beam theory

One of the main laser beam magnitudes that determine the processes in materials processing data analysis is the pulse energy per unit area, known as fluence. The intensity distribution for a Gaussian beam that is propagating in the  $z$  direction in cylindrical coordinates is the following:

$$F(r, z) = \frac{2E}{\pi\omega^2(z)} \exp\left(-2\frac{r^2}{\omega^2(z)}\right). \quad (2.1)$$

where  $F(r, z)$  is the laser fluence,  $E$  is the energy of the pulse,  $\omega(z)$  is the laser beam radius at a given  $z$  position and  $r$  is the radial coordinate. The peak fluence  $F_p$  is given by:

$$F_p = \frac{2E}{\pi\omega^2(z)}. \quad (2.2)$$

Since the beam preserves the Gaussian distribution after passing through optical elements, when the laser beam is used to ablate a material with a fluence abla-

tion threshold  $F_{th}$ , the radius  $r_0$  of the ablation crater can be determined from the equation 2.1 (Figure 2.8):

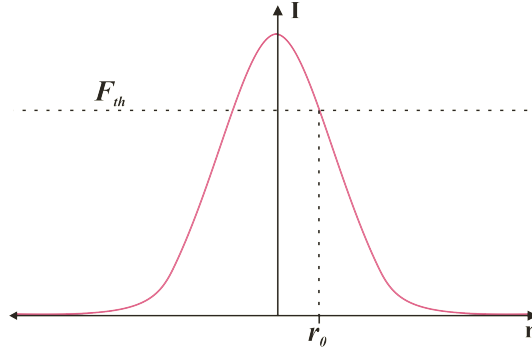


**Figure 2.8:** When a material is irradiated with a laser pulse intensity that overcomes a threshold fluence  $F_{th}$ , it will ideally produce a crater on the material with radius  $r_0$ .

$$r_0^2 = \frac{\omega^2(z)}{2} \ln \left( \frac{F_p}{F_{th}} \right). \quad (2.3)$$

This expression allows finding the beam radius  $\omega(z)$  and threshold fluence  $F_{th}$  of the irradiated material from measurements of the spots made on the surface of the sample and the corresponding incident pulse energies. For example, Figure 2.9 shows the result of an ablation experiment performed on polymethyl-methacrylate. During the experiment, the sample was irradiated with different incident energies at different positions on the XY plane but at the same  $z$  position, producing craters from which the radii were measured.

The radius of the beam changes along the propagation direction according to:

$$\omega(z) = \omega_0 \left[ 1 + \left( \frac{\lambda z}{\pi \omega_0^2} \right)^2 \right]^{1/2}, \quad (2.4)$$

where  $\lambda$  is the laser wavelength and  $z$  is the distance that the beam has propagated from the beam waist  $\omega_0$  (position where the wavefront is flat).

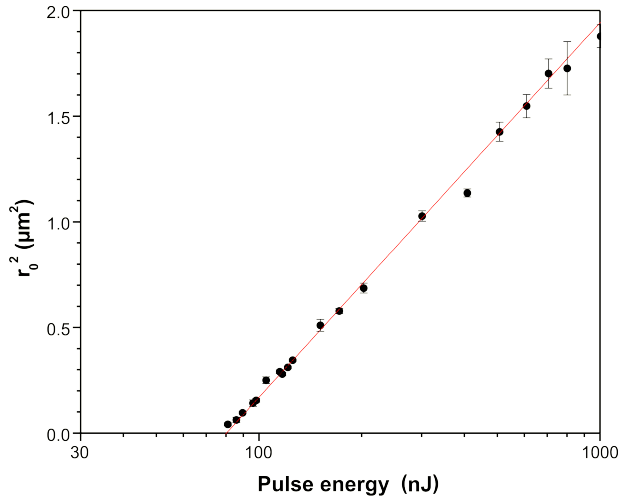


**Figure 2.9:** Plot of the craters radius squared vs the pulse energy. The intercept of the fitted line with the x axis corresponds to the energy threshold for ablation.

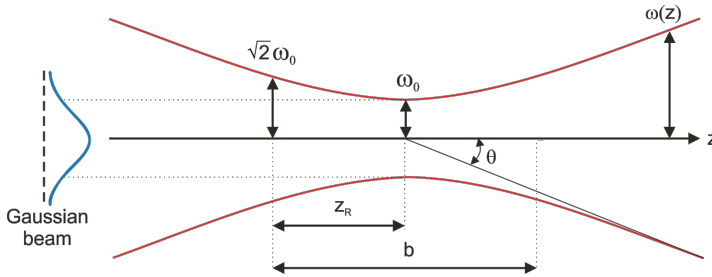


**Figure 2.10:** Gaussian beam parameters associated with angular divergence [106].

The axial range over which the beam can be considered to be collimated is known as the confocal parameter  $b$  (Figure 2.10), which corresponds to two times the Rayleigh length  $z_R$  (equation 2.5). It is also referred to as the depth of focus when focusing a Gaussian beam.

$$z_R = \frac{\pi\omega_0^2}{\lambda}. \quad (2.5)$$

For distances much longer than the Rayleigh length, the radius increases linearly with the propagation distance  $z$ :

$$\omega(z) \cong \frac{\lambda z}{\pi \omega_0}, \quad (2.6)$$

and from here, the divergence of a Gaussian beam is given by:

$$\theta = \frac{\lambda}{\pi \omega_0}. \quad (2.7)$$

Most real beams, however, do not correspond exactly to a perfect Gaussian beam; therefore, an additional parameter which describes how similar the real beam is to the ideal one is introduced. It is known as the quality factor  $M^2$  which is a positive number greater than or equal to 1. The values for the the real divergence  $\Theta_r$  and the real laser beam waist  $W_{0r}$  are then modified a factor  $M^2$  as follows:

$$\Theta_r W_{0r} = \frac{M^2 \lambda}{\pi} \quad (2.8)$$



# 3 Subtractive laser direct-writing

## 3.1. Z-scan focusing technique

This summary contains the results that were published in Papers 1 to 3, corresponding to the development and characterization of the z-scan focusing method.

One of the biggest challenges for the laser ablation of transparent materials with ultrashort laser pulses is producing high resolution patterns on the surface of the sample. This is not a trivial task because slight changes in the position where the energy is being delivered could produce either modification in the bulk material or no modification at all. For this reason, in the presented papers we dedicate special attention to study the z-scan focusing technique that would allow the micromachining of transparent samples on the surface with spatial resolutions that can overcome the diffraction limit. For all the experiments, we used samples of polymethyl-methacrylate (PMMA), which has high transparency in the visible range and chemical stability that makes it a biocompatible material for the fabrication of lab-on-a-chip devices and many biological sensors.

The z-scan method was originally devised as a technique for the measurement of the non-linear refraction index of transparent materials. In this case, changes in the transmitted energy are detected by placing both an aperture and an energy detector after the sample [107]. Our approach is firstly presented in Paper 1, and it follows essentially the same principle as the z-scan technique, but with slightly higher energies and without any aperture between the sample and the energy detector. The principle of operation is simple: series of laser pulses are fired on a transparent sample. Then, a previously calibrated energy detector placed after the sample measures the transmitted energy of each pulse. For every transmittance measurement the sample was also moved horizontally in order to avoid cumulative effects. The sample is then displaced in very small steps<sup>1</sup> towards the position of

---

<sup>1</sup>In Paper 1 the moving steps were of 1  $\mu\text{m}$  while for Papers 2 and 3 the moving steps were of 100  $\text{nm}$ .

the focus, in this case, the Z axis. When the position of the sample is close enough to the focus position, the energy density in the surface increases until it overcomes a threshold for absorption. Thus, the measurements of the transmittance register a decrease, indicating that the material is absorbing part of the incident laser radiation (Figure 3.1A). The drop of the transmittance occurs in a range of positions in the proximity of the laser beam waist. In order to identify with more accuracy the best position where the sample should be placed to produce the smallest modification on the surface (i.e. the position of the laser beam waist), it was necessary to characterize different positions along the transmittance curve. This characterization can be found in Paper 2, where ablation experiments were performed placing the sample at three positions: 'up', 'middle' and 'down' corresponding to transmittance values of 90, 75 and 65 % respectively (Figure 3.1B).

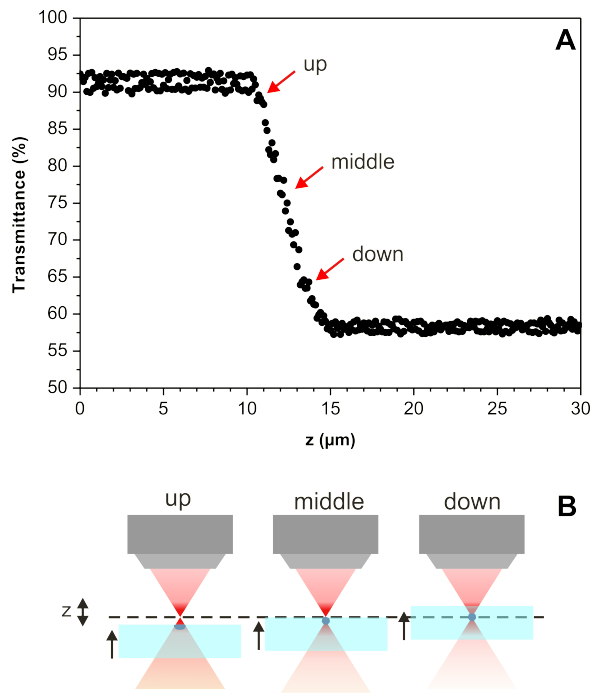


**Figure 3.1:** (A) Typical transmittance curve made at 200 nJ incident energy on a PMMA sample. Three positions are chosen to characterize the z-scan: up, middle and down, where laser ablation experiments at different energies were performed. (B) Sketch of the focusing conditions in the three selected positions close to the sample surface.

Before starting the ablation experiments, the sample had to be perpendicular to the beam axis. A procedure to measure the tilt of the sample along an axis consisted in performing a scan at a fixed  $z$  position. We assume that the perpendicularity of the sample is the appropriate to begin the ablation experiments when longitudinal displacements either in X or Y axis present variations of less than 5 %, that correspond to the fluctuations of the measurements in a steady position. If any modification on the tilting of the sample need to be performed, it can be adjusted by micrometric screws placed in the sample holder. Once the sample is perpendicular to the laser beam, the ablation experiments can take place. They consisted in firing laser pulses of different energy over the sample, producing crater shaped modifications on the surface. Figure 3.2 shows a plot that contains the radii of the craters obtained at the different three positions, and a logarithmic fit for the middle and down positions. Taking into account that the energy distribution of the beam is Gaussian and that there is a fluence threshold for ablation ( $F_{th}$ ), the square of the radius of the crater ( $r_0$ ) should follow a logarithmic trend with the pulse energy ( $E$ ), as mentioned in the Experimental section. Thus, the logarithmic fit would allow finding the values for the laser beam waist  $\omega(z)$  and the threshold fluence for ablation  $F_{th}$  using the following equation:

$$r_0^2 = \frac{\omega^2(z)}{2} \ln(E) - \frac{\omega^2(z)}{2} \ln\left(\frac{F_{th}\pi\omega^2}{2}\right). \quad (3.1)$$

After analyzing the data from the measurements of the crater sizes, the best position to achieve the smallest surface modifications on PMMA corresponds to the middle position. Additionally, this is the best place on the  $z$ -scan curve to detect any change on the  $z$  position in-situ during the ablation process, whereas craters formed at the up position present an irregular shape. Therefore, the up position should be disregarded for high precision ablation. In the case of the down position, the sizes of the craters are similar to the ones produced in the middle positions, but changes in the transmittance cannot be detected when the laser beam waist is in the bulk material.

An improvement to the  $z$ -scan focusing method is presented in Paper 3. The incorporation of an additional energy detector in conjunction with an extra beam splitter placed properly in the optical path allowed measuring the reflected radiation by the sample. In this way, the obtained data from the transmittance mea-



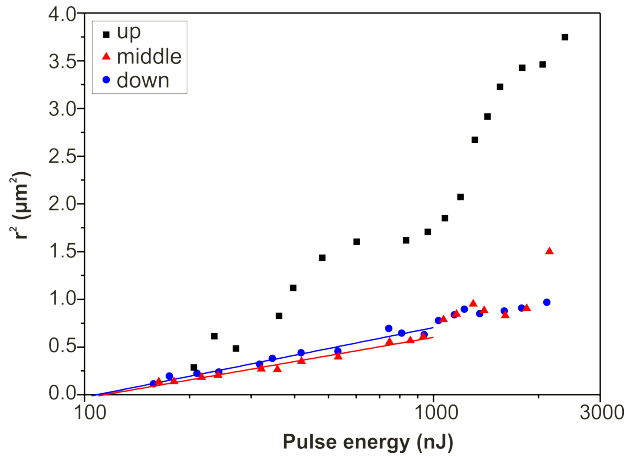


**Figure 3.2:** Plot of the square radius of the craters vs. pulse energy for the three positions where ablation experiments were performed. Solid lines correspond to logarithmic fits for the middle and down series.

measurements is completed by the reflectance data. When comparing reflectance and transmittance measurements, it can be observed that they point out the close presence of the sample surface with respect to the beam waist. Nevertheless, it has to be noted that transmittance measurements can be used with incident energies close to the ablation threshold, while changes in the reflectance can only be detected at higher energies. Figure 3.3 shows the range of positions where changes in the transmittance and the reflectance measurements are detected. Note that for this incident energy, the transmittance changes are detected in a range of  $z$  positions of about  $4 \mu\text{m}$ , while reflectance range is of about  $6 \mu\text{m}$ . The increasing in the accuracy for placing the sample is more evident when it is desired to perform ablation experiments when the sample is placed in the down part of the transmittance curve. The reflectance measurements allows placing the sample in those positions since changes in the reflectance can still be detected, increasing the range where positioning can take place in a controlled way (red shaded area in Figure 3.3).

The smallest ablated craters using only transmission measurements during the  $z$ -scan focusing method had dimensions of about  $200 \text{ nm}$  obtained with an incident energy of  $80 \text{ nJ}$  and  $z$ -steps of  $1 \mu\text{m}$ , which is well below the Airy disk dimensions for the focusing objective at the laser wavelength. The combination of the transmittance and reflectance measurements allows controlling the sample with more

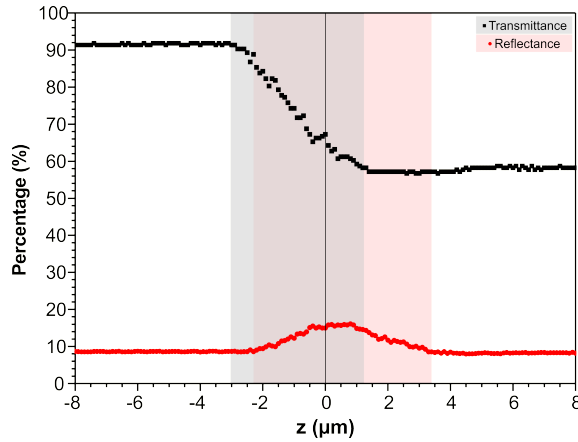


**Figure 3.3:** Plot of the transmittance and the reflectance of PMMA under a z-scan experiment. The incident laser energy was 200 nJ.

accuracy, allowing the production of even smaller craters of 66 nm at 80 nJ with z-steps of 100 nm.

## 3.2. Surface ablation of polymethyl-methacrylate

This summary contains the results that were published in Papers 4 and 5, corresponding to the implementation of the z-scan focusing method to produce surface ablation on polymethyl-methacrylate (PMMA) samples.

Z-scan focusing technique has been characterized before to produce ablation over transparent samples. The results presented in section 3.1 showed that the control on the sample positioning allows obtaining surface modifications with sizes that overcome the diffraction limit. Different studies of ablation using the z-scan focusing method are presented in papers 4 and 5, with the aim to characterize the damage of the sample at different positions of a z-scan and identify the exact position in our system where ablation on the surface is produced. This was done following different analysis: the first one was the characterization of the irradiated areas in the surface through AFM measurements and also in the bulk material using focused ion beam (FIB). The second one was the comparison between the experimental measurements of the crater sizes and the theoretical ones using a simulation of the laser beam radius along the propagation direction. With these

results, we could find the position of the laser beam waist by comparing both experimental and theoretical data, and at the same time, determine the best position to perform laser ablation *only* in the surface. Finally, since the surface fabrication of 2D patterns requires the overlap of single pulses, we investigated the changes on the transmittance curves when the accumulation of pulses takes place in the surface micromachining of lines.

In Paper 4, we performed z-scan experiments with different energies over a PMMA sample. Figure 3.4A shows a plot of the experimental average diameter versus z-position for the four different z-scans. In order to compare this data with theoretical diameters, it was necessary to calculate the laser beam radius along the Z axis. As a first approximation, we implemented the  $M^2$  model [106], that takes into account the quality factor of the laser Gaussian beam. Using a 0.55 NA focusing objective, the theoretical value for the laser beam waist  $\omega_0$  is  $0.6 \mu\text{m}$  at this wavelength. Since the experimentally obtained value for  $\omega_0$  results to be  $0.8 \mu\text{m}$ , the real quality factor is calculated as  $M^2=1.5$ . From this simulation, the theoretical values for the craters diameters were obtained, and the data is plotted in Figure 3.4B. Unfortunately, the obtained results using this model do not agree with the trend followed by the experimental data. Therefore, we used vector diffraction theory, taking into consideration the clipping factor between the beam diameter and the rear objective aperture, in our experimental setup  $\gamma=1.2$ . The theoretical crater diameters using this model are shown in Figure 3.4C, and in contrast to the  $M^2$  model, it describes much better the experimental data. From this plot the position of the laser beam waist is defined at  $z = 0 \mu\text{m}$ . Figure 3.4D contains a plot of the laser beam radius along the z-axis for both models. The main differences are found especially in the positions close to the beam waist. The vector diffraction theory simulation presents an elongated beam waist which supposes a wider range of positions where ablation occurs, as it is confirmed by the theoretical diameters shown in Figure 3.4C.

It has to be noted that the vector diffraction theory data describes well enough the experimental measurements when the laser beam waist is outside the sample (negative positions on z). Since the maximum energy density is located outside the sample, there is no major interaction in bulk and modification of the surface is only dependent on the local laser fluence. In contrast, when the beam waist is located inside the sample (positive positions on z), the focalization in bulk might

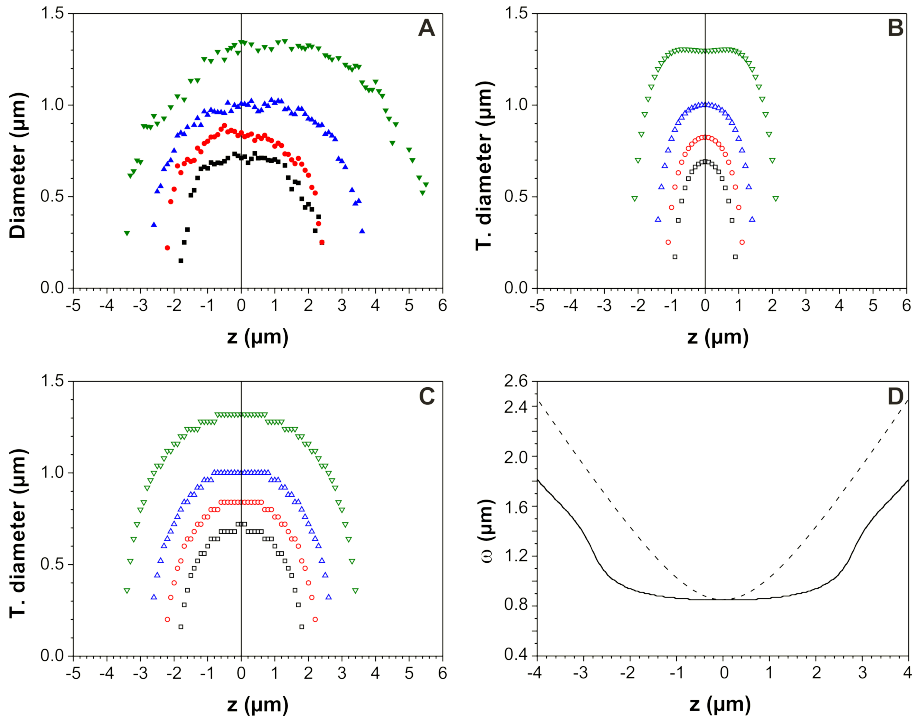


**Figure 3.4:** (A) Plot of the average diameter versus  $z$ -position. (B) Theoretical diameters following the  $M^2$  model. (C) Theoretical diameters following the vector diffraction theory. (D) Plot of the beam radius along  $z$ -axis following two different methods: the dashed line plot was calculated following the  $M^2$  model, while the continuous line plot was determined through vector diffraction theory.

produce modifications inside the material that cannot be predicted only with the analysis of the fluence in the surface.

Interestingly, after an inspection through AFM measurements, the craters at the beginning and the end on the transmittance curve of a  $z$ -scan present similar morphology and depth despite that a different amount of energy was absorbed. Besides, under some specific experimental conditions, surface swelling in form of bumps with submicrometric dimensions have been observed. An additional characterization was performed inside the material under the irradiated areas, since presumably the incident energy was causing damage inside the sample. Thus, FIB ablation technique was used to ablate some of the craters of the  $z$ -scan made at 125 nJ (Figure 3.5).

The morphological study shows that the bulk material below the irradiated area is damaged in most of the z-positions. These modifications present a porous structure that displaces along the z-axis according to the position of the sample relative to the beam waist. When working with ultra-short laser pulses, and besides non-linear absorption, some non-linear propagation effects such as self-focusing are usually presented [108]. This occurs when a beam of sufficient intensity travels through a material and produces refractive index changes in the volume that is exposed to the incoming laser radiation. As a consequence, the material itself acts as a lens producing the subsequent focusing effect. The enlargement of the porous structure presented during our experiments is likely produced by self-focusing, since the critical power to produce this effect in PMMA (40 kW) is vastly overcome in our experiments [109]. Importantly, the only positions in the z-scan that remained undamaged in bulk correspond to positions where the transmittance drop begins. Therefore, modifications only on the surface will occur if the sample is placed in those positions.

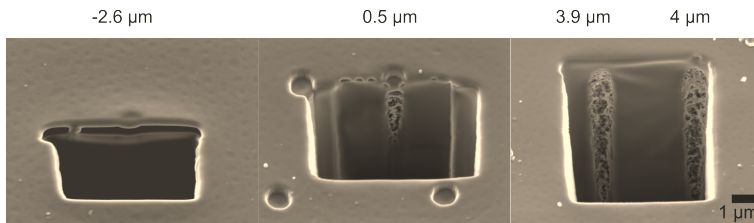


**Figure 3.5:** SEM images of the craters produced in a z-scan made at 125 nJ showing a transverse section made on the material through FIB ablation (tilt: 45°). Z positions correspond to -2.6, 0.5, 3.9 and 4 μm in a transmittance curve made at 125 nJ of incident energy.

The feasibility for the production of lines over a sample of PMMA was also tested by overlapping consecutive shots on the surface of the sample. Experiments at different positions over a transmittance curve from a z-scan were used to produce continuous lines in the surface of the material, and at the same time transmittance measurements were acquired. The comparison between the transmittance curve of single shot experiments with the ones obtained during the formation of the lines shows that the transmittance values are generally lower. This effect is more pronounced for increasing incident energies. Besides, the range in z where the transmittance decreases is wider. These can be associated to accumulative effects

that occur when the spots overlap. In terms of the morphology of the ablated lines, if the sample is positioned in the upper position of the transmittance curve, the lines presented some discontinuities, but as the distance between the sample and the laser beam waist decreases, the lines became continuous and presented similar morphology over a wide range of z-positions. The inner roughness of the lines had a quasi-periodic porous structure with some ripple ordering for some incident energies. The average periodicity of the ripples seemed to be independent of pulse energy and z-position. Although at high energies, the porous structures became more randomly distributed with similar orientation (perpendicular to the line direction). In order to evaluate the inner morphology of the material, cross-section experiments were performed (Figure 3.6).

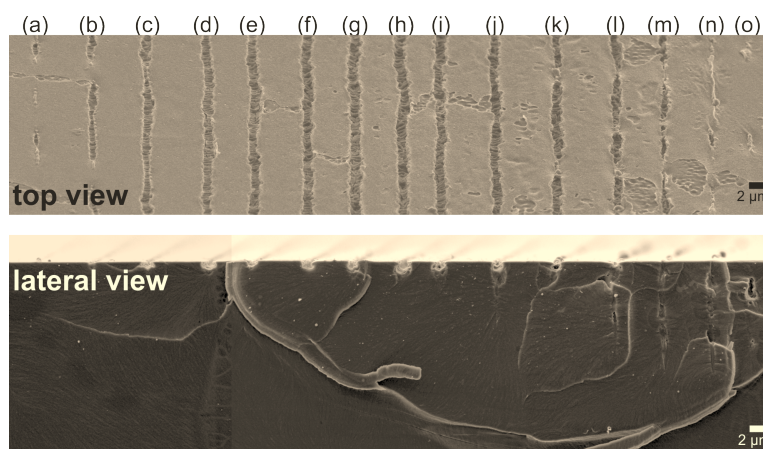


**Figure 3.6:** SEM images of the PMMA surface after the incidence of pulses of 100 nJ separated 0.2 μm at different positions along the Z axis: (a) -2.8, (b) -2.2, (c) -1.6, (d) -1.1, (e) -0.5, (f) 0.1, (g) 0.6, (h) 1.2, (i) 1.8, (j) 2.3, (k) 2.9, (l) 3.5, (m) 4.0, (n) 4.6, and (o) 5.2 μm.

From these results it can be concluded that there is a region of positions on the transmittance curve where the sample can be placed close to the laser beam waist and produce modifications on the surface of the sample with control of the z-position. However, it has to be noticed that true surface modification without bulk damage is only possible in the upper positions on a transmittance curve of a z-scan, as it has been confirmed with the FIB ablation characterization. Finally, the production of lines by overlapping laser shots on the surface of the PMMA was

proven feasible by controlling the position of the sample through the transmittance measurements.

# 4 Additive laser direct-writing

## 4.1. High speed printing

This summary corresponds to the results that were published in Paper 6, devoted to the analysis of the interaction between adjacent jets addressed to investigate very high speed printing. That work was carried out in collaboration with the French laboratory LP3 from the Aix Marseille University (leader: P. Delaporte) and the Swiss company DI Projekt AG (leader: G. Hennig).

LIFT has been demonstrated to be a suitable technique for the controlled high-resolution printing of a wide range of materials in several applications. Despite all the research aiming to optimize the LIFT of liquids (studies on the laser pulse energy, pulse duration, or solution properties, among many others), the influence of the printing speed has not yet been analysed in detail. This is relevant because the processing speed is an essential parameter for in-line fabrication such as in roll-to-roll production.

The feasibility for high speed printing with LIFT has been proven before. The DI Projekt AG company, from Switzerland, developed an industrial-scale machine for printing through LIFT in the packaging industry that allowed unprecedented throughputs of 1.3 m<sup>2</sup>/min at 600 dpi resolution [110]. One of the problems that DI Projekt AG had to face, though, was that at the highest printing speeds two consecutive laser pulses expected to produce two separated pixels in fact resulted in only one distorted pixel, something with a detrimental impact in the printing outcomes. The motivation of this paper arised from our attempt to solve this problem, a solution which led to the discovery of a phenomenon of interaction between liquid jets which understanding results essential when printing at very high speeds.

The machine of DI Projekt AG used a high repetition rate laser (24 MHz) operating at scanning speeds of 1016 m/s. Since the average jet lifetime in a print-



ing event is about a few hundreds of microseconds, at MHz laser pulse rates two consecutive jets are formed almost simultaneously; therefore, it is possible that consecutive jets that are produced at very small separation distances present certain interaction that may affect the quality of the printed outcomes. In order to study the printing dynamics at those speeds, the same printing conditions should be ideally reproduced, but such high speeds cannot be replicated in our experimental setup. Given that consecutive jets formed at those speeds are practically simultaneous, we can emulate the high speed printing conditions by generating two simultaneous laser pulses, with the corresponding laser spots separated a distance which can be varied at will. This is achieved by the division of the main laser beam in two quasi-identical beams by the use of beam splitters and mirrors. Then, the beams are focused simultaneously on the donor substrate by a microscope objective, as it is depicted in Figure 4.1.

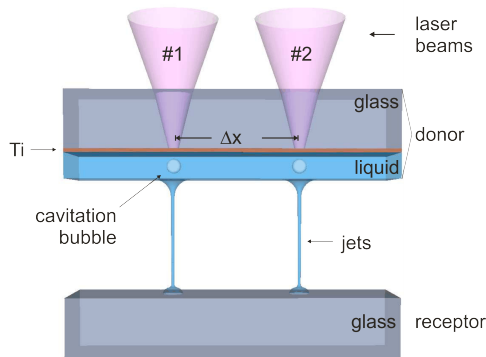


**Figure 4.1:** Sketch of the two-beam LIFT printing setup. Both jets are generated simultaneously using different inter-beam distances  $\Delta x$ .

The experiments were performed in two correlated steps. The first one was the characterization of the printed outcomes for simultaneous (both beams) and alternate (first beam #1 and then #2) modes at different inter-beam distances  $\Delta x$ . The second one was a time-resolved imaging study of the jetting dynamics taking place during the previous experiments. Basically, three different situations were analysed based on the inter-beam distances. A first situation presented when that distance is much larger than the droplet diameter showed the printing of separated droplets using both printing modes, alternate and simultaneous. The time-resolved imaging study confirmed that jet-jet interaction was not present. This situation is

not different from the printing of single jets studied before [111]. Isolated droplets were printed independently of the printing mode, since the separation between droplets was large enough to avoid droplet contact in the receptor substrate.

The second situation corresponded to very small separations, smaller than the droplet diameter: in this case, the printing outcomes in the receptor substrate were elongated droplets for both modes, alternate and simultaneous. In the case of the alternate printing mode, the droplets overlap in the receptor substrate. On the other hand, in the simultaneous mode, the time-resolved imaging study showed the formation of almost a single jet which originated from two bubbles that contact each other during their expansion in the donor film.

A third situation using intermediate printing distances (but larger than the droplet diameter) showed unprecedented results: the alternate printing mode produced two isolated droplets, while the simultaneous produced only one droplet with an elongated shape, similar to the one obtained using very small printing distances. The time-resolved imaging study showed that the interaction between consecutive jets occurs from the early stages of the bubble formation. In comparison with the classical single-beam printing, the presented dynamics has additional elements such as the formation of a second thicker jet, or the thin jet deflection which provide clear evidence of the interaction of two consecutively generated jets. A selection of results for the first and third situations are presented in Figure 4.2.

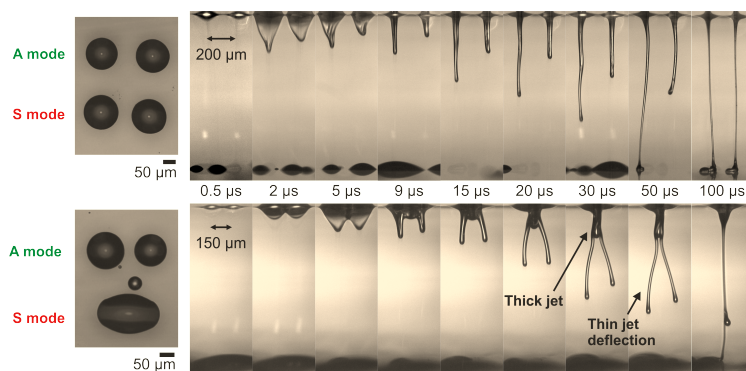


**Figure 4.2:** Selection of results for 200 and 150 μm separation distances. On the left: printed outcomes in both modes, alternate (A mode) and simultaneous (S mode). On the right: images of the time-resolved study in simultaneous printing mode. The laser is impinging the donor substrate from above, propelling the liquid towards the receptor substrate placed at the bottom.

All these results indicate that depending on the inter-beam separation there is significant jet-jet interaction that leads to the printing of substantially different outcomes. The observed dynamics has been attributed to changes in the pressure distribution inside the liquid induced by the contact of the two bubbles with each other. This jet interaction may have important implications during high-speed liquids printing since it could lead to undesired deviations from the expected printing outcomes.

## 4.2. Line printing

This summary corresponds to the results that were published in Paper 7, devoted to the development of strategies for the printing of continuous and stable lines aimed to fabricate functional conductive paths. That work was carried out in collaboration with the English companies Oxford Lasers (leader: D. Karnakis) and CPI (leader: S. Ogier), and the Catalan company Sensofar Tech (leader: R. Artigas).

The production of electronic devices in an ever decreasing scale requires the fabrication of functional electric interconnections with small dimensions. Direct-write techniques such as LIFT can potentially be used for the formation of continuous lines of functional conductive materials with high spatial resolution. In spite that most of the work on the LIFT of liquids has devoted the attention to depositing isolated droplets, there has been some research on printing lines as well. The feasibility of LIFT to produce lines of conductive materials from solid donor films and liquid nanoparticle inks has actually been reported before [102, 104, 105]. However, in many cases the most common printing defects are still present<sup>1</sup>: on one side, long lines often present discontinuities that compromise their functionality as conductive paths, and on the other side, the printed liquid usually results in the formation of bulges of material that can produce unwanted short-circuits between adjacent lines. In this work we present effective printing strategies aiming to demonstrate the feasibility of LIFT to fabricate continuous and stable lines of conductive inks for the fabrication of bulge-free conductive paths.

---

<sup>1</sup>Those defects are not exclusive to LIFT. They are also found in more conventional printing techniques, like in ink-jet printing [31, 34, 112].

The experiments consisted in printing series of single droplets with different separations  $\Delta x$  (measured from center to center of two consecutive droplets). As  $\Delta x$  decreases, first the droplets start to coalesce forming dashed lines and then, interestingly, in all the separations where a continuous line is printed, the formation of a bulge of liquid takes place, mainly at the beginning of the line and occasionally at the middle. Bulging is attributed to capillary flows arising from an instability produced inside the liquid due to small variations in curvature of the line between the newly printed droplets and the previously printed line.

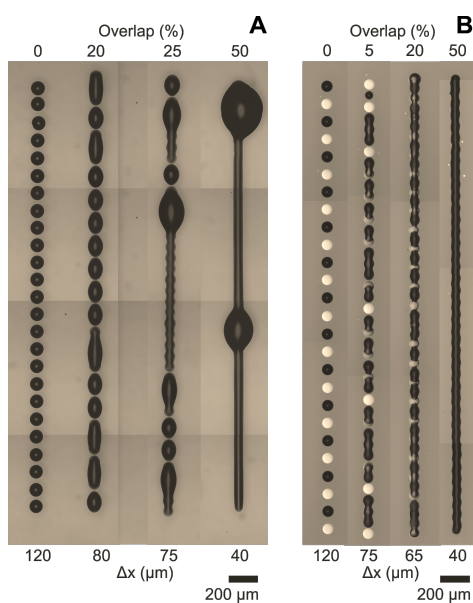


**Figure 4.3:** Ag ink lines printed with different printing separations between adjacent droplets ( $\Delta x$ , measured from center to center) decreasing from left to right following (A) alternate printing mode, where bulges are perfectly visible, and (B) alternate printing mode with an intermediate drying step; bulging has been completely eliminated. The dark dots/lines correspond to liquid ink, while white dots correspond to dried droplets.

A second experiment aimed to understand the origin of the bulge formed at the beginning of the line consisted in printing lines with increasing number of droplets (1,2,3...). The experiment demonstrated that the initial bulge starts forming at the very early stages of the line growth, but that it keeps growing all the time, being fed by capillary flow originated at distant positions along the line. Such directionality in bulge formation suggested a second printing strategy, devised to minimize

the inner liquid flow that can be present during the formation of the line. It consisted in the alternate printing of droplets separated in two different sets: even droplets were printed first without overlap between them, and then the odd ones followed. In this way, the continuous line formation occurs only when the second set of droplets is printed. The results of this experiment showed a decrease of bulging for some of the printing separations, but not its total elimination.

A third printing sequence was tested taking into account that alternate printing managed to reduce bulge formation. In this case, odd droplets were printed on the receptor substrate followed by an intermediate drying step. Thus, when the even droplets were printed, the odd ones were completely dried. Following this printing sequence it was possible to mitigate the capillary flow inside the printed liquid, allowing the fabrication of long continuous and stable lines completely free from bulging. Finally, the conductivity measured on laser sintered lines reached values close to the nominal, which is a positive indicator that the lines can be used as functional conductive paths.

### **4.3. Microlenses fabrication**

In this section, and for the sake of completeness, we include additional unpublished work presented in Paper 8, which has been sent for publication to ACS Materials and Interfaces. In this work, it is presented a printing approach based on LIFT aimed to the fabrication of high quality polymeric microlenses. The work was carried out in collaboration with the Italian research center IIT (leader: A. Diaspro).

The fabrication of micro-optical components is playing an important role in the development of functional devices such as detectors, organic solar cells and camera sensors [113, 114]. Fabrication methods that implement masks or molds such as photolithography, microcontact printing and chemical etching have been used for the fabrication of microlenses before, but its customization and positioning at user defined locations are often expensive and time consuming process. Direct-write techniques appear more suitable to address these challenges, but they present some drawbacks that have to be considered; ink-jet printing, for example, is seriously constrained by the rheology and viscosity of the liquids, requiring in most of the cases either an extensive work of engineering on the ink and/or expensive customization of the used setup. In particular, liquid optical prepolymers that are

adequate candidates for the fabrication of microlenses are too viscous to be printed with conventional ink-jet systems, which typical operational viscosities range from 1 to 50 mPa.s. LIFT is presented as an interesting alternative since it allows the transfer of liquids with a wider range of viscosities. Therefore, in Paper 8 we present a LIFT based approach that allows the printing of a highly viscous optical prepolymer (dynamic viscosity ranging between 120 and 150 mPa.s) for the fabrication of tailored high quality microlenses with different optical properties at specific positions on a receptor substrate.

Basically, our approach consisted in two steps: first, we performed LIFT using a donor film of a photo-curable optical polymer, producing microdroplets on the receptor substrate which size can be controlled by adjusting the incoming laser energy. Then, the receptor substrate with the printed droplets was exposed to a curing treatment with UV radiation in order to promote the cross-linking of the polymer. The surface tension of the polymer when it is still liquid provided the printed microdroplets with an almost perfect spherical shape that is preserved after curing, allowing the production of plano-convex microlenses. Since the microdroplets were positioned exactly where the laser beam impinged the donor film, this printing procedure allows the fabrication of microlenses at user-defined positions. Arrays of microlenses in PDMS and glass are presented in Figure 4.4. The overall process is reproducible and in all cases the fabricated microlenses present high optical quality. It is important to note that following this process, the transferred volumes (that ranged from 25 fL to 9 pL for PDMS and from 220 fL to 9 pL for glass), are well below the limits of conventional ink-jet systems.

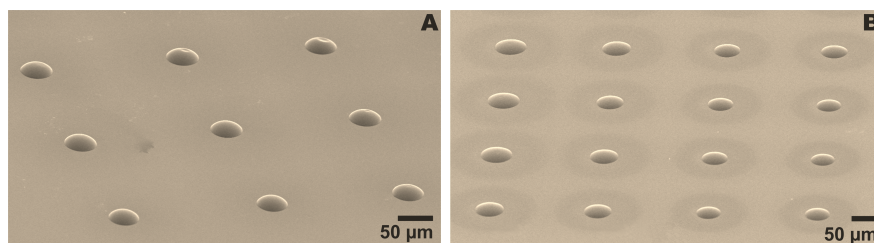


**Figure 4.4:** (A) SEM image of microlens arrays fabricated on PDMS, and (B) on glass. Images were acquired with a 60° viewing angle.

Experiments using a wide range of energies were carried out in order to find

the best printable conditions for the controlled fabrication of microlenses. Then, arrays with different diameters were printed on both substrates and then characterized. SEM and AFM morphology images confirmed the high overall quality of the microlenses surface in terms of their roughness and sphericity, as it can be observed in Figure 4.5A-B. Root mean square error (RMSE) values obtained from the acquired data corresponded to high precision grade lenses. From point spread function (PSF) measurements it was possible to determine that the focal length increases with the lens diameter for both PDMS and glass substrates, but due to the presence of spherical aberration the experimental focal lengths cannot be described using paraxial optics. Instead, theory of third order aberrations was used to model the focal lengths, showing a good agreement between theoretical and experimental values. Furthermore, and also in good agreement with this theory, the numerical aperture of the microlenses only depends on the refractive index and contact angle of the polymer with the substrate. Therefore, for a given polymer the liquid microlenses can be fabricated with different numerical apertures by only changing the receptor substrate.

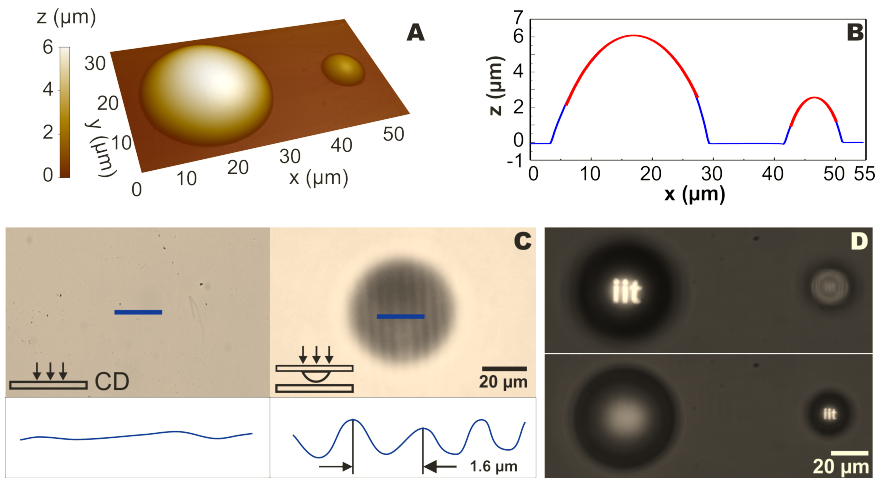


**Figure 4.5:** (A) AFM topography map of two microlenses with diameters of 7 and 26  $\mu\text{m}$ . (B) Profile along the X axis of the droplets presented in (A) showing a nearly perfect spherical shape (red line fitting curve). (C) Optical microscope image of the surface of a CD (line pitch 1.6  $\mu\text{m}$ ) without and with the microlens on top. The increased resolution allows resolving the CD lines. (D) The projected image of a mask (IIT) appears in or out of focus depending on the focal length of each microlens.

In order to demonstrate the functionality of the printed microlenses, imaging experiments were carried out. For example, they were used to enhance the resolving power of an optical system to visualize the fringes on the surface of a CD through a conventional optical microscope (Figure 4.5C). In another experiment, the image of a mask with the letters IIT was projected through a microlens array and collected with a microscope objective, showing that the produced image is in or out of focus depending on the focal length of the microlenses (Figure 4.5D.)

In conclusion, these results prove the feasibility of LIFT for the printing of a highly viscous prepolymer for the fabrication of customized microlenses which optical properties can be selected by changing the laser parameters and the wetting properties of the receptor substrate.





# 5 Combined approaches

## 5.1. Nanopatterning with liquid microlenses

This summary corresponds to the results that were published in Paper 9, corresponding to the fabrication of liquid microlenses through LIFT for the surface nanopatterning of materials. That work was carried out in collaboration with the Italian research center IIT (leader: A. Diaspro).

Usually, optical systems are inherently limited by diffraction, which imposes a barrier to the maximum achievable resolution. This problem is also present in laser direct-write systems, in which the minimum feature size is limited to almost half of the wavelength that is used to irradiate the material of interest. In order to overcome this barrier, the incorporation of microlenses to use the near field effects allows producing deep sub-wavelength patterning, which is of clear interest for nanopatterning with visible and infrared wavelengths. An interesting solution is the use of solid immersion lenses that consist in the use of dielectric hemispherical lenses placed in contact to the substrate. These lenses increase the numerical aperture of an optical system that in turn increases its lateral resolution, only limited by the quality of the microlenses and the refractive index of the material used to fabricate them. However, this solution establishes additional challenges in terms of the fabrication techniques to produce high quality microlenses at specific locations.

Current techniques such as polymerization, chemical etching and microcontact printing are multi-step and time consuming procedures that besides require complex control systems to place the microlenses at user-defined positions. As an alternative allowing to overcome this drawbacks, in Paper 9 we present a droplet-assisted laser processing (DALP) approach that uses liquid microdroplets as microlenses to increase the resolution of a conventional direct-write laser system. The LIFT of a thin layer of liquid is performed with the aim of printing microdroplets at specific locations on the receptor substrate, and the process is then completed by

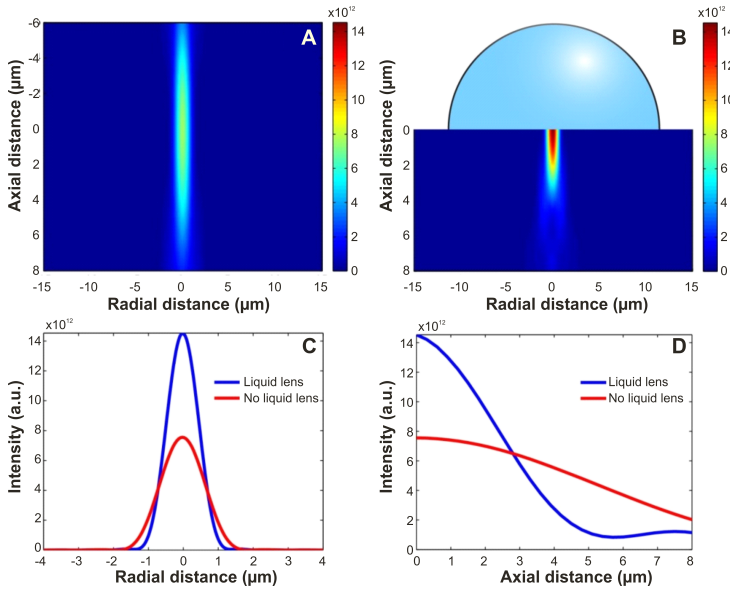


**Figure 5.1:** (A) Colormap plot of the intensity distribution of a Gaussian beam focused through a 0.27 N.A. objective, (B) corresponding colormap plot after a hemispherical droplet ( $n = 1.4$ ) has been placed at the laser focus. (C) Plot of the beam intensity versus radial distance at focus. (D) Plot of the beam intensity versus axial distance along the optical axis.

focusing laser pulses through the liquid microdroplets on the surface of the receptor substrate in order to thus generate a spot with reduced dimensions.

The formation of liquid microlenses with a contact angle on the substrate of about  $90^\circ$  is especially desirable; in this way, they will present an almost perfect hemispherical shape, so that the effective numerical aperture of the optical system is increased a factor that corresponds exactly to the refractive index of the printed liquid. In order to better understand the optical behaviour of the droplets, we performed simulations of the intensity distribution of the focused radiation through a microscope objective with and without the droplet (Figure 5.1). The results using the droplet show an increase of the total intensity at the focus position and a reduction of the Rayleigh length that is in accordance with the increased numerical aperture. Besides, the radial intensity distribution using the droplet shows a reduction of the full width at half maximum, which is ideal to increase the spatial resolution of the patterned features.

The fabrication of the microlenses was performed by printing a solution of water, glycerol and surfactant to produce the droplets through LIFT on a thin layer of PDMS. This combination of liquid-substrate was chosen since they allow the formation of contact angles of around  $90^\circ$ . The droplet diameter was controlled by changing the incident pulse energy. Then, the substrate that contained the liquid donor film was removed and the position of the laser beam waist was adjusted to match the planar surface of the already formed microlens. At this point, the DALP approach can be used following two different modes: the first one, that can operate at high incident energies, allows the production of a single spot per liquid microlens. Under these conditions the droplet could be deformed or even destroyed when the laser pulse is fired, but this does not constitute a critical drawback since the liquid droplets can be re-printed again at the desired position to produce another spot. The second mode is devised to operate at very low energies and it is specially suitable for the production of 2D patterns; because of the low energies, the droplet remains unaltered after focusing consecutive laser pulses. Thus, if the pattern dimensions are small enough, this can be produced inside a single droplet by simply scanning the surface with overlapping spots.

In order to find the optimum operation conditions of DALP, we performed ablation experiments with very low energies using droplets of  $100\ \mu\text{m}$  diameter. Thus, arrays of craters at different  $z$  positions along the beam axis were produced. The results showed an axial and radial range where the sizes and depths of the craters are practically constant, in agreement with numerical simulations for different droplet sizes. In order to compare the conventional laser direct-writing method with DALP, ablation experiments in the absence of the droplet were performed with different pulse energies at the same axial positions (same focusing conditions). Results show that resolution is indeed improved with DALP, which is in good agreement with the increment of the effective numerical aperture. Interestingly, at very low energies, the ablation with DALP is feasible, producing craters with nanometric dimensions ( $250\ \text{nm}$  with a wavelength of  $1027\ \text{nm}$ ) while the laser processing without the droplet does not produce any visible modification on the surface at all.

Finally, the feasibility for nanopatterning was demonstrated by scanning the surface of a droplet using very low energies, allowing the production of 2D patterns on the surface of the irradiated material (Figure 5.2).

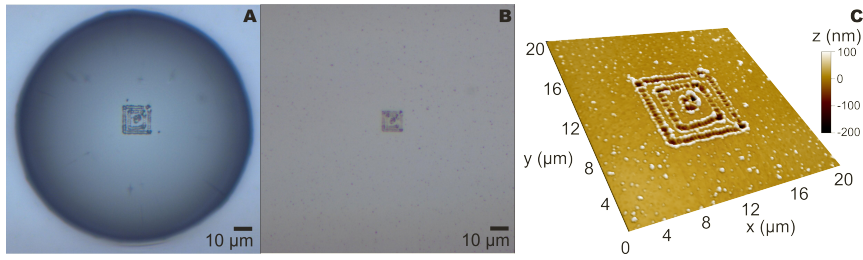


**Figure 5.2:** Optical micrograph of a pattern fabricated with a 100  $\mu\text{m}$  droplet, (A) with the droplet still in place and (B), without droplet. The drop produces a magnification of about a factor of 1.5. (C) AFM characterization of the pattern.

## 5.2. Line printing in fluidic guides

This summary contains the results that were published in Paper 10, devoted to the laser microfabrication of fluidic channels for the formation of high quality conductive lines printed through LIFT. That work was carried out in collaboration with the English companies Oxford Lasers (leader: D. Karnakis) and CPI (leader: S. Ogier), and the Catalan company Sensofar Tech (leader: R. Artigas).

The LIFT technique has already been proved feasible for the printing of lines of functional materials to fabricate electrical interconnections. However, as shown in Section 4.2, the formation of continuous lines free from defects (bulging and scalloping) is not a trivial task. In the same section we presented a LIFT based approach that consisted in the fabrication of continuous lines free from bulge by printing overlapping droplets with an intermediate drying step. In spite of the success of the approach, the whole process was time consuming and the line edge presented some residual scalloping that is detrimental for the overall printing quality. Therefore, alternative printing strategies are needed to address all these challenges. In this work we present a different approach that consists in the printing of conductive inks through LIFT inside previously laser ablated fluidic guides that allow confining the liquid following the geometry of the pre-fabricated pattern.

The experiments to demonstrate the feasibility of the proposed approach are divided in two parts: first, fluidic guides were created on a substrate through laser ablation. Then, a silver nanoparticle ink was printed inside the guides through LIFT. It is important to note that the whole process is done using the same laser

for ablation and printing. The used substrate was glass covered with a thin layer of polymer. Then, laser pulses were focused on the surface of the polymer to produce the selective ablation of the layer, leaving intact the glass substrate underneath. Thus, the depth of the fluidic guides is determined by the thickness of the polymer layer, in our case  $1\ \mu\text{m}$ . Importantly, the polymer layer surface was substantially more hydrophobic than the glass substrate in order to produce a good liquid confinement once the liquid is deposited inside the fluidic channel.

A first printing experiment was performed using the same separation distance between two consecutive droplets (measured from center to center) inside pre-fabricated fluidic guides of different widths (Figure 5.3A). The results of this experiment showed that the liquid is confined within the guides until some extent; the finishing quality of the border is affected by the presence of debris that remained after the laser ablation process.

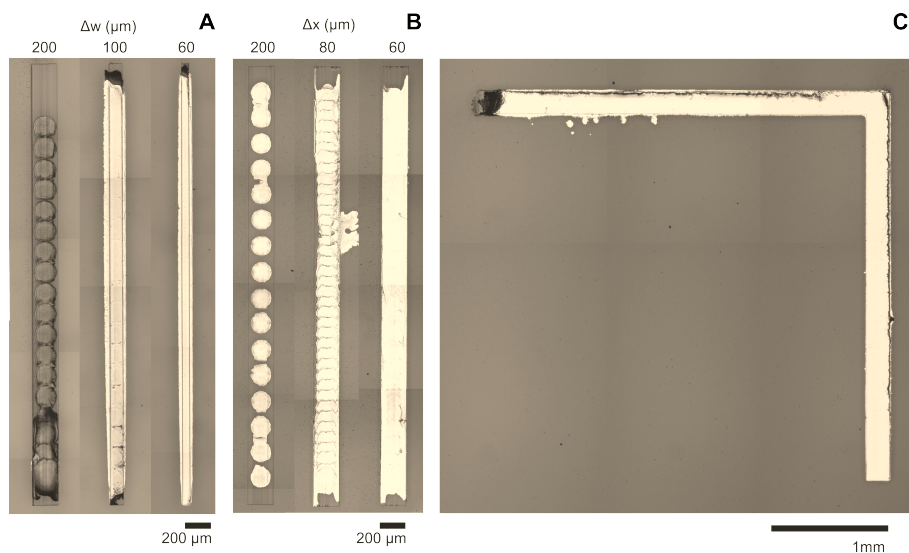


**Figure 5.3:** Conductive lines generated by printing silver ink droplets with (A) a constant printing separation ( $\Delta x$ ) of  $160\ \mu\text{m}$  inside different widths ( $\Delta w$ ) fluidic guides, and (B) at different printing separations inside fluidic guides of  $200\ \mu\text{m}$  width. (C) Pattern of two straight long lines forming an angle of  $90^\circ$  between them, formed by printing droplets separated  $60\ \mu\text{m}$  inside fluidic guides of  $200\ \mu\text{m}$  width.

In a second experiment, the accumulation of debris was avoided by the use of an air flow on the surface of the substrate during the ablation procedure. Then, printing experiments using different separations between consecutive printed droplets were used on fluidic guides of the same width. As the printing distance was gradually reduced, the droplets coalesced to eventually form a continuous line. Figure 5.3B shows a selection of results of this experiment, where it is observed that a high quality printed line with no bulging or scalloping confines almost perfectly the liquid within the fluidic guide, so that the approach indeed leads to a significant improvement in line definition.

In order to demonstrate the degree of control and definition that is possible to achieve with the proposed approach, we performed the realization of a challenging pattern: two long connected lines forming a  $90^\circ$  angle (Figure 5.3C). This pattern is a clear indicator that the proposed approach has the potential to create complex geometries with exceptional printing quality. Finally, the feasibility to work as electrical interconnections was demonstrated by performing conductivity measurements; the lines were first dried and then laser sintered with a CW laser to improve the conductivity of the silver ink. The results showed conductivities very close to the nominal value provided by the supplier.

## 6 Conclusions

The following conclusions can be drawn from the results obtained along the thesis work:

### **Subtractive laser direct-writing**

- The proposed z-scan focusing technique has proven to be a suitable method for the positioning of a transparent sample close to the laser beam waist. The characterization of the z-scan along different positions on the beam propagation axis allowed determining the optimum position to produce ablation on the surface of a transparent sample of PMMA. Ablation experiments allowed determining the fluence threshold for ablation in this material, as well as the minimum laser beam waist of the used optical system.
- The agreement between experimental and theoretical data found with vector diffraction theory simulations of the laser beam allows finding the position of the laser beam waist among the z range provided by the z-scan. This results to be an useful parameter to take into account for large area processing of transparent materials with high spatial resolution.
- An overall improvement that allows controlling the sample position in a wider z range has been demonstrated by registering simultaneously the energy transmitted and reflected by the sample during the surface ablation experiments. This allows controlling the sample tilt in larger areas allowing the fabrication of continuous and long lines on the surface of a transparent sample. Besides, due to the high control on the positioning, the proposed z-scan focusing method has allowed the generation of surface sub-diffraction-limited features along relatively long distances.



## Additive laser direct-writing

- Liquid transfer through LIFT emulating very high printing speeds has revealed the presence of significant interaction between adjacent jets. The time-resolved imaging studies carried out have confirmed that this interaction originates when the laser generated bubbles contact each other during the very early stages of their expansion. The liquid ejection dynamics resulting from that interaction presents new elements, such as the two thin jets that coalesce into a single one, which can compromise severely the pixel quality when printing at very high speeds.
- It is feasible to print through LIFT functional conductive lines that overcome common defects such as discontinuities and bulging by using a printing strategy that consists in the transfer of alternate droplets (the odd ones first and then the even ones) with an intermediate drying step. This allows mitigating the unwanted capillary flows inside the printed lines which are ultimately responsible for the bulge formation.
- LIFT has been proved to be a feasible technique to print very small volumes of a highly viscous polymer for the fabrication of tailored high precision grade polymeric microlenses. The proposed fabrication approach consisting in only two steps (LIFT printing and UV polymer cross-linking) allows controlling the microlenses diameter by simply adjusting the laser parameters, which makes possible to control the resulting focal length of the microlenses.

## Combined approaches

- The combination of a conventional laser direct-write approach with hemispherical liquid microlenses printed through LIFT has been proved successful to generate deep sub-wavelength modifications in a solid substrate. By using this approach, the effective numerical aperture of the optical system is increased a factor that corresponds exactly to the refractive index of the liquid. The potential impact of the proposed approach for 2D nanopatterning is demonstrated by the fabrication of complex geometry patterns using a single microdroplet during the entire fabrication process.

- The printing of liquids through LIFT inside laser ablated fluidic guides has been successfully used for the fabrication of high quality conductive lines free from the most common printing defects, specially bulging and scalloping. The fabrication of two connected lines forming a 90° angle demonstrates the potential of the proposed approach for the fabrication of complex geometry patterns with an unprecedented degree of definition.



# Bibliography

- [1] J. A. Lewis and G. M. Gratson, "Direct writing in three dimensions," *Materials Today*, vol. 7, pp. 32–39, 2004.
- [2] R. Chau, B. Doyle, S. Datta, J. Kavalieros, and K. Zhang, "Integrated nano-electronics for the future," *Nature Materials*, vol. 6, pp. 810–812, 2007.
- [3] E. W. Esch, A. Bahinski, and D. Huh, "Organs-on-chips at the frontiers of drug discovery," *Nature Reviews Drug Discovery*, vol. 14, pp. 248–260, 2015.
- [4] A. Hierlemann, O. Brand, C. Hagleitner, and H. Baltes, "Microfabrication techniques for chemical/biosensors," *Proceedings of the IEEE*, vol. 91, pp. 839–863, 2003.
- [5] D. B. Weibel, W. R. DiLuzio, and G. M. Whitesides, "Microfabrication meets microbiology," *Nature Reviews Microbiology*, vol. 5, pp. 209–218, 2007.
- [6] J. Bohandy, B. F. Kim, and F. J. Adrian, "Metal deposition from a supported metal film using an excimer laser," *Journal of Applied Physics*, vol. 60, pp. 1538–1539, 1986.
- [7] A. Piqué, D. B. Chrisey, R. C. Y. Auyeung, J. Fitz-Gerald, H. D. Wu, R. A. McGill, S. Lakeou, P. K. Wu, V. Nguyen, and M. Duignan, "A novel laser transfer process for direct writing of electronic and sensor materials," *Applied Physics A: Materials Science & Processing*, vol. 284, pp. 279–284, 1999.
- [8] C. B. Arnold, P. Serra, and A. Piqué, "Laser direct-write techniques for printing of complex materials," *MRS Bulletin*, vol. 32, pp. 23–31, 2007.
- [9] P. Serra, M. Duocastella, J. Fernández-Pradas, and J. Morenza, *Advances in Laser Materials Processing: Technology, research and applications*, ch. The laser-induced forward transfer technique for microprinting, pp. 367–393. Woodhead Publishing Series in Welding and Other Joining Technologies, Woodhead Publishing Ltd, 2010.

- [10] P. Delaporte and A.-P. Alloncle, "Laser-induced forward transfer: a high resolution additive manufacturing technology," *Optics & Laser Technology*, vol. 78, pp. 33–41, 2016.
- [11] T. H. Mainman, "Stimulated optical radiation in ruby," *Nature*, vol. 187, pp. 493–494, 1960.
- [12] K. Thyagarajan and A. Ghatak, *Lasers, fundamentals and applications*. Graduate Texts in Physics, Boston, MA: Springer US, 2011.
- [13] J. C. Miller, *Laser ablation*, vol. 28 of *Springer Series in Materials Science*. Berlin, Heidelberg: Springer Berlin Heidelberg, 1994.
- [14] D. Dijkkamp, A. S. Gozdz, T. Venkatesan, and X. D. Wu, "Evidence for the thermal nature of laser-induced polymer ablation," *Physical Review Letters*, vol. 58, pp. 2142–2145, 1987.
- [15] F. Korte, J. Serbin, J. Koch, A. Egbert, C. Fallnich, A. Ostendorf, and B. N. Chichkov, "Towards nanostructuring with femtosecond laser pulses," *Applied Physics A: Materials Science & Processing*, vol. 77, pp. 229–235, 2003.
- [16] J. Bohandy, B. F. Kim, F. J. Adrian, and A. N. Jette, "Metal deposition at 532 nm using a laser transfer technique," *Journal of Applied Physics*, vol. 63, pp. 1158–1162, 1988.
- [17] G. B. Blanchet, Y.-L. Loo, J. a. Rogers, F. Gao, and C. R. Fincher, "Large area, high resolution, dry printing of conducting polymers for organic electronics," *Applied Physics Letters*, vol. 82, pp. 463–465, 2003.
- [18] M. Duocastella, J. M. Fernández-Pradas, J. Domínguez, P. Serra, and J. L. Morenza, "Printing biological solutions through laser-induced forward transfer," *Applied Physics A Materials Science & Processing*, vol. 93, pp. 941–945, 2008.
- [19] J. Wang, R. C. Y. Auyeung, H. Kim, N. A. Charipar, and A. Piqué, "Three-dimensional printing of interconnects by laser direct-write of silver nanopastes," *Advanced Materials*, vol. 22, pp. 4462–4466, 2010.
- [20] M. Zenou, A. Sa'ar, and Z. Kotler, "Laser transfer of metals and metal alloys for digital microfabrication of 3D objects," *Small*, vol. 11, pp. 4082–4089, 2015.

- [21] M. Colina, M. Duocastella, J. M. Fernández-Pradas, P. Serra, and J. L. Morenza, "Laser-induced forward transfer of liquids: study of the droplet ejection process," *Journal of Applied Physics*, vol. 99, p. 084909, 2006.
- [22] M. Duocastella, J. M. Fernández-Pradas, P. Serra, and J. L. Morenza, "Jet formation in the laser forward transfer of liquids," *Applied Physics A Materials Science & Processing*, vol. 93, pp. 453–456, 2008.
- [23] M. Duocastella, J. M. Fernández-Pradas, J. L. Morenza, and P. Serra, "Time-resolved imaging of the laser forward transfer of liquids," *Journal of Applied Physics*, vol. 106, p. 084907, 2009.
- [24] Y. Song, J. Hormes, and C. S. S. R. Kumar, "Microfluidic synthesis of nanomaterials," *Small*, vol. 4, pp. 698–711, 2008.
- [25] K. Paul, M. Prentiss, and G. Whitesides, "Patterning spherical surfaces at the two-hundred-nanometer scale using soft lithography," *Advanced Functional Materials*, vol. 13, pp. 259–263, 2003.
- [26] H. Mekar, T. Yamada, S. Yan, and T. Hattori, "Microfabrication by hot embossing and injection molding at LASTI," *Microsystem Technologies*, vol. 10, pp. 682–688, 2004.
- [27] C. G. Khan Malek, "Laser processing for bio-microfluidics applications (part II)," *Analytical and Bioanalytical Chemistry*, vol. 385, pp. 1362–1369, 2006.
- [28] J. L. Wilbur, A. Kumar, E. Kim, and G. M. Whitesides, "Microfabrication by microcontact printing of self-assembled monolayers," *Advanced Materials*, vol. 6, pp. 600–604, 1994.
- [29] A. Perl, D. N. Reinhoudt, and J. Huskens, "Microcontact printing: limitations and achievements," *Advanced Materials*, vol. 21, pp. 2257–2268, 2009.
- [30] P. Tseng, C. Murray, D. Kim, and D. Di Carlo, "Research highlights: printing the future of microfabrication," *Lab on a Chip*, vol. 14, p. 1491, 2014.
- [31] B. Derby, "Inkjet printing of functional and structural materials: fluid property requirements, feature stability, and resolution," *Annual Review of Materials Research*, vol. 40, pp. 395–414, 2010.
- [32] R. J. Young, "Micro-machining using a focused ion beam," *Vacuum*, vol. 44, pp. 353–356, 1993.

- [33] A. Ostendorf and B. N. Chichkov, "Two-photon polymerization: a new approach to micromachining," *Photonics Spectra*, vol. 40, pp. 72–79, 2006.
- [34] G. Cummins and M. P. Desmulliez, "Inkjet printing of conductive materials: a review," *Circuit World*, vol. 38, pp. 193–213, 2012.
- [35] D. Jang, D. Kim, and J. Moon, "Influence of fluid physical properties on ink-jet printability," *Langmuir*, vol. 25, pp. 2629–2635, 2009.
- [36] D. Soltman and V. Subramanian, "Inkjet-printed line morphologies and temperature control of the coffee ring effect," *Langmuir*, vol. 24, pp. 2224–2231, 2008.
- [37] A. Lee, K. Sudau, K. H. Ahn, S. J. Lee, and N. Willenbacher, "Optimization of experimental parameters to suppress nozzle clogging in inkjet printing," *Industrial & Engineering Chemistry Research*, vol. 51, pp. 13195–13204, 2012.
- [38] M. von Allmen, *Laser-beam interactions with materials*, vol. 2 of *Springer Series in Materials Science*. Berlin, Heidelberg: Springer Berlin Heidelberg, 1987.
- [39] C. B. Schaffer, A. Brodeur, and E. Mazur, "Laser-induced breakdown and damage in bulk transparent materials induced by tightly focused femtosecond laser pulses," *Measurement Science and Technology*, vol. 12, pp. 1784–1794, 2001.
- [40] S. H. Chung and E. Mazur, "Femtosecond laser ablation of neurons in *C. elegans* for behavioral studies," *Applied Physics A: Materials Science & Processing*, vol. 96, pp. 335–341, 2009.
- [41] R. R. Gattass and E. Mazur, "Femtosecond laser micromachining in transparent materials," *Nature Photonics*, vol. 2, pp. 219–225, 2008.
- [42] K. C. Phillips, H. H. Gandhi, E. Mazur, and S. K. Sundaram, "Ultrafast laser processing of materials: a review," *Advances in Optics and Photonics*, vol. 7, pp. 684–712, 2015.
- [43] H. Becker and C. Gärtner, "Polymer microfabrication technologies for microfluidic systems," *Analytical and Bioanalytical Chemistry*, vol. 390, pp. 89–111, 2008.

- [44] L. Rusen, M. Cazan, C. Mustaciosu, M. Filipescu, S. Sandel, M. Zamfirescu, V. Dinca, and M. Dinescu, "Tailored topography control of biopolymer surfaces by ultrafast lasers for cell–substrate studies," *Applied Surface Science*, vol. 302, pp. 256–261, 2014.
- [45] A. Vogel and V. Venugopalan, "Mechanisms of pulsed laser ablation of biological tissues," *Chemical reviews*, vol. 103, pp. 577–644, 2003.
- [46] C. De Marco, R. Suriano, M. Levi, S. Turri, S. Eaton, G. Cerullo, and R. Osellame, "Femtosecond laser fabrication and characterization of microchannels and waveguides in methacrylate-based polymers," *Microsystem Technologies*, vol. 18, pp. 183–190, 2012.
- [47] E. N. Glezer, M. Milosavljevic, L. Huang, R. J. Finlay, T. H. Her, J. P. Callan, and E. Mazur, "Three-dimensional optical storage inside transparent materials.," *Optics Letters*, vol. 21, pp. 2023–2025, 1996.
- [48] Y. Hu, Y. Chen, J. Li, D. Hu, J. Chu, Q. Zhang, and W. Huang, "Femtosecond laser induced surface deformation in multi-dimensional data storage," *Applied Physics Letters*, vol. 101, p. 251116, 2012.
- [49] R. Osellame, H. Hoekstra, G. Cerullo, and M. Pollnau, "Femtosecond laser microstructuring: an enabling tool for optofluidic lab-on-chips," *Laser & Photonics Reviews*, vol. 5, pp. 442–463, 2011.
- [50] S. M. Eaton, C. De Marco, R. Martinez-Vazquez, R. Ramponi, S. Turri, G. Cerullo, and R. Osellame, "Femtosecond laser microstructuring for polymeric lab-on-chips.," *Journal of biophotonics*, vol. 5, pp. 687–702, 2012.
- [51] C. G. Khan Malek, "Laser processing for bio-microfluidics applications (part I)," *Analytical and Bioanalytical Chemistry*, vol. 385, pp. 1351–1361, 2006.
- [52] A. Kurella, "Review paper: surface modification for bioimplants: the role of laser surface engineering," *Journal of Biomaterials Applications*, vol. 20, pp. 5–50, 2005.
- [53] Y. Ou, Q. Yang, F. Chen, Z. Deng, G. Du, J. Wang, H. Bian, J. Yong, and X. Hou, "Direct fabrication of microlens arrays on PMMA with laser-induced structural modification," *IEEE Photonics Technology Letters*, vol. 27, pp. 2253–2256, 2015.



- [54] M. T. B. Najam, K. M. Arif, and Y.-G. Lee, "Novel method for laser focal point positioning on the cover slip for TPP-based microfabrication and detection of the cured structure under optical microscope," *Applied Physics B*, vol. 111, pp. 141–147, 2013.
- [55] M. Antti, H. Ville, and V. Jorma, "Precise online auto-focus system in high speed laser micromachining applications," *Physics Procedia*, vol. 39, pp. 807–813, 2012.
- [56] S. Campbell, F. C. Dear, D. P. Hand, and D. T. Reid, "Single-pulse femtosecond laser machining of glass," *Journal of Optics A: Pure and Applied Optics*, vol. 7, pp. 162–168, 2005.
- [57] M. L. Levene, R. D. Scott, and B. W. Siryj, "Material transfer recording," *Applied Optics*, vol. 9, pp. 2260–2265, 1970.
- [58] Z. Kántor, Z. Tóth, T. Szörényi, and A. L. Tóth, "Deposition of micrometer sized tungsten patterns by laser transfer technique," *Applied Physics Letters*, vol. 64, pp. 3506–3508, 1994.
- [59] V. Veiko, E. Shakhno, V. Smirnov, A. Miaskovski, and G. Nikishin, "Laser-induced film deposition by lift: Physical mechanisms and applications," *Laser and Particle Beams*, vol. 24, pp. 203–209, 2006.
- [60] D. A. Willis and V. Grosu, "Microdroplet deposition by laser-induced forward transfer," *Applied Physics Letters*, vol. 86, p. 244103, 2005.
- [61] F. J. Adrian, J. Bohandy, B. F. Kim, A. N. Jette, and P. Thompson, "A study of the mechanism of metal deposition by the laser-induced forward transfer process," *Journal of Vacuum Science & Technology B*, vol. 5, pp. 1490–1494, 1987.
- [62] T. Sano, H. Yamada, T. Nakayama, and I. Miyamoto, "Experimental investigation of laser induced forward transfer process of metal thin films," *Applied Surface Science*, vol. 186, pp. 221–226, 2002.
- [63] Y. Nakata, T. Okada, and M. Maeda, "Microscopic and spectroscopic imaging of laser-induced forward transfer and its application to material transfer," *SPIE 5399, Laser-assisted micro- and nanotechnologies 2003*, vol. 5399, pp. 156–170, 2004.

- [64] P. Serra, M. Duocastella, J. M. Fernández-Pradas, and J. L. Morenza, *Cell and organ printing*, ch. Laser-induced forward transfer: a laser-based technique for biomolecules printing, pp. 53–80. Dordrecht: Springer Netherlands, 2010.
- [65] R. J. Baseman, F. N. M. A. J. C., and Z. Schlesinger, “Minimum fluence for laser blow-off of thin gold films at 248 and 532 nm,” *Applied Physics Letters*, vol. 56, pp. 1412–1414, 1990.
- [66] V. Schultze and M. Wagner, “Laser-induced forward transfer of aluminium,” *Applied Surface Science*, vol. 52, pp. 303–309, 1991.
- [67] Z. Kántor, Z. Tóth, and T. Szörényi, “Laser induced forward transfer: the effect of support-film interface and film-to-substrate distance on transfer,” *Applied Physics A: Materials Science & Processing*, vol. 54, pp. 170–175, 1992.
- [68] Z. Tóth, T. Szörényi, and A. Tóth, “Ar+ laser-induced forward transfer (lift): a novel method for micrometer-size surface patterning,” *Applied Surface Science*, vol. 69, pp. 317–320, 1993.
- [69] J. A. Greer and T. E. Parker, “Laser-induced forward transfer of metal oxides to trim the frequency of surface acoustic wave resonator devices,” *Proc. SPIE, Excimer Beam Applications*, vol. 998, pp. 113–125, 1988.
- [70] I. Zergioti, D. Papazoglou, A. Karaiskou, N. Vainos, and C. Fotakis, “Laser microprinting of inox active optical structures and time resolved imaging of the transfer process,” *Applied Surface Science*, vol. 197–198, pp. 868–872, 2002.
- [71] K. S. Kaur, R. Fardel, T. C. May-Smith, M. Nagel, D. P. Banks, C. Grivas, T. Lippert, and R. W. Eason, “Shadowgraphic studies of triazene assisted laser-induced forward transfer of ceramic thin films,” *Journal of Applied Physics*, vol. 105, p. 113119, 2009.
- [72] W. A. Toldbert, I. Y. S. Lee, M. M. Doxtader, E. W. Ellis, and D. D. Dlott, “High-speed color imaging by laser ablation transfer with a dynamic release layer: Fundamental mechanisms,” *Journal of Imaging Science*, vol. 37, pp. 411–421, 1993.
- [73] A. Doraiswamy, R. Narayan, T. Lippert, L. Urech, A. Wokaun, M. Nagel, B. Hopp, M. Dinescu, R. Modi, R. Auyeung, and D. Chrisey, “Excimer laser

- forward transfer of mammalian cells using a novel triazene absorbing layer,” *Applied Surface Science*, vol. 252, pp. 4743–4747, 2006.
- [74] R. Fardel, M. Nagel, F. Nüesch, T. Lippert, and A. Wokaun, “Laser forward transfer using a sacrificial layer: Influence of the material properties,” *Applied Surface Science*, vol. 254, pp. 1322–1326, 2007.
- [75] S. H. Ko, H. Pan, S. G. Ryu, N. Misra, C. P. Grigoropoulos, and H. K. Park, “Nanomaterial enabled laser transfer for organic light emitting material direct writing,” *Applied Physics Letters*, vol. 93, p. 151110, 2008.
- [76] N. T. Kattamis, N. D. McDaniel, S. Bernhard, and C. B. Arnold, “Laser direct write printing of sensitive and robust light emitting organic molecules,” *Applied Physics Letters*, vol. 94, p. 103306, 2009.
- [77] M. Duocastella, J. M. Fernández-Pradas, J. L. Morenza, and P. Serra, “Sessile droplet formation in the laser-induced forward transfer of liquids: a time-resolved imaging study,” *Thin Solid Films*, vol. 518, pp. 5321–5325, 2010.
- [78] A. Palla-Papavlu, M. Dinescu, A. Wokaun, and T. Lippert, “Laser-induced forward transfer of single-walled carbon nanotubes,” *Applied Physics A Materials Science & Processing*, vol. 117, pp. 371–376, 2014.
- [79] P. Wu, B. Ringeisen, J. Callahan, M. Brooks, D. Bubb, H. Wu, A. Piqué, B. Spargo, R. McGill, and D. Chrisey, “The deposition, structure, pattern deposition, and activity of biomaterial thin-films by matrix-assisted pulsed-laser evaporation (MAPLE) and MAPLE direct write,” *Thin Solid Films*, vol. 398-399, pp. 607–614, 2001.
- [80] P. Serra, M. Colina, J. M. Fernández-Pradas, L. Sevilla, and J. L. Morenza, “Preparation of functional DNA microarrays through laser-induced forward transfer,” *Applied Physics Letters*, vol. 85, pp. 1639–1641, 2004.
- [81] A. Palla-Papavlu, V. Dinca, C. Luculescu, J. Shaw-Stewart, M. Nagel, T. Lippert, and M. Dinescu, “Laser induced forward transfer of soft materials,” *Journal of Optics*, vol. 12, p. 124014, 2010.
- [82] A. Palla-Papavlu, A. Patrascioiu, F. Di Pietrantonio, J. M. Fernández-Pradas, D. Cannatà, M. Benetti, S. D’Auria, E. Verona, and P. Serra, “Preparation of surface acoustic wave odor sensors by laser-induced forward transfer,” *Sensors and Actuators B: Chemical*, vol. 192, pp. 369–377, 2014.

- [83] F. Guillemot, A. Souquet, S. Catros, B. Guillotin, J. Lopez, M. Faucon, B. Pippenger, R. Bareille, M. Rémy, S. Bellance, P. Chabassier, J. Fricain, and J. Amédée, “High-throughput laser printing of cells and biomaterials for tissue engineering,” *Acta Biomaterialia*, vol. 6, pp. 2494–2500, 2010.
- [84] I. A. Paun, M. Zamfirescu, M. Mihailescu, C. R. Luculescu, C. C. Mustaciosu, I. Dorobantu, B. Calenic, and M. Dinescu, “Laser micro-patterning of biodegradable polymer blends for tissue engineering,” *Journal of Materials Science*, vol. 50, pp. 923–936, 2015.
- [85] C. B. Arnold, T. Sutto, H. Kim, and A. Piqué, “Direct-write laser processing creates tiny electrochemical systems,” *Laser Focus World*, vol. 40, p. S9, 2004.
- [86] N. T. Kattamis, P. E. Purnick, R. Weiss, and C. B. Arnold, “Thick film laser induced forward transfer for deposition of thermally and mechanically sensitive materials,” *Applied Physics Letters*, vol. 91, p. 171120, 2007.
- [87] C. Boutopoulos, V. Tsouti, D. Goustouridis, S. Chatzandroulis, and I. Zergioti, “Liquid phase direct laser printing of polymers for chemical sensing applications,” *Applied Physics Letters*, vol. 93, p. 191109, 2008.
- [88] M. Baum, H. Kim, I. Alexeev, A. Piqué, and M. Schmidt, “Generation of transparent conductive electrodes by laser consolidation of LIFT printed ITO nanoparticle layers,” *Applied Physics A: Materials Science & Processing*, vol. 111, pp. 799–805, 2013.
- [89] P. K. Wu, B. R. Ringeisen, D. B. Krizman, C. G. Frondoza, M. Brooks, D. M. Bubb, R. C. Y. Auyeung, A. Piqué, B. Spargo, R. a. McGill, and D. B. Chrisey, “Laser transfer of biomaterials: matrix-assisted pulsed laser evaporation (MAPLE) and MAPLE direct write,” *Review of Scientific Instruments*, vol. 74, p. 2546, 2003.
- [90] J. Barron, R. Rosen, J. Jones-Meehan, B. Spargo, S. Belkin, and B. Ringeisen, “Biological laser printing of genetically modified *Escherichia coli* for biosensor applications,” *Biosensors and Bioelectronics*, vol. 20, pp. 246–252, 2004.
- [91] P. Serra, J. M. Fernández-Pradas, F. Berthet, M. Colina, J. Elvira, and J. L. Morenza, “Laser direct writing of biomolecule microarrays,” *Applied Physics A Materials Science & Processing*, vol. 79, pp. 949–952, 2004.

- [92] V. Dinca, A. Patrascioiu, J. M. Fernández-Pradas, J. L. Morenza, and P. Serra, "Influence of solution properties in the laser forward transfer of liquids," *Applied Surface Science*, vol. 258, pp. 9379–9384, 2012.
- [93] V. Dinca, M. Farsari, D. Kafetzopoulos, A. Popescu, M. Dinescu, and C. Fotakis, "Patterning parameters for biomolecules microarrays constructed with nanosecond and femtosecond UV lasers," *Thin Solid Films*, vol. 516, pp. 6504–6511, 2008.
- [94] V. Dinca, A. Ranella, and M. Farsari, "Quantification of the activity of biomolecules in microarrays obtained by direct laser transfer," *Biomedical Microdevices*, vol. 10, pp. 719–725, 2008.
- [95] A. Palla-Papavlu, I. Paraico, J. Shaw-Stewart, V. Dinca, T. Savopol, E. Kovacs, T. Lippert, A. Wokaun, and M. Dinescu, "Liposome micropatterning based on laser-induced forward transfer," *Applied Physics A Materials Science & Processing*, vol. 102, pp. 651–659, 2011.
- [96] D. Young, R. Auyeung, A. Piqué, D. Chrisey, and D. D. Dlott, "Plume and jetting regimes in a laser based forward transfer process as observed by time-resolved optical microscopy," *Applied Surface Science*, vol. 197–198, pp. 181–187, 2002.
- [97] J. A. Barron, H. D. Young, D. D. Dlott, M. M. Darfler, D. B. Krizman, and B. R. Ringeisen, "Printing of protein microarrays via a capillary-free fluid jetting mechanism," *Proteomics*, vol. 5, pp. 4138–4144, 2005.
- [98] N. T. Kattamis, N. D. McDaniel, S. Bernhard, and C. B. Arnold, "Ambient laser direct-write printing of a patterned organo-metallic electroluminescent device," *Organic Electronics*, vol. 12, pp. 1152–1158, 2011.
- [99] J. Shaw-Stewart, T. Mattle, T. Lippert, M. Nagel, F. Nüesch, and A. Wokaun, "The optimisation of the laser-induced forward transfer process for fabrication of polyfluorene-based organic light-emitting diode pixels," *Applied Surface Science*, vol. 278, pp. 341–346, 2013.
- [100] A. Piqué, "Digital microfabrication by laser decal transfer," *Journal of Laser Micro/Nanoengineering*, vol. 3, pp. 163–169, 2008.

- [101] S. A. Mathews, R. C. Y. Auyeung, H. Kim, N. A. Charipar, and A. Piqué, “High-speed video study of laser-induced forward transfer of silver nano-suspensions,” *Journal of Applied Physics*, vol. 114, p. 064910, 2013.
- [102] H. Kim, R. C. Y. Auyeung, S. H. Lee, a. L. Huston, and a. Piqué, “Laser-printed interdigitated Ag electrodes for organic thin film transistors,” *Journal of Physics D: Applied Physics*, vol. 43, p. 085101, 2010.
- [103] L. Rapp, J. Ailuno, A. P. Alloncle, and P. Delaporte, “Pulsed-laser printing of silver nanoparticles ink: control of morphological properties,” *Optics Express*, vol. 19, pp. 21563–21574, 2011.
- [104] I. Zergioti, “Laser printing of organic electronics and sensors,” *Journal of Laser Micro/Nanoengineering*, vol. 8, pp. 30–34, 2013.
- [105] E. Biver, L. Rapp, A.-P. Alloncle, and P. Delaporte, “Multi-jets formation using laser forward transfer,” *Applied Surface Science*, vol. 302, pp. 153–158, 2014.
- [106] W. T. Silfvast, *Laser fundamentals*. Cambridge University Press, 2nd ed., 2004.
- [107] L. Pálfalvi, B. C. Tóth, G. Almási, J. a. Fülöp, and J. Hebling, “A general Z-scan theory,” *Applied Physics B*, vol. 97, pp. 679–685, 2009.
- [108] L. Shah, J. Tawney, M. Richardson, and K. Richardson, “Self-focusing during femtosecond micromachining of silicate glasses,” *IEEE Journal of Quantum Electronics*, vol. 40, pp. 57–68, 2004.
- [109] M. Miwa, S. Juodkazis, T. Kawakami, S. Matsuo, and H. Misawa, “Femtosecond two-photon stereo-lithography,” *Applied Physics A Materials Science & Processing*, vol. 73, pp. 561–566, 2001.
- [110] G. Hennig, T. Baldermann, C. Nussbaum, M. Rossier, A. Brockelt, L. Schuler, and G. Hochstein, “Lasersonic LIFT process for large area digital printing,” *Journal of Laser Micro/Nanoengineering*, vol. 7, pp. 299–305, 2012.
- [111] A. Patrascioiu, J. M. Fernández-Pradas, A. Palla-Papavlu, J. L. Morenza, and P. Serra, “Laser-generated liquid microjets: correlation between bubble dynamics and liquid ejection,” *Microfluidics and Nanofluidics*, vol. 16, pp. 55–63, 2014.

- 
- [112] P. C. Duineveld, "The stability of ink-jet printed lines of liquid with zero receding contact angle on a homogeneous substrate," *Journal of Fluid Mechanics*, vol. 477, pp. 175–200, 2003.
- [113] A. E. Gamal and H. Eltoukhy, "Cmos image sensors," *IEEE Circuits and Devices Magazine*, vol. 21, pp. 6–20, 2005.
- [114] W. Cao and J. Xue, "Recent progress in organic photovoltaics: device architecture and optical design," *Energy & Environmental Science*, vol. 7, pp. 2123–2144, 2014.

# Included Publications

## Subtractive laser direct-writing

### Paper 1

Femtosecond laser ablation of polymethyl-methacrylate with high focusing control

J.M. Fernández-Pradas, C. Florian, F. Caballero-Lucas, J.L. Morenza, P. Serra.

Published at: Applied Surface Science

Year: 2013

Impact factor JDR 2013: 2.538 - (Q1)

DOI: 10.1016/j.apsusc.2013.03.032







Contents lists available at SciVerse ScienceDirect

Applied Surface Science

journal homepage: [www.elsevier.com/locate/apsusc](http://www.elsevier.com/locate/apsusc)

## Femtosecond laser ablation of polymethyl-methacrylate with high focusing control



J.M. Fernández-Pradas\*, C. Florian, F. Caballero-Lucas, J.L. Morenza, P. Serra

Departament de Física Aplicada i Òptica, Universitat de Barcelona, Martí i Franquès 1, E-08028 Barcelona, Spain

### ARTICLE INFO

#### Article history:

Received 29 June 2012

Received in revised form 5 March 2013

Accepted 8 March 2013

Available online 21 March 2013

#### Keywords:

Femtosecond laser

Z-scan

Polymethyl-methacrylate

### ABSTRACT

The interest of laser ablation of transparent polymers with short pulses relies on the possibility of ablating the material with little thermal damage and high spatial resolution. This enables microscopic design features needed for microfluidic devices and micromachining. Laser ablation of polymethyl-methacrylate (PMMA) surface with an Yb:KYW laser beam was carried out in air environment at room temperature. The laser had a wavelength of 1027 nm and the pulse duration was 450 fs. An open aperture z-scan procedure was used as a method to determine with high precision and control the best focusing conditions of the laser beam on the surface of the samples. For this, the transmitted energy was measured with a photodiode detector placed beyond the sample. This was possible due to the high transparency of PMMA to the laser wavelength. Ablation craters produced on the PMMA surface at different laser pulse energies after the z-scan focusing process were characterized by means of optical and scanning electron microscopies. The fluence threshold found for ablation of PMMA is  $3.2 \text{ J/cm}^2$ . Well-defined craters, with diameters as small as 200 nm, can be obtained with pulse energies near the ablation threshold.

© 2013 Elsevier B.V. All rights reserved.

### 1. Introduction

Laser direct-write techniques appear as an alternative to photolithography in the production of miniaturized devices, especially when customization or rapid design modifications are required [1]. Designs are directly transferred from a computer file to the device by the relative motion between the laser beam and the piece being fabricated, thus avoiding the expensive and time-consuming production of masks. One application of lasers for microfabrication is to use them as tools for material removal. Ablation occurs when the laser beam intensity is high enough to transform the irradiated material into plasma. The resolution of the patterns that can be done is limited by the beam size and the extension of thermal and mechanical collateral damages [2]. Beam size is limited by diffraction and it depends on the focusing conditions, laser wavelength and beam quality. Smallest beam sizes can be achieved by tight focusing Gaussian beams with high numerical aperture focusing lenses. Thermal and mechanical damages depend on the energy delivery in the sample. These collateral damages can be greatly reduced by using ultrashort laser pulses. In one hand, femtosecond laser pulses minimize heat transfer to the lattice. On the other hand, very high intensities capable of ablation can be reached with a really small amount of energy per pulse. Consequently, collateral

ablation effects are minimized. Additionally, the non-linear nature of absorption of femtosecond laser pulses allows processing areas below the diffraction limit [2].

The interaction of femtosecond laser pulses with polymethyl-methacrylate (PMMA) is being studied for years [3]. PMMA is a transparent plastic polymer that is often used as a substitute of glass. It has good biocompatibility and is being used as material for implants or for dynamic drug release [4]. Owing to its transparency and good environmental stability PMMA can also be found as substrate material for microfluidic and lab-on-a-chip devices [5]. Microchannels and waveguides can be fabricated with femtosecond lasers with wavelengths in the near infrared, not only in surface but also inside the bulk of PMMA [6–9]. Femtosecond lasers can also modify the hydrophobicity of the PMMA surface [10,11] or enhance its ability for binding proteins on it [12]. Consequently, femtosecond lasers are very promising tools for the fabrication and modification of microfluidic and biomedical devices in PMMA.

When very high resolution of patterns in the surface is required, this must be precisely placed in the beam waist, where the beam size is minimum. Otherwise the beam size on the surface can increase rapidly when using high numerical aperture focusing lenses. In this paper, we present a z-scan method for determining the sample position with respect the beam waist in order to find the best focusing conditions with control. Z-scans are generally applied for measuring optical non-linearities of transparent materials by using the thin-film approximation [13,14]. For these measurements, the material thickness must be much shorter than

\* Corresponding author. Tel.: +34 934039216.  
E-mail address: [jmfernandez@ub.edu](mailto:jmfernandez@ub.edu) (J.M. Fernández-Pradas).

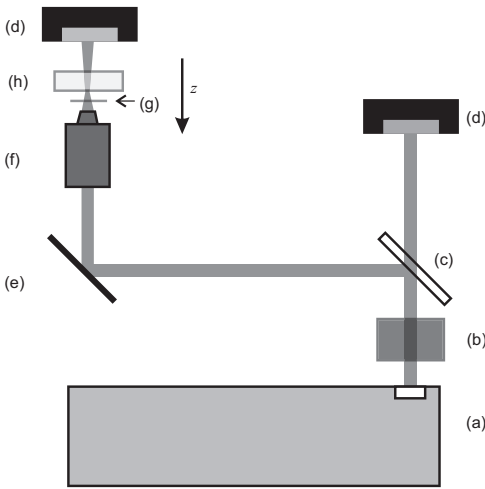


**Fig. 1.** Scheme of the experimental setup: (a) laser, (b) attenuator, (c) beam splitter, (d) photodiode, (e) mirror, (f) focusing objective, (g) cover slip, and (h) PMMA sample.

the beam waist and absorption is generally neglected. For our purpose, z-scan is used in a semi-infinite medium approximation, where the material thickness is much longer than the beam waist and absorption detection is the basis for determining the sample surface position with respect to the beam waist. In this work, the ablation of the PMMA surface with femtosecond laser pulses is studied under these tight focusing conditions.

## 2. Experimental

Rectangular PMMA blocks of 10 mm × 25 mm and thickness of 4 mm were used in the experiments. The PMMA blocks were placed on a motorized platform allowing a minimal incremental motion of 0.5 μm for the horizontal x- and y-axes and of 1 μm in the vertical z-axis. A scheme of the setup used for the experiments is shown in Fig. 1. A chirped pulse amplified laser with Yb:KYW as active medium delivered 450 fs pulses at 1027 nm wavelength on demand triggered by an external pulse generator. The intensity distribution of the laser beam was nearly Gaussian. The pulse energy was varied in the 10<sup>1</sup>–10<sup>3</sup> nJ range by rotating a half-wave plate placed before a fixed polarizer. The pulse energy was monitored in situ through a calibrated photodiode that received part of the beam transmitted by a beamsplitter. The reflected beam was directed by different laser line mirrors to the entrance of a microscope objective with 0.55 numerical aperture that focuses it at about 13 mm of its outer lens. A glass coverslip was placed between the objective and the sample in order to prevent the objective from ablation debris deposition.

The focusing procedure consisted in open aperture z-scan experiments [13,14]. Hence, a second calibrated photodiode was placed just after the sample, so the full beam entered in the detector area. The first photodiode was calibrated in order to indicate the same energy arriving into the second detector when there is no sample in between. Initially, the PMMA sample was placed beyond the beam waist and then it was progressively approached to the focusing objective in 1 μm steps (z-direction). For each step, the transmittance of a single pulse was determined by comparing the energy measurements in both photodiodes. Standard deviation of

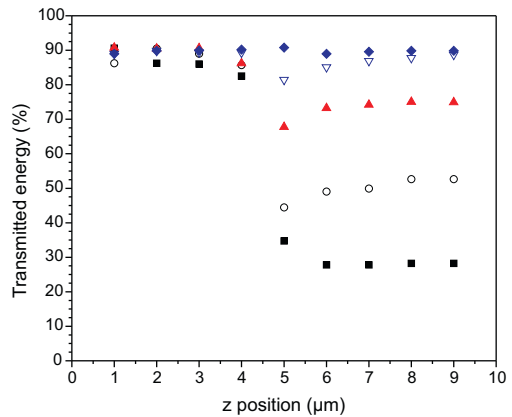


**Fig. 2.** Plot of the transmitted energy vs z at different incident pulse energies: (◆) 40 nJ, (▽) 65 nJ, (▲) 90 nJ, (○) 200 nJ, (■) 1.0 μJ.

the energy measurements is generally below 1% and occasionally reaches 2% as a maximum. For every transmittance measurement the sample was also moved horizontally in order to impinge in a fresh area of the sample and thus avoiding cumulative effects.

After the z-scan process with different energies, the sample surface was placed in the beam waist, and it was irradiated with single pulses at different energies in order to evaluate the positioning method. The energy impinging the sample and the energy arriving at the photodiode placed after the sample were recorded for every pulse. The effects of the pulses on the PMMA surface were inspected by optical and scanning electron (SEM) microscopies.

## 3. Results and discussion

The z-scan experiment was done for different pulse energies in decreasing order. The results are presented in Fig. 2. When the sample is placed outside the beam waist, 90% of the pulse energy passes through the PMMA sample, what corresponds to the losses by reflection with no signs of absorption. The first signs of absorption appear when approaching the sample to the beam waist so the intensity is high enough to promote absorption processes. As it can be seen in Fig. 2, the transition from total transmission to absorption occurs in a distance range of about 2 μm. Such abrupt changes in transmission are due to the non-linear character of absorption and can be easily detected. The band gap of PMMA was estimated near 4.58 eV [15], which is much higher than the 1.21 eV of a single photon of the laser beam. For this reason PMMA is in general transparent to the laser beam, but if the intensity is high enough non-linear absorption processes become possible. For high-energy pulses, the change in transmission is more evident but the transition zone from no absorption to maximum absorption is larger than for low energy pulses. Thus, high energy pulses can be used to do the first approximation of the sample surface to the beam waist, and then the pulse energy of the following z-scans can be progressively decreased in order to place the sample surface in the beam waist position with the highest precision.

Once the sample surface is placed in the beam waist and ready for performing ablation, variations in the energy transmitted can serve to monitor in situ possible modifications in the position of the sample's surface that can be rapidly corrected.

The measurements for the transmitted energy ratio at different incident energies with the sample's surface placed in the beam waist following the above mentioned method are presented in

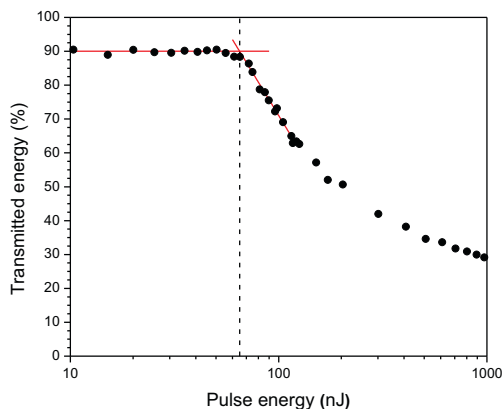


Fig. 3. Plot of the transmitted energy vs pulse energy.

Fig. 3. This transmittance plot reveals the presence of an energy threshold. Hence, the PMMA is transparent for pulses with energy below this threshold. Above the threshold the PMMA partially absorbs the energy of the pulses and the transmission ratio decreases as the pulse energy increases. This behavior is associated with the non-linear nature of the absorption process [16]. Because it is difficult to directly identify the energy at which the transmittance starts decreasing, the energy threshold for absorption was determined at 65 nJ as the cross-point of the horizontal line corresponding to the points of total transmittance with the straight line fitted to the first points where absorption is clear.

The inspection of the PMMA surface in the optical microscope revealed the presence of surface changes for pulse energies higher than 80 nJ (Fig. 4). A sub-micrometric dark spot can be glimpsed where a 80 nJ pulse impinged. Circular dark spots of few microns in diameter surrounded by a small ring are clearly visible in the case of higher pulse energies. The diameter of the spot increases as the energy of the pulse increases. The SEM characterization of the spots (Fig. 5) shows that the dark area corresponds to a round crater. The crater is surrounded by a rim of material elevated from the surface that corresponds to the ring observed in the optical microscope.

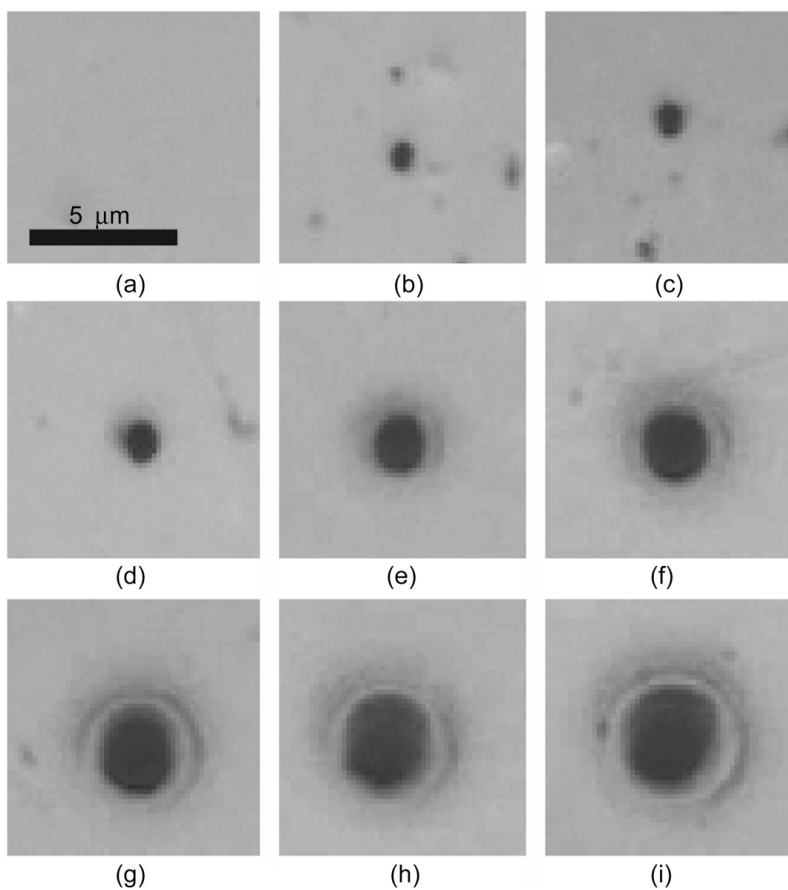


Fig. 4. Optical microscopy images of the PMMA surface after the incidence of a pulse of (a) 70 nJ, (b) 80 nJ, (c) 90 nJ, (d) 100 nJ, (e) 200 nJ, (f) 300 nJ, (g) 500 nJ, (h) 800 nJ, and (i) 1.0  $\mu$ J.

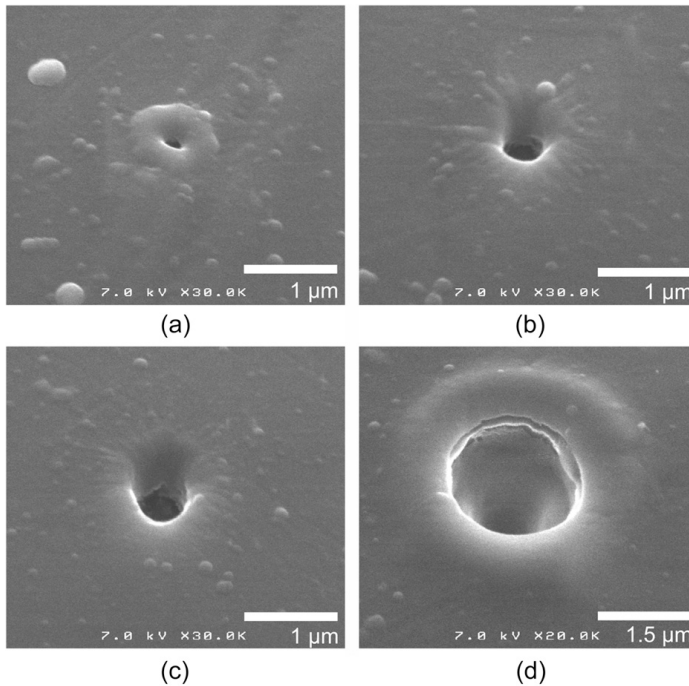


Fig. 5. SEM images of the PMMA surface after the incidence of a pulse of (a) 80 nJ, (b) 85 nJ, (c) 100 nJ, and (d) 1.0  $\mu$ J.

The smallest holes found were done with 80 nJ pulses and they have dimensions of about 200 nm (Fig. 5a), which is well below the Airy disk dimensions for the focusing objective at the laser wavelength. Below this pulse energy no signs of surface modification were detected. The SEM images of bigger craters done with higher pulse energies show that the walls of the craters are smooth. The morphology of the rim around the craters suggests that some melting occurred around the ablation area. Some swelling attributed to resolidified molten material was already found for the irradiation of PMMA with single 150 fs pulses at 800 nm wavelength near the ablation threshold [17]. So it seems reasonable to think that this is also occurring with longer pulses.

The radius of the craters ( $r_0$ ) was measured and its squared value plotted versus the pulse energy ( $E_p$ ) (Fig. 6). The experimental points show a logarithmic relationship. Hence, assuming a Gaussian distribution of the energy of the laser beam, this means that an ablation fluence threshold ( $F_{th}$ ) exists [18] and it can be determined by fitting the experimental points to the expression:

$$r_0^2 = -\frac{\omega^2}{2} \ln\left(\frac{F_{th}\pi\omega^2}{2}\right) + \frac{\omega^2}{2} \ln(E_p) \quad (1)$$

where  $\omega$  is the radius of the laser beam. Thus, for the experimental conditions of this work, the beam radius on the surface was 1.2  $\mu$ m and the fluence threshold for ablation of PMMA with 450 fs pulses at 1027 nm wavelength is 3.2 J/cm<sup>2</sup>. As expected, the value of the fluence threshold is higher than those determined before for shorter pulse durations and smaller wavelengths [17,19]. Anyway, the size of the ablation craters are well below the beam diameter, what shows that non-linear absorption process of femtosecond laser pulses allows going beyond the diffraction limit [2]. The small

size of the craters obtained corroborates the z-scan focusing procedure as a good method for placing the surface on the beam waist.

The peak fluence ( $F_p$ ) of a Gaussian beam is given by:

$$F_p = \frac{2E_p}{\pi\omega^2} \quad (2)$$

Thus, in the conditions of our experiment the pulse energy at which the peak fluence corresponds to the fluence threshold is 72 nJ. This is in good agreement with the fact that no changes were observed

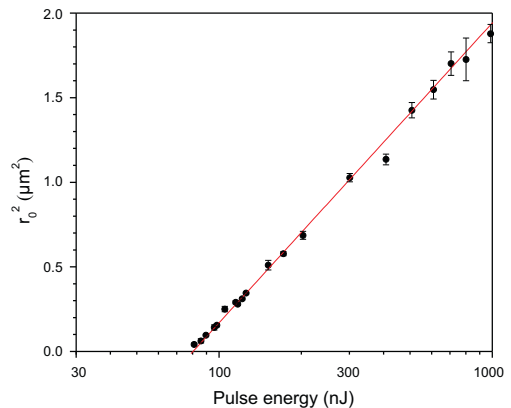


Fig. 6. Plot of the square radius of the craters vs the pulse energy.

in the morphology of the surface irradiated with a pulse of 70 nJ, and that the first signs of ablation were seen with pulses of 80 nJ. However, PMMA starts the absorption of pulses with energies a little bit lower than the threshold for ablation. In this small range of energies below the ablation threshold, some PMMA properties such as the density or the index of refraction can be changed without producing ablation damage in the surface [15].

#### 4. Conclusion

The surface of PMMA can be placed in the beam waist of a laser beam with a precision of  $\pm 1 \mu\text{m}$  following a progressive z-scan focusing procedure. This allows sub-micrometric resolution in the ablation of PMMA with 450 fs laser pulses at 1027 nm wavelength. The pulse energy must be just above the value required to overcome the fluence threshold for ablation, which is  $3.2 \text{ J}/\text{cm}^2$  for our experimental conditions. For pulse energies just below this ablation threshold absorption in the PMMA surface can be still detected, but the surface morphology remains unchanged.

#### Acknowledgements

This work is part of a research program funded by MCI of the Spanish Government (Projects MAT2010-15905 and CSD2008-00023), and Fondo Europeo de Desarrollo Regional (FEDER).

#### References

- [1] A. Piqué, D.B. Chrisey, Direct-Write Technologies for Rapid Prototyping Applications. Sensors, Electronics, and Integrated Power Sources, Academic Press, San Diego, 2002.
- [2] M. Ali, T. Wagner, M. Shakoob, P.A. Molian, Review of laser nanomachining. Journal of Laser Applications 20 (2008) 169–184.
- [3] S. Küper, M. Stuke, Femtosecond UV excimer laser ablation, Applied Physics A 44 (1987) 199–204.
- [4] E. Spyratou, I. Asproudis, D. Tsoutsis, C. Bacharis, K. Moutsouris, M. Makropoulou, A.A. Serafetinides, UV laser ablation of intraocular lenses: SEM and AFM microscopy examination of the biomaterial surface, Applied Surface Science 256 (2010) 2539–2545.
- [5] H. Becker, C. Gärtner, Polymer microfabrication technologies for microfluidic systems, Analytical and Bioanalytical Chemistry 390 (2008) 89–111.
- [6] K. Yamasaki, S. Juodkazis, S. Matsuo, H. Misawa, Three-dimensional microchannels in polymers: one-step fabrication, Applied Physics A 77 (2003) 371–373.
- [7] W. Watanabe, S. Sowa, T. Tamaki, K. Itoh, J. Nishii, Three-dimensional waveguides fabricated in poly(methyl methacrylate) by a femtosecond laser, Japanese Journal of Applied Physics 45 (2006) L765–L767.
- [8] R. Suriano, A. Kuznetsov, S.M. Eaton, R. Kiyan, G. Cerullo, R. Osellame, B.N. Chichkov, M. Levi, S. Turri, Femtosecond laser ablation of polymeric substrates for the fabrication of microfluidic channels, Applied Surface Science 257 (2011) 6243–6250.
- [9] C.D. Marco, R. Suriano, M. Levi, S. Turri, S.M. Eaton, G. Cerullo, R. Osellame, Femtosecond laser fabrication and characterization of microchannels and waveguides in methacrylate-based polymers, Microsystem Technologies 18 (2012) 183–190.
- [10] Z.K. Wang, H.Y. Zheng, C.P. Lim, Y.C. Lam, Polymer hydrophilicity and hydrophobicity induced by femtosecond laser direct irradiation, Applied Physics Letters 95 (2009) 111110.
- [11] Z.K. Wang, H.Y. Zheng, Y.C. Lam, Investigation on femtosecond laser irradiation energy in inducing hydrophobic polymer surfaces, Applied Surface Science 257 (2011) 10427–10433.
- [12] X. Ma, H. Huo, M. Wei, L. Wang, M. Shen, C. Barry, J. Mead, Enhanced protein binding on femtosecond laser ablated poly(methylmethacrylate) surfaces, Applied Physics Letters 98 (2011) 171101.
- [13] M. Sheik-Bahae, A.A. Said, T.H. Wei, D.J. Hagan, E.W. Van Stryland, Sensitive measurement of optical nonlinearities using a single beam, IEEE Journal of Quantum Electronics 26 (1990) 760–769.
- [14] L. Pálfalvi, B.C. Tóth, G. Almási, J.A. Fülöp, J. Hebling, A general Z-scan theory, Applied Physics B 97 (2009) 679–685.
- [15] A. Baum, P.J. Scully, W. Perrie, D. Jones, R. Issac, D.A. Jaroszynski, Pulse-duration dependency of femtosecond laser refractive index modification in poly(methyl methacrylate), Optics Letters 33 (2008) 651–653.
- [16] D. Du, X. Liu, G. Korn, J. Squier, G. Mourou, Laser-induced breakdown by impact ionization in  $\text{SiO}_2$  with pulse widths from 7 ns to 150 fs, Applied Physics Letters 64 (1994) 3071–3073.
- [17] S. Baudach, J. Bonse, J. Krueger, W. Kautek, Ultrashort pulse laser ablation of polycarbonate and polymethylmethacrylate, Applied Surface Science 154–155 (2000) 555–560.
- [18] N. Sanner, O. Utéza, B. Bussiere, G. Coustiller, A. Leray, T. Itina, M. Sentis, Measurement of femtosecond laser-induced damage and ablation thresholds in dielectrics, Applied Physics A 94 (2009) 889–897.
- [19] D. Klinger, R. Sobierajski, R. Nietubyc, J. Krzywiński, J. Peřka, L. Juha, M. Jurek, D. Zymierska, S. Guizard, H. Merdji, Surface modification of polymethylmethacrylate irradiated with 60 fs single laser pulses, Radiation Physics and Chemistry 78 (2009) S71–S74.



## Paper 2

# Surface ablation of transparent polymers with femtosecond laser pulses

C. Florian, F. Caballero-Lucas, J.M. Fernández-Pradas, J.L. Morenza, P. Serra.

Published at: Applied Surface Science

Year: 2014

Impact factor JDR 2014: 2.711 - (Q1)

DOI: 10.1016/j.apsusc.2013.10.145







Contents lists available at ScienceDirect

## Applied Surface Science

journal homepage: [www.elsevier.com/locate/apsusc](http://www.elsevier.com/locate/apsusc)

## Surface ablation of transparent polymers with femtosecond laser pulses



C. Florian, F. Caballero-Lucas, J.M. Fernández-Pradas\*, J.L. Morenza, P. Serra

Departament de Física Aplicada i Òptica, Universitat de Barcelona, Martí i Franquès 1, E-08028 Barcelona, Spain

## ARTICLE INFO

## Article history:

Received 28 June 2013  
 Received in revised form 22 October 2013  
 Accepted 23 October 2013  
 Available online 5 November 2013

## Keywords:

Femtosecond laser  
 z-scan  
 Poly methyl-methacrylate (PMMA)

## ABSTRACT

In this work, a study of the laser ablation on the surface of poly methyl-methacrylate (PMMA) is presented. Experiments were performed with a femtosecond laser delivering 450 fs pulses at a wavelength of 1027 nm. The laser beam energy was controlled through a polarizer based attenuator and measured by a calibrated photodiode energy meter. A focusing method called z-scan is used to place the sample on the beam waist. This method uses a second energy meter placed behind the sample, which was used to monitor the energy transmitted across the sample in situ. Thus, the absorption was evaluated by comparing the measurements of both energy meters. The z-scan method is evaluated by studying the laser ablation in three different positions between the sample and the laser beam waist. It is found that above a threshold energy that depends on the focusing conditions, the absorbance of the samples increases with the pulse energy. After irradiation, dimensional analysis of the craters produced at different pulse energies is performed in order to determine the best focusing conditions and the ablation threshold for ablation of PMMA samples.

© 2013 Elsevier B.V. All rights reserved.

### 1. Introduction

In the latest years, laser direct-write techniques have been used as a precision method to modify a wide variety of materials [1]. In comparison with photolithography and thermoforming techniques, it is not necessary to use masks or any master piece in order to obtain small features on the material [2]. This allows making design changes on the run decreasing time and costs of production. The resolution of laser direct-write techniques is limited by factors such as the laser focusing conditions, the wavelength of the laser and the duration of the pulse, as well as the composition of the sample [3]. Nevertheless, when laser ablation is produced it is common to find damaged material around the irradiated area. This region is formed when the transference of the laser energy to the material takes enough time to produce thermal damage in the surroundings. One alternative to significantly decrease this thermal damage on the material is the use of lasers with sub-picosecond pulse duration. With these lasers the energy is transferred to the material in a very short period of time. Additionally, lasers with shorter pulses produce higher peaks of power allowing the modification of even transparent and dielectric materials [4–6].

Polymers have been chosen as substrate materials for many applications in bioanalysis systems due to properties like its high

transparency in VIS and IR, chemical stability and ease of manufacture [7]. It has been shown that by using tightly focused femtosecond lasers it is possible to modify their surface roughness [8] and to ablate the irradiated material achieving a spatial resolution under the diffraction limit [9]. However, this is not a trivial task because the ablation on the surface is strongly dependent on the control over the position of the sample relative to the laser focus [10]. If the laser focus is located inside the material, the energy is absorbed in bulk instead of the surface. Some techniques have been developed to ensure that the surface of the material is on the laser focus position.

Probably, the most common method consists in forming lines on the surface of the material at different positions between the sample and the laser focus [11]. The lines are produced by overlapping laser pulses. Once the lines are produced, the observer has to estimate where the position of the thinnest and best defined line is, based on the images provided by a CCD camera. Then, the sample is displaced until it reaches the position where the thinnest lines were done, and subsequently the visualization system has to be adjusted to focus on that position. The main drawback is that the measurement depends strongly on the visual perception of the observer, the depth of focus of the imaging system and the energy used to produce the lines.

Another method consists in the measurement of the sample surface position using a confocal point sensor. Once the position is located, an actuator performs a correction to focus the laser beam on the surface at any given height variation [12]. This method

\* Corresponding author. Tel.: +34 934 039 216; fax: +34 934 021 139.  
 E-mail address: [jmfernandez@ub.edu](mailto:jmfernandez@ub.edu) (J.M. Fernández-Pradas).

provides better resolution than the previous method, but it is difficult to implement and synchronize at high speeds and it can only be used in one direction of the  $xy$  plane.

A  $z$ -scan method has been also proposed to evaluate that the surface of the material is on the laser focus [10]. This method is mainly based on the method used previously to measure optical non-linear behaviors on transparent materials where the absorption of energy is neglected [13,14]. It consists in measuring the incident and the transmitted energy at different  $z$  positions between the sample and the laser beam waist. The objective is to measure the amount of transmitted energy in each position and then identify which is the most adequate position to work on the surface of the material. In a previous work, the  $z$ -scan method has been used as a focusing procedure on PMMA samples by using large  $z$  steps (1  $\mu\text{m}$ ) between measurements.

In this work we characterize the  $z$ -scan method in order to get high positioning control of the sample along the laser beam waist for producing surface ablation on transparent materials. For this we used a  $z$  step of 0.1  $\mu\text{m}$  in order to improve the resolution of the method. The experiments were performed on poly methyl-methacrylate (PMMA) samples. Laser ablation experiments at three different positions in the  $z$ -scan were analyzed in detail in order to evaluate the focusing procedure.

## 2. Experimental

The experiments were done on Goodfellow PMMA samples, prepared in rectangular pieces of 20 mm  $\times$  10 mm and thickness of 1.1 mm. The samples were irradiated using a pulsed laser of Amplitude Systemes whose active medium is a crystal of Yb:KYW. It has pulse duration of 450 fs at a wavelength of 1027 nm. The laser was focused using a high numerical aperture objective NA=0.55 with a working distance of 13 mm. The energy distribution profile of the beam was Gaussian with a quality factor of  $M^2 = 1.3$ . The samples were placed on a holder in which the tilt of the sample can be corrected by means of two micrometric screws. Moreover, the samples were moved by a motorized stage in the three perpendicular axes. The setup includes two energy detectors. One placed before the focusing objective measures the incident energy with the help of a beam splitter. The other one is placed behind the sample for measuring the transmitted energy. A CCD camera was placed coaxially to the laser beam for the visualization of the sample in situ. The focal plane of the camera was located near to the focal plane of the laser, so that the focused image of the CCD gave a good estimation of the position of the laser beam waist. The distribution of the elements and further details about the setup are described in [10].

The first step to perform a  $z$ -scan is to place the sample around 30  $\mu\text{m}$  over the laser beam waist position. This is possible using the image of the CCD camera. At this point, the laser focus is far enough of the sample and, if the material is transparent to the laser wavelength, there should not be energy absorption. Every time that a laser pulse is fired, the positioning system moves the sample 0.1  $\mu\text{m}$  in the  $z$  axis direction by decreasing the distance between the surface and the laser beam waist. At the same time, the sample is moved in the  $xy$  plane in order to fire the next laser pulse with a separation of 5  $\mu\text{m}$  horizontally and hence avoiding cumulative effects. Both incident and transmitted energies are recorded for every pulse and, after data analysis, the values for transmittance and absorbance are obtained. Since the used energies are well below the critical energy to produce the self-focusing effect in air (a few mJ), non-linear effects are negligible before the beam enters inside the PMMA sample [15,16].

The selected energy to perform the  $z$ -scan was  $200 \pm 2$  nJ based on previous studies [10]. The transmittance curve variation in each  $z$  position along 30  $\mu\text{m}$  starting from a certain point close to the

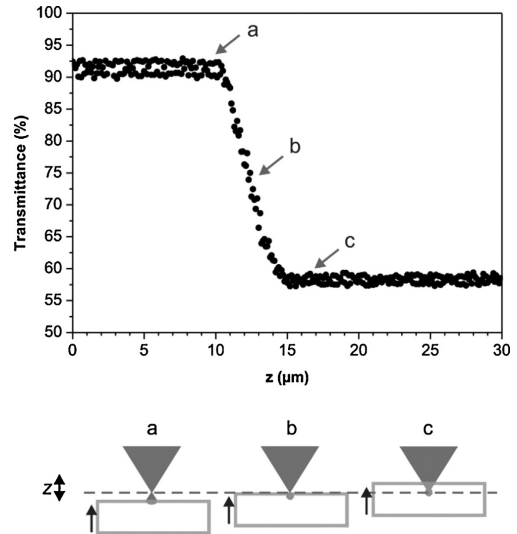


**Fig. 1.** (Top) Plot of the transmitted energy vs.  $z$  position at 200 nJ of incident energy. (Bottom) scheme of the laser focus at different  $z$  positions during the  $z$ -scan. (a) slightly out of the sample, (b) on the surface, and (c) inside the sample.

surface is shown in Fig. 1. In this plot, it is possible to identify 3 stages. The first stage corresponds to a region where the surface of the sample is getting closer to the laser focus but the energy intensity is not high enough to be absorbed. Therefore, the transmittance value presents its maximum value ( $91 \pm 3\%$ ). As the sample gets closer to the beam waist, the energy intensity in the surface increases until a point where it is high enough to promote energy absorption. Thus, a decrease in the transmittance values is presented at those positions (point a in Fig. 1). During the second stage, the sample approaches the beam waist where the intensity reaches its maximum so that the energy absorption increases significantly. Thus, the transmittance decreases in each step (zone b in Fig. 1). At a certain point the energy absorption of the sample reaches a maximum (point c in Fig. 1). Beyond this point, the transmittance in all the subsequent positions reaches a constant value around  $58 \pm 3\%$ , indicating that the sample overpasses the beam waist position and it is already inside the material.

It has to be pointed out that the  $z$ -scan should be performed when the samples are placed perpendicular to the beam axis, so the  $xy$  motion of the samples does not imply an unwanted modification of the surface position. For this reason, a procedure called 'scan' is used in order to achieve that perpendicularity before any  $z$ -scan experiment. 'Scans' are made in the  $xy$  plane along a total distance of 2 mm in steps of 5  $\mu\text{m}$ . It is essentially a scan of the sample in the  $xy$  direction without variations in the  $z$  position.

Three scans made at  $200 \pm 2$  nJ of incident energy are shown in Fig. 2. The first one (squares) was made with the sample in a position over the a point in Fig. 1. Consequently, the transmittance curve shows a horizontal trend at its maximum value because there is no energy absorption. This gives an estimation of the uncertainty in the transmittance measurements. In the second 'scan' (circles), the sample was placed in a position where the transmittance value initially corresponds to the point b in Fig. 1. At this position, the performed 'scan' reveals a variation in the transmittance along the horizontal direction, indicating that the sample was tilted. Then, the sample holder tilt was adjusted by using two micrometric screws

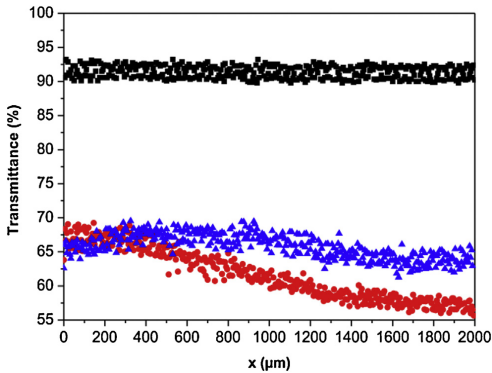


Fig. 2. Scans on PMMA with the laser focus at different positions on a length of 2000 μm along the x axis, (■) out of the sample, (●) within a tilted sample, and (▲) within a sample after tilt correction.

each for x and y axis until the performed scan follows a trend with a ±5% variation in the transmittance along the scan similar to the third one presented in Fig. 2 (triangles). At this point, it is assumed that the tilt of the sample is adequate to perform the experiments.

Once the horizontality of the sample was controlled, a z-scan was performed. Three different positions were identified in the transmittance curve: up, middle and down, corresponding to transmittances of 90 ± 5%, 75 ± 5% and 65 ± 5%, respectively (Fig. 1). Afterwards, the sample was placed in these positions by sending pulses at 200 nJ and moving the sample in the z-axis until the transmittance reaches the corresponding value. Then, laser pulses were fired at different energies from 30 nJ up to 2 μJ, keeping the same z position. After irradiation, the surface modifications were characterized by atomic force microscopy (AFM).

3. Results and discussion

A plot of the transmittance as a function of the pulse energy for the up, middle and down positions is shown in Fig. 3. Each point in the plot is the average of three consecutive pulses fired onto the sample that were separated 5 μm or 10 μm depending on the used energy. For the lowest energies, the transmittance curves show a

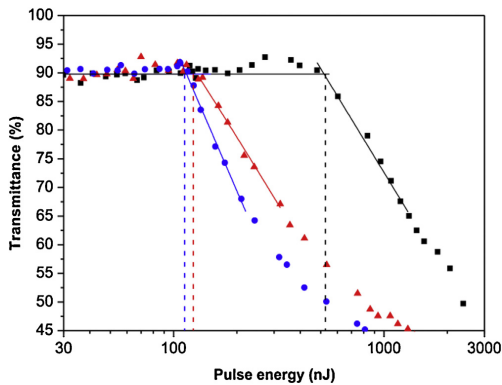


Fig. 3. Plot of the transmitted energy vs. pulse energy for (■) up, (▲) middle, and (●) down positions. Dot lines correspond to the cross-point analysis for critical energy determination.

plateau at 90 ± 5% indicating a lack of absorption for pulse energies below some critical energy value. For pulse energies higher than the critical value, which is different for every sample position, the transmittance progressively decreases showing that part of the pulse energy was absorbed in the sample. Since the exact energy at which the sample starts to absorb is difficult to determine with precision, the critical energy for absorption was determined as the cross-point of the horizontal line corresponding to the points presenting no absorption with the straight line fitted to the first points in the semi-log plot where absorption is clear. Following this method, the values obtained for the critical energy are 112 nJ, 123 nJ, and 533 nJ for down, middle, and up positions, respectively. Thus, in terms of absorption, the difference between the down and middle positions is small, while the up position is significantly different from them.

Some AFM reconstruction images of the surface of the irradiated areas are shown in Fig. 4. Different modifications were produced depending on where the sample surface was placed and the laser pulse energy used. As it has been found in the transmittance curves, the middle and down series show quite similar morphologies and evolution. The first signs of surface ablation for the up position appear at higher pulse energy than for the down and middle positions. For the up series, ablation starts for pulse energies above 170 nJ, while for middle and down series the first signs of ablation appear at 110 nJ. Surprisingly, ablation appears in the up series at pulse energies well below the critical energy determined before from the transmittance curve, while the values of critical energy for the middle and down series coincide quite well with the pulse energies where ablation starts. The ablated areas have the morphology of circular and ellipsoidal craters surrounded by a small rim, which height is one order of magnitude lower than the depth of the crater. In all the cases, the size of the craters increases with the pulse energy. Craters formed at the up position present an irregular shape. Therefore, this position should be disregarded for high precision ablation. Despite the similarities between the middle and down series, the spots produced with the sample at the middle position seem to be slightly smaller than the spots obtained with the same incident energy at the down position. Additionally, submicrometric bumps with a height around 20 nm appear when sending pulses of 100 nJ and 105 nJ at the down position, however, these bumps do not appear in the middle series. It has been shown that the irradiation of PMMA at fluences near the ablation threshold produces bumps of material due to the hydrodynamic expansion of the hot material under the surface [17]. These bumps may appear in the down position because the energy absorption would take place in a position located slightly inside of the sample at incident energies close to the energy threshold, while for the middle position the energy would be focused on the surface of the material.

For pulse energies above 1 μJ, some irregularities in the morphology of the craters can be observed. This behavior seems to correspond with changes in the energy distribution of the laser beam. These could be produced by the self-focusing effect in the glass elements of the focusing device [18]. Taking into account that the critical power for the glass is 2.5 MW [19] and that the pulse duration is 450 fs, this effect would appear for pulse energies higher than 1.1 μJ.

The radii of the craters were measured at a depth corresponding to a 10% of the total depth of each crater. Taking into account that the energy distribution of the beam is Gaussian and that there is a fluence threshold for ablation ( $F_{th}$ ), the square of the radius of the crater ( $r_0$ ) should follow a logarithmic trend with the pulse energy ( $E_p$ ):

$$r_0^2 = -\frac{\omega^2}{2} \ln\left(\frac{F_{th}\pi\omega^2}{2}\right) + \frac{\omega^2}{2} \ln(E_p) \tag{1}$$

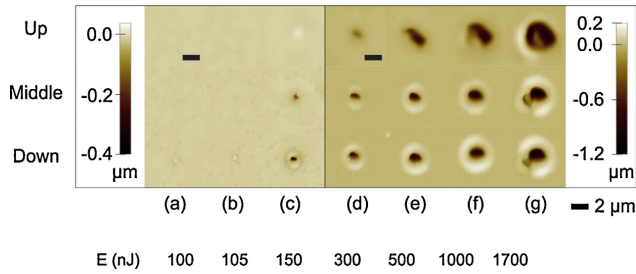


Fig. 4. AFM images of the PMMA surface after the incidence of a pulse of (a) 100 nJ, (b) 105 nJ, (c) 150 nJ, (d) 300 nJ, (e) 500 nJ, (f) 1000 nJ, and (g) 1700 nJ at different positions up, middle and down. The height scale on the left is for (a), (b) and (c), while the height scale on the right is for (d), (e), (f) and (g).

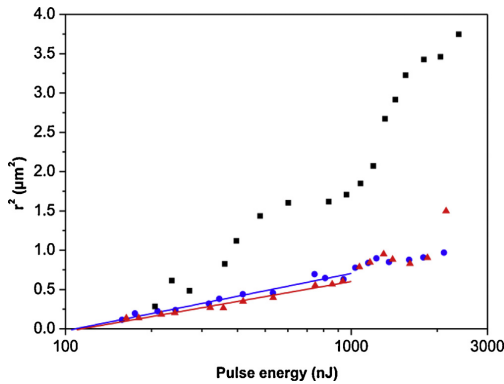


Fig. 5. Plot of the square radius of the craters vs. pulse energy for (■) up, (▲) middle, and (●) down positions. Solid lines correspond to fits of expression (1) for the middle and down series.

where  $\omega$  is the laser beam radius. Indeed, the plot of the square of the radius against the pulse energy (Fig. 5) follows this logarithmic behavior for the down and middle series in the range of 135 nJ–1  $\mu\text{m}$ , where no self-focusing effects interfere. However, this behavior is not clear for the up series. The next observation that stands out is the confirmation that, for the same incident energy, craters

produced in the middle position are similar or slightly smaller than those produced in the down position. The craters in the up series are much bigger than the ones obtained at the middle or down positions. These results corroborate that working on conditions where the transmittance is just starting to decrease is not the best choice for getting precision and control in producing surface ablation. On the other hand, there is a range of around 1  $\mu\text{m}$  between middle and down positions, where the sample surface can be placed and where very similar features can be obtained with precision and control.

$F_{th}$  and  $\omega$  in the middle and down positions were determined by fitting the data of the middle and down series in Fig. 5 with expression (1). Thus, the values found for  $\omega$  are  $0.7 \pm 0.1 \mu\text{m}$  and  $0.8 \pm 0.1 \mu\text{m}$  for middle and down positions, respectively. The corresponding threshold fluences found are  $13 \pm 4 \text{ J/cm}^2$  for the middle series and  $10 \pm 4 \text{ J/cm}^2$  for the down series.

Given that the peak fluence ( $F_p$ ) of a Gaussian beam follows the expression:

$$F_p = \frac{2E_p}{\pi\omega^2} \tag{2}$$

the corresponding pulse energy thresholds for the middle and down positions are  $101 \pm 42 \text{ nJ}$  and  $104 \pm 48 \text{ nJ}$ , respectively. These energy threshold values for ablation correspond quite well with the critical energy values for absorption found before from the transmission measurements (Fig. 3), taking into account the experimental margin of error. However, according to the results found for the up position, the method used for finding the critical energy cannot be extended for all the positions in the z-scan.

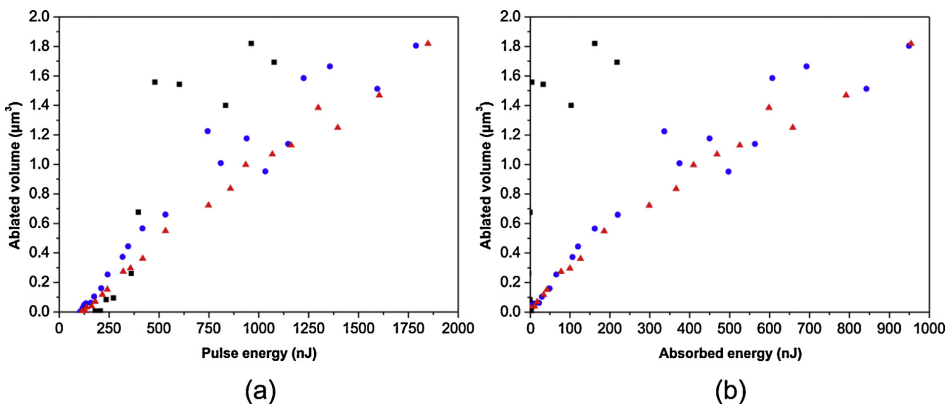


Fig. 6. Plot of the ablated volume vs. (a) the pulse energy, and (b) the absorbed energy for (■) up, (▲) middle, and (●) down positions.

The ablated volume of the craters was calculated from the AFM measurements. The results are plotted in Fig. 6a against the laser pulse energy. The ablated volume follows a linear trend with the pulse energy for energies up to 400–500 nJ depending on the series. At higher energies, the ablated volume continues increasing but with higher dispersion. The middle series presents the lowest dispersion in all the range of pulse energies studied. At low pulse energy, the down position shows the best efficiency in material ablation from the point of view of the energy sent to the sample. However, if the ablated volume is represented as a function of the energy absorbed during the process (Fig. 6b), there are almost no differences between the down and middle series. This indicates a direct correlation between the amount of material removed during ablation and the amount of energy absorbed.

All these results show that there is a range between the middle and down positions in the z-scan where the performance of the ablation in the surface does not significantly change. Anyway, it is in the middle position where the best resolution for ablation on the surface of the sample can be achieved. Thus, we can infer that the middle position would correspond to the position where the surface of the sample is closer to the beam waist in comparison to the up and down positions. Furthermore, any change in the relative position between the sample surface and the laser beam waist can be easily detected by monitoring the transmittance and then corrected in-situ during the ablation process.

#### 4. Conclusions

The z-scan method has been evaluated for the surface ablation of PMMA with high focusing control through the characterization of three representative positions along it. It has been found that there is a range of positions between the middle and down points that provide similar finishing quality and allow the production of craters with submicrometric diameter. The z-scan method allows placing the sample with good accuracy for obtaining high reproducibility on the crater shape modifications even for the smaller craters where the conditions are critical. According to the obtained results, the best position to achieve surface modification on a transparent sample of PMMA is the middle point. Additionally, this is the best place on the z-scan curve to detect any change on the z position in-situ during the ablation process.

#### Acknowledgements

This work is part of a research program funded by MCI of the Spanish Government (Projects MAT2010-15905 and

CSD2008-00023), and Fondo Europeo de Desarrollo Regional (FEDER).

#### References

- [1] A. Kurella, N.B. Dahotre, Review paper: surface modification for bioimplants: the role of laser surface engineering, *J. Biomater. Appl.* 20 (2005) 5–50.
- [2] C.B. Arnold, P. Serra, A. Piqué, Laser direct-write techniques for printing of complex materials, *MRS Bull.* 32 (2007) 23–31.
- [3] L. Torrisi, S. Gammino, A.M. Mezzasalma, A.M. Visco, J. Badziak, P. Parys, J. Wolowski, E. Woryna, J. Krása, L. Láska, M. Pfeiffer, K. Rohlena, F.P. Boody, Laser ablation of UHMWPE-polyethylene by 438 nm high energy pulsed laser, *Appl. Surf. Sci.* 227 (2004) 164–174.
- [4] P. Balling, J. Schou, Femtosecond-laser ablation dynamics of dielectrics: basics and applications for thin films, *Rep. Prog. Phys.* 76 (2013) 036502.
- [5] R.R. Gattass, E. Mazur, Femtosecond laser micromachining in transparent materials, *Nat. Photonics* 2 (2008) 219–225.
- [6] R. Suriano, A. Kuznetsov, S.M. Eaton, R. Kiyon, G. Cerullo, R. Osellame, B.N. Chichkov, M. Levi, S. Turri, Femtosecond laser ablation of polymeric substrates for the fabrication of microfluidic channels, *Appl. Surf. Sci.* 257 (2011) 6243–6250.
- [7] H. Becker, C. Gärtner, Polymer microfabrication technologies for microfluidic systems, *Anal. Bioanal. Chem.* 390 (2008) 89–111.
- [8] Z.K. Wang, H.Y. Zheng, C.P. Lim, Y.C. Lam, Polymer hydrophilicity and hydrophobicity induced by femtosecond laser direct irradiation, *Appl. Phys. Lett.* 95 (2009) 111110.
- [9] S. Ibrahim, D.A. Higgins, T. Ito, Direct-write multiphoton photolithography: a systematic study of the etching behaviors in various commercial polymers, *Langmuir* 23 (2007) 12406–12412.
- [10] J.M. Fernández-Pradas, C. Florian, F. Caballero-Lucas, J.L. Morenza, P. Serra, Femtosecond laser ablation of polymethyl-methacrylate with high focusing control, *Appl. Surf. Sci.* 278 (2013) 185–189.
- [11] M.T. Bin Najam, K.M. Arif, Y.G. Lee, Novel method for laser focal point positioning on the cover slip for TPP-based microfabrication and detection of the cured structure under optical microscope, *Appl. Phys. B* 111 (2013) 141–147.
- [12] M. Antti, H. Ville, V. Jorma, Precise online auto-focus system in high speed laser micromachining applications, *Phys. Procedia* 39 (2012) 807–813.
- [13] G. Fan, S. Ren, S. Qu, Z. Guo, Q. Wang, Y. Wang, R. Gao, Mechanisms for fabrications and nonlinear optical properties of Pd and Pt nanoparticles by femtosecond laser, *Opt. Commun.* 295 (2013) 219–225.
- [14] L. Páfalvi, B.C. Tóth, G. Almási, J.A. Fülöp, J. Hebling, A general Z-scan theory, *Appl. Phys. B* 97 (2009) 679–685.
- [15] E.T.J. Nibbering, G. Grillon, M.A. Franco, B.S. Prade, A. Mysyrowicz, Determination of the inertial contribution to the nonlinear refractive index of air, N<sub>2</sub>, and O<sub>2</sub> by use of unfocused high-intensity femtosecond laser pulses, *J. Opt. Soc. Am. B* 14 (1997) 650–660.
- [16] S. Campbell, F.C. Dear, D.P. Hand, D.T. Reid, Single-pulse femtosecond laser machining of glass, *J. Opt. A: Pure Appl. Opt.* 7 (2005) 162–168.
- [17] J.M. Guay, A. Villafranca, F. Baset, K. Popov, L. Ramunno, V.R. Bhardwaj, Polarization-dependent femtosecond laser ablation of poly-methyl methacrylate, *New J. Phys.* 14 (2012) 085010.
- [18] L. Shah, J. Tawney, M. Richardson, K. Richardson, Self-focusing during femtosecond micromachining of silicate glasses, *IEEE J. Quantum Electron.* 40 (2004) 57–68.
- [19] M. Miwa, S. Juodkazis, T. Kawakami, S. Matsuo, H. Misawa, Femtosecond two-photon stereo-lithography, *Appl. Phys. A: Mater. Sci. Process.* 73 (2001) 561–566.



### **Paper 3**

## **Beam waist position study for surface modification of polymethyl-methacrylate with femtosecond laser pulses**

F. Caballero-Lucas, C. Florian, J.M. Fernández-Pradas, J.L. Morenza, P. Serra.

Published at: Applied Surface Science

Year: 2016

Impact factor JDR 2014: 2.711 - (Q1)

DOI: 10.1016/j.apsusc.2015.12.135







## Beam waist position study for surface modification of polymethyl-methacrylate with femtosecond laser pulses

F. Caballero-Lucas, C. Florian, J.M. Fernández-Pradas\*, J.L. Morenza, P. Serra

Departament de Física Aplicada i Òptica, Universitat de Barcelona, Martí i Franquès 1, Barcelona, E-08028, Spain



### ARTICLE INFO

#### Article history:

Received 23 June 2015  
Received in revised form  
11 November 2015  
Accepted 17 December 2015  
Available online 23 December 2015

#### Keywords:

Femtosecond laser  
Z-scan  
Polymethyl-methacrylate (PMMA)  
Surface modification

### ABSTRACT

Femtosecond lasers are versatile tools to process transparent materials. This optical property poses an issue for surface modification. In this case, laser radiation would not be absorbed at the surface unless the beam is just focused there. Otherwise, absorption would take place in the bulk leaving the surface unperturbed. Therefore, strategies to position the material surface at the laser beam waist with high accuracy are essential.

We investigated and compared two options to achieve this aim: the use of reflectance data and transmittance measurements across the sample, both obtained during z-scans with pulses from a 1027 nm wavelength laser and 450 fs pulse duration. As the material enters the beam waist region, a reflectance peak is detected while a transmittance drop is observed. With these observations, it is possible to control the position of the sample surface with respect to the beam waist with high resolution and attain pure surface modification. In the case of polymethyl-methacrylate (PMMA), this resolution is 0.6  $\mu\text{m}$ . The results prove that these methods are feasible for submicrometric processing of the surface.

© 2015 Elsevier B.V. All rights reserved.

### 1. Introduction

In the last years, the use of femtosecond lasers in the fabrication of microdevices has been increasing. The applications of these devices include different areas such as microfluidics, optical waveguides and materials surface functionalization [1–3]. This short pulse duration produces really high power peaks that trigger non-linear absorption processes like multi-photon absorption, tunneling ionization [4,5] and avalanche ionization [6,7]. These processes make possible the absorption of the laser radiation and therefore modification of even transparent materials [8,9].

Among these materials, polymers are chosen for the production of microdevices because of their ease and low cost of manufacture, biocompatibility and optical transparency. One of the polymers used as substrate for microfluidic devices, polymethyl-methacrylate (PMMA), is especially appropriate because of its adequate properties such as moderate hydrophilicity, good transmission at visible wavelengths (about 90%), and biocompatibility. Thus, PMMA substrates were also chosen for several applications in the field of biology that range from analysis of biomolecules to a wide diversity of observations in cellular biology [10].

Surface modification of the materials is crucial in this kind of studies since changes in the properties like the roughness of the material surface affects the flow resistance of liquids or the protein and cell adsorption efficiency on the surface [11–14]. Therefore, a controlled and precise surface modification of the material surface is essential for these studies.

Several studies with lasers of various wavelengths and pulse durations have shown that laser ablation can be a good microfabrication process on PMMA [15–17]. Nevertheless, thermal effects during the energy transfer to the material limit the resolution of the ablation. This problem can be minimized if the duration of the pulse is shorter than the time of the energy transfer to the lattice. In this regime, electron–electron impact ionization leads to the rapid formation of plasma that expands and ends producing ablation of the material, all confined in the tight region where the laser is focused [18]. The timescale of this exposure (some femtoseconds) is shorter than the energy transfer to the lattice (in the range of the picoseconds) and ablation occurs through direct plasma formation or non-thermal melting of the material [19]. Thus, thermal damage is markedly reduced in comparison with ablation produced by longer pulse duration lasers [20,21].

Since non-linear absorption processes are involved, tightly focused femtosecond lasers can produce modifications with lower size than the laser wavelength, overcoming the diffraction limit. This can be achieved by using laser pulses with incident fluence values slightly higher than the ablation threshold. In this way,

\* Corresponding author. Tel.: +34 934 039 216; fax: +34 934 021 139.  
E-mail address: [jmfernandez@ub.edu](mailto:jmfernandez@ub.edu) (J.M. Fernández-Pradas).

transparent polymers have been modified with ultrashort pulsed lasers achieving submicrometric resolution [22].

High energy densities are necessary for these processes to take place, which are reached by tight focusing the laser beam at the material. Consequently, a good control of the relative position between the sample surface and the beam waist is necessary for precise surface modification. In case that the main objective is the surface functionalization, only surface changes should be produced. However, the modification of the surface of a transparent sample is not a trivial task, since finding out where the surface is depends largely on the implemented experimental system. Currently, some methods allow the adjustment of the position of the surface of transparent samples in the laser beam waist with few micrometers accuracy [23–25].

One of them is the z-scan method [26]. In this work we take advantage from this method to get a precise control on the sample surface position in regard to the beam waist to be able to optimize the fabrication of spots produced at the material surface and achieve high resolution for the dimensions of the spots. A sample of PMMA was irradiated at different incident energies and values for the relative position between the sample surface and the laser beam waist. Simultaneous reflectance and transmittance measurements were performed during sample irradiation. Finally, in order to characterize the results of the surface modification, scanning electron microscopy (SEM) images of the surface after irradiation were taken.

## 2. Experimental

The used laser produces pulses of linearly polarized near-infrared radiation with a wavelength of 1027 nm and duration of 450 fs in an active medium consisting of a crystal of Yb:KYW. These pulses arrive at the sample after being reflected and passing through different optical elements. The beam is focused by a 50 $\times$ , 0.55 numerical aperture objective at about 13 mm of its outer lens. A glass coverslip between the objective and the sample surface was also included to prevent ablation debris to deposit on the objective lens. The energy distribution profile after the objective was Gaussian.

The experimental setup was equipped with three energy detectors that allowed the measurement of reflectance and transmittance through the sample for each laser pulse. One detector was used to control the energy of the incident light. The reflected light was collected by the same objective after being reflected at the sample surface facing the objective. After leaving the objective, the reflected beam followed the same path as the light coming from the laser until it encounters the coated side of a beam-splitter, which reflects it to a lens that collects this energy and focuses it into the energy detector for the reflected light. For the transmitted light, it was measured by a detector placed just after the sample.

The experiments were performed on samples of PMMA with rectangular shape (20 mm  $\times$  10 mm, 1 mm thickness) cut with a diamond blade saw from a commercial 100% pure PMMA sheet available by Goodfellow. No special treatment was needed for the sample preparation before or after laser irradiation.

Previous to the fabrication of the spots, the sample was scanned horizontally in a total range of 2 mm at steps of 10  $\mu$ m while transmittance and reflectance were tracked in order to correct the tilt of the sample surface. When the sample was not perpendicular to the laser beam, a non flat tendency for the measured values was obtained. The horizontality of the sample surface plane with reference to the beam propagation axis was assumed when a flat tendency of the transmittance with a  $\pm$ 5% variation along the sample surface was observed.

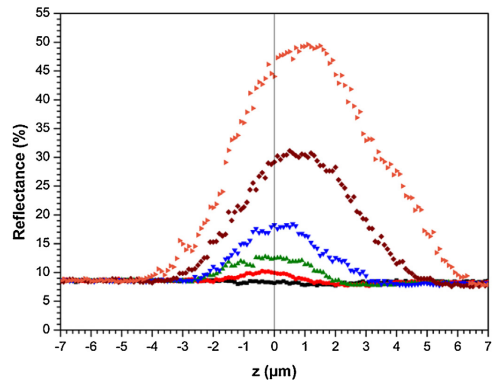


Fig. 1. Plot of reflectance vs. z-position at (■) 100 nJ, (●) 125 nJ, (▲) 150 nJ, (▼) 200 nJ, (◆) 300 nJ, and (★) 500 nJ of incident energy. The experimental error for the reflectance data is  $\pm$ 0.3%.

During spot production, series at fixed incident energy and with 5  $\mu$ m separation between the impinging laser pulses on the surface were produced. The used incident energies took values in the range of 50–500 nJ. While keeping the incident energy of the pulses fixed, spots at different z-positions (relative position between the sample surface and the beam waist) were produced by scanning the sample surface horizontally along a total distance of 2 mm. In this way, laser pulses always impinged in pristine areas of the material. Reflectance and transmittance measurements were performed simultaneously to the spot production.

The range of z-position values at which lines were produced was 20  $\mu$ m with the center of this range in the position  $z = 0 \mu$ m where the sample surface lays at the beam waist. Additional details and a further description about the setup and the z-scan method can be found in [25,26].

After laser irradiation, the modified surface of the sample was inspected through scanning electron microscopy (SEM).

## 3. Results and discussion

Reflectance changes for each single pulse on pristine material for different z-positions are shown in Fig. 1. Negative values for z indicate that the beam waist is outside the sample, while positive values correspond to positions where the beam waist is inside the sample.

These observed tendencies for reflectance measurements can be contrasted with transmittance measures that were simultaneously taken. These values are represented in Fig. 2 in the same way as reflectance measurements were plotted in Fig. 1. As it has been observed and explained in previous studies [25–27], the transmittance decrease observed as the sample enters the beam waist can be used to monitor the relative position between the sample surface and the beam waist and makes possible to ensure a good position control during the experiments. It also allows determining the beam waist position  $z = 0 \mu$ m and therefore correct the z-position values for the experimental data [28]. The correction is based on the fact that at  $z = 0 \mu$ m, the corresponding transmittance value is found approximately at an 83% decrease of the total transmittance difference between the transmittance value where no absorption is detected (91.4%) and the bulk transmittance value for the corresponding incident energy.

This correction makes that the z-position of the reflectance peak is found close to the value corresponding to the sample surface

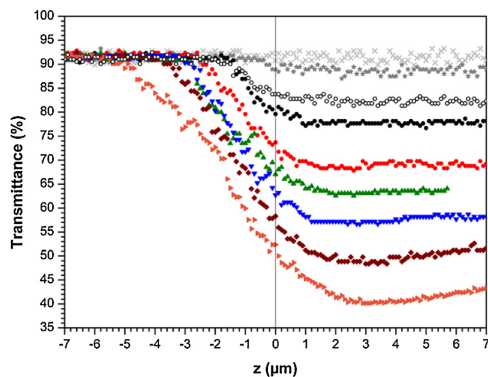


Fig. 2. Plot of transmittance vs. z-position at (×) 50 nJ, (★) 80 nJ, (○) 90 nJ, (■) 100 nJ, (▲) 125 nJ, (▲) 150 nJ, (▼) 200 nJ, (◆) 300 nJ, and (►) 500 nJ of incident energy. Transmittance data have an experimental error of ±3%.

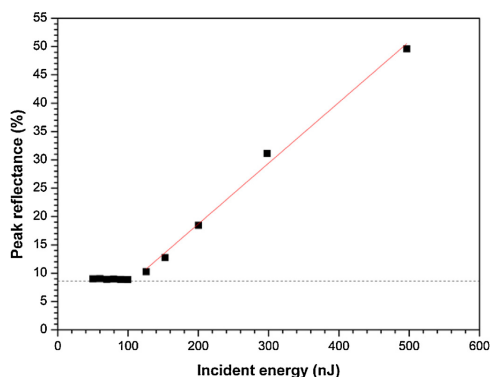


Fig. 3. Peak reflectance values for the different studied incident energies. The fitted line describes the linear tendency that these values follow in the range of energies between 125 nJ and 500 nJ. The experimental error for the peak reflectance values is ±0.3%.

laying at the beam waist position. This also means that performing reflectance measurements is a good way to determine the beam waist position because the detection of a maximum is enough. For this reason, the beam waist position determination by reflectance measurements is much easier than when done by a tracking of transmittance data.

Reflectance measurements show a peak for the series of spots produced at 125 nJ and higher incident energies (see Fig. 1). For z-positions where the sample surface is far from the beam waist, a flat tendency of the reflectance was observed as the pulse energy is not absorbed by the PMMA and only the light reflected by the surface (refractive index change) is measured, which for the laser wavelength (1027 nm) corresponds to a reflectance value of 8.6%. As the sample surface is brought closer to the beam waist, fluence increases and when it overcomes a certain threshold value, absorption of the laser radiation starts taking place. At this point, transmittance starts decreasing and reflectance starts increasing. Reflectance continues increasing as the surface gets closer to the beam waist position until it reaches its maximum value around the position  $z = 0 \mu\text{m}$ . Then, the reflectance starts decreasing as the fluence at the surface gets lower and higher fluences are inside

the bulk. Finally, when the beam waist is deep inside the bulk, the reflectance recovers the original value.

The reflectance peak tends to shift slightly for increasing incident energies to z-positions where the beam waist is below the sample surface. At the same time, the peak width and height also increase while going to higher incident energy values. This tendency of the peak height can be observed in Fig. 3. It can be seen that the peak maximum value increases linearly with increasing incident energies. This behavior makes possible to find a threshold energy value that has to be overcome to start observing a peak in the reflectance. This value can be found when the line fitted to the data meets the reflectance value of 8.6% corresponding to the usual reflectance of the PMMA for light at 1027 nm. This energy value is 106 nJ. Experimental results agree to this value, as no peak could be observed for energies lower than 125 nJ. The presence of this threshold for the observation of a reflectance peak could be related to the formation of a plasma at the sample surface. In view that ablation is always observed when reflectance is higher than 8.6%, it can be assumed that an electron-ion gas-like plasma is generated as indicated in previous simulations of the process of PMMA

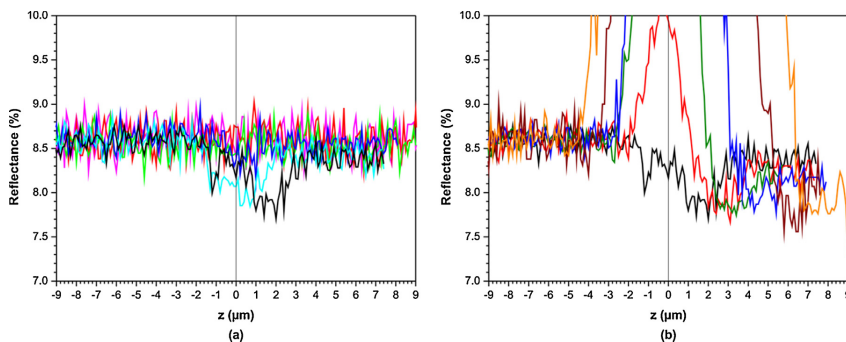
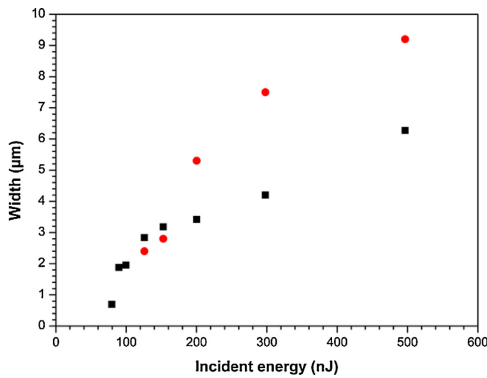


Fig. 4. Plot of reflectance vs. z-position for incident energies of the pulse between (a) 50 nJ and 100 nJ, and (b) 100 nJ and 500 nJ. For lines in (a), the energy values are (magenta) 50 nJ, (red) 60 nJ, (green) 70 nJ, (blue) 80 nJ, (cyan) 90 nJ, and (black) 100 nJ. For (b), the line colors correspond to the following energies: (black) 100 nJ, (red) 130 nJ, (green) 150 nJ, (blue) 200 nJ, and (wine) 300 nJ, and (orange) 500 nJ. The lines only link data points (separated by  $0.1 \mu\text{m}$ ) to make easier following the data tendency. Experimental error for all reflectance data is ±0.3%. (For interpretation of the references to color in this figure legend, the reader is referred to the web version of the article.)





**Fig. 5.** Plot of the width of the z-position range where the sample surface can be detected by the two presented options: reflectance and transmittance measurements. Width values are plotted vs. the incident energy of the laser pulses. Black squares (■) correspond to transmittance measurements (width of the range of the transmittance drop, experimental error  $\pm 0.2 \mu\text{m}$ ) and red dots (●) show the width of the reflectance peaks measured at their basis, with an experimental error of  $\pm 0.3 \mu\text{m}$  for all the values. (For interpretation of the references to color in this figure legend, the reader is referred to the web version of the article.)

ablation [29,30]. The increase of the reflectance is directly related to the increase of the plasma density.

A more detailed observation of the reflectance values for 90 and 100 nJ (below the threshold for peak observation) reveals a small reflectance decrease in form of a valley (Fig. 4a). The position of the valley is found around the beam waist ( $z=0 \mu\text{m}$ ) but also slightly shifted to z-positions corresponding to the beam waist being below the surface. For energies higher than the peak observation threshold (see Fig. 4b), the reflectance decrease (valley) is still present following the peak. Nevertheless, the reflectance minimum does not seem to change much for the different incident energies studied. On the other hand, after the peak and the valley, the reflectance value follows again a flat tendency corresponding to the situation when the beam waist is inside the bulk. All these phenomena can be interpreted according to previous studies on some semiconductors like silicon, where the evolution of the reflectance behavior is studied with respect to the excited electron-hole density at the material surface [31,32]. According to this research, the density of the plasma created on the surface by the impinging laser pulse modifies the optical response of the material that can be explained by the Drude model, which is characterized by a decrease of the reflectivity at lower densities and a drastic increase at higher densities.

When comparing reflectance and transmittance measurements, it can be observed that they point out the close presence of the sample surface with respect to the beam waist in a similar way: the reflectance peak starts at the same position as the transmittance drop begins. However, the end of the reflectance peak is found at higher values for the z-position than the end of the transmittance drop. The later end of the reflectance peak can be used to monitor the z-positions where spots are still produced but the transmittance has already reached the bulk flat value. Fig. 5 shows the width of the range where the z-position of the surface can be determined by reflectance or transmittance measurements. The values were obtained by measuring the width of the transmittance drop and the width of the basis of the reflectance peak. The results show that for the studied incident energies, both measurements give comparable margins for the sample surface position determination and, therefore, can be used similarly as position control methods. Nevertheless, it has to be noted that transmittance measurements

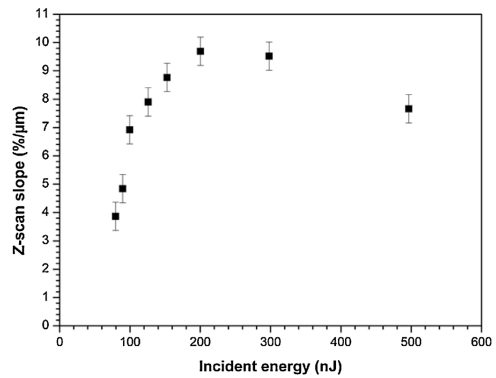


**Fig. 6.** Plot of the z-scan slope (transmittance decrease rate) for the different studied values of the incident energy of the pulses. This decrease rate corresponds to the transmittance reduction observed when the sample enters the beam waist region. The experimental error of the plotted slope values is  $\pm 0.5\%/ \mu\text{m}$ .

can go down to incident energies close to the ablation threshold, while changes in the reflectance can only be detected at higher energies. On the other hand, reflectance measurements provide an extended range for the determination of z-positions where surface modification is still present.

In this way, both reflectance and transmittance data can be put to work to correct the sample surface position with respect to the beam incident direction. Any change in the values would detect a tilt of the sample surface. Transmittance measurements provide an easier way for correcting this tilt considering that the sign of the change of the measured transmittance gives the direction for the correction of the sample tilt: a lower transmittance value indicates that the sample surface is going inside the beam waist. On the contrary, reflectance measurements require more steps for doing this correction because the peak behavior of the data does not give directly the direction needed for the tilt correction (see Fig. 1): a decrease at the left of the reflectance peak means the sample surface going further from the beam waist while at the right of the peak, it means just the contrary. In this case, additional measurements are necessary for being able to correct the sample tilt.

In order to evaluate the precision of the positioning method through transmittance measurements, we analyzed the slope of the transmittance drop in the z-scans. This slope was calculated by fitting a line to the experimental data. The tendency that these values follow has been represented in Fig. 6. For incident energies close to the ablation threshold, the slope rapidly increases until 200 nJ. The higher the value of the transmittance drop slope, the higher the sensitivity to detect a change in the z-position. Therefore, the control of the z-position with transmittance measurements presents the best precision for incident energies around 200 nJ. For higher energies, the method still has a good performance as a position control procedure since the slope value only decreases a little. If we take  $8.5\%/ \mu\text{m}$  as an average value for the slope at these energies (100–500 nJ), the 5% margin for the surface horizontality in transmittance values commented in the experimental section gives a precision in the determination of the z-position of  $0.6 \mu\text{m}$ . This number can be considered a good representative value for the precision of the z-scan method as a position determination procedure.

However, for energies very close to the ablation threshold, which are used to produce very small spots, transmittance measurements cannot ensure such a good position control. In this situation, only a reduced range of z-positions where fluence

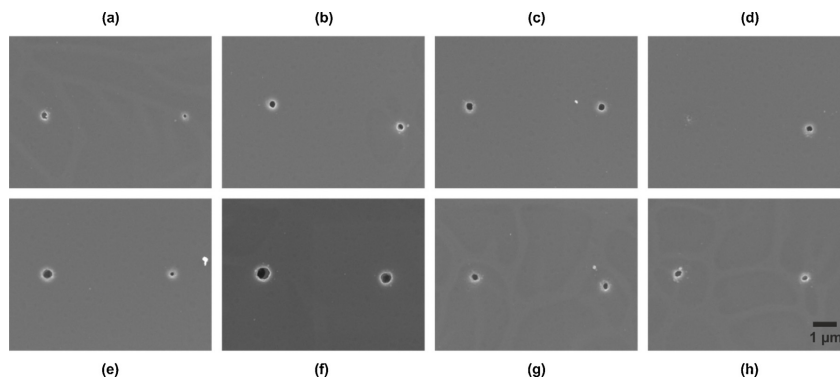


**Fig. 7.** SEM images of the first two craters produced each one by one pulse with the same incident energy when the sample is entering the beam waist region and the fluence at the surface overcomes the threshold value. The right crater is the first one, while the left crater is produced when the sample surface is  $0.1 \mu\text{m}$  closer to the beam waist. The images correspond to different incident energy values: (a) 80 nJ, (b) 90 nJ, (c) 100 nJ, (d) 125 nJ, (e) 150 nJ, (f) 200 nJ, (g) 300 nJ, and (h) 500 nJ.

overcomes the ablation threshold is suitable for spot production and the relative position of the sample surface with respect to the beam waist becomes more critical. However, small spots can be also produced at higher energies. Spots shown in Fig. 7 were obtained at the two first positions where a transmittance decrease is detected. Their dimensions are visibly smaller than the diffraction limit of the focused laser beam. There is a change in the z-position of  $0.1 \mu\text{m}$  between the two spots visible at each image and the incident energy values at which they were produced go from 80 nJ (just above the ablation threshold) until 500 nJ. The radii of these spots are in the range between 66 nm for the smallest one (obtained at 80 nJ) and 340 nm for the largest one (obtained at 200 nJ). Even with 500 nJ of incident energy, spots with radii below 300 nm were obtained.

These results certainly show that in situ reflectance or transmittance measurements during the surface modification process make possible a high precision position control of the sample surface with respect to the beam waist and, consequently, a good control of the dimensions of the produced surface modifications. As well, this optimization of the surface modification procedure contributed to the surface ablation of spots with sizes in the submicrometric domain without being restricted just to incident energies very close to the ablation threshold. Precise surface ablation is also possible with pulse energies clearly higher than the ablation threshold.

#### 4. Conclusions

Reflectance and transmittance measurements performed simultaneously to surface modification of PMMA gave valuable data about the surface position with respect to the beam waist and, in consequence, surface modification can be optimized to produce spots with submicrometric dimensions. Spots with a radius of 66 nm were ablated on the surface. This is much smaller than the diffraction limited spot for the laser wavelength at 1027 nm. Thanks to the high precision of the z-scan as a positioning method, higher energies can be also applied to produce these small spots.

#### Acknowledgments

This work is part of a research program funded by MCI of the Spanish Government (Project TEC2014-54544), and Fondo Europeo de Desarrollo Regional (FEDER).

#### References

- [1] H.T. Schek, A.J. Hunt, Micropatterned structures for studying the mechanics of biological polymers, *Biomed. Microdev.* 7 (2005) 41–46.
- [2] S. Lee, R. An, A.J. Hunt, Liquid glass electrodes for nanofluidics, *Nat. Nanotechnol.* 5 (2010) 412–416.
- [3] K. Sugioka, Y. Cheng, Femtosecond laser processing for optofluidic fabrication, *Lab Chip* 12 (2012) 3576–3589.
- [4] P.G. Eliseev, O.N. Krokhin, I.N. Zavestovskaya, Nonlinear absorption mechanism in ablation of transparent materials by high power and ultrashort laser pulses, *Appl. Surf. Sci.* 248 (2005) 313–315.
- [5] D.F. Farson, H.W. Choi, B. Zimmerman, J.K. Steach, J.J. Chalmers, S.V. Olesik, L.J. Lee, Femtosecond laser micromachining of dielectric materials for biomedical applications, *J. Micromech. Microeng.* 18 (2008) 035020.
- [6] P. Balling, J. Schou, Femtosecond-laser ablation dynamics of dielectrics: basics and applications for thin films, *Rep. Prog. Phys.* 76 (2013) 036502.
- [7] X. Yu, Q. Bian, Z. Chang, P.B. Corkum, S. Lei, Femtosecond laser nanomachining initiated by ultraviolet multiphoton ionization, *Opt. Express* 21 (2013) 24185–24190.
- [8] A.P. Joglekar, H. Liu, E. Meyhöfer, G. Mourou, A.J. Hunt, Optics at critical intensity: applications to nanomorphing, *Proc. Natl. Acad. Sci. U.S.A.* 101 (2004) 5856–5861.
- [9] R.R. Gattass, E. Mazur, Femtosecond laser micromachining in transparent materials, *Nat. Photonics* 2 (2008) 219–225.
- [10] H. Becker, C. Gärtner, Polymer microfabrication technologies for microfluidic systems, *Anal. Bioanal. Chem.* 390 (2008) 89–111.
- [11] Z.K. Wang, H.Y. Zheng, H.M. Xia, Femtosecond laser-induced modification of surface wettability of PMMA for fluid separation in microchannels, *Microfluid. Nanofluid.* 10 (2010) 225–229.
- [12] X. Ma, H. Huo, M. Wei, L. Wang, M. Shen, C. Barry, J. Mead, Enhanced protein binding on femtosecond laser ablated poly(methyl methacrylate) surfaces, *Appl. Phys. Lett.* 98 (2011) 171101.
- [13] M.S. Ahsan, F. Dewanda, M.S. Lee, H. Sekita, T. Sumiyoshi, Formation of superhydrophobic soda-lime glass surface using femtosecond laser pulses, *Appl. Surf. Sci.* 265 (2013) 784–789.
- [14] P. Danilevicius, L. Georgiadi, C.J. Pateman, F. Claeysens, M. Chatzinikolaïdou, M. Farsari, The effect of porosity on cell ingrowth into accurately defined, laser-made, polylactide-based 3D scaffolds, *Appl. Surf. Sci.* 336 (2015) 2–10.
- [15] L. Juha, M. Bittner, D. Chvostova, V. Letal, J. Krasa, Z. Otcenasek, M. Kozlova, J. Polana, A.R. Präg, B. Rus, M. Stupka, J. Krzywinski, A. Andrejczuk, J.B. Pelka, R. Sobierajski, L. Ryc, J. Feldhaus, F.P. Boody, M.E. Grisham, G.O. Vaschenko, C.S. Menoni, J.J. Rocca, XUV-laser induced ablation of PMMA with nano-, pico-, and femtosecond pulses, *J. Electron Spectrosc. Relat. Phenom.* 144–147 (2005) 929–932.
- [16] J. Lawrence, L. Li, Modification of the wettability characteristics of polymethyl methacrylate (PMMA) by means of CO<sub>2</sub> Nd:YAG, excimer and high power diode laser radiation, *Mater. Sci. Eng. A* 303 (2001) 142–149.
- [17] F. Baset, A. Villafranca, J.-M. Guay, R. Bhardwaj, Femtosecond laser induced porosity in poly-methyl methacrylate, *Appl. Surf. Sci.* 282 (2013) 729–734.
- [18] F. Korte, J. Serbin, J. Koch, A. Egbert, C. Fallnich, A. Ostendorf, B.N. Chichkov, Towards nanostructuring with femtosecond laser pulses, *Appl. Phys. A Mater. Sci. Process.* 77 (2003) 229–235.
- [19] B. Rethfeld, K. Sokolowski-Tinten, D. von der Linde, S.I. Anisimov, Timescales in the response of materials to femtosecond laser excitation, *Appl. Phys. A* 79 (2004) 767–769.

- [20] D. Dijkkamp, A.S. Gozdz, T. Venkatesan, X.D. Wu, Evidence for the thermal nature of laser-induced polymer ablation, *Phys. Rev. Lett.* 58 (1987) 2142–2145.
- [21] R. Suriano, A. Kuznetsov, S.M. Eaton, R. Kiyari, G. Cerullo, R. Osellame, B.N. Chichkov, M. Levi, S. Turri, Femtosecond laser ablation of polymeric substrates for the fabrication of microfluidic channels, *Appl. Surf. Sci.* 257 (2011) 6243–6250.
- [22] S.M. Eaton, C. De Marco, R. Martinez-Vazquez, R. Ramponi, S. Turri, G. Cerullo, R. Osellame, Femtosecond laser microstructuring for polymeric lab-on-chips, *J. Biophoton.* 702 (2012) 687–702.
- [23] M.T. Bin Najam, K.M. Arif, Y.-G. Lee, Novel method for laser focal point positioning on the cover slip for TPP-based microfabrication and detection of the cured structure under optical microscope, *Appl. Phys. B* 111 (2013) 141–147.
- [24] M. Antti, H. Ville, V. Jorma, Precise online auto-focus system in high speed laser micromachining applications, *Phys. Procedia.* 39 (2012) 807–813.
- [25] C. Florian, F. Caballero-Lucas, J.M. Fernández-Pradas, J.L. Morenza, P. Serra, Surface ablation of transparent polymers with femtosecond laser pulses, *Appl. Surf. Sci.* 302 (2014) 226–230.
- [26] J.M. Fernández-Pradas, C. Florian, F. Caballero-Lucas, J.L. Morenza, P. Serra, Femtosecond laser ablation of polymethyl-methacrylate with high focusing control, *Appl. Surf. Sci.* 278 (2013) 185–189.
- [27] F. Caballero-Lucas, C. Florian, J.M. Fernández-Pradas, J.L. Morenza, P. Serra, Precise surface modification of polymethyl-methacrylate with near-infrared femtosecond laser, *Appl. Surf. Sci.* 336 (2015) 170–175.
- [28] C. Florian, F. Caballero-Lucas, J.M. Fernández-Pradas, S. Bosch, J.L. Morenza, P. Serra, Femtosecond laser surface ablation of polymethyl-methacrylate with position control through z-scan, *J. Phys. D: Appl. Phys.* 48 (2015) 335302.
- [29] J.-M. Guay, A. Villafranca, F. Baset, K. Popov, L. Ramunno, V.R. Bhardwaj, Polarization-dependent femtosecond laser ablation of poly-methyl methacrylate, *New J. Phys.* 14 (2012) 085010.
- [30] F. Baset, K. Popov, A. Villafranca, J.-M. Guay, Z. Al-Rekabi, A.E. Pelling, L. Ramunno, R. Bhardwaj, Femtosecond laser induced surface swelling in poly-methyl methacrylate, *Opt. Express.* 21 (2013) 12527–12538.
- [31] K. Sokolowski-Tinten, D. von der Linde, Generation of dense electron-hole plasmas in silicon, *Phys. Rev. B* 61 (2000) 2643–2650.
- [32] P.A. Danilov, A.A. Ionin, S.I. Kudryashov, S.V. Makarov, A.A. Rudenko, P.N. Saltuganov, L.V. Seleznev, V.I. Yurovskikh, D.A. Zayarny, T. Apostolova, Silicon as a virtual plasmonic material: acquisition of its transient optical constants and the ultrafast surface plasmon-polariton excitation, *J. Exp. Theor. Phys.* 120 (2015) 946–959.

## **Paper 4**

# Femtosecond laser surface ablation of polymethylmethacrylate with position control through z-scan

C. Florian, F. Caballero-Lucas, J.M. Fernández-Pradas, S. Bosch, J.L. Morenza, P. Serra.

Published at: Journal of Physics D: Applied Physics

Year: 2015

Impact factor JDR 2014: 2.721 - (Q1)

DOI: 10.1088/0022-3727/48/33/335302





# Femtosecond laser surface ablation of polymethyl-methacrylate with position control through z-scan

C Florian, F Caballero-Lucas, J M Fernández-Pradas, S Bosch, J L Morenza and P Serra

Departament de Física Aplicada i Òptica, Universitat de Barcelona, Martí i Franquès 1, E-08028 Barcelona, Spain

E-mail: [jmfernandez@ub.edu](mailto:jmfernandez@ub.edu)

Received 26 January 2015, revised 9 June 2015

Accepted for publication 17 June 2015

Published 16 July 2015



CrossMark

## Abstract

Spatial resolution of laser micromachining of polymers can be improved with the use of femtosecond laser pulses. Due to the short interaction time, thermal effects are significantly reduced. Additionally, the non-linear character of the interaction of ultrashort laser pulses with transparent materials allows the modification inside their bulk also. However, this creates the challenge to accurately focus the laser beam in the surface when only surface ablation is required. Thus, this work presents a study of the laser ablation of a transparent polymer at different pulse energies and focusing positions controlled through z-scan transmittance measurements. Experiments were performed using an Yb:KYW laser with 450 fs pulses and 1027 nm wavelength. Morphological analysis of the polymer surface after irradiation was performed using scanning electron microscopy. Similar ablation craters were found for a range of sample positions around the beam waist. However, focused ion beam cross-sections of the craters unveil significant inner modifications under most of the focusing conditions leading to surface ablation. Hence, surface ablation without damaging the bulk material only occurs at critical positions where the beam waist is located slightly outside the sample. *In situ* monitoring of the sample position can be made through transmittance measurements.

Keywords: femtosecond laser ablation, surface patterning, polymers, micro- and nanoscale patterning

Online supplementary data available from [stacks.iop.org/JPhysD/48/335302/mmedia](http://stacks.iop.org/JPhysD/48/335302/mmedia)

(Some figures may appear in colour only in the online journal)

## 1. Introduction

During the latest years, the design and fabrication of micro-devices have increased the usage of femtosecond lasers for applications such as lab-on-a-chip and microfluidic devices, optical waveguides and materials surface functionalization [1–3]. Their versatility relies on the short time that the sample is exposed to the laser radiation. The short pulse duration produces very high power peaks that enable non-linear absorption processes as multi-photon absorption, tunneling ionization [4] and multi-photon ionization [5] besides other

non-linear propagation effects as self-focusing and plasma defocusing [6–8] involved when modifying transparent materials. Electrons in the valence band are firstly promoted to the conduction band by multi-photon absorption or tunneling ionization. This initial electron density in the conduction band initiates ablation through further excitation of these electrons by the high intensity of the focused laser beam. Thus, electron–electron impact ionization leads to the rapid formation of plasma that expands and ends producing ablation of the material, all confined in the tight region where the laser is focused [9]. The timescale of this exposure (some femtoseconds) is

shorter than the time by which this energy can be transferred to the lattice (in the range of the picoseconds) and ablation occurs through direct plasma formation or non-thermal melting of the material [10]. Thus, thermal damage decreases dramatically in comparison with ablation produced by longer pulse duration [11].

Since non-linear absorption processes are involved, tightly focused femtosecond lasers can produce modifications with lower size than the laser wavelength, overcoming the diffraction limit [12]. This can be achieved by using laser pulses with incident energy values slightly higher than the ablation threshold. This precise energy deposition allows improving spatial resolution and finishing quality which are needed in specific applications like the fabrication of microchannels in biocompatible materials and the production of optical waveguides [13, 14]. For instance, transparent polymers have been modified with ultrashort pulsed lasers achieving submicrometric resolution [15].

Most of the femtosecond laser interaction studies with transparent materials have been performed in glass and fused silica where the modification of the material occurs in bulk [16, 17]. However, some applications such as micromachining for microfluidics and micro-optics require the best control over the position where the energy is delivered [18]. In case that the main objective is the surface functionalization without modifications in the bulk, only surface changes should be produced. However, the modification of the surface of a transparent sample is not a trivial task, since to find out where the surface is depends largely on the implemented experimental system for both focusing the laser light and positioning the sample. If the focusing system incorporates high enough numerical aperture objectives, the Rayleigh length can be short enough so that small changes in the relative position between the sample and the beam waist can easily lead to deposit the energy in the bulk instead of the surface or to focus the beam outside the sample [19]. Currently, some methods allow the adjustment of the position of the surface of transparent samples in the laser beam waist with few micrometers accuracy [20–22].

One of them is the  $z$ -scan method [22]. During a  $z$ -scan experiment, pulses at a fixed energy are sent to the sample surface. The incident and transmitted energies are measured at different sample positions in the  $z$ -axis relative to the laser beam waist. As a result, a transmittance curve along a range of  $z$ -positions is obtained. The information of the transmittance curve can be used to place and control the position of the sample in the  $z$ -axis with high accuracy.

In this work, we study the relation between the resulting modifications produced by the laser irradiation at different sample positions along the beam axis and the transmittance values during  $z$ -scan experiments. Typically the surface modifications are craters produced by material ablation, but depending on the focusing conditions and the laser fluence, some protuberating bump structures are also produced. One objective is to identify the position in the transmittance curve where the laser beam waist is located. Another objective is to determine the best position to produce modifications in the surface of the sample. For this, atomic force microscopy (AFM) and scanning electron microscopy (SEM) images of

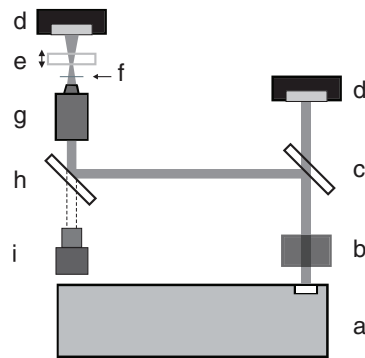


**Figure 1.** Scheme of the experimental setup: (a) laser, (b) attenuator, (c) beam splitter, (d) photodiode, (e) PMMA sample, (f) cover slip, (g) focusing objective, (h) mirror, and (i) CCD camera.

the surface after irradiation were taken, registering the change of the morphology at different  $z$ -positions of the sample. A selection of modified areas was ablated using focused ion beam (FIB) technique in order to obtain cross-sections. Then, SEM images were taken in order to visualize the inner morphology of the material beneath the irradiated areas.

## 2. Experimental details

The laser pulses were generated by a diode-pumped Yb:KYW laser system of Amplitude Systemes, with 1027 nm wavelength and 450 fs pulse duration. The energy distribution profile corresponds to a Gaussian beam with nominal quality factor  $M^2 = 1.3$  and diameter of 5 mm at  $1/e^2$  of the peak intensity before entering the objective. The pulses were focused using a  $50\times$  objective with numerical aperture 0.55, working distance 13 mm and rear aperture diameter of 6 mm. Experiments were performed with pulse energies of  $87 \pm 1$  nJ,  $100 \pm 2$  nJ,  $125 \pm 2$  nJ and  $200 \pm 2$  nJ. Using these energies and the beam waist size obtained in section 3 we could calculate the peak fluences and intensities that range from  $7.8$  to  $18$  J cm $^{-2}$  and from 17 to 40 TW cm $^{-2}$ , respectively.

The material used in the experiments was polymethylmethacrylate (PMMA) disposed in rectangular pieces of  $20 \times 10$  mm and thickness of 1.1 mm. The system allowed moving the sample in three perpendicular axes with minimum incremental steps of 100 nm by the action of motorized stages. The tilting of the sample was corrected by adjusting two micrometric screws properly placed in the sample holder. Two energy detectors were used; the first one measured the incident pulse energy after the laser beam passes through a beam splitter, and the second one was placed behind the sample for measuring the transmitted energy. Visualization of the sample *in situ* was performed with a CCD camera placed coaxially with the laser beam. Figure 1 shows a diagram of the general setup used for the ablation experiments.

In a  $z$ -scan experiment, single pulses are fired to pristine sample areas and the amount of transmitted energy is

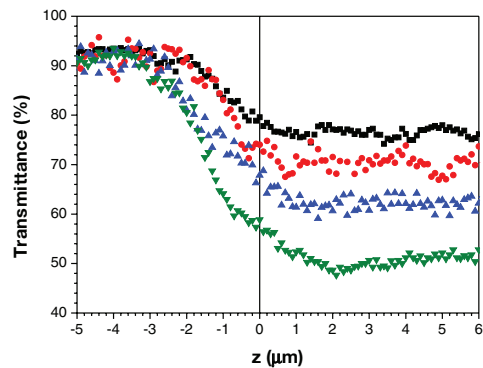
measured at different  $z$ -positions. Therefore, the horizontal motion of the sample must not imply an uncontrolled  $z$ -position change in order to get accurate  $z$ -scan data. Previous experiments show that the transmitted energy changes along different positions on the  $xy$  plane if the sample is tilted [23]. Thus, this horizontality was achieved by modifying the tilting of the sample while sending pulses of  $135 \pm 2$  nJ until the transmittance value showed variations below the signal to noise ratio of  $\pm 5\%$  along the area of interest. Once the sample tilt is corrected, the focus of the laser beam is placed near the surface of the sample by means of the image obtained in the CCD camera. The focal plane of the camera and the position of the laser beam waist are close enough to place the surface near the laser focus based on the image of the camera. Then, the sample is displaced a distance of around  $10 \mu\text{m}$  farther from the objective, in order to assure the position of the beam waist outside the sample with no significant energy absorption. Starting from this position, the laser fires pulses one by one and the position of the sample is modified in steps of  $100$  nm in the  $z$ -axis and  $5 \mu\text{m}$  along the  $x$ -axis, thus only one laser pulse impinges on the same region of the sample.

After irradiation, the sample surface was characterized through AFM and SEM. Finally, FIB technique was used to ablate material in some of the irradiated spots of one  $z$ -scan in order to visualize a cross-section of the produced modifications and the bulk material beneath the irradiated areas. As the material is very sensitive to thermal changes, the energy of the ion beam was kept very low and long exposure times were needed to avoid unwanted damage on the sample (5 kV, 20 min). After FIB ablation, the sample was covered with a graphite thin film of  $\sim 20$  nm for SEM imaging. SEM images after FIB ablation were taken with tilting of  $45^\circ$  with respect to the surface plane in order to visualize the cross-sections of the ablated zones.

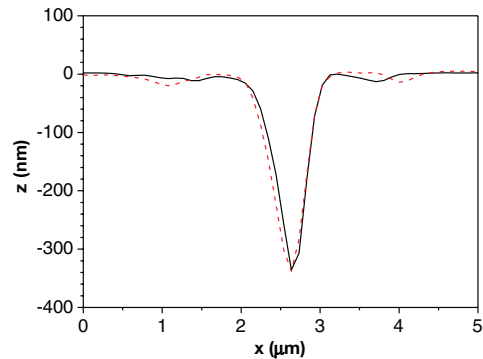
### 3. Results and discussion

Figure 2 shows the plots of the transmittance versus the  $z$ -position corresponding to incident pulse energies of 87, 100, 125 and 200 nJ. In this figure the  $z$ -positions start at  $-5 \mu\text{m}$  and end at  $6 \mu\text{m}$ . The negative values correspond to sample positions where the beam waist is outside the sample. This range was chosen in view of the change in the transmittance along a complete  $z$ -scan of  $20 \mu\text{m}$ . During the first positions, the value for the transmittance corresponds to the maximum value of  $91 \pm 5\%$ .

In these positions, the beam waist is far enough from the sample so the intensity in the surface is not high enough to modify the material. As the sample moves towards the beam waist, the fluence at the surface increases and the transmittance decreases during a range of  $z$ -positions. This range begins at different positions depending on the incident pulse energy. For instance, the position where the transmittance starts changing for the curve of 87 nJ is  $z = -1.8 \mu\text{m}$  while for 200 nJ it starts at  $z = -3.1 \mu\text{m}$ . This is reasonable since an energy increase means a fluence increase on the surface that allows obtaining surface modifications at farther positions from the laser beam waist. Afterwards, for all the curves, there



**Figure 2.** Transmittance values for  $z$ -scans produced with pulse energies of (■) 87 nJ, (●) 100 nJ, (▲) 125 nJ and (▼) 200 nJ. The position  $z = 0 \mu\text{m}$  corresponds to the position of the laser beam waist determined from what is found in figure 5(b).



**Figure 3.** AFM profile of craters produced in the series made of 125 nJ of incident energy. The corresponding positions are (solid line)  $z = -1.9 \mu\text{m}$  and (dashed line)  $z = 0 \mu\text{m}$ .

is a position from which the transmittance presents a plateau with constant value. The transmittance value of the plateau presents lower values as the pulse energy increases. Despite that the sample is moving in steps of  $100$  nm, the range for positioning the sample close to the beam waist can be estimated by the  $z$  range where the transmittance decreases from the maximum value to the plateau value, being different for each incident energy. For 125 nJ, the  $z$  range starts from  $z = -2.6 \mu\text{m}$  to  $z = 1.4 \mu\text{m}$  resulting in a  $z$  range or  $\sim 4 \mu\text{m}$ .

According to AFM data, the morphology of most of the surface modifications corresponds to a crater shape (figure 3). It can be observed that as the pulse energy increases, the depth of the craters also increases. In addition, it is remarkable that the crater depth and shape are similar despite the position changes in the  $z$ -axis for all the studied energies. Some craters produced during the  $z$ -scans made at pulse energies of 87, 100, 125 and 200 nJ are shown in figure 4. In general, the craters have circular shape during the first positions of the  $z$ -scans, but after certain position the morphology becomes

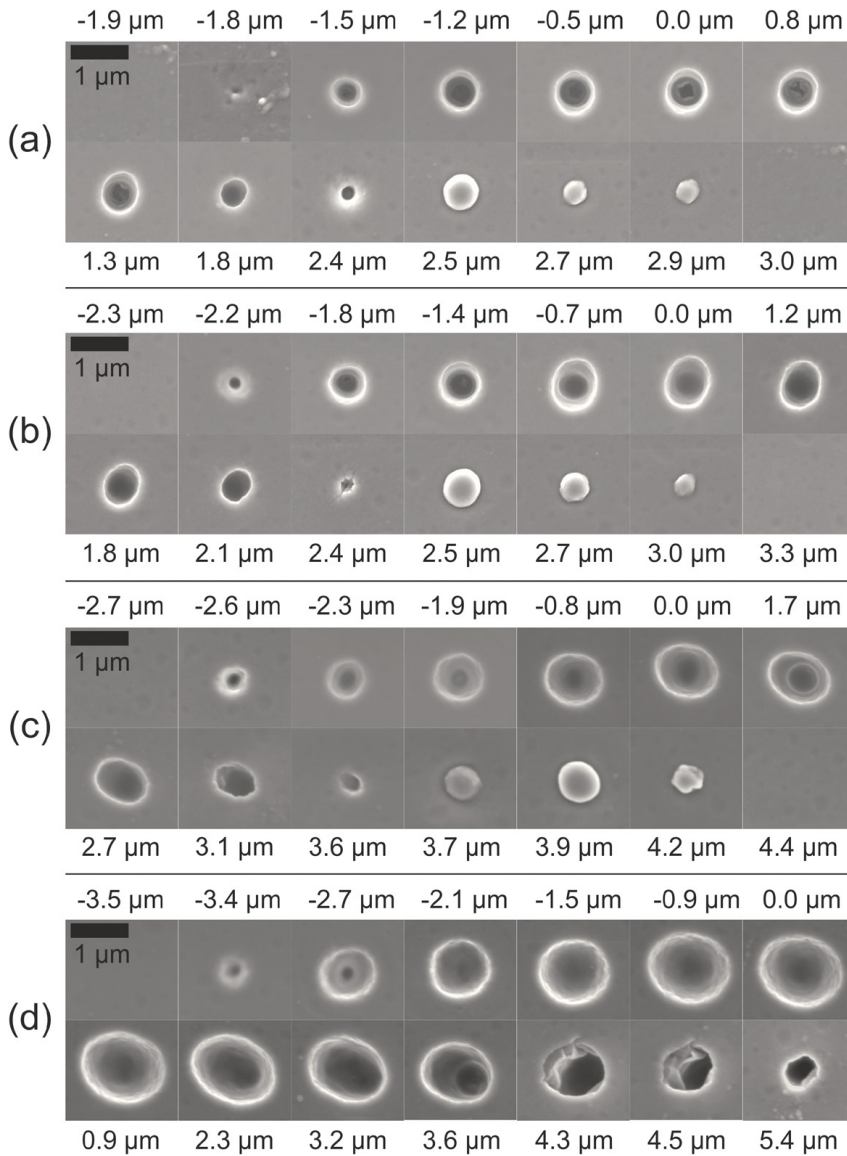


**Figure 4.** SEM images of surface modifications. The corresponding pulse energies in each series are (a) 87 nJ, (b) 100 nJ, (c) 125 nJ and (d) 200 nJ. The sample position is indicated next to each image.

a bit elliptical. The modifications on the surface are shown from left, where the beam waist is far from the sample, to right, where the sample moves towards the beam waist and ends with it inside.

In this way, the first presented image shows the closer position where the laser does not produce any surface modification. After this position, the sample moves towards the beam

wast and the fluence at the surface is high enough to produce ablation. The craters size starts increasing as  $z$ -position increases until it is reached a range where the size seems to be more or less constant. After this range, the crater sizes decrease gradually until the appearance of bump shaped modifications. Their morphology consists of bubble shaped structures that protrude over the surface level. The sizes of the

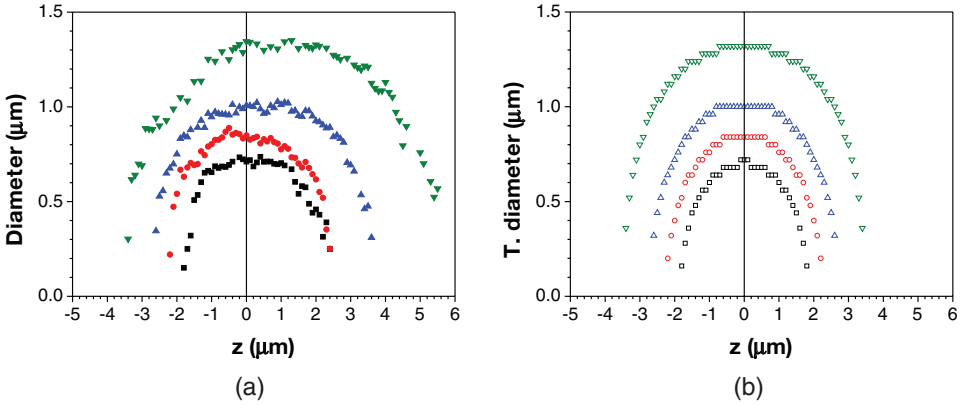


**Figure 5.** (a) Plot of the average diameter versus  $z$ -position. (b) Plot of the theoretical diameter versus  $z$ -position. The series were produced with pulse energies of (■) 87 nJ, (●) 100 nJ, (▲) 125 nJ and (▼) 200 nJ.

bumps decrease as  $z$ -position continues increasing until there is no visible modification or ablation on the sample surface. Bumps are present for all the studied  $z$ -scans although they are not shown in figure 4(d).

Lazare *et al* [24] proposed a model to predict the evolution of the absorption for a silk protein during the femtosecond laser pulse by evaluating the ionization probabilities considering multiphoton ionization and electron impact ionization and the density of ionizable electrons of the material. Results show that only a fraction of the energy is absorbed in the first 10 nm of the surface, so great part of the laser pulse energy continues propagating inside. The amount of absorbed energy increases with increasing laser fluence. Taking into account the values corresponding to the peak intensities used in our experiments and the band gap of 3.7 eV for the PMMA samples (calculated from an UV-visible transmittance spectrum), we find that the Keldysh parameter [4] takes values ranging from 1 for the highest energy pulses to 2 for the lowest ones. Thus, the first ionization mechanism occurring in our experiments is probably produced by multiphoton absorption, although some contribution from tunneling ionization cannot be completely disregarded. However, once the critical density for impact ionization is reached, most of the ionized electrons are generated by this last mechanism and results should not be highly dependent on the first ionization mechanism probabilities. The density of ionizable electrons ( $n_a$ ) for PMMA has been evaluated from its theoretical density and the number of single C–O bonds of the PMMA monomer as they contain the most ionizable electrons [25]. In our case  $n_a = 7.17 \times 10^{21} \text{ cm}^{-3}$ , which is one order of magnitude lower than the value reported by Lazare for silk protein [24]. Consequently, absorption probability would be lower and transmittance higher.

Figure 5(a) shows a plot of the measured crater diameter versus the  $z$ -position. The measurements were obtained from the SEM images. Comparing the size evolution with the  $z$ -scans in figure 2, we can identify that the first and smaller craters are produced just in the positions of each  $z$ -scan where the transmittance starts decreasing. The transmittance

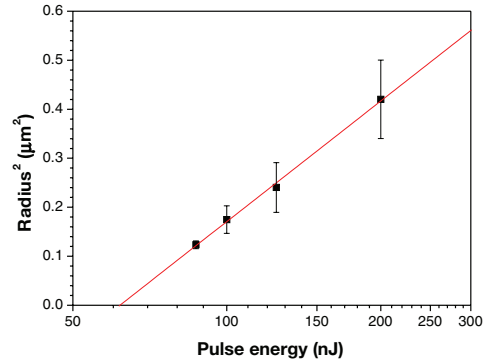


**Figure 6.** Plot of the radius squared versus the pulse energy. The error bars correspond to the experimental errors of the crater measurements.

at this position almost corresponds to the highest value and virtually no absorption is detected. Afterwards, the transmittance values decrease gradually as the size of the diameters increases. Then, there is a range of  $z$ -positions where the crater size is more or less the same, while transmittance values continue decreasing. This range ends at positions where the transmittance has already reached the plateau. The same trend can be observed in all the different pulse energies. The average diameter in the flat central zone is  $700 \pm 20 \text{ nm}$  for 87 nJ,  $835 \pm 25 \text{ nm}$  for 100 nJ,  $980 \pm 30 \text{ nm}$  for 125 nJ, and  $1.30 \pm 0.04 \mu\text{m}$  for 200 nJ. It is noteworthy that although the transmittance values change significantly, there is no significant change in the crater sizes for all the  $z$ -scan experiments. It is at the transmittance plateau region that there is a decrease of the crater size and, finally, the later bump formation.

Based on the above results, the often used method to locate the position of the laser beam waist by searching the smallest modification produced in the sample surface at a given pulse energy is not correct since the smallest modifications are

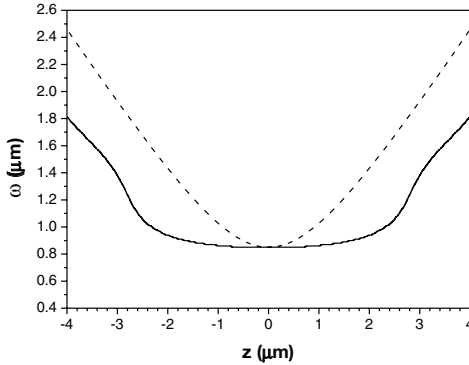


**Figure 7.** Plot of the beam radius along  $z$ -axis following two different methods: the dashed line plot was calculated following the  $M^2$  model [28], while the continuous line plot was determined through vector diffraction theory taking into consideration the clipping factor between the beam diameter and the rear objective aperture [30].

obtained when the laser beam waist is located far from the surface, outside or inside the sample, as it can be seen in figure 5(a). Presumably, the position of the laser beam waist is located somewhere among the positions where the diameters of the craters are more or less constant. Assuming this hypothesis, we represented the average values of the crater squared radii around the maximum values versus the laser pulse energy (figure 6) in order to get information of the laser beam waist.

The logarithmic correlation shown in the plot of figure 6 suggests that the beam intensity profile is Gaussian at the beam waist, and that PMMA ablation is activated when the fluence on the surface overcomes certain threshold value ( $F_{th}$ ) [26, 27]. Therefore, the following equation (1), which gives the crater radius ( $r$ ) ablated at a given pulse energy ( $E$ ) in a Gaussian beam, can be used to find the beam radius ( $\omega$ ) at the beam waist and the fluence threshold.

$$r^2 = -\frac{\omega^2}{2} \ln\left(\frac{F_{th}\pi\omega^2}{2}\right) + \frac{\omega^2}{2} \ln(E). \quad (1)$$

The logarithmic fit gives a value for the threshold fluence of  $5.5 \pm 2.0 \text{ J cm}^{-2}$  and for the radius at the beam waist of  $0.84 \pm 0.11 \mu\text{m}$ . Based on these experimental results, their comparison with the theoretical ones for our focusing system gives a  $M^2$  factor of 1.5, since the theoretical beam waist would have to be  $0.55 \mu\text{m}$ . Following the  $M^2$  model for the propagation of the laser beam, the radius at different  $z$ -positions is given by equation (2):

$$\omega^2(z) = \omega_0^2 \left[ 1 + \left( \frac{M^2 \lambda z}{\pi \omega_0^2} \right)^2 \right] \quad (2)$$

where  $\omega_0$  is the radius at the beam waist,  $\lambda$  is the laser wavelength and  $z = 0$  the position of the laser beam waist [28]. The size of the laser beam around the beam waist following this equation is plotted as a dashed line in figure 7 for our

experimental values. When substituting the theoretical values of the beam size in equation (1) together with the experimental values for the beam waist radii and fluence threshold, in order to calculate the theoretical evolution of the crater radius with  $z$ -position (media 1) ([stacks.iop.org/JPhysD/48/335302/mmedia](http://stacks.iop.org/JPhysD/48/335302/mmedia)), it results that the maximum crater size occurs at the beam waist position and that the craters of minimum size are obtained at the two symmetrical outermost points of the range at which craters should be present. However, this range is notably shorter than the experimental one and it does not show a plateau of constant size craters for most of the simulated pulse energies.

Gillen *et al* [29] demonstrated analytically that the  $M^2$  model fails in the description of the propagation of clipped focused Gaussian beams. Depending on the clipping factor (named  $\gamma$  and defined as the ratio between the size of the objective rear aperture radius and the size of the laser beam waist before entering the objective) the energy distribution around the laser beam waist can change considerably. However, in this work the beam configuration corresponds to a very low NA focusing configuration (the clipping is being performed on a Gaussian beam converging from  $5\sqrt{2}$  to  $5 \mu\text{m}$ , in a Rayleigh range of 10 mm). Thus in our case where we work with a 0.55 NA objective, we have used the Richards–Wolf theory for simulating the propagation of the laser beam in our experimental system and for finding the precise intensity distribution around the beam waist. This electromagnetic theory is the standard rigorous description of the focusing of a near paraxial beam through a high numerical aperture optical system (as in our case) and takes into account relevant quantities defining our experiment: size of the input laser beam, focusing lens data, working distances and specially the clipping factor, which in our experimental setup is  $\gamma = 1.2$  [30]. Our calculations show that cross-sections of simulated intensity profiles close to the beam waist are nearly Gaussian. The simulated beam size is plotted with a continuous line in figure 7. Firstly, it has to be noted that the simulated results agree quite well with the size of the beam waist found experimentally. Besides, it can be observed that in these computed results there is a range of  $z$ -positions around the beam waist where the beam has similar size. This zone is much flatter and homogeneous than the presented on the  $M^2$  model. According to these results, the simulated clipped beam propagation should match better the experimental results.

Using this simulation, the theoretical crater diameters for all the different  $z$ -positions were also determined using equation (1). Figure 5(b) shows the plot of the theoretical diameters versus the  $z$ -position. The position  $z = 0 \mu\text{m}$  corresponds to the position of the laser beam waist. We used this position as a reference for all the other plots in this paper. Comparing the information plotted in figures 5(a) and (b), we can see that, indeed, the theoretical diameters are now in better agreement with the experimental data. It is remarkable that diameter sizes of the modifications produced when the laser beam waist is outside of the sample agree quite well for all the studied incident energies, both in size and  $z$ -positioning. Afterwards, there is a region of  $z$ -positions where the diameter of the craters has a similar value. This trend can be associated with the



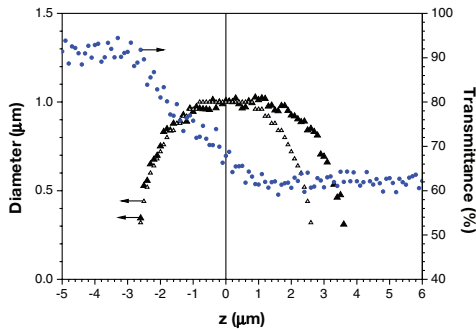


**Figure 8.** Plot of the experimental (▲) and theoretical (Δ) diameters (left axis) and the corresponding transmittance curve (●, right axis) for a  $z$ -scan experiment produced at incident pulse energy of 125 nJ.

flattened zone near the focus where the beam size is almost constant. Nevertheless, the plotted points for positions after  $z = 0 \mu\text{m}$  on each series do not fit so accurately with the experimental results. The real diameters are bigger and modifications are present in a deeper range of  $z$ -positions.

In order to better compare theoretical and experimental results, we gather all the results from the  $z$ -scan experiment made at 125 nJ in figure 8. Hence, this figure shows three different plots: the transmittance curve of the  $z$ -scan, the experimental diameters of the produced craters and the theoretical diameters. In this plot it can be observed that the first surface modifications start at positions where the transmittance starts decreasing, as shown in figure 4(c). As the PMMA surface approaches the position of the beam waist, the size of the modifications increases and the transmittance decreases gradually. After  $z = 0 \mu\text{m}$ , it can be seen that the experimental craters have a bigger size in comparison with the theoretical ones. Besides, the last crater observed on the surface corresponds to the position  $z = 3.6 \mu\text{m}$ , while the theoretical results suggest the position of the last one at  $z = 2.6 \mu\text{m}$ . For the positions where the beam waist is out of the sample, the maximum energy density is located outside the sample; therefore, there is no major interaction in bulk and modification of the surface is only dependent on the local laser fluence.

In contrast, when the beam waist is located inside the sample, the focalization in bulk might produce certain modifications inside the material that can induce side-effects on the surface, modifying the expected size given by the fluence threshold. Furthermore, the formation of bumps only when the focalization of the laser beam occurs well inside the material reinforces the hypothesis that the effects inside the bulk material affect the surface as well. Thus, the energy absorption in bulk may produce a fracture of the polymer and the creation of gas which expands inside the material, leading to the increment of the crater sizes beyond the area limited by the fluence threshold and the formation of bump like modifications when the peak fluence at the surface is well below this threshold [27].

In order to observe the inner morphology of the material below the irradiated areas, FIB ablation technique was used to ablate some of the craters of the  $z$ -scan made at 125 nJ. SEM images of the FIB ablated areas are shown in figure 9.

In those images it can be seen that the bulk material below the irradiated area is damaged in some of the  $z$ -positions. These modifications present a porous structure which displaces along the  $z$ -axis according to the position of the sample relative to the beam waist. For the positions shown in figures 9(a) and (b), the produced craters do not present any visible structure underneath. Starting from figure 9(c), it can be observed that the crater is accompanied by the formation of a porous structure whose length increases as the beam waist moves into the sample (figures 9(c)–(k)). This porous structure remains for all the rest of positions and at some point it is not possible to observe the real length because the structure seems to be elongating even more as the beam waist is entering the material. In figures 9(l) and (m), the FIB ablation of two bump shape modifications and porous structures beneath the irradiated area are shown. This structure would be produced due to the expansion of the material near the surface, and this in turn produces the formation of bumps that can be seen in figures 9(l') and (m') on an intermediate phase of FIB ablation. It is noteworthy that neither the diameter nor the depths of the craters seem to have drastic changes for the different  $z$ -positions as already seen with AFM, but certainly the processes occurring inside the material that produce the porous structure also affect the surface. The enlargement of the porous structure is likely produced by self-focusing, since the critical power to produce this effect (40 kW) is vastly overcome in our experiments [31].

There are some studies that simulate the behaviour of the interaction between femtosecond lasers and different materials [20, 27–34], but a complete explanation of the ablation mechanisms remains unaccounted. According to molecular dynamic simulations of the ablation of PMMA with a pulsed laser in the femtosecond regime [35], the formation of a crater on the surface of PMMA is consequence of the formation of surface swelling followed by an expansion of the material underneath the irradiated area, and finally the expulsion of the irradiated material producing a crater in the surface of the polymer. The reported porous structure beneath the irradiated area in the simulation [35] can be associated with the porous structure of the experimental results observed in figure 9. This absorption depends strongly on the position of the laser beam waist relative to the position of the sample surface and it can be clearly observed that the size of the porous structures increases as the laser beam waist enters into the sample. In this way, the drop in the transmittance can be associated with the formation of the porous structure due to the energy absorption. This result is in good agreement with the transmittance drop in all the  $z$ -scan experiments shown in figure 2.

In view of these results, we can see that the craters made at positions where the transmittance value is the closest to the maximum of  $91 \pm 5\%$  correspond to the  $z$ -positions where the sample has to be placed to produce surface ablation without modifying the bulk material (figures 9(a) and (b)). This position is very critical, since slight changes on the position between



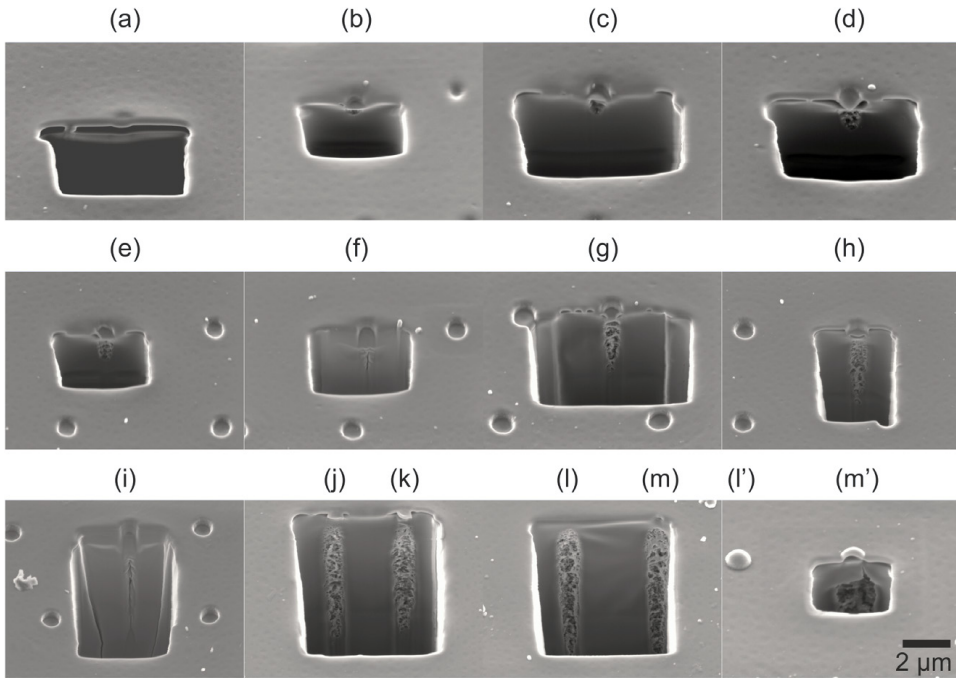


**Figure 9.** SEM images of the craters produced in a  $z$ -scan made at 125 nJ showing a transverse section made on the material through FIB ablation (tilt:  $45^\circ$ ). The  $z$ -positions at which the craters were produced are (a)  $-2.6 \mu\text{m}$ , (b)  $-2.3 \mu\text{m}$ , (c)  $1.9 \mu\text{m}$ , (d)  $-0.8 \mu\text{m}$ , (e)  $-0.4 \mu\text{m}$ , (f)  $0 \mu\text{m}$ , (g)  $0.5 \mu\text{m}$ , (h)  $1.7 \mu\text{m}$ , (i)  $2.7 \mu\text{m}$ , (j)  $3.1 \mu\text{m}$ , (k)  $3.2 \mu\text{m}$ . The images showed in (l)  $3.9 \mu\text{m}$  and (m)  $4.0 \mu\text{m}$  correspond to  $z$ -positions where the irradiated area showed a bump instead of a crater. In (l') and (m') it can be seen the protuberances on the surface of the material in an intermediate phase of the FIB ablation.

the sample and the beam waist can lead to the energy absorption in bulk or not absorption at all. If the placement of the laser beam waist on the surface is required, the sample has to be placed in an intermediate zone on the transmittance curve. For this, the sample position is not so critical since there is a range where the size of the modifications does not vary significantly. Besides, the position can be controlled with high accuracy through the transmittance values at each  $z$ -position. But, it is important to know that the material will be modified not only on the surface but also in bulk, as shown in figures 9(c)–(m). Finally, in order to produce bump structures, the sample has to be placed in positions where the transmittance curve shows the plateau region. Again, this position is very critical, since slight changes of the position between the sample and the beam waist can lead to unwanted crater formation or not bump formation due to the absorption in bulk with no effect on the surface morphology. Additionally, there is no control in the positioning through the transmittance values because they correspond to the plateau region of constant value.

#### 4. Conclusion

Depending on the incident pulse energy, the  $z$ -scan transmittance values provide a range of positions in the  $z$ -axis where

the sample can be placed in order to obtain surface modifications with high reproducibility and similar feature sizes. The position of the  $z$ -scan where the laser beam waist is located can be found at the end of the transmittance drop but before the bottom plateau in the transmittance curve. Dimensions of the craters are determined by a fluence threshold for  $z$ -positions where the beam waist is located outside the sample. A porous structure inside the bulk is also generated when the laser irradiation is absorbed inside the sample. This structure is attributed to the expansion of gas inside the bulk material, leading to the formation of larger craters and bumps on the surface beyond the regions limited by the fluence threshold. The position for the production of surface features avoiding the modification of bulk material is located at positions in the  $z$ -scan where the transmittance value is the closest to the maximum.

#### Acknowledgments

This work is part of a research program funded by MCI of the Spanish Government (Projects TEC2014-54544, FIS2012-38244-C02-02 and CSD2008-00023), Fondo Europeo de Desarrollo Regional (FEDER) and by the European Commission (EU-OLAE+: DigiPRINT).

## References

- [1] Becker H and Gärtner C 2008 *Anal. Bioanal. Chem.* **390** 89–111
- [2] Gattass R R and Mazur E 2008 *Nat. Photonics* **2** 219–25
- [3] Balling P and Schou J 2013 *Rep. Prog. Phys.* **7** 036502
- [4] Farson D F, Choi H W, Zimmerman B, Steach J K, Chalmers J J, Olesik S V, and Lee L J 2008 *J. Micromech. Microeng.* **18** 035020
- [5] Yu X, Bian Q, Chang Z, Corkum P B and Lei S 2013 *Opt. Express* **21** 24185–90
- [6] Couairon A and Mysyrowicz A 2007 *Phys. Rep.* **441** 47–189
- [7] Popov V S 2004 *Phys.-Usp.* **47** 855–85
- [8] Shah L, Tawney J, Richardson M and Richardson K 2004 *IEEE J. Quantum Electron.* **40** 57–68
- [9] Korte F, Serbin J, Koch J, Egbert A, Fallnich C, Ostendorf A and Chichkov B N 2003 *Appl. Phys. A Mater. Sci. Process.* **77** 229–35
- [10] Rethfeld B, Sokolowski-Tinten K, Von der Linde D and Anisimov S I 2004 *Appl. Phys. A Mater. Sci. Process.* **79** 767–9
- [11] Dijkkamp D, Gozdz A S, Venkatesan T and Wu X D 1987 *Phys. Rev. Lett.* **58** 2142–5
- [12] Reif J 2010 *Laser Processing of Materials. Fundamentals, Applications and Developments (Springer Series in Materials Science 139)* ed. Schaaf (Berlin: Springer) pp 113–29
- [13] Peng J, Grojo D, Rayner D M and Corkum P B 2013 *Appl. Phys. Lett.* **102** 161105
- [14] Cheng Y, Sugioka K, Midorikawa K, Masuda M, Toyoda K, Kawachi M and Shihoyama K 2003 *Opt. Lett.* **28** 1144–6
- [15] Eaton S M, De Marco C, Martinez-Vazquez R, Ramponi R, Turri S, Cerullo G, and Osellame R 2012 *J. Biophotonics* **5** 687–702
- [16] Schaffer C B, Brodeur A and Mazur E 2001 *Meas. Sci. Technol.* **12** 1784–94
- [17] Schaffer C B, Jamison A O and Mazur E 2004 *Appl. Phys. Lett.* **84** 1441–3
- [18] Giridhar M S, Seong K, Schülzgen A, Khulbe P, Peyghambarian N and Mansuripur M 2004 *Appl. Opt.* **43** 4584–9
- [19] Alda J 2003 *Encyclopedia of Optical Engineering* (New York: Marcel Dekker Inc.) pp 999–1013
- [20] Najam M T B, Arif K M and Lee Y-G 2013 *Appl. Phys. B* **111** 141–7
- [21] Antti M, Ville H and Jorma V 2012 *Phys. Proc.* **39** 807–13
- [22] Florian C, Caballero-Lucas F, Fernández-Pradas J M, Morenza J L and Serra P 2014 *Appl. Surf. Sci.* **302** 226–30
- [23] Fernández-Pradas J M, Florian C, Caballero-Lucas F, Morenza J L and Serra P 2013 *Appl. Surf. Sci.* **278** 185–9
- [24] Lazare S, Sionkowska A, Zaborowicz M, Planecka A, Lopez J, Dijoux M, Louména C and Hernandez M C 2012 *Appl. Phys. A Mater. Sci. Process.* **106** 67–77
- [25] Xiao-Li Z, Shi-Bing L, Tao C, Yi-Jian J and Tie-Chuan Z 2005 *Chin. Phys. Lett.* **22** 1526–9
- [26] Baudach S, Bonse J, Krüger J and Kautek W 2000 *Appl. Surf. Sci.* **154-155** 555–60
- [27] Krüger J, Martin S, Mädebach H, Urech L, Lippert T, Wokaun A and Kautek W 2005 *Appl. Surf. Sci.* **247** 406–11
- [28] Silfvast W T 1996 *Laser Fundamentals* (Cambridge: Cambridge University Press) pp 402–32
- [29] Gillen G D, Seck C M and Guha S 2010 *Opt. Express* **18** 4023–40
- [30] Novotny L and Hetch B 2012 *Principles of Nano-Optics* (Cambridge: Cambridge University Press) pp 45–84
- [31] Miwa M, Juodkazis S, Kawakami T, Matsuo S and Misawa H 2001 *Appl. Phys. A Mater. Sci. Process.* **73** 561–6
- [32] Afanasiev Y V, Isakov V A, Zavestovskaya I N, Chichkov B N, Von Alvensleben F and Welling H 1997 *Appl. Phys. A Mater. Sci. Process.* **64** 561–72
- [33] Wellershoff S-S, Hohlfeld J, Güdde J and Matthias E 1999 *Appl. Phys. A Mater. Sci. Process.* **69** S99–S107
- [34] Momma C, Nolte S, Chichkov B N, Von Alvensleben F and Tunnermann A 1997 *Appl. Surf. Sci.* **109-110** 15–9
- [35] Baset F, Popov K, Villafranca A, Guay J-M, Al-Rekabi Z, Pelling A E, Ramunno L and Bhardwaj R 2013 *Opt. Express* **21** 12527–38



## **Paper 5**

# Precise surface modification of polymethyl-methacrylate with near-infrared femtosecond laser

F. Caballero-Lucas, C. Florian, J.M. Fernández-Pradas, J.L. Morenza, P. Serra.

Published at: Applied Surface Science

Year: 2015

Impact factor JDR 2014: 2.711 - (Q1)

DOI: 10.1016/j.apsusc.2014.10.128





Contents lists available at ScienceDirect

## Applied Surface Science

journal homepage: [www.elsevier.com/locate/apsusc](http://www.elsevier.com/locate/apsusc)

## Precise surface modification of polymethyl-methacrylate with near-infrared femtosecond laser



F. Caballero-Lucas, C. Florian, J.M. Fernández-Pradas\*, J.L. Morenza, P. Serra

Departament de Física Aplicada i Òptica, Universitat de Barcelona, Martí i Franquès 1, E-08028 Barcelona, Spain

## ARTICLE INFO

## Article history:

Received 30 June 2014

Received in revised form 22 October 2014

Accepted 24 October 2014

Available online 6 November 2014

## Keywords:

Femtosecond laser

z-Scan

Polymethyl-methacrylate (PMMA)

Line ablation

## ABSTRACT

The fabrication of lines at the surface of polymethyl-methacrylate (PMMA) was studied. A femtosecond laser with pulse duration of 450 fs and wavelength of 1027 nm was used. The z-scan method was employed as a focusing procedure to control the sample position with respect to the beam waist through transmittance measurements. This allowed the production of continuous lines with a length of 2 mm on the surface of the PMMA sample. The variation of the lines profiles and dimensions was studied for different values of the sample position with reference to the beam waist. Also effects on the lines fabricated at different values of incident energy and separation on the sample surface between consecutive impinging laser pulses were investigated. A range of positions where lines with similar features and sizes were produced was obtained. Submicrometric surface modifications were achieved as surface swelling in form of successive bumps. After inspecting the sample cross section, it was observed that depending on the relative position of the beam waist regarding the sample surface, inner modifications appear under the modified material surface.

© 2014 Elsevier B.V. All rights reserved.

## 1. Introduction

Microfluidic devices, substrates with enhanced protein binding or lab-on-chip (LoC) devices require precise control in the micro-fabrication techniques used to obtain the desired patterns and structures that help to accomplish the function of their design [1–4]. Another important point for the design of these devices is the material used to manufacture them. Regarding that, polymers are adequate because of their ease and low cost of manufacture, biocompatibility and optical transparency. Furthermore, because of their chemical composition polymers allow producing microscopic characteristics that are harder to obtain on other materials. Among the group of polymers used as substrates for microfluidic devices, polymethyl-methacrylate (PMMA) is specially appropriate because of its moderate hydrophilicity, good transmission at visible wavelengths (about 90%), strength similar to aluminum, resistance against chemical attack of several compounds, permeability of oxygen and carbon dioxide, and biocompatibility. All these good properties make possible to use PMMA substrates for several applications in the field of biology that range from analysis of biomolecules to a wide diversity of observations in cellular biology [5]. In order to be able to carry out these functionalities on

substrates for microfluidic devices, a controlled and precise surface modification of the materials is highly desirable since changes in the properties like the roughness of the material surface affects the flow resistance of liquids or the protein adsorption efficiency on the surface [2,3,6].

Various methods have been used to fabricate microfluidic devices such as photolithography, micromilling, injection molding and hot embossing technologies. All these techniques are based on a controlled manipulation of the material during the manufacturing process with a significant level of precision. This can also be achieved by laser ablation. Laser light is very directional, coherent and monochromatic. All these characteristics allow focusing the light tightly in a relatively small space region when using adequate objectives, producing large energy densities that can ablate specific regions of a sample. Therefore, laser ablation presents an alternative to the conventional methods before commented.

The use of lasers is preferred in front of other techniques during the early stages of the development of a device, when producing prototypes. This is because of its flexibility; injection molding, hot embossing and photolithography are attractive for mass production, but for prototypes laser ablation is more flexible and does not require costly molds or patterns with features at the microscale or smaller. The designed patterns can be reproduced by the laser faster than when a mold is required. Thus, changes in the design can be implemented also more quickly.

\* Corresponding author. Tel.: +34 934 039 216; fax: +34 934 021 139.  
E-mail address: [jmfernandez@ub.edu](mailto:jmfernandez@ub.edu) (J.M. Fernández-Pradas).

Micromilling, a widely used technology for the production of LoC prototypes, suffers from limited resolution (50–100  $\mu\text{m}$ ) [7,8] and surface quality because of the size of the tool. Regarding other direct-write methods such as this one, lasers make possible to obtain (with the use of adequate objectives) higher precision of the fabricated patterns in the microfabrication process.

Several studies with lasers of various wavelengths and duration of the pulse have shown that laser ablation can be a good microfabrication process on PMMA [9,10]. Nevertheless, thermal effects during the energy transfer to the material limit the resolution of the ablation. This problem can be minimized if the duration of the pulse is shorter than the time of the energy transfer to the lattice. Therefore, lasers with pulse duration of femtoseconds are more adequate to achieve better quality results in microfabrication compared to other lasers with longer pulse duration [11]. Furthermore, the surface patterning of PMMA with a femtosecond laser at fluences close to the ablation threshold does not produce significant variations in the chemical properties of the surface [1].

When a femtosecond laser is employed, even near-infrared radiation (in this case, with a wavelength of 1027 nm) can be used for material ablation. Despite the transparency of the PMMA at these wavelengths, this radiation can be absorbed through non-linear processes. Apart from the reduced thermal effects from the short pulse duration, these processes also provide better precision in the material affected region because of their non-linearity. High energy densities are necessary for these processes to take place, which are reached by tight focusing the laser beam at the material. Consequently, a good control of the relative position between the sample surface and the beam waist is necessary for precise surface modification.

In this work we use the z-scan method [12] to get a precise control on the sample surface position in regard to the beam waist to be able to study the influence of this position over the features and dimensions of the fabricated lines at the material surface. A sample of PMMA was irradiated at different incident energies and two values for the separation between the spots (scanning speeds) to produce the lines. Transmittance measurements were also performed during line production.

## 2. Experimental

The experiments were performed on samples of PMMA with rectangular shape (20 mm  $\times$  10 mm, 1 mm thickness) and an average surface roughness of 3 nm. Samples were cut with a diamond blade saw from a commercial 100% pure PMMA sheet available by Goodfellow. Before irradiation, samples were cleaned with ethanol and distilled water in an ultrasonic bath and dried with nitrogen. No other special treatment was performed during sample preparation. The employed laser produces pulses of linearly polarized near-infrared radiation with a wavelength of 1027 nm and duration of 450 fs in an active medium consisting of a crystal of Yb:KYW. These pulses arrive at the sample after being reflected at a beam-splitter and two mirrors and passing through a 50 $\times$ , 0.55 numerical aperture objective that focuses the beam at about 13 mm of its outer lens. A glass coverslip between the objective and the sample surface was also included to prevent ablation debris to deposit on the objective lens. The energy distribution profile after the objective was Gaussian. Previous studies showed that the beam waist obtained under these tight focusing conditions was  $0.8 \pm 0.1 \mu\text{m}$  [13].

The experimental setup was equipped with two energy detectors that allowed the measurement of the transmittance of every laser pulse through the sample. Previous to the fabrication of the lines, the sample was scanned horizontally in a total range of 2 mm at steps of 10  $\mu\text{m}$  while the transmittance was tracked in order to correct the tilt of the sample surface. When the sample was not

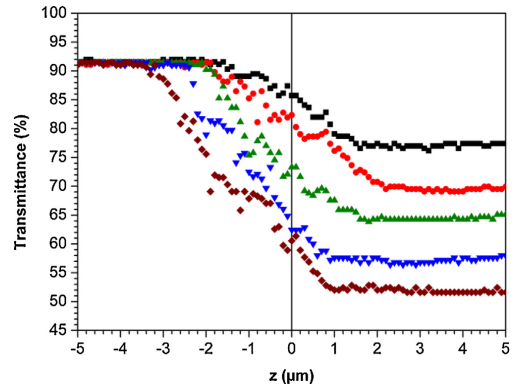


Fig. 1. Plot of the transmitted energy vs z-position at (■) 100, (●) 130, (▲) 150, (▼) 200, and (◆) 300 nJ of incident energy. The experimental relative error corresponding to all transmittance data is 5%.

perpendicular to the laser beam, a non flat tendency for the measured transmittance values was obtained. The horizontality of the sample surface plane with reference to the beam propagation axis was assumed when a flat tendency of the transmittance with a  $\pm 5\%$  variation along the sample surface was observed.

The transmittance measurements also allowed the realization of z-scans previously to the production of each series of lines. In Fig. 1, it can be seen how the transmittance changes for a single pulse on pristine material for different positions of the sample surface with reference to the beam waist (z-positions) at the incident energies used in the experiments. The value  $z = 0 \mu\text{m}$  corresponds to the case where the sample surface lays at the beam waist position according to the results in previous studies [13]. Negative values for z indicate that the beam waist is outside the sample, while positive values correspond to positions where the beam waist is inside the sample. The transmittance decrease produced as the sample enters the beam waist is used to monitor the relative position between the sample surface and the beam waist and makes possible to ensure a good position control during the experiments.

Each series was produced at fixed incident energy and separation between the impinging laser pulses, this means, fixed scan speed. The used incident energies took values in the range of 100–300 nJ. These energies together with the small size of the beam waist lead to peak intensities higher than  $1 \text{ TW}/\text{cm}^2$ , where non-linear absorption processes are expected [14]. Two values for the separation between consecutive laser pulses were explored: 0.2  $\mu\text{m}$  and 0.5  $\mu\text{m}$ , which correspond, respectively, to 200  $\mu\text{m}/\text{s}$  and 500  $\mu\text{m}/\text{s}$  scan speeds at a laser repetition rate of 1 kHz. While keeping these parameters fixed, lines at different z-positions were produced by scanning the sample surface horizontally along 2 mm in the direction perpendicular to the laser polarization. The range of z-position values at which lines were produced was chosen according to the transmittance drop range for the different incident energy values. This range gets wider for higher incident energy values (Fig. 1). Transmittance was also measured during line ablation for all the series. Additional details and a further description about the setup and the z-scan method can be found in [12,13].

After laser irradiation, the modified surface and cross section of the sample was inspected through scanning electron microscopy (SEM). The cross section could be visualized thanks to a previous split of the sample. This was carried out without any special treatment after cutting by saw two incisions perpendicular to the lines

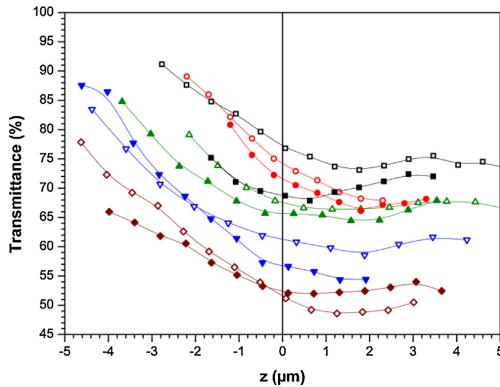


**Fig. 2.** Plot of the average transmitted pulse energy vs  $z$ -position for ( $\square$  empty symbols)  $0.2 \mu\text{m}$ , and ( $\blacksquare$  filled symbols)  $0.5 \mu\text{m}$  of spot separation and for ( $\blacksquare$ ) 100, ( $\bullet$ ) 130, ( $\blacktriangle$ ) 150, ( $\blacktriangledown$ ) 200, and ( $\blacklozenge$ ) 300 nJ of incident energy. The average value corresponds to transmittance measurements done during the fabrication of each line. Lines connecting data points are just an eye guide. The experimental relative error corresponding to all transmittance data is 5%.

in order to guide the crack at the beginning of the split, which was performed by hand.

### 3. Results and discussion

Following the methods described in the experimental section, the transmittance measurements were also extended to the line production process. This made possible to obtain the average transmittance of the laser pulses employed for the line fabrication for every line. The obtained series of data are represented in Fig. 2 for the different conditions used to fabricate the lines. The average transmittance measured during line production (Fig. 2) follows trends similar to the  $z$ -scans obtained with single spots (Fig. 1). In both cases, the transmittance decrease range of the  $z$ -position widens with increasing incident energy, as well as the transmittance values get lower for increasing incident energies. On the other hand, the transmittance values measured at the same experimental conditions (incident energy and  $z$ -position) are generally lower in the case of average transmittances measured during line fabrication than in previous  $z$ -scans. This comparison also shows that the range in  $z$  where the transmittance decreases is clearly wider for line ablation than for single shot ablation. Both, the wider range of the transmittance decrease and the lower transmittance values for lines than for single spots, can be associated to accumulative effects due to spot overlap [15].

If we look at Fig. 3, we can relate the transmittance decrease with lines ablation at the surface. This figure shows SEM images of one series of produced lines at 100 nJ of incident energy and  $0.2 \mu\text{m}$  of spot separation between consecutively impinging laser pulses. It can be observed that continuous lines at the surface are obtained for  $z$ -positions around  $z = 0 \mu\text{m}$ . More concretely, at these conditions continuous lines are observed on the surface from  $z = -1.6 \mu\text{m}$  (Fig. 3(c)) to  $z = 2.3 \mu\text{m}$  (Fig. 3(j)). This corresponds to  $z$ -positions in the transmittance decrease range in Fig. 2. This correspondence has also been observed for the other experimental conditions of incident energy and spot separation at which lines were produced.

The morphology of the lines at the sample surface can be inspected as well as its cross section profile. In the surface visualization, it can be observed from left to right how the progressive approach and entrance of the sample surface into the beam waist region affects the obtained lines. At the beginning, the external

situation of the beam waist with reference to the sample surface produces that the fluence at the surface is not high enough to reach the ablation threshold along all the scanned distance and the lines are not continuous. For pulses of 100 nJ and  $0.2 \mu\text{m}$  of spot separation, these correspond to  $z$ -position values of Fig. 3(a) and (b). Here the position of the sample is very critical and irregularities larger than the surface roughness like small movements of the sample holder and stages, defects, scratches, and other imperfections on the sample surface result in a discontinuity of the lines.

For closer positions of the sample to the beam waist, lines are continuous along all the scanned distance (2 mm), Fig. 3(c)–(j). At first sight, the width of the lines does not significantly change during these different  $z$ -positions. Only at the beginning and at the end of this range of  $z$ -positions lines look slightly thinner than for the central  $z$ -positions. Deeper positions of the beam waist with respect to the sample surface make that the pulse energy is mostly concentrated below the surface (range of Fig. 3(k)–(n)). Thus, the fluence at the surface is not high enough to ensure a continuous line ablation at the surface and lines start to become discontinuous again. Here some swelling of the not superficially ablated part of the line is observed. Finally, when the beam waist is well inside the sample, almost no surface modification is present except in some segments, where small surface swelling is visible. This corresponds to the case of  $z$ -position value in the sample of Fig. 3(o). No surface modification would be expected for deeper positions of the beam waist with regard to the sample surface [5].

Another feature that can be examined in the surface images is the roughness of the bottom of the channels. The roughness presents a quasi-periodic porous structure with some ripple ordering for incident energies up to 150 nJ. The direction of these porous structures is perpendicular to the line direction. This characteristic has been previously observed in similar studies [16] where the ripple direction coincides with the incident linear laser polarization, which is parallel to the sample surface and perpendicular to the scan direction of the lines. For higher energies, the porous structures become more randomly distributed in terms of the profile of the structures, but the orientation of the ripples perpendicular to the line direction is kept. The average periodicity of the ripples seems to be independent of pulse energy and  $z$ -position, and has a value  $\sim 350 \text{ nm}$ , which is in agreement with results in [17]. The origin of these ripples has been previously explained through interference between the incident energy and the surface scattering wave or surface plasmon polaritons [17,18].

The bottom part of Fig. 3 corresponds to the cross section of the PMMA sample and allows the visualization of the profiles of the lines and the material modifications produced under the surface. In the same way as in the surface images, here the effect of the beam waist entering the sample can be studied. At a very external position of the beam waist with respect to the sample surface (Fig. 3(a)), no inner modification is visible. Just some surface swelling in form of bumps can be seen at the surface, forming the previously commented discontinuous line. When the sample approaches to the beam waist, lines are produced at the surface (Fig. 3(b)–(j)). We can distinguish two groups, which in this case correspond from Fig. 3(b) to (f) and from (g) to (j). In the first one, only the profile of the lines can be seen, without any modification under the channels. The profiles of these lines show quite vertical walls and a flat bottom. The profiles of the second group of lines show a narrower width at the surface and a circular profile. The dimensions of the profiles become smaller for higher values of the  $z$ -position. Furthermore, inner modifications appear in the material under the bottom of the lines. These modifications elongate as the beam waist goes deeper into the sample. For lines produced at deeper positions (Fig. 3(k)–(n)), the sample surface clearly presents swelling in form of a line of successive bumps. At these positions, the inner modifications become considerably more elongated and go some microns



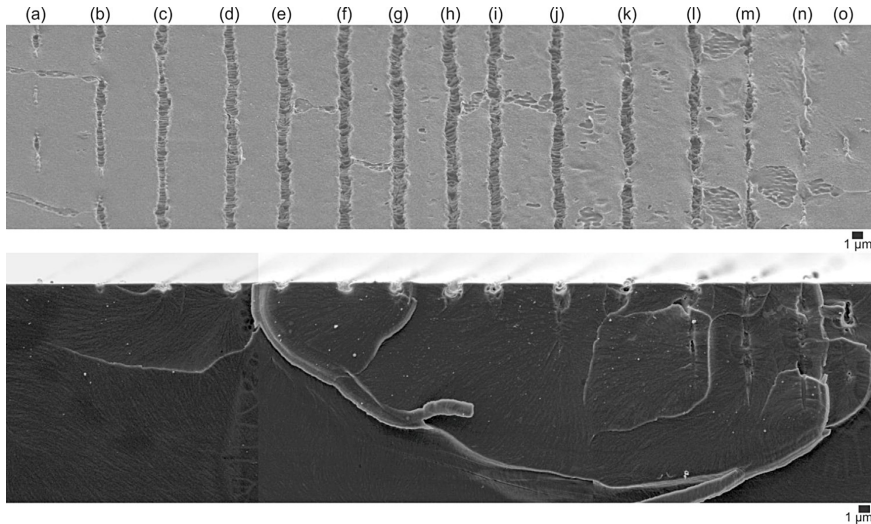


**Fig. 3.** (Top) SEM images of the PMMA surface after the incidence of pulses of 100 nJ separated  $0.2 \mu\text{m}$  at (a)  $-2.8$ , (b)  $-2.2$ , (c)  $-1.6$ , (d)  $-1.1$ , (e)  $-0.5$ , (f)  $0.1$ , (g)  $0.6$ , (h)  $1.2$ , (i)  $1.8$ , (j)  $2.3$ , (k)  $2.9$ , (l)  $3.5$ , (m)  $4.0$ , (n)  $4.6$ , and (o)  $5.2 \mu\text{m}$  for the  $z$ -position values. For these surface images, the sample had a tilt of  $30^\circ$ . (Bottom) Corresponding SEM images of the PMMA cross section and part of the surface.

inside the material in the incident beam direction. Lastly, it can be observed that for an inner  $z$ -position any surface modification is not observable (Fig. 3(o)). Instead of this, a cavity appears under the surface. Also here material modifications under this cavity can be seen. The presence of a region with modified material under surface ablated areas has been already obtained in simulations that study the femtosecond laser radiation absorption in PMMA [19] and also observed in studies of craters and lines produced at the surface of PMMA [16]. Thermal expansion of the material with formation of gaseous nanopores at the region where the laser pulse is focused and multiple filamentation inside the material for the case of doped PMMA are two mechanisms that can explain the presence of this region with modified material [16,19].

Low thermal affectation is observed in the SEM images of the lines. Well-defined contours in the surface image as well as profiles from the cross section, and the observable roughness of the bottom of the channels lead to non noticeable thermal side effects despite accumulation is present because of the pulse overlapping used to produce continuous lines.

The general behavior of the line production regarding different  $z$ -position values for the rest of experimental conditions of incident energy and spot separation at which lines were produced is the same as the described above, with some differences in the  $z$ -position values.

Measurements done in the SEM images taken for all the produced lines allowed the study of the line width and depth dependence with the experiment variables (Fig. 4). First of all, a general behavior is present in all the cases: the width and depth of the channels have larger values for higher incident energies. Another general trend for width values (Fig. 4(a) and (b)) is that they do not significantly change at fixed incident energy for different  $z$ -positions except in the case of 300 nJ, where there is a clear transition between two ranges of  $z$ -position values. In the first one, which corresponds to the situation where the beam waist is outside the sample, lines about  $3.2 \mu\text{m}$  wide can be obtained. At positions of the second range, the line width is thinner with a value around  $1.8 \mu\text{m}$ . Apart from this behavior at 300 nJ, the fact

that lines show similar widths at fixed energy independently of the  $z$ -position at which they are fabricated establishes a wide margin in the  $z$ -position that goes from  $4 \mu\text{m}$  at 100 nJ to almost  $8 \mu\text{m}$  at 200 nJ for producing lines with similar sizes at the sample surface. Concerning the line width, slightly thinner lines are obtained for  $0.2 \mu\text{m}$  spot separation than for  $0.5 \mu\text{m}$ .

The analysis of the depth data of the lines (Fig. 4(c) and (d)) shows some different behaviors in comparison with the trends of line width. For all the studied incident energies, but especially for 200 nJ and 300 nJ, the depth of the lines tends to increase as the beam waist enters the sample. This satisfies the expected behavior: lines produced when the beam waist is closer to the sample are deeper. However this increase of the depth with increasing  $z$ -position values stabilizes at some point, approximately  $1 \mu\text{m}$  before the beam waist reaches the sample surface ( $z = -1 \mu\text{m}$ ). This also allows the determination of a certain range of  $z$ -positions where the depth of the channels shows similar values. Nevertheless this range is not as wide as in the case of the line width because at some point corresponding to higher values of the  $z$ -position the depth tends to slowly decrease. As an example, this range of lines with similar depths is  $4 \mu\text{m}$  wide at 200 nJ, while lines with similar widths can be obtained in a range of  $8 \mu\text{m}$  at the same incident energy.

In the comparison of the two different values for the separation between spots, the lines obtained with a spot separation of  $0.2 \mu\text{m}$  tend to be deeper than in the case of  $0.5 \mu\text{m}$ , particularly for higher incident energies (200 nJ and 300 nJ). The fact that a higher overlap produces deeper channels is in agreement with previous studies [6,20].

At some specific experimental conditions, surface swelling in form of bumps with submicrometric dimensions has been observed. These conditions correspond to two different cases. In the first case, bumps are observed at low incident energies (up to 150 nJ) and small negative values of  $z$ -position, this is, when the beam waist is outside the sample. Some of the bumps produced at these conditions had a width of  $340 \pm 10 \text{ nm}$  (Fig. 5), which is much lower than the laser wavelength value of  $1027 \text{ nm}$ . No inner modifications, only the presence of bumps have been observed. In

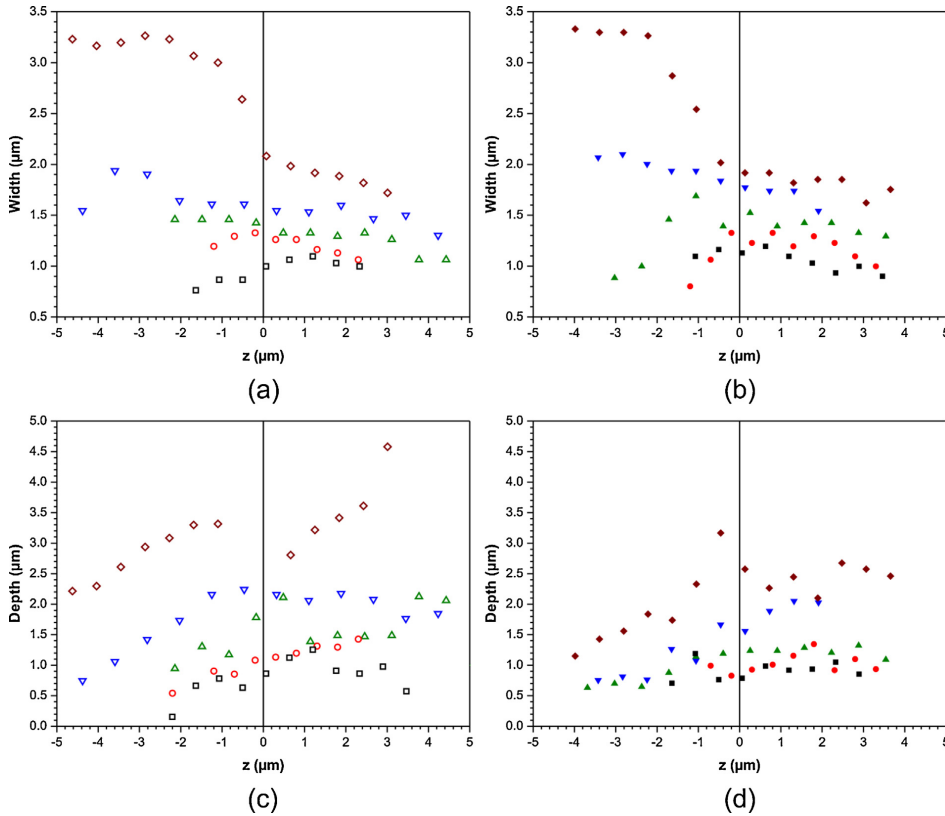


**Fig. 4.** Plots of the dimensions of the channels vs  $z$ -position. The measurements were obtained from SEM images of the sample surface and cross section. (a) and (b) correspond to width measurements while (c) and (d) show the depth of the lines. Colors and shapes of the represented data correspond to ( $\square$  empty symbols)  $0.2 \mu\text{m}$ , and ( $\blacksquare$  filled symbols)  $0.5 \mu\text{m}$  of spot separation and ( $\blacksquare$ ) 100, ( $\bullet$ ) 130, ( $\blacktriangle$ ) 150, ( $\blacktriangledown$ ) 200, and ( $\blacklozenge$ ) 300 nJ of incident energy. All width and depth measurements have an experimental error of  $\pm 0.1 \mu\text{m}$ .

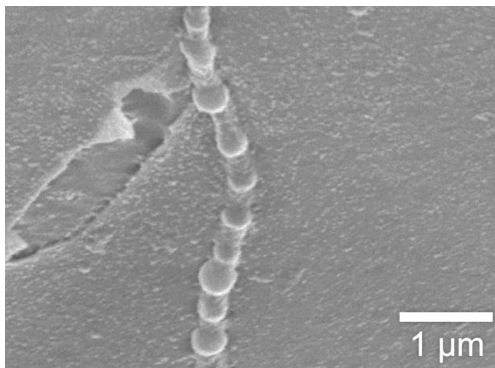


**Fig. 5.** SEM image (surface) of a line of bumps obtained at 150 nJ of incident energy,  $0.5 \mu\text{m}$  of spot separation and  $-3.7 \mu\text{m}$  for  $z$ -position.

the second case, bumps also appear at higher incident energies when the beam waist is inside the material but still close to the surface and the internal expansion produces some swelling at the surface in form of bumps. In this case, the expansion is not strong enough to ablate the surface material. This process has been also explained in dynamic simulations corresponding to the thermal processes related to the energy absorption [19]. In agreement with the simulation results, inner modifications are clearly visible under the bumps obtained at these conditions.

After the analysis of the data of the produced lines, some results on the positioning of the sample to ensure a precise surface modification by line fabrication can be presented. First of all, there is a margin of some microns in the  $z$ -position around  $z = 0 \mu\text{m}$  (beam waist at the material surface) to obtain lines with similar features, particularly for the line width. This range of  $z$ -positions is the best option for a reliable surface modification with reduced affectation from possible vibrations of the setup. Second, there are two possibilities for obtaining submicrometric features. These are surface modification in form of bumps (obtained at two different experimental conditions) or the use of low energies close to the ablation threshold to produce lines with the smallest feasible dimensions. This last case presents a smaller variation of width and depth, with

width values close to 1  $\mu\text{m}$  and depths around 0.7  $\mu\text{m}$ . Finally, in order to avoid the presence of any kind of inner modifications under the modified surface, recommended positions are when the beam waist is outside the sample surface, shortly before entering it. Hence keeping the sample at a specific  $z$ -position is essential. This can be achieved by monitoring the sample position through transmittance measurements during line ablation. As a consequence of these results, depending on the preferences for the desired surface modification results, the most suitable position for fabricating lines can be chosen.

#### 4. Conclusions

The use of the  $z$ -scan has allowed a good position control for the surface modification of PMMA in form of lines. The study of the evolution of the obtained lines with the experimental parameters showed that there is a range of positions where lines with similar features are produced, especially for the line width but also with similar depths. This range corresponds to positions around the location where the beam waist lays directly at the material surface. It was also observed that there are two different experimental conditions at which submicrometric surface modifications in form of lines of bumps are produced. The inspection of the cross section of the modified material also showed that depending on the  $z$ -position, inner modifications can appear below the modified surface.

#### Acknowledgements

This work is part of a research program funded by MCI of the Spanish Government (Project CSD2008-00023), DigiPRINT project (EU-OLAE+), and Fondo Europeo de Desarrollo Regional (FEDER).

#### References

- [1] C. De Marco, S.M. Eaton, R. Suriano, S. Turri, M. Levi, R. Ramponi, G. Cerullo, R. Osellame, Surface properties of femtosecond laser ablated PMMA, *ACS Appl. Mater. Interfaces* 2 (2010) 2377–2384.
- [2] Z.K. Wang, H.Y. Zheng, H.M. Xia, Femtosecond laser-induced modification of surface wettability of PMMA for fluid separation in microchannels, *Microfluid. Nanofluid.* 10 (2010) 225–229.
- [3] X. Ma, H. Huo, M. Wei, L. Wang, M. Shen, C. Barry, J. Mead, Enhanced protein binding on femtosecond laser ablated poly(methyl methacrylate) surfaces, *Appl. Phys. Lett.* 98 (2011) 171101.
- [4] R. Osellame, H.J.W.M. Hoekstra, G. Cerullo, M. Pollnau, Femtosecond laser microstructuring: an enabling tool for optofluidic lab-on-chips, *Laser Photonics Rev.* 5 (2011) 442–463.
- [5] K. Sugioka, Y. Cheng, Femtosecond laser processing for optofluidic fabrication, *Lab Chip* 12 (2012) 3576–3589.
- [6] T.-L. Chang, T.-K. Tsai, H.-P. Yang, J.-Z. Huang, Effect of ultra-fast laser texturing on surface wettability of microfluidic channels, *Microelectron. Eng.* 98 (2012) 684–688.
- [7] C.R. Friedrich, M.J. Vasile, Development of the micromilling process for high-aspect-ratio microstructures, *J. Microelectromech. Syst.* 5 (1996) 33–38.
- [8] F.J. Del Campo, Miniaturization of electrochemical flow devices: a mini-review, *Electrochem. Commun.* 45 (2014) 91–94.
- [9] L. Juha, M. Bittner, D. Chvostova, V. Letal, J. Krasa, Z. Otcenasek, M. Kozlova, J. Polana, A.R. Prág, B. Rus, M. Stupka, J. Krzywinski, A. Andrejczuk, J.B. Pelka, R. Sobierajski, L. Ryc, J. Feldhaus, F.P. Boody, M.E. Grisham, G.O. Vaschenko, C.S. Menoni, J.J. Rocca, XUV-laser induced ablation of PMMA with nano-, pico-, and femtosecond pulses, *J. Electron Spectrosc. Relat. Phenom.* 144–147 (2005) 929–932.
- [10] J. Lawrence, L. Li, Modification of the wettability characteristics of polymethyl methacrylate (PMMA) by means of  $\text{CO}_2$ , Nd:YAG, excimer and high power diode laser radiation, *Mater. Sci. Eng., A* 303 (2001) 142–149.
- [11] R. Suriano, A. Kuznetsov, S.M. Eaton, R. Kiyon, G. Cerullo, R. Osellame, B.N. Chichkov, M. Levi, S. Turri, Femtosecond laser ablation of polymeric substrates for the fabrication of microfluidic channels, *Appl. Surf. Sci.* 257 (2011) 6243–6250.
- [12] J.M. Fernández-Pradas, C. Florian, F. Caballero-Lucas, J.L. Morenza, P. Serra, Femtosecond laser ablation of polymethyl-methacrylate with high focusing control, *Appl. Surf. Sci.* 278 (2013) 185–189.
- [13] C. Florian, F. Caballero-Lucas, J.M. Fernández-Pradas, J.L. Morenza, P. Serra, Surface ablation of transparent polymers with femtosecond laser pulses, *Appl. Surf. Sci.* 302 (2014) 226–230.
- [14] C.B. Schaffer, A. Brodeur, E. Mazur, Laser-induced breakdown and damage in bulk transparent materials induced by tightly focused femtosecond laser pulses, *Meas. Sci. Technol.* 12 (2001) 1784–1794.
- [15] D. Gómez, I. Goenaga, On the incubation effect on two thermoplastics when irradiated with ultrashort laser pulses: broadening effects when machining microchannels, *Appl. Surf. Sci.* 253 (2006) 2230–2236.
- [16] J.-M. Guay, A. Villafranca, F. Baset, K. Popov, L. Ramunno, V.R. Bhardwaj, Polarization-dependent femtosecond laser ablation of poly-methyl methacrylate, *New J. Phys.* 14 (2012) 085010.
- [17] F. Baset, A. Villafranca, J.-M. Guay, R. Bhardwaj, Femtosecond laser induced porosity in poly-methyl methacrylate, *Appl. Surf. Sci.* 282 (2013) 729–734.
- [18] E. Rebolgar, J.R. Vázquez de Aldana, I. Martín-Fabiani, M. Hernández, D.R. Rueda, T.A. Ezquerro, C. Domingo, P. Moreno, M. Castillo, Assessment of femtosecond laser induced periodic surface structures on polymer films, *Phys. Chem. Chem. Phys.* 15 (2013) 11287–11298.
- [19] F. Baset, K. Popov, A. Villafranca, J.-M. Guay, Z. Al-Rekabi, A.E. Pelling, L. Ramunno, R. Bhardwaj, Femtosecond laser induced surface swelling in poly-methyl methacrylate, *Opt. Express* 21 (2013) 12527–12538.
- [20] D. Teixidor, F. Orozco, T. Thepsonthi, J. Cuirana, C.A. Rodríguez, T. Özel, Effect of process parameters in nanosecond pulsed laser micromachining of PMMA-based microchannels at near-infrared and ultraviolet wavelengths, *Int. J. Adv. Manuf. Technol.* 67 (2012) 1651–1664.

## Additive laser direct-writing

### Paper 6

#### Interaction between jets during laser-induced forward transfer

A. Patrascioiu, C. Florian, J.M. Fernández-Pradas, J.L. Morenza, G. Hennig, P. Delaporte, P. Serra.

Published at: Applied Physics Letters

Year: 2014

Impact factor JDR 2014: 3.302 - (Q1)

DOI: 10.1063/1.4889802





## Interaction between jets during laser-induced forward transfer

A. Patrascioiu,<sup>1</sup> C. Florian,<sup>1</sup> J. M. Fernández-Pradas,<sup>1</sup> J. L. Morenza,<sup>1</sup> G. Hennig,<sup>2</sup>  
P. Delaporte,<sup>3</sup> and P. Serra<sup>1,a)</sup>

<sup>1</sup>Departament de Física Aplicada i Òptica, Universitat de Barcelona, Martí i Franquès 1,  
E-08028 Barcelona, Spain

<sup>2</sup>DI Projekt AG, Flugplatz, CH-3368 Bleienbach, Switzerland

<sup>3</sup>Aix Marseille University, CNRS, LP3 UMR 7341, 163 Avenue de Luminy, 13288 Marseille, France

(Received 10 April 2014; accepted 29 June 2014; published online 8 July 2014)

Simultaneous two-beam laser-induced forward transfer (LIFT) was carried out for various inter-beam separations, analyzing both the resulting printing outcomes and the corresponding liquid transfer dynamics. In a first experiment, droplets of an aqueous solution were printed onto a substrate at different inter-beam distances, which proved that a significant departure from the single-beam LIFT dynamics takes place at specific separations. In the second experiment, time-resolved imaging analysis revealed the existence of significant jet-jet interactions at those separations; such interactions proceed through a dynamics that results in remarkable jet deflection for which a possible onset mechanism is proposed. © 2014 AIP Publishing LLC.

[<http://dx.doi.org/10.1063/1.4889802>]

Digital manufacturing techniques are at the core of today's printing industry. This is a competitive market in a constant demand for better strategies capable of increasing the speed, control, or resolution of the printing processes while in the same time decreasing the production costs. The excellent performances currently achieved by digital printing techniques have dramatically extended their field of application beyond the graphics arts industry and towards such promising areas as the fabrication of organic electronic or biomedical devices.

The most prominent laser-based digital printing technique is possibly the laser-induced forward transfer (LIFT), which enables the controlled high-resolution printing of a wide range of materials for a plethora of applications.<sup>1–14</sup> LIFT can also provide superior cost-efficient printing throughputs,<sup>13</sup> as well as an almost unrestricted range of materials choice (e.g., it can print a wide variety of ink pigment sizes) which is otherwise not possible to achieve with inkjet printing. Its working principle consists in focusing a pulsed laser beam into a thin film of donor material placed on a laser-transparent substrate. As a result of the laser pulse absorption, a high-pressure bubble forms inside the liquid, and it then rapidly expands to produce a fast and thin jet which propagates away from the donor film. The jet contacts the nearby-placed acceptor substrate and leads to the deposition of a tiny droplet on its surface.<sup>15–23</sup> In spite that significant research effort has been dedicated to the understanding of the influence of several LIFT process parameters (e.g., laser pulse energy, pulse duration, or solution properties) for the optimization of the technique, such a critical and cost-decisive printing parameter as the printing speed has not yet been analyzed in detail.<sup>23</sup> Moreover, this is of special interest since LIFT high-speed printing has already been proved feasible: DI Projekt AG has developed an industrial-scale, large-area printing machine (0.53 m web size) based on the

LIFT technique which achieves unprecedented throughputs of 1.3 m<sup>2</sup>/min at 600 dpi resolution. The device employs an ultrafast laser scanning method at a speed of 1016 m/s and at such high repetition rate as 24 MHz. If the resolution requirements are lowered to 300 dpi, though, a higher throughput of 2.6 m<sup>2</sup>/min can even be achieved, working at a scanning speed of 2116 m/s and at a repetition rate of 25 MHz.<sup>13</sup> However, the use of such high laser repetition rates can lead to situations for which the time between successive laser shots becomes shorter than the average lifetime of a single jet. In this instance, the initial jet might not even have time to reach the acceptor substrate before the next one is emitted. Actually, since the jet lifetime is about a few hundreds of microseconds, at MHz laser pulse rates the consecutive jets are practically simultaneous. In this case, it can be expected that for jets generated close enough to each other (the jet inter-distance being determined by the printing speed), non-negligible jet-jet interaction can take place, which could significantly alter the printing dynamics. Therefore, a deeper understanding of this phenomenon and its underlying dynamics is needed. Such knowledge is important not only for high-speed printing applications but also from a more fundamental point of view, since little knowledge on such liquid interaction is currently available.

In this work, we present a time-resolved imaging study of the jet-jet interaction dynamics that takes place in LIFT printing and we correlate it with the actual deposits on the acceptor substrate. The experiment investigates the interaction between two simultaneous jets generated at various separations relative to one another. In this way, the experiment provides with a simple situation that allows the study of jet interaction, which in turn corresponds to conditions close to the ones typical of LIFT printing at very high laser repetition rates.

The experimental apparatus consists of a LIFT printing setup coupled to a time-resolved imaging setup. LIFT was carried out through the use of a pulsed Nd:YAG laser (355 nm wavelength, 10 ns pulse duration) whose main beam

<sup>a)</sup>Author to whom correspondence should be addressed. Electronic mail: [pserra@ub.edu](mailto:pserra@ub.edu)

was split into two quasi-identical beams by means of a series of beam splitters and mirrors. The beams were simultaneously focused by a  $15\times$  microscope objective onto the donor substrate, a glass slide covered by a 50 nm thick Ti laser-absorbing film, as shown in Fig. 1(a). The optical setup was constructed in such way that the two beams traveled very similar distances, arriving at the focusing objective at about the same time. The inter-beam separation could be finely adjusted using the tuning knob of one of the mirrors of the optical system. For both beams, the laser spot size on the Ti film was of about  $40\ \mu\text{m}$ , and the laser pulse energy of around  $70\ \mu\text{J}$ , leading to an estimated average laser fluence of  $5.5\ \text{J}/\text{cm}^2$ . The printing liquid, consisting of a 50% (v/v) water and glycerol mixture plus 2 mg/ml of sodium dodecyl sulphate, embodies characteristics that are typical for many inks currently used in the printing industry (6 mPa s viscosity, 30 mN/m surface tension). A  $30\ \mu\text{m}$  thick liquid film was prepared from this solution by blade-coating it onto the donor substrate. The acceptor substrate was a glass slide placed at a relatively large distance (1 mm) from the donor. Such large gap, which is not common in most LIFT experiments, was especially chosen in order to facilitate the imaging conditions of a rather difficult time-resolved imaging experiment.

The time-resolved imaging setup was a stroboscopic system able to take sequential, side-view images of the liquid transfer process, each image corresponding to a unique transfer event. It consisted of a home-made illuminating source comprising a LED coupled to a driver that controls it and allows setting pulse widths down to 100 ns. This system was coupled to a condenser lens, and it was triggered through a delay generator which in turn controlled the laser pulse and the aperture of a 2 Mp CCD camera. The camera was coupled to a  $15\times$  microscope objective and placed at grazing incidence respect to the donor film.

In the first experiment, series of droplets of the aqueous solution were printed through LIFT at different separations

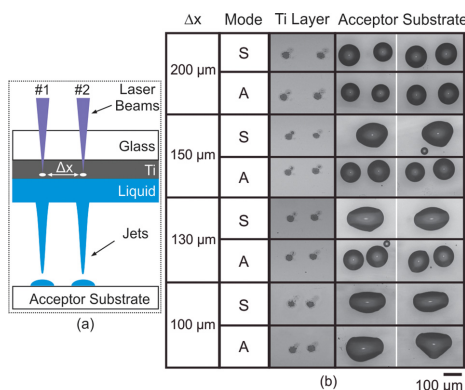


FIG. 1. (a) Sketch of the two-beam LIFT printing setup (not on scale), and (b) optical microscopy image of the droplets deposited on the acceptor substrate after carrying out two-beam LIFT printing, and the corresponding laser-generated spots on the Ti film at different separation distances ( $\Delta x$ ) between the two laser beams. The droplets were generated using either a simultaneous beam sequence (mode S) or an alternate one (mode A).

between the two laser beams ( $\Delta x = 100, 130, 150,$  and  $200\ \mu\text{m}$ ), with the corresponding results being presented in Fig. 1(b). For each distance, the droplets were generated using either two simultaneous laser pulses (mode S), in which the transfer was carried out with both beams arriving unrestricted to the donor, or through alternate laser pulses (mode A). The latter consisted of the following two step sequence: one droplet printing with one beam blocked followed by another droplet printing with the other beam blocked.

Three different situations can be pointed out. At the largest beam separation ( $200\ \mu\text{m}$ ), the transfer results in the formation of individual droplets that present a similar morphology for both printing modes (A or S). Only small differences are observed in the resulting outcomes: in mode S the printed droplets appear to be slightly larger than those of mode A. This effect, however, does not seem to be very significant, since it can be easily due to minute fluctuations in the laser pulse energy and/or small non-uniformities in the liquid film thickness. However, for the smallest distance ( $100\ \mu\text{m}$ ), and regardless of the printing mode, the outcome consists in the formation of a single, larger, and elongated droplet with a slightly irregular shape. In this case, droplet coalescence certainly takes place in mode A, because the beam inter-spacing ( $100\ \mu\text{m}$ ) is smaller than the diameter of an individual, single-beam printed droplet ( $120\ \mu\text{m}$ ). However, nothing could be yet inferred for mode S, since at such short separations jet-jet interaction appears to be possible. Nevertheless, it can be stated that overall, the printing outcomes of these two extreme cases are consistent, at least in their final form, with the classical picture of independent, non-interacting jets.

However, both of the other two separation cases ( $150$  and  $130\ \mu\text{m}$ ) mark a clear difference from the classically expected deposits, and therefore, this strongly indicates that significant jet-jet interaction takes place. In such intermediate cases, the inter-beam distance is larger than the single droplet diameter ( $120\ \mu\text{m}$ ), and therefore in the alternate printing mode two individual, non-coalesced droplets are printed on the substrate. However, for the same inter-beam separation, simultaneous beam printing results in the formation of a single and larger elongated droplet. The difference between the two printing modes in this case is obvious.

The second experiment presents four complete stop-action movies of jetting events (Fig. 2) that correspond well to the previously analyzed cases. In all of the images, the donor substrate is situated at the top of the frame, with the laser beam impinging downwards, and with the acceptor substrate visible at the bottom of the image. Fig. 2 shows that for the largest inter-beam separation, the overall two-jet dynamics leads to separated droplets printing, in accordance with the results of the previous experiment. No noticeable interaction between the two jets is observed, and the individual jet dynamics is identical to the one observed in single-beam LIFT experiments.<sup>15–17</sup> For each beam, the expanding cavitation bubble produces symmetrical liquid flows around the bubble wall that collide at the bubble top pole and generate a localized high-pressure area within the fluid; the resultant flow velocity approaches zero. Such a special zone, also known as stagnation point, is characterized by a high static pressure



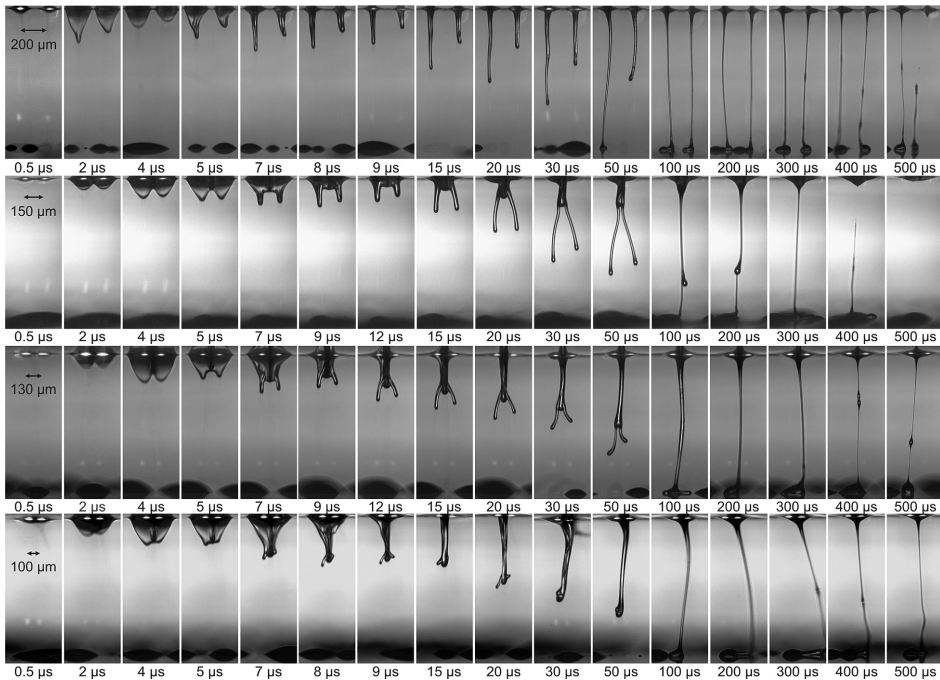


FIG. 2. Series of time-resolved images of two-beam LIFT events for various inter-beam separations (marked with arrow bars). In every image, the laser beam is impinging the donor substrate from above, with the acceptor substrate being placed at a distance of 1 mm respect to the donor one.

that is released through the formation of a jet and counter-jet pair as sketched in Fig. 3(a).<sup>19–22,24,25</sup> In this case, the beam spacing is large enough that the adjacent flows around the two bubbles have practically no influence on the liquid situated in between those bubbles. The flow symmetry and the large separation are responsible for the vertical direction of jet propagation, with both jets traveling parallel to one another at an average speed of about 1.5 m/s until they contact the substrate.

The next two rows of Fig. 2 show a series of stop-action movies that correspond to the intermediate cases of Fig. 1(b). The larger separation (150  $\mu\text{m}$ ) depicts a situation for which, unlike the previous case, the two bubbles interact, with their boundaries clearly touching each other at the moment of maximum expansion (4–5  $\mu\text{s}$ ). This contact is likely responsible for the dark border observed between the two bubbles in the 7  $\mu\text{s}$  frame; at this time the jets are already formed. Subsequently, the two jets propagate almost parallel to one another up until 9  $\mu\text{s}$ , when bubble collapse is practically complete. Starting at 15  $\mu\text{s}$ , and clearly visible at 20  $\mu\text{s}$ , a new central and thicker jet emerges and subsequently propagates away at a speed of 0.8 m/s. This new jet is considerably slower than the previously emitted thin jets, which travel at a speed of about 1.5 m/s. Meanwhile, the thin jets bases approach each other, and at about 30  $\mu\text{s}$  the jets appear to both originate from the thick jet front. However, the 50–100  $\mu\text{s}$  transition displays a quite surprising jet dynamics: during this interval the two thin jets merge, appearing in

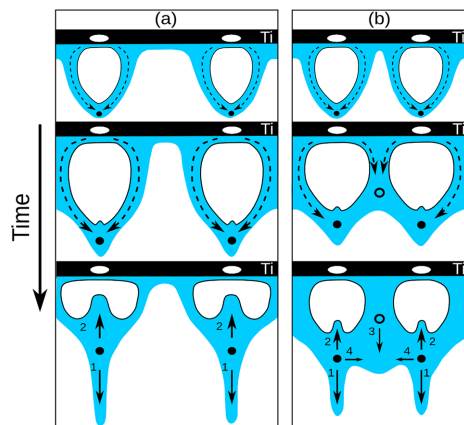


FIG. 3. Sketches depicting essential stages of the liquid transfer dynamics for the (a) largest and (b) intermediate inter-beam separations (not on scale). The dashed lines represent liquid flows around the bubble walls, the solid dots indicate the formation of stagnation points, the circles represent high pressure areas within the liquid, and the solid lines show the induced effects of such flows on the overall liquid dynamics. Several effects are depicted: the release of the high-pressure stagnation points through the ejection of two oppositely propagating thin liquid jets, denominated as jet (1) and counter-jet (2), the formation of the central thick jet (3) as a result of the high pressure area located beneath it, and the deflection of the thin jets (4) as a consequence of the unbalanced liquid flows around the bubble walls.



contact with the acceptor substrate (100  $\mu\text{s}$ ). In the same time, the thick jet seems to suffer a recession and disappears into the donor substrate by enlarging the jets base.

For the other intermediate separation (130  $\mu\text{m}$ ), the bubble boundaries at their maximum expansion (4  $\mu\text{s}$ ) clearly overlap, leading to even more pronounced interaction effects than in the previous case. Subsequent to a fast expansion phase, the two bubbles start to collapse as an apparently unified structure. Jetting arises during such bubble collapse: two thin jets are ejected from the bubbles tips at about 5–7  $\mu\text{s}$ , to subsequently propagate away at a speed of about 1 m/s. The thin jets ejection is followed by the emission of a much more prominent thick jet which, in contrast to the previous case, can now reach the acceptor substrate, advancing at a speed of 0.8 m/s. Even if the separation distance was decreased by only 13% from the previous case, the resulting jet dynamics is remarkably different, producing important changes to the final jet geometry. The two thin jets do not merge now, but advance together, forming a horn-like structure situated at the front of a much more elongated thick jet.

These results correlate well with the experiments presented in Fig. 1(b), where a single unified droplet was obtained on the substrate. Indeed, the deposits observed in the time-resolved imaging experiments for both of the intermediate separations show that a unique feature is printed on the acceptor substrate despite the fact that the two cases present several differences in their jet dynamics. This is clearly visible in the 130  $\mu\text{m}$  case, and also suggested in the 150  $\mu\text{m}$  case by the rather unsharpened but still appreciable liquid deposits. The enlarged single droplets are elongated along the direction of the line connecting the two laser spots, and the effect appears to be more dominant for smaller separations. The elongation of the droplets could be attributed to the wetting asymmetry created by the horn-like structure that contacts the substrate before the thick jet arrival. In this case, the droplet preferentially grows in the direction that connects the impact points of the horns with the substrate.

In the above described cases, the thick jet represents a novel element of the liquid dynamics not observed in previous LIFT experiments. Its origin can be attributed to the formation of a high pressure center at the interface between the two bubbles, which would be released in the form of a thick jet, as sketched in Fig. 3(b). The small separation between the two expanding bubbles makes possible that the adjacent lateral flows converge in the central zone, enhancing significantly the overall liquid flow in the area between the two bubbles, and therefore, the local pressure. The formation of this high pressure center between the bubbles not only disrupts the symmetry of the liquid flows around the walls of the individual bubbles but also favors an upward net liquid flow in the central area. Such flow in an individual bubble would have been deflected around the wall profile towards its top pole. An additional effect of the liquid flows interaction is a net jet deflection, as the two thin jets progressively approach each other, moving towards the central symmetry line. The deflection can be understood in terms of the above mentioned asymmetry of the liquid flows around each bubble. Thus, after the formation of the high pressure central zone, the non-adjacent flows around an individual bubble dominate over the corresponding adjacent component (that

mostly contributes to the thick jet formation). This leads to a sideways net flow for each jet, as suggested in the sketches of Fig. 3(b) by the sideways solid arrows labeled with “4.” The resulting force tends to unite the bases of the thin jets, increasing in magnitude with the decrease of inter-beam separation. Finally, for the smallest separation case presented in Fig. 2, the boundaries of the two bubbles at maximum expansion (4  $\mu\text{s}$ ) considerably overlap, appearing as a single and enlarged expanding bubble. As a result, the liquid dynamics is similar to the single jet case which resulted from the single bubble expansion. The jetting dynamics is now completely dominated by the prominent thick jet that advances at about 1 m/s, whereas just a small horn-like structure positioned at its front reminds of the incipient thin jets existence. This is consistent with the corresponding deposit found in mode S of Fig. 1(b)—a single, larger, and slightly elongated droplet—which is actually very similar to the one obtained in mode A. However, although the printing outcomes of both modes are similar, the mechanisms that lead to droplet formation are quite different. In this respect, the single droplet obtained in the alternate mode is due to coalescence of individual droplets arising from independent jets, a coalescence that takes place on the acceptor substrate. On the other hand, in the simultaneous mode a single and larger jet is formed, and it is its contact with the acceptor substrate that is responsible for the single droplet generation.

In conclusion, LIFT printing through separate simultaneous pulses presents a much enriched liquid dynamics in respect to the classical single-beam LIFT; depending on inter-beam separation, it can display very different printing outcomes as a result of significant jet-jet interaction. This arises from the liquid flows that originated during bubble expansion, and which superpose in the central area between the two bubbles to modify the pressure distribution inside the liquid, which is ultimately responsible for the generation of jets. This jet interaction may have a profound impact in high-speed printing since it can finally result in pixel distortion: separate pixels in the digital file containing the printing data may appear as a single elongated droplet on the printed substrate. Such pixel distortions, caused by interaction and displacement of the jets have been observed along the scan direction at DI Projekt AG’s high speed printing machine when printing continuous line segments.<sup>13</sup>

The authors acknowledge financial support from MCI of the Spanish Government (Project Nos. MAT2010-15905 and CSD2008-00023), and Fondo Europeo de Desarrollo Regional (FEDER), as well as fruitful conversations with Dr. M. Duocastella on aspects regarding the imaging setup.

<sup>1</sup>A. Piqué, D. B. Chrisey, R. A. McGill, R. C. Y. Auyeung, H. D. Wu, S. Lakeou, V. Nguyen, R. Chung, and M. Duignan, *J. Mater. Res.* **15**, 1872 (2000).

<sup>2</sup>P. Serra, M. Colina, J. M. Fernández-Pradas, L. Sevilla, and J. L. Morenza, *Appl. Phys. Lett.* **85**, 1639 (2004).

<sup>3</sup>I. Zergioti, A. Karaiskou, D. G. Papazoglou, C. Fotakis, M. Kapsetaki, and D. Kafetzopoulos, *Appl. Phys. Lett.* **86**, 163902 (2005).

<sup>4</sup>B. Hopp, T. Smausz, N. Kresz, N. Barna, Z. Bor, L. Kolozsvári, D. B. Chrisey, A. Szabó, and A. Nógrádi, *Tissue Eng.* **11**, 1817 (2005).

<sup>5</sup>N. T. Kattamis, P. E. Purnick, R. Weiss, and C. B. Arnold, *Appl. Phys. Lett.* **91**, 171120 (2007).

- <sup>6</sup>C. B. Arnold, P. Serra, and A. Piqué, *Mater. Res. Soc. Bull.* **32**, 23 (2007).
- <sup>7</sup>V. Dinca, A. Ranella, M. Farsari, D. Kafetzopoulos, M. Dinescu, A. Popescu, and C. Fotakis, *Biomed. Microdevices* **10**, 719 (2008).
- <sup>8</sup>C. Boutopoulos, V. Tsouti, D. Goustouridis, S. Chatzandroulis, and I. Zergioti, *Appl. Phys. Lett.* **93**, 191109 (2008).
- <sup>9</sup>L. Rapp, A. K. Diallo, A. P. Alloncle, C. Vidélot-Ackermann, F. Fages, and P. Delaporte, *Appl. Phys. Lett.* **95**, 171109 (2009).
- <sup>10</sup>F. Guillemot, A. Souquet, S. Catros, B. Guillotin, J. Lopez, M. Faucon, B. Pippenger, R. Bareille, M. Rémy, S. Bellance, P. Chabassier, J. C. Fricain, and J. Amédée, *Acta Biomater.* **6**, 2494 (2010).
- <sup>11</sup>C. Mézel, A. Souquet, L. Hallo, and F. Guillemot, *Biofabrication* **2**, 014103 (2010).
- <sup>12</sup>L. Rapp, J. Ailuno, A. P. Alloncle, and P. Delaporte, *Opt. Express* **19**, 21563 (2011).
- <sup>13</sup>G. Hennig, T. Baldermann, C. Nussbaum, M. Rossier, A. Brockelt, L. Schuler, and G. Hochstein, *J. Laser Micro/Nanoeng.* **7**, 299 (2012).
- <sup>14</sup>C. Boutopoulos, D. P. Papageorgiou, I. Zergioti, and A. G. Papatheasios, *Appl. Phys. Lett.* **103**, 024104 (2013).
- <sup>15</sup>M. Duocastella, J. M. Fernández-Pradas, P. Serra, J. L. Morenza, and J. Domínguez, *Appl. Phys. A* **93**, 453 (2008).
- <sup>16</sup>M. Duocastella, J. M. Fernández-Pradas, J. L. Morenza, and P. Serra, *J. Appl. Phys.* **106**, 084907 (2009).
- <sup>17</sup>M. Duocastella, J. M. Fernández-Pradas, P. Serra, and J. L. Morenza, *Thin Solid Films* **518**, 5321 (2010).
- <sup>18</sup>M. Duocastella, A. Patrascioiu, J. M. Fernández-Pradas, J. L. Morenza, and P. Serra, *Opt. Express* **18**, 21815 (2010).
- <sup>19</sup>C. Unger, M. Gruene, L. Koch, J. Koch, and B. N. Chichkov, *Appl. Phys. A* **103**, 271 (2010).
- <sup>20</sup>M. S. Brown, N. T. Kattamis, and C. B. Arnold, *Microfluid. Nanofluid.* **11**, 199 (2011).
- <sup>21</sup>M. S. Brown, C. F. Brasz, Y. Ventikos, and C. B. Arnold, *J. Fluid Mech.* **709**, 341 (2012).
- <sup>22</sup>A. Patrascioiu, J. M. Fernández-Pradas, A. Palla-Papavlu, J. L. Morenza, and P. Serra, *Microfluid. Nanofluid.* **16**, 55 (2014).
- <sup>23</sup>E. Biver, L. Rapp, A. P. Alloncle, and P. Delaporte, *Appl. Surf. Sci.* **302**, 153 (2014).
- <sup>24</sup>P. B. Robinson, J. R. Blake, T. Kodama, A. Shima, and Y. Tomita, *J. Appl. Phys.* **89**, 8225 (2001).
- <sup>25</sup>A. Pearson, E. Cox, J. R. Blake, and S. R. Otto, *Eng. Anal. Boundary Elem.* **28**, 295 (2004).



## **Paper 7**

# Conductive silver ink printing through the laser-induced forward transfer technique

C. Florian, F. Caballero-Lucas, J.M. Fernández-Pradas, R. Artigas, S. Ogier, D. Karnakis, P. Serra.

Published at: Applied Surface Science

Year: 2015

Impact factor JDR 2014: 2.711 - (Q1)

DOI: 10.1016/j.apsusc.2014.12.100





Contents lists available at ScienceDirect

Applied Surface Science

journal homepage: [www.elsevier.com/locate/apsusc](http://www.elsevier.com/locate/apsusc)

## Conductive silver ink printing through the laser-induced forward transfer technique



C. Florian<sup>a</sup>, F. Caballero-Lucas<sup>a</sup>, J.M. Fernández-Pradas<sup>a</sup>, R. Artigas<sup>b</sup>, S. Ogier<sup>c</sup>,  
D. Karnakis<sup>d</sup>, P. Serra<sup>a,\*</sup>

<sup>a</sup> Departament de Física Aplicada i Òptica, Universitat de Barcelona, Martí i Franquès 1, E-08028 Barcelona, Spain

<sup>b</sup> Sensofar-Tech S.L., Parc Audiovisual de Catalunya, Crta. BV1274 Km1, E-08225 Terrassa, Spain

<sup>c</sup> Center for Process Innovation Ltd, The Wilton Centre, TS10 4RF Cleveland, United Kingdom

<sup>d</sup> Oxford Lasers Ltd, Unit 8 Moorbrook Park, OX11 7HP Didcot, United Kingdom

### ARTICLE INFO

#### Article history:

Received 30 June 2014

Received in revised form

21 November 2014

Accepted 15 December 2014

Available online 30 December 2014

#### Keywords:

Laser forward transfer

LIFT

Laser printing

Lines printing

Conductive inks

### ABSTRACT

Laser induced forward transfer (LIFT) is a technique which allows printing a wide variety of materials. It presents several advantages over inkjet printing, such as a potentially higher resolution, being free from clogging issues, and the possibility to work with a much broader range of viscosities. LIFT appears, therefore, as an interesting alternative in all those fields where miniaturization is a major requirement, as in the microelectronics industry. The fabrication of electronic devices requires the printing of small, narrow and thin conductive lines, and in this work we investigate the printing of continuous lines of conductive silver ink on glass substrates through LIFT. Lines are initially formed through sequentially printing adjacent droplets with different overlaps. We show that above a certain overlap continuous lines can be obtained, but unfortunately they show bulging, a problem which compromises the functionality of the lines. In order to solve the problem, other printing strategies are tested; they consist in printing adjacent droplets in alternate sequences. It is found that the alternate printing of two overlapping sets of droplets with an intermediate drying step allows obtaining functional continuous lines without bulging.

© 2014 Elsevier B.V. All rights reserved.

### 1. Introduction

The feasibility of the laser induced forward transfer (LIFT) technique to transfer a large variety of materials for diverse applications has been widely proved. Originally, LIFT was applied to print materials from thin solid films [1,2], but some years later it was demonstrated that it was also possible to transfer materials in the liquid phase [3,4]. In comparison with inkjet printing, LIFT does not present problems of nozzle clogging or head contamination since the transfer process is contact-free. Additionally, LIFT allows working with a wider range of viscosities ( $1-10^3$  mPa s), attaining high degrees of spatial resolution and transferring sensitive materials without significant damage [5–8]. Thus, LIFT has been used to print materials as diverse as DNA for sensors [9], ITO nanoparticles for

thin film solar cells [10] or organic semiconductors for organic light emitting diodes (OLEDs) [11] among others.

Despite that most of the work devoted to the LIFT of liquids has been focused on depositing isolated droplets, the problem of printing continuous lines appears to be especially interesting, since one of the main applications of any printing technique is the realization of interconnects in microelectronic devices. Actually, the feasibility of printing conductive lines through LIFT has already been proved, both from solid metallic films [12] and from nanoparticle inks [13–17]. In spite that the very small line widths achieved through the LIFT of solid metallic films make this option really attractive in applications requiring very high resolutions, there are still some issues like the presence of splatter or the short length of the printed lines which still limit its industrial implementation. The LIFT of nanoparticle inks on the other hand constitutes a more conventional approach, probably closer to the current industrial demands. However, it is not free from problems either: it is in general difficult to find the right process parameters to obtain stable continuous lines free from bulging [18–21]. This problem is not specific from LIFT, but also common to other even more conventional techniques, such as inkjet printing, for instance. This not

\* Corresponding author at: Universitat de Barcelona, Departament de Física Aplicada i Òptica, Martí i Franquès 1, E-08028 Barcelona, Spain. Tel.: +34 934 039 216; fax: +34 934 021 139.

E-mail address: [pserra@ub.edu](mailto:pserra@ub.edu) (P. Serra).

<http://dx.doi.org/10.1016/j.apsusc.2014.12.100>

0169-4332/© 2014 Elsevier B.V. All rights reserved.

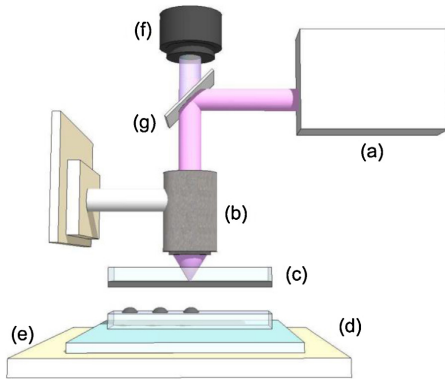


**Fig. 1.** Sketch of the experimental setup: (a) laser, (b) focusing objective, (c) Ag layer, (d) vacuum chuck, (e) stages, (f) CCD camera, and (g) IR mirror.

only limits the spatial resolution and quality of the printed feature, but also compromises its functionality: the presence of bulges can result in undesired short-circuits between adjacent parallel conductive lines. The objective of this work is, therefore, the development of strategies which allow printing continuous conductive lines through LIFT avoiding the problem of bulge formation. In order to do so, different printing experiments were performed using LIFT to transfer silver conductive inks on glass substrates. Once a successful strategy was found, the bulge-free printed lines were laser cured and their functionality was tested through resistivity measurements.

## 2. Experimental setup

The printing system uses an Amplitude Systems Yb:KYW laser with an output wavelength at 1027 nm and pulse duration of 450 fs. The laser beam is focused through a microscope objective of 50 $\times$ , with a working distance of 1.3 mm and numerical aperture of 0.55. The laser spot diameter was 12  $\mu\text{m}$  and it remained fixed during all the experiments. The objective is mounted on a translation stage which allows changing the focusing conditions on the sample. A CCD camera placed coaxially to the laser beam axis allows controlling the position of the laser beam focus on the sample. The sample is mounted on a vacuum chuck to ensure the steadiness while the printing process is taking place. The vacuum chuck is in turn mounted on a translation stage to move the sample in the XY plane. A scheme of the setup used is shown in Fig. 1.

A commercially available Ag nanoparticle dispersion from Sigma Aldrich<sup>®</sup> is used in all the LIFT experiments. The particle size is  $\leq 50$  nm and the solid content is around 30–35%. The donor film is prepared by blade coating thin layers of the ink on glass microscope slides, with film thicknesses between 20 and 30  $\mu\text{m}$ ; such relatively large thicknesses should help to improve the uniformity of the donor film, avoiding its fast drying. The acceptor substrates are also glass slides and they are separated from the donor substrates by a 200  $\mu\text{m}$  gap through cover slips used as spacers. Although during LIFT experiments it is usual to use a sacrificial absorbing layer [22], in our experiments it is not used because the Ag ink itself absorbs well the laser radiation.

After printing the lines are left to dry and once dried its conductivity is measured. Next, they are laser cured with a CW Nd:YAG laser (Baasel LBI 6000, 1064 nm wavelength, 1.2 W output power) operating at a speed of 2 mm/s with an irradiance on the sample of

12 kW/cm<sup>2</sup>. At the end of the process the conductivity of the lines is measured again and compared with the initial value.

## 3. Results and discussion

The printing process begins just after the preparation of the donor film since the drying time affects the donor layer quality in terms of both viscosity and thickness [22]. Series of equally spaced droplets are printed in order to generate lines. Different drop to drop shifts (measured from center to center) are set with the aim of investigating the influence of this parameter on the morphology of the resulting lines, and the total number of droplets is adjusted to always produce 3 mm long lines. The translation stages are moved between consecutive droplets, but these are printed with the stages at rest. The purpose of this procedure, otherwise inefficient from an industrial point of view, is to analyze the bulging problem under the simplest conditions. Issues related with the relative motion between laser beam and sample, and the influence of printing speed on the process are in progress [23].

Fig. 2 shows the results of the first experiment, carried out at a laser fluence of 530 mJ/cm<sup>2</sup> following the procedure described above. The shift between adjacent droplets in each line increases from left to right, and consecutive lines have been printed in alternate directions, with the first line starting in the upper left corner of the figure; since whenever bulging appears in a line it always does it at the beginning of that line (though not exclusively), such alternate printing sequence allows minimizing the chance of coalescence between bulges corresponding to adjacent lines. The average diameter of an isolated droplet is around 100  $\mu\text{m}$  (two first lines, with no droplet overlap), and all the droplets show a high degree of uniformity and excellent definition which actually constitutes a proof of the success in the preparation of the uniform donor film. When the printing distance between adjacent droplets reaches 90  $\mu\text{m}$  the droplets start to coalesce, though such coalescence is not enough to result in a continuous line yet. As the printing distance decreases, the frequency of droplet coalescence increases, until a shift of 70  $\mu\text{m}$  is reached, for which a continuous line with some scalloping is observed and a significant bulge in its starting point is formed. Further on, the continuous lines become more uniform but they are always accompanied by bulges, especially in the beginning and occasionally in the middle. In all cases the average width of the lines is around 65  $\mu\text{m}$ , substantially smaller than isolated droplets. All along the experiment no continuous line free from bulging is ever obtained. As it has already been pointed out in the Introduction, it is not surprising to find bulging in the printed continuous lines. Previous work on conductive ink printing, both through LIFT and through inkjet, has shown the persistent presence of such detrimental effect in continuous lines [21,24,25].

Duineveld [25] has analyzed the stability of continuous lines deposited by inkjet printing and he has established a dynamic model which provides an explanation for the bulge formation process. In this model, bulge formation is attributed to capillary flow arising from an instability produced inside the liquid due to variations in the contact angle along the line between the newly printed droplets and the previously printed feature. According to this explanation, it is not surprising that bulging appears at random positions along the printed line. However, the model does not account for the systematic formation of the initial bulge.

The question which arises is: is the initial bulge formed during printing of the first droplets, or rather at some later time, once an incipient line has already been printed? In order to find that out, an experiment was carried out where lines with increasing number of droplets were printed. Fig. 3 shows the results of such experiment, with the number of droplets in each line increasing from left to right and with printing direction always from bottom to top

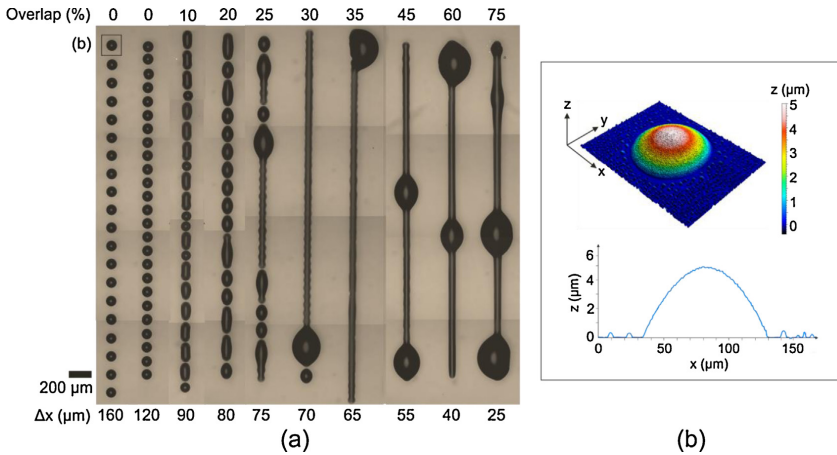


**Fig. 2.** Optical microscopy image of (a) lines printed with different printing distances between adjacent droplets ( $\Delta x$ , measured from center to center) decreasing from left to right, and (b) 3D confocal microscopy and 2D profile of a single liquid droplet after printing. Odd series, starting on the left, were printed from the bottom to the top of the image, and even ones in the opposite direction.

in the figure. In this case the average droplet diameter of a single droplet is around  $90 \mu\text{m}$  (slightly smaller than in the experiment of Fig. 2, probably due to slight differences in film thickness) and the shift between adjacent droplets remains constant at  $40 \mu\text{m}$ , i.e. 45% overlap in length. It can be observed that as the number of droplets increases the size of the resulting feature increases. When the number of droplets is 3 and 5, the printed outcome is an elongated and larger droplet. When the number of droplets increases to 10, the formation of bulging followed by a small line is observed. As the number of droplets continues increasing, the line formed is longer and the dimensions of the initial bulge size increase. The average width of the lines produced is around  $70 \mu\text{m}$ . This experiment confirms that the initial bulge already starts with the very first

droplets, though its dimension keeps growing as long as the length of the printed line is increased, probably being fed by capillary flow originated at distant positions along the line. Such directionality in the initial bulge formation suggests that the phenomenon could be possibly avoided, or at least minimized, by changing the printing sequence.

In order to test the last hypothesis, a third experiment was performed: lines were printed through varying the printing distance in a similar way to that of the experiment presented in Fig. 2, but this time the printing sequence was different. Instead of printing the droplets sequentially, odd and even droplets were printed alternately. That is, odd droplets were printed first, and the process was repeated immediately after for even droplets. The corresponding results are presented in Fig. 4, with odd droplets printed from bottom to top in the figure and even droplets printed in the opposite direction. In this way, the amount of liquid which coalesced at the beginning on the acceptor substrate should be lower than the one in the previous printing sequence. The first line from the left in Fig. 4 corresponds to non-overlapping odd droplets, and the second one to the corresponding even ones. The diameter is similar in both series ( $95 \mu\text{m}$ ) and the distance between droplets is  $160 \mu\text{m}$ . In the subsequent lines, the alternate printing of odd and even droplets presents different outcomes. As the shift between adjacent droplets is decreased, they overlap forming small groups in broken lines. This is the case for drop to drop shifts between 80 and  $65 \mu\text{m}$ . At larger overlaps a continuous line is formed, with some scalloping and an average width of  $75 \mu\text{m}$ . Unfortunately, the initial bulge is still present.

A close inspection of the results of Fig. 4, however, shows that despite bulging is not being eliminated, it is less prominent and it appears at larger overlaps than in the first experiment (Fig. 2). In consequence, it can be concluded that changing the printing sequence results in some improvement. The main drawback arises from the fact that shifts between adjacent droplets such as 70 and  $65 \mu\text{m}$  that previously resulted in continuous lines (Fig. 2), now they are bulge-free but broken, possibly due to the way that droplets coalesce in the new printing sequence. This suggests that if flow between adjacent droplets during coalescence could be minimized (or eliminated), printing of bulge-free continuous lines should be possible, and this could be attained through increasing the viscosity of odd droplets before the even ones were printed, for

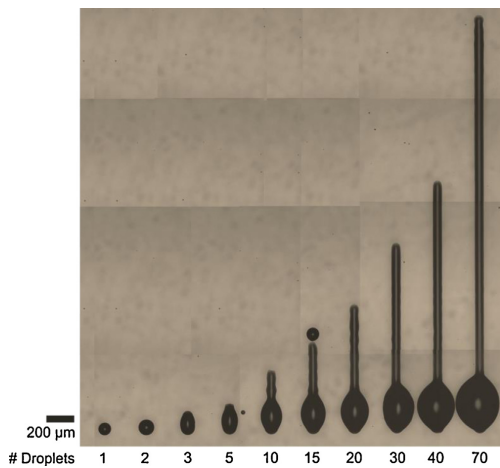


**Fig. 3.** Optical microscopy image of lines corresponding to different numbers of droplets printed with a constant shift between them of  $40 \mu\text{m}$  (45% overlap). The number of printed droplets increases from left to right. The printing direction was from the bottom to the top of the image in all the cases. Numbers in the bottom of each line indicate the number of droplets per line.



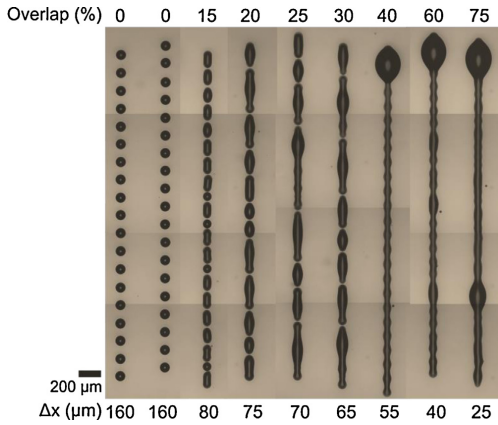


**Fig. 4.** Optical microscopy image of lines formed by droplets printed with different printing distances between adjacent droplets ( $\Delta x$ , measured from center to center) in which  $\Delta x$  decreases from left to right (except for the first two lines). The first line of non-overlapping droplets, from left to right, is identical to the second line, but with a printing shift which corresponds exactly to half the printing distance between adjacent droplets. All the other lines have been printed in an alternate sequence: first odd droplets were printed, and then even ones. The printing direction for all the odd droplets was from the bottom to the top of the image, while for the even ones it was the opposite.

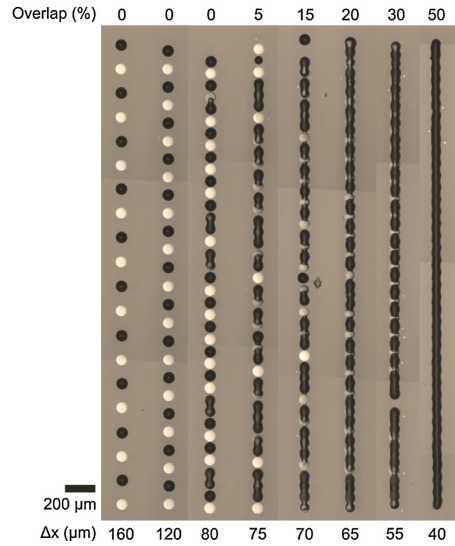


**Fig. 5.** Optical microscopy image of lines of droplets printed with different printing distances between adjacent droplets ( $\Delta x$ , measured from center to center) in which  $\Delta x$  decreases from left to right. Droplets have been printed in an alternate sequence. After printing odd droplets, they were dried (bright spots) prior to even droplets printing (dark droplets).

example, through drying them. Thus, the next printing experiment uses the same printing sequence as that of Fig. 4, i.e. odd–even droplet printing, but this time by setting a drying delay of a few minutes between the deposition of odd and even droplets.

The results of this last experiment are shown in Fig. 5. The odd dried droplets correspond to the brighter pixels while the even ones are the darker ones, since they were still liquid on the acceptor substrate when the image was taken. In this way, when the even droplets reach the substrate, the odd droplets are not liquid anymore. The two lines on the left correspond to odd and even droplets printed with no droplet overlap between them. The droplet diameters are similar (80  $\mu\text{m}$ ), even after the delay needed for the drying step. When the shift between adjacent droplets equaled the droplet diameter, some liquid droplets contacted the dried ones, forming broken lines. It can be observed that the liquid flowed along the dried pixels and in some cases it covered them almost completely, as found at 80 and 75  $\mu\text{m}$  drop to drop shifts. At 65 and 55  $\mu\text{m}$  shifts an almost continuous line was formed. The odd discontinuity

in the 55  $\mu\text{m}$  shift line is probably due to a missing laser pulse (the total absence of any ink residue in that position suggests it). Finally, at a 40  $\mu\text{m}$  shift the degree of droplet overlap was high enough to produce a perfectly continuous line completely free from bulging. Actually, bulging is totally absent along the entire experiment, in clear contrast with the previous strategy for LIFTing, where it appeared whenever continuous lines were obtained.

It can be concluded, therefore, that the combination of alternate printing and drying allows eliminating bulging. It is clear, though, that the strategy still requires some refinement. On one hand, such long drying delays as the ones used in the experiment are not practical from an industrial perspective; concerning this, however, the process could be substantially accelerated if using a laser for the drying step. A similar approach has been employed, for example, for drying and sintering both source and drain contacts in thin film transistors [26] with success. On the other hand, the morphology

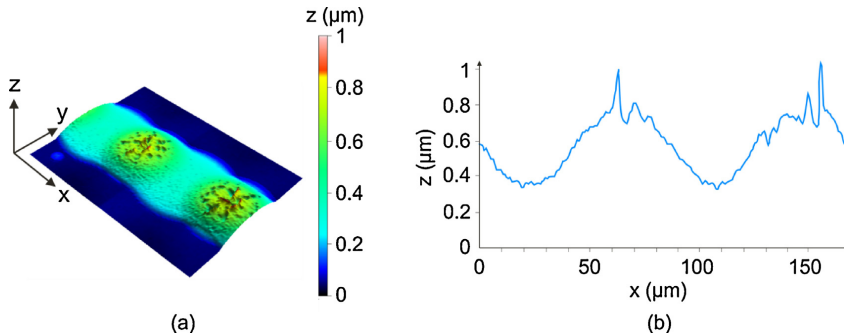


**Fig. 6.** (a) Confocal microscopy image of the dried continuous line produced with a printing distance of 40  $\mu\text{m}$  between adjacent droplets (measured from center to center) shown in Fig. 5. (b) Profile along the printing direction.

of the bulge-free lines is not as uniform as it would be expected: not only the contact line shows some scalloped morphology but also there is an excess of Ag ink in the positions corresponding to the droplets printed prior to the drying step (Fig. 6). First, it has to be mentioned that this is a minor problem when compared to bulging; actually, the functionality of the lines does not seem seriously affected by these morphological issues, as it will be shown later, while bulging can have very detrimental effects on a printed device if it results in undesired short-circuit. Second, it can be considered that it would be possible to eliminate the mentioned non-uniformities through partial drying of the first set of printed droplets before the second one is printed. Indeed, in this way their viscosity would be dramatically increased through partial evaporation of the ink solvent without achieving total drying, which would allow mitigating the flow between coalescing droplets without eliminating it completely. This could also be carried out through laser irradiation, which would require tuning of the laser parameters to attain the desired evaporation rate.

Finally the conductivity of the continuous bulge-free lines was measured in order to test their functionality as interconnects. Its value immediately after drying was found to be  $1.9 \times 10^3$  S/m, three orders of magnitude below the ink nominal value after curing,  $9.1 \times 10^6$  S/m (according to the Sigma Aldrich® datasheet). The conductivity of the printed ink, though, raises to  $10.4 \times 10^6$  S/m after laser curing, a value very close to the nominal one, which not only indicates that the printed lines are functional, but that the laser curing step provides analogous results to those corresponding to the more conventional oven curing process, with the advantage of being much faster (1.5 s over 40–50 min) and less invasive to regions adjacent to the lines.

#### 4. Conclusions

Bulging is a common problem in most printing techniques, and as such LIFT is not immune to it. We have proved that the problem can be eliminated through a strategy which combines the alternate deposition of two sets of droplets with an intermediate drying step. First, a set of equally spaced non-overlapping droplets is printed. In a second step, they are dried. Finally, the second set of equally spaced droplets is printed, with a shift with respect to the first set which corresponds exactly to half the distance between adjacent non-overlapping droplets (measured from center to center). This process allows mitigating the capillary flow along the printed line which is responsible for both bulging and line breakup, thus obtaining continuous stable lines free from bulging. After a laser sintering process, the printed lines present a conductivity very close to that of the ink after curing in an oven.

#### Acknowledgment

This work is funded by project DigiPRINT (FP7 ERA-NET OLA+).

#### References

- [1] M.L. Levene, R.D. Scott, B.W. Stryj, Material transfer recording, *Appl. Opt.* 9 (1970) 2260–2265.
- [2] J. Bohandy, B.F. Kim, F.J. Adrian, Metal deposition from a supported metal film using an excimer laser, *J. Appl. Phys.* 60 (1986) 1538–1539.
- [3] A. Piqué, D.B. Chrisey, J.M. Fitz-Gerald, R.A. McGill, R.C.Y. Auyeung, H.D. Wu, S. Lakeou, V. Nguyen, R. Chung, M. Duignan, Direct writing of electronic and sensor materials using a laser transfer technique, *J. Mater. Res.* 15 (2000) 1872–1875.
- [4] C. Boutopoulos, V. Tsouti, D. Goustouridis, S. Chatzandroulis, I. Zergioti, Liquid phase direct laser printing of polymers for chemical sensing applications, *Appl. Phys. Lett.* 93 (2008), 191109/1–3.
- [5] A. Piqué, D.B. Chrisey, R.C.Y. Auyeung, J. Fitz-Gerald, H.D. Wu, R.A. McGill, S. Lakeou, P.K. Wu, V. Nguyen, M. Duignan, A novel laser transfer process for direct writing of electronic and sensor materials, *Appl. Phys. A Mater. Sci. Process.* 284 (1999) 279–284.
- [6] M. Ollinger, H. Kim, T. Sutto, F. Martin, A. Piqué, Laser direct-write of polymer nanocomposites, *J. Laser Micro Nanoeng.* 1 (2006) 102–105.
- [7] A.T. Smith, D. Simonson, N.A. Charipar, A. Piqué, Laser direct write fabrication of meta-antennas for electro-optic conversion, *J. Laser Micro Nanoeng.* 7 (2012) 306–310.
- [8] M. Kandyła, C. Pandis, S. Chatzandroulis, P. Pissis, I. Zergioti, Direct laser printing of thin-film polyaniline devices, *Appl. Phys. A Mater. Sci. Process.* 110 (2012) 623–628.
- [9] M. Colina, P. Serra, J.M. Fernández-Pradas, L. Sevilla, J.L. Morenza, DNA deposition through laser induced forward transfer, *Biosens. Bioelectron.* 20 (2005) 1638–1642.
- [10] M. Baum, H. Kim, I. Alexeev, A. Piqué, M. Schmidt, Generation of transparent conductive electrodes by laser consolidation of LIFT printed ITO nanoparticle layers, *Appl. Phys. A Mater. Sci. Process.* 111 (2013) 799–805.
- [11] J. Shaw-Stewart, T. Mattie, T. Lippert, M. Nagel, F. Nüesch, A. Wokaun, The optimisation of the laser-induced forward transfer process for fabrication of polyfluorene-based organic light-emitting diode pixels, *Appl. Surf. Sci.* 278 (2013) 341–346.
- [12] J.A. Grant-Jacob, B. Mills, M. Feinaeugle, C.L. Sones, G. Oosterhuis, M.B. Hoppenbrouwers, R.W. Eason, Micron-scale copper wires printed using femtosecond laser-induced forward transfer with automated donor replenishment, *Opt. Mater. Express.* 3 (2013) 747–754.
- [13] R.C.Y. Auyeung, H. Kim, S.A. Mathews, A. Piqué, Laser direct-write of metallic nanoparticle inks, *J. Laser Micro Nanoeng.* 2 (2007) 21–25.
- [14] L. Rapp, J. Ailuno, A.P. Alloncle, P. Delaporte, Pulsed-laser printing of silver nanoparticles ink: control of morphological properties, *Opt. Express* 19 (2011) 21563–21574.
- [15] M. Duocastella, H. Kim, P. Serra, A. Piqué, Optimization of laser printing of nanoparticle suspensions for microelectronic applications, *Appl. Phys. A Mater. Sci. Process.* 106 (2012) 471–478.
- [16] C. Boutopoulos, I. Kalpyris, E. Serpetzoglou, I. Zergioti, Laser-induced forward transfer of silver nanoparticle ink: time-resolved imaging of the jetting dynamics and correlation with the printing quality, *Microfluid. Nanofluid.* 16 (2014) 493–500.
- [17] L. Rapp, E. Biver, A.P. Alloncle, P. Delaporte, High-speed laser printing of silver nanoparticles ink, *J. Laser Micro Nanoeng.* 9 (2014) 5–9.
- [18] A. Palla-Papavlu, C. Córdoba, A. Patrascioiu, J.M. Fernández-Pradas, J.L. Morenza, P. Serra, Deposition and characterization of lines printed through laser-induced forward transfer, *Appl. Phys. A* 110 (2013) 751–755.
- [19] H. Kim, R.C.Y. Auyeung, S.H. Lee, A.L. Huston, A. Piqué, Laser forward transfer of silver electrodes for organic thin-film transistors, *Appl. Phys. A Mater. Sci. Process.* 96 (2009) 441–445.
- [20] S.A. Mathews, R.C.Y. Auyeung, H. Kim, N.A. Charipar, A. Piqué, High-speed video study of laser-induced forward transfer of silver nano-suspensions, *J. Appl. Phys.* 114 (2013), 064910/1–9.
- [21] E. Biver, L. Rapp, A.-P. Alloncle, P. Delaporte, Multi-jets formation using laser forward transfer, *Appl. Surf. Sci.* 302 (2014) 153–158.
- [22] C. Boutopoulos, A.P. Alloncle, I. Zergioti, P. Delaporte, A time-resolved shadowgraphic study of laser transfer of silver nanoparticle ink, *Appl. Surf. Sci.* 278 (2013) 71–76.
- [23] A. Patrascioiu, C. Florian, J.M. Fernández-Pradas, J.L. Morenza, G. Hennig, P. Delaporte, P. Serra, Interaction between jets during laser-induced forward transfer, *Appl. Phys. Lett.* 105 (2014), 014101/1–5.
- [24] I. Zergioti, Laser printing of organic electronics and sensors, *J. Laser Micro Nanoeng.* 8 (2013) 30–34.
- [25] P.C. Duineveld, The stability of ink-jet printed lines of liquid with zero receding contact angle on a homogeneous substrate, *J. Fluid Mech.* 477 (2003) 175–200.
- [26] S.G. Bucella, G. Nava, K.C. Vishunubhatla, M. Caironi, High-resolution direct-writing of metallic electrodes on flexible substrates for high performance organic field effect transistors, *Org. Electron.* 14 (2013) 2249–2256.



**Paper 8**

## Direct laser printing of tailored polymeric microlenses

C. Florian, S. Piazza, A. Diaspro, P. Serra , M. Duocastella.

Sent for publication to ACS Materials and Interfaces.

Year: 2016



# Direct Laser Printing of Tailored Polymeric Microlenses

*Camilo Florian<sup>1</sup>, Simonluca Piazza<sup>2</sup>, Alberto Diaspro<sup>2</sup>, Pere Serra<sup>1</sup> and Martí Duocastella<sup>2\*</sup>*

<sup>1</sup>Universitat de Barcelona, Departament de Física Aplicada, Martí i Franqués 1, 08028  
Barcelona, Spain

<sup>2</sup>Istituto Italiano di Tecnologia, Nanophysics, Via Morego 30, 16163 Genoa, Italy

## KEYWORDS

microlenses, laser direct-write, photopolymerization, microscopy, laser-induced forward transfer

**ABSTRACT** We report a laser-based approach for the fast fabrication of high optical quality polymeric microlenses and microlens arrays with controllable geometry and size. Our strategy consists in the direct laser printing of microdroplets of a highly viscous UV-prepolymer at targeted positions, followed by photo-curing. We study the morphological characteristics and imaging performance of the microlenses as a function of substrate and laser parameters, and investigate optimal printing conditions and printing mechanisms. We show that microlens size and focusing properties can be easily tuned by the laser pulse energy, with minimum volumes below 20 fL and focal lengths ranging from 7 to 50  $\mu\text{m}$ .

Micro-lenses are becoming a key component of a growing number of functional devices in fields as important as energy harvesting or camera manufacturing.<sup>1,2</sup> This has spurred the development of technologies not only capable of producing high-quality micro-optical elements, but also to position them on a specific target.<sup>3</sup> Among existing approaches, those based on the use of masks or molds are prevailing, with main examples including soft-lithography and photolithography.<sup>4-6</sup> Despite successful efforts in trying to simplify the multi-step nature of these techniques,<sup>7,8</sup> the preparation of a mask or mold still remains a time-consuming and potentially costly step that limits the overall process efficiency. This is particularly aggravating with the advent of additive manufacturing tools and the consequent trend towards small customized units. In these instances, direct-write technologies (DWT) such as ink-jet printing or laser micromachining, capable of building structures without intermediate steps, appear more suitable.<sup>9</sup> However, several shortcomings still constrain the use of DWT for fabrication of micro-optical components. Conventional ink-jet printing, for instance, is limited by the rheology of the inks, with typical operational viscosities in the range of 1 to 50 mPa-s,<sup>10,11</sup> insufficient for most thermosetting polymers with adequate optical properties in terms of transparency or dispersion. Even if customized ink-jet systems can provide pressures high enough to induce jetting of highly viscous inks, obtaining single droplets on demand remains challenging. Alternatives such as pyro-electrohydrodynamic printing offer a promising solution, although reproducibility and resolution are still an issue.<sup>12,13</sup> Problems also arise in common laser-based techniques such as laser swelling or two-photon polymerization,<sup>14-16</sup> where high-quality micro-lenses can only be obtained of limited number of materials and control of the lens positioning on a surface of interest remains elusive.

Here, we propose a one pot method to fabricate tailored microlenses at defined positions on a substrate that addresses the challenges encountered with current direct-write approaches. Our method uses high intensity laser pulses to propel a UV-curable liquid prepolymer from a donor film onto a substrate. As a result, microdroplets are formed whose size can be controlled by adjusting the laser pulse energy. Notably, surface tension provides the printed microdroplets with almost perfect spherical shape and hence high optical quality. Upon UV exposure, the droplets can be cross-linked and converted into solid plano-convex microlenses. We demonstrate our approach by fabricating lenses with different diameters and by characterizing their morphology and optical properties.

A scheme of the microlens fabrication process is shown in Figure 1A. First, laser-induced forward transfer (LIFT) is used to print droplets at specific positions on a substrate.<sup>17,18</sup> More in detail, femtosecond laser pulses are focused on a donor film that contains the prepolymer to be printed and that is placed in close proximity to the substrate. In this experiment, the donor consisted of a glass slide coated with a 50 nm thick titanium film and a 2  $\mu\text{m}$  layer of the UV-curable polymeric glue Norland NOA164. This is an optical glue commonly used in microfluidics and optics, with excellent transmission spectra in the visible, high refractive index (1.64) and a dynamic viscosity ranging between 120 and 150 mPa-s. When a laser pulse is fired into the donor film, and due to the transparency of glass to the laser radiation, all the beam energy is absorbed within a fraction of the titanium film, upon which it is volatilized. This phenomenon induces the creation of a cavitation bubble in the prepolymer and the subsequent generation of a jet that propels a fraction of the liquid toward the substrate.<sup>19-21</sup> The impact of the jet with the substrate results in a printed droplet.<sup>22,23</sup> Since the droplet is positioned where the laser was fired, plano-convex microlenses can be fabricated at user-defined positions with high



precision and accuracy. After printing, a second step consisting in the exposure of the droplets to UV light completes the microlens fabrication process (Experimental details are included in Supplementary Material 1). Note a fundamental difference between inkjet printing and LIFT: whereas the first requires very specific conditions to assure jet breakup in the form of a single droplet that flies to the substrate, the latter overcomes this issue by allowing the jet to impact the substrate before breakup. In fact, LIFT can be used to print at conditions where jet breakup does not even occur.<sup>24</sup> This greatly facilitates the printing of highly viscous materials which tend to form ultra-stable jets, such as the polymeric glue used in these experiments.<sup>25</sup> In addition, the nozzle-free nature of LIFT relaxes the condition of high-pressures characteristic of ink-jet printing of highly viscous inks.

A study of the laser energy range suitable for microlens printing is presented in Figure 1B. In this case, we prepared 2 different lens microarrays at different energy conditions, one on glass and another on PDMS. Each individual microlens was obtained by firing a single laser pulse. Interestingly, control of the droplet diameter can be obtained by simply changing the laser energy, from around 7  $\mu\text{m}$  to 50  $\mu\text{m}$  for PDMS or 20 to 70  $\mu\text{m}$  in the case of glass. Within this range, lenses present a well-defined circular shape and uniform morphology. Importantly, by considering the contact angle between prepolymer and substrate ( $50^\circ$  for PDMS and  $31^\circ$  for glass), the volume of the printed droplets range from 25 fL to 9 pL for PDMS and from 220 fL to 9 pL for glass, values well below the limits of conventional ink-jet systems.<sup>26</sup> Note that the minimum energy required for printing depends on the particular substrate used. In this way, an energy of 13  $\mu\text{J}$  suffices to print droplets on glass, whereas for PDMS at least 15  $\mu\text{J}$  are required. This difference can be attributed to the adhesion forces (wetting) between substrate and printed material. More in detail, at energies just above the printing threshold and due to the elasticity of

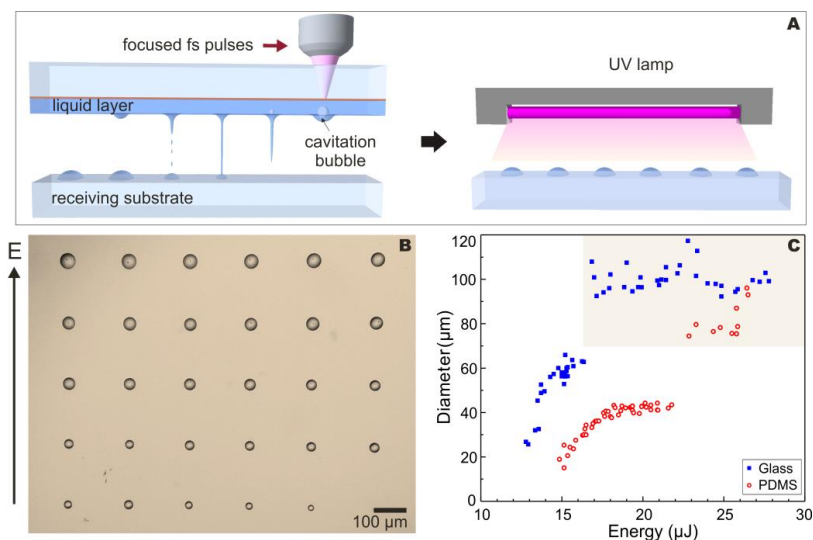


**Figure 1:** (A) Schematic diagram of the laser-based microlens printing process. First, a laser pulse impinges on the donor substrate containing a film of the viscous liquid monomer NOA 164. As a result, a jet is ejected toward a receiving substrate, where a circular droplet is collected. Patterns can be generated at will by translation of the laser beam relative to the donor substrate. In a second step, droplets are polymerized using a UV lamp that triggers the polymerization of NOA164 producing solid microlenses. (B) Characterization of the printing process. Optical micrograph of an array of microlenses obtained at different laser pulse energies. (C) Plot of the diameter versus laser pulse energy for lenses fabricated on glass (■) and on PDMS (○).

the polymer, the laser induced jet can recede after being formed without ever breaking up. Under these conditions, when a substrate is placed at a distance within the jet pathway (Supplementary Figure S1), contact between jet and substrate occur, after which the jet recedes back to the donor film. At this point, only the force interplay between substrate adhesion and jet pulling force (capillary force) dictates the amount of material that remains on the substrate.

Hence, for a substrate that presents high affinity with the printed materials such as glass (contact angle of  $31^\circ$ ), the energy threshold for printing is lower than in the case of PDMS (contact angle of  $50^\circ$ ). As the laser energy increases, the jet pulling force diminishes due to higher kinetic energy of the jet toward the substrate, allowing more material to be deposited. This explains the increase in lens diameter with energy. Eventually, and due to the high viscosity of the printed prepolymer, the jet pulling force is low enough to allow the formation of a stable capillary bridge between donor film and the receiving substrate (Supplementary Figure S1). Such phenomenon is confirmed by SEM images obtained after polymerizing in-situ both donor film and substrate prior to its separation (Supplementary Figure S2). Notably, when conditions leading to capillary bridge formation are reached, the lens diameter experiences a sudden rise and maintains approximately this value even if the energy is further increased (gray area in Figure 1C). A possible interpretation of this behavior is the long settling time given to the capillary bridge to stabilize –from firing until the donor film is separated from the substrate. Thus, the exact shape of the bridge will be predominantly given by capillary forces rather than the laser pulse energy.<sup>27</sup> In fact, at this condition the procedure of capillary bridge breakage by pulling off the donor film becomes the truly parameter that determines the final amount of printed material, which can explain the higher dispersion in the microlens diameters observed at this stage.

One of the key elements in the fabrication of microlenses is the roughness and sphericity of their overall surface. To this end, we characterized different microlenses obtained at conditions suitable for printing. A scanning electron micrograph of a couple of representative lenses with a diameter of 7 and 26  $\mu\text{m}$  on PDMS (Figure 2A) clearly illustrates the high quality of the fabricated structures, with no scratches or digs. The respective atomic force microscopy (AFM) topography maps shown in Figure 2B confirm this observation. From the AFM measurements it

is also possible to quantify the spherical shape of the printed microlenses (Figure 2C). In particular, a standard figure of merit to evaluate the accuracy of the surface of an optical element is the root mean square error (RMSE). The RMSE is given by the standard deviation of the measured surface relative to an ideal spherical reference. In this experiment, the reference surface is obtained through fitting (red line, Figure 2C). The mean RMSE values obtained when analyzing 50 lenses of different diameters at a wavelength of 632 nm are  $\lambda/18$  on glass and  $\lambda/27$  on PDMS. Note that lenses with such RMSE values are considered to be of high precision grade, and tend to be extremely difficult and costly to fabricate. Contrary to this, our technique exploits the fact that microlenses are initially prepared in liquid form; thereby surface tension provides them with perfect smooth and spherical quality, prior to polymerization. In fact, we had previously demonstrated that liquid microdroplets could behave as solid immersion lenses to improve the resolution of a laser direct write system due to their high optical quality.<sup>28</sup>

Further analysis of the optical performance of microlenses is presented in Figure 2D-E. In this case, we acquired a series of snapshots of the intensity of a laser beam at different axial positions after passing through the lens – the initially collimated beam was incident from the planar surface of the microlens corresponding to the Z axis. The 2D representation of such intensity in the XZ plane for a 26  $\mu\text{m}$  lens on PDMS (Figure 2D), a parameter known as axial point spread function (PSF), is a direct indicator of the lens imaging capabilities. From this information, the resolving power and focal length of the microlens can be determined.<sup>29</sup> In this particular case, the resolving power is 1.2  $\mu\text{m}$ , as extracted from the lateral size of the PSF (full with half maximum) at its maximum intensity. Note that the PSF does not show a defined focal spot, but rather presents several fringes parallel to the optical axis. This effect is due to the presence of spherical aberration. Indeed, this type of aberration is characteristic of spherical surfaces with

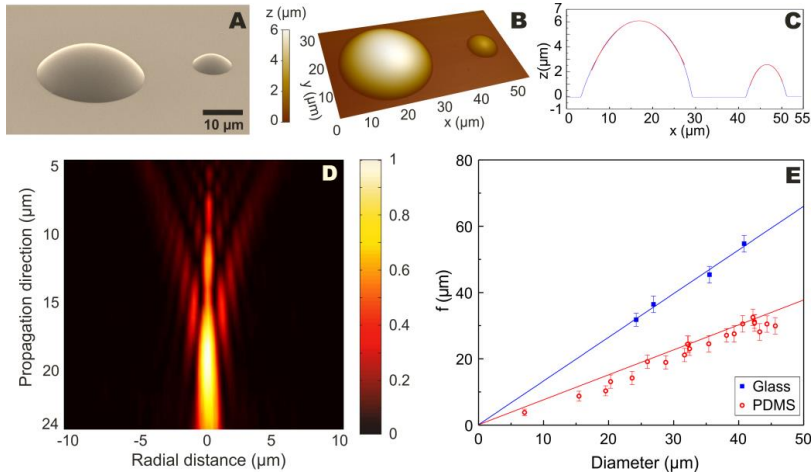


**Figure 2:** (A) SEM image of two lenses printed on PDMS at different energy conditions, with diameters of 7 and 26  $\mu\text{m}$  (viewing angle: 60°). (B) AFM topography map of the two microlenses and (C) corresponding profile showing a near perfect spherical shape (red line fitting curve). (D) XZ intensity plot of the experimental PSF of a 26  $\mu\text{m}$  microlens printed on PDMS. The incident light source was a collimated beam from a 632 nm CW laser. (E) Plot of the focal length versus laser pulse energy for microlenses printed on glass and PDMS. The continuous lines are the values expected from third order aberration theory.

high curvature, as that of a microlens, which cause marginal rays to be deviated from the paraxial focus. A plot of the focal length (distance between lens curved surface and maximum intensity of the PSF) for microlenses of different diameters is presented in Figure 2E. Interestingly, the focal length increases with the lens diameter  $D$ , for both glass and PDMS substrates. However, due to the presence of spherical aberration, the experimental focal lengths cannot be properly modeled using paraxial optics that predicts:

$$f_p = \frac{R}{n-1} = \frac{D}{2\sin\theta(n-1)}, \quad (1)$$

where  $R$  is the radius of curvature,  $n$  the lens refractive index and  $\theta$  the lens contact angle. Instead, theory of third order aberrations predicts a focal length  $f_s$ , given by (Supplementary Material 2):

$$f_s = \frac{R}{n-1} \left[ 1 - \frac{1}{2} \left( \frac{1}{1+8R^2D^{-2}n^{-2}} \right) \right] = \frac{D}{2\sin\theta(n-1)} \left[ 1 - \frac{1}{2} \left( \frac{1}{1+2(n\sin\theta)^{-2}} \right) \right], \quad (2)$$

which is in good agreement with experiment. Note that, in the case of lenses printed on PDMS and for diameters below 20  $\mu\text{m}$ , the experimental focal length is smaller than the theoretically estimated one. These shortened focal lengths could be an indication of the presence of near-field effects.<sup>30</sup> In any case, by knowing the relationship between lens diameter and laser pulse energy (Figure 1), and the contact angle between printed material and substrate, our approach enables the direct fabrication of microlenses at user-defined positions and with a specific focal length. Another important property of any focusing element is its numerical aperture (NA). For the case of microlenses, it can be estimated to be  $NA \approx nD/(2f_s)$ . Based on Equation 2, this parameter is independent of the diameter, and only depends on the refractive index and contact angle of the polymer with the substrate. For the present experiment, the NA of the fabricated polymeric microlenses is relatively high, with a value of 0.3 for glass substrate and 0.45 for PDMS.

To demonstrate the fabrication possibilities of our technique, we prepared different patterns of microlenses on glass as well as on PDMS (Figure 3A-C). A variety of patterns can be obtained by the simple translation of the laser beam relative to the donor film and substrate, ranging from microlens arrays to more complex geometries (Figure 3C). The overall process is reproducible and, in all cases, microlenses present a high optical quality. The fabricated patterns are also functional, as shown in Figure 3D. In this case, we used a microlens placed on top of the surface of a compact disk (CD) to enhance the resolving power of an optical system (microscope with a

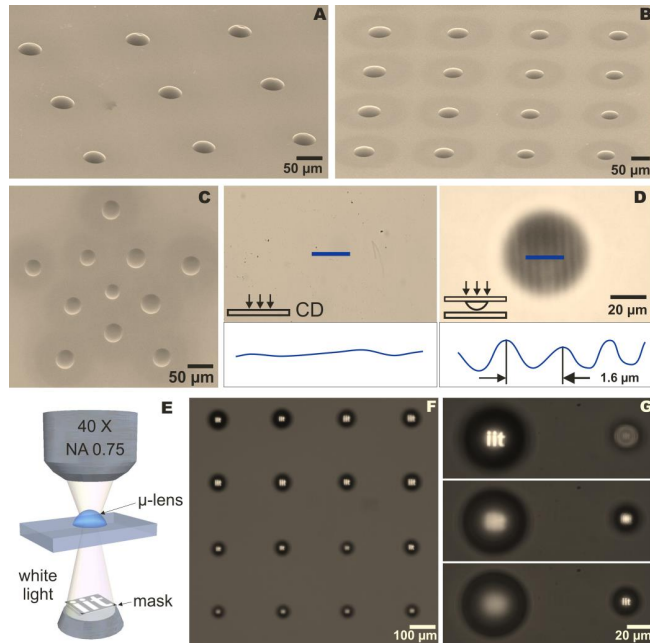


**Figure 3:** (A) SEM image of microlens arrays fabricated on PDMS, and (B) on glass. Images were acquired with a  $60^\circ$  viewing angle (C) SEM image of a star shaped pattern of microlenses. (D) Optical microscope image of the surface of a CD (line pitch  $1.6 \mu\text{m}$ ) without and with the microlens on top. The use of the microlens increases the effective resolution of the optical system allowing the visualization of the CD lines. (E) Schematic diagram of the implemented imaging setup. A light source illuminates a mask containing the letters IIT, and the image formed after the microlens is collected by a microscope objective. (F) Imaging process through a microlens array. (G) By changing the distance between objective focal plane and microlens array, the projected images appear in or out of focus depending on the focal length of each microlens.

Nikon Plan Fluor  $10\times$ ,  $0.3 \text{ NA}$  objective). Without microlens, the  $1.6 \mu\text{m}$  spacing between lines of the CD cannot be resolved. Instead, the microlens enables one to clearly resolve the

periodic pattern (Figure 3D). A printed transparency containing the letters IIT was illuminated and the projected image after passing through the microlens array was collected with a microscope objective (Nikon Plan Fluor 40 $\times$ , 0.75 NA in Figure 3E). The lensing properties of an array composed of microlenses with different diameters are presented in Figure 3F. Interestingly, by axially displacing the microlens array using a mechanical stage (Figure 3G, Supplementary Video), images of the letters come in and out of focus depending on the lens diameter (focal length). This illustrates the potential of our technique for fabricating functional and arbitrarily-designed microlenses at chosen positions on a substrate.

In summary, the use of laser printing of a highly viscous photocurable prepolymer provides a simple two-step approach for the fabrication of tailored microlens patterns. The process is fast, reproducible and allows the control of both lens diameter and lateral position by adjusting the laser parameters. We demonstrated that within the range suitable for printing, all microlenses present high optical quality with an RMS value below  $\lambda/18$ . The versatility of our approach allows for the direct fabrication of functional microlens patterns on a variety of substrates, including glass and PDMS. In the conditions herein, the minimum microlens diameter was 7  $\mu\text{m}$ , with a volume of only 27 fL. However, this value depends on the wettability of the printed prepolymer with the substrate, and we believe that the combination of our approach with substrates with lower affinity can result in the generation of nanoscale lenses with a control, in terms of diameter and position, currently inaccessible.



## ASSOCIATED CONTENT

**Supporting Information.** Additional figures, video and experimental details are included as supplementary material (PDF, AVI). This material is available free of charge via the Internet at <http://pubs.acs.org>.

## AUTHOR INFORMATION

**Corresponding Author**

\* E-mail: [marti.duocastella@iit.it](mailto:marti.duocastella@iit.it) (M.D)

**Author Contributions**

C.F. and M.D. designed and performed the experiments, analyzed the results and wrote the manuscript. The manuscript was revised and improved through contributions of all authors. All authors have given approval to the final version of the manuscript.

**Notes**

The authors declare no competing financial interest.

## ACKNOWLEDGMENT

M. Duocastella thanks Compagnia di San Paolo SIME 2015-0682 for financial support; C. Florian and P. Serra acknowledge support from MINECO of the Spanish Government (Project TEC2014-54544-C2-1-P), and Fondo Europeo de Desarrollo Regional (FEDER).

## REFERENCES

- (1) Cao, W.; Xue, J. Recent Progress in Organic Photovoltaics: Device Architecture and Optical Design. *Energy Environ. Sci.* **2014**, *7* (7), 2123–2144.
- (2) El Gamal, A.; Eltoukhy, H. CMOS Image Sensors. *IEEE Circuits Devices Mag.* **2005**, *21* (3), 6–20.
- (3) Hou, T.; Zheng, C.; Bai, S.; Ma, Q.; Bridges, D.; Hu, A.; Duley, W. W. Fabrication, Characterization, and Applications of Microlenses. *Appl. Opt.* **2015**, *54* (24), 7366–7376.
- (4) Kim, M.-S.; Scharf, T.; Haq, M. T.; Nakagawa, W.; Herzig, H. P. Subwavelength-Size Solid Immersion Lens. *Opt. Lett.* **2011**, *36* (19), 3930–3932.
- (5) Kang, D.; Pang, C.; Kim, S. M.; Cho, H. S.; Um, H. S.; Choi, Y. W.; Suh, K. Y. Shape-Controllable Microlens Arrays via Direct Transfer of Photocurable Polymer Droplets. *Adv. Mater.* **2012**, *24* (13), 1709–1715.
- (6) Yang, S.; Chen, G.; Megens, M.; Ullal, C. K.; Han, Y.-J.; Rapaport, R.; Thomas, E. L.; Aizenberg, J. Functional Biomimetic Microlens Arrays with Integrated Pores. *Adv. Mater.* **2005**, *17* (4), 435–438.
- (7) Dorrer, C.; Prucker, O.; Rhe, J. Swellable Surface-Attached Polymer Microlenses with Tunable Focal Length. *Adv. Mater.* **2007**, *19* (3), 456–460.
- (8) Feng, W.; Li, L.; Du, X.; Welle, A.; Levkin, P. A. Single-Step Fabrication of High-Density Microdroplet Arrays of Low-Surface-Tension Liquids. *Adv. Mater.* **2016**, n/a – n/a.

- (9) Piqué, A.; Chrisey, D. B. Chapter 1 – Introduction to Direct-Write Technologies for Rapid Prototyping. In *Direct-Write Technologies for Rapid Prototyping*; 2002; pp 1–13.
- (10) de Gans, B.-J.; Duineveld, P. C.; Schubert, U. S. Inkjet Printing of Polymers: State of the Art and Future Developments. *Adv. Mater.* **2004**, *16* (3), 203–213.
- (11) Jang, D.; Kim, D.; Moon, J. Influence of Fluid Physical Properties on Ink-Jet Printability. *Langmuir* **2009**, *25* (5), 2629–2635.
- (12) Kuang, M.; Wang, L.; Song, Y. Controllable Printing Droplets for High-Resolution Patterns. *Adv. Mater.* **2014**, *26* (40), 6950–6958.
- (13) Vespini, V.; Coppola, S.; Todino, M.; Paturzo, M.; Bianco, V.; Grilli, S.; Ferraro, P. Forward Electrohydrodynamic Inkjet Printing of Optical Microlenses on Microfluidic Devices. *Lab Chip* **2016**, *16* (2), 326–333.
- (14) Ou, Y.; Yang, Q.; Chen, F.; Deng, Z.; Du, G.; Wang, J.; Bian, H.; Yong, J.; Hou, X. Direct Fabrication of Microlens Arrays on PMMA With Laser-Induced Structural Modification. *IEEE Photonics Technol. Lett.* **2015**, *27* (21), 2253–2256.
- (15) Guo, R.; Xiao, S.; Zhai, X.; Li, J.; Xia, A.; Huang, W. Micro Lens Fabrication by Means of Femtosecond Two Photon Photopolymerization. *Opt. Express* **2006**, *14* (2), 810–816.
- (16) Malinauskas, M.; Gilbergs, H.; Žukauskas, A.; Purlys, V.; Paipulas, D.; Gadonas, R. A Femtosecond Laser-Induced Two-Photon Photopolymerization Technique for Structuring Microlenses. *J. Opt.* **2010**, *12* (3), 035204/1–8.
- (17) Arnold, C. B.; Serra, P.; Piqué, A. Laser Direct-Write Techniques for Printing of Complex Materials. *MRS Bull.* **2007**, *32*, 23–31.

- (18) Delaporte, P.; Alloncle, A.-P. Laser-Induced Forward Transfer: A High Resolution Additive Manufacturing Technology. *Opt. Laser Technol.* **2016**, *78*, 33–41.
- (19) Duocastella, M.; Fernández-Pradas, J. M.; Serra, P.; Morenza, J. L. Jet Formation in the Laser Forward Transfer of Liquids. *Appl. Phys. A Mater. Sci. Process.* **2008**, *93* (2008), 453–456.
- (20) Brown, M. S.; Kattamis, N. T.; Arnold, C. B. Time-Resolved Dynamics of Laser-Induced Micro-Jets from Thin Liquid Films. *Microfluid. Nanofluidics* **2011**, *11* (2), 199–207.
- (21) Patrascioiu, A.; Morenza, J. L.; Serra, P. Laser-Generated Liquid Microjets : Correlation between Bubble Dynamics and Liquid Ejection. *Microfluid. Nanofluidics* **2014**.
- (22) Duocastella, M.; Fernández-Pradas, J. M.; Serra, P.; Morenza, J. L. Sessile Droplet Formation in the Laser-Induced Forward Transfer of Liquids: A Time-Resolved Imaging Study. *Thin Solid Films* **2010**, *518* (18), 5321–5325.
- (23) Unger, C.; Gruene, M.; Koch, L.; Koch, J.; Chichkov, B. N. Time-Resolved Imaging of Hydrogel Printing via Laser-Induced Forward Transfer. *Appl. Phys. A* **2011**, *103* (2), 271–277.
- (24) Duocastella, M.; Fernández-Pradas, J. M.; Morenza, J. L.; Serra, P. Time-Resolved Imaging of the Laser Forward Transfer of Liquids. *J. Appl. Phys.* **2009**, *106* (8), 084907/1–7.
- (25) Eggers, J.; Villermaux, E. Physics of Liquid Jets. *Reports Prog. Phys.* **2008**, *71* (3), 036601/1-79.
- (26) Singh, M.; Haverinen, H. M.; Dhagat, P.; Jabbour, G. E. Inkjet Printing-Process and Its

- Applications. *Adv. Mater.* **2010**, *22* (6), 673–685.
- (27) Vagharchakian, L.; Restagno, F.; Léger, L. Capillary Bridge Formation and Breakage: A Test to Characterize Antiadhesive Surfaces. *J. Phys. Chem. B* **2009**, *113* (12), 3769–3775.
- (28) Duocastella, M.; Florian, C.; Serra, P.; Diaspro, A. Sub-Wavelength Laser Nanopatterning Using Droplet Lenses. *Sci. Rep.* **2015**, *5*, 16199/1–9.
- (29) Baranski, M.; Perrin, S.; Passilly, N.; Froehly, L.; Albero, J.; Bargiel, S.; Gorecki, C. A Simple Method for Quality Evaluation of Micro-Optical Components Based on 3D IPSF Measurement. *Opt. Express* **2014**, *22* (11), 13202–13212.
- (30) Lee, J. Y.; Hong, B. H.; Kim, W. Y.; Min, S. K.; Kim, Y.; Jouravlev, M. V.; Bose, R.; Kim, K. S.; Hwang, I.-C.; Kaufman, L. J.; Wong, C. W.; Kim, P.; Kim, K. S. Near-Field Focusing and Magnification through Self-Assembled Nanoscale Spherical Lenses. *Nature* **2009**, *460* (7254), 498–501.

## Supporting Information

# Direct Laser Printing of Tailored Polymeric Microlenses

*Camilo Florian<sup>1</sup>, Simonluca Piazza<sup>2</sup>, Alberto Diaspro<sup>2</sup>, Pere Serra<sup>1</sup> and Martí Duocastella<sup>2\*</sup>*

<sup>1</sup>Universitat de Barcelona, Departament de Física Aplicada, Martí i Franqués 1, 08028 Barcelona,  
Spain

<sup>2</sup>Istituto Italiano di Tecnologia, Nanophysics, Via Morego 30, 16163 Genova, Italy

### Corresponding Author

\* E-mail: [marti.duocastella@iit.it](mailto:marti.duocastella@iit.it) (M.D)

**Supplementary Material 1: Experimental details**

Micro lens fabrication: The printing system consisted of a femtosecond Ti:Sapphire regenerative amplifier (Coherent Evolution, wavelength 800 nm, 100 fs pulse duration) operating in single shot mode, a 50× 0.55 NA long working distance microscope objective (Mitutoyo M Plan Apo 50×) and an XYZ mechanical translation stage (Prior Scientific FB204). A CMOS camera (Thorlabs DCC1645C) and a dichroic mirror (reflected 800 nm and transmitted the visible spectrum) enabled real-time visualization of the laser-induced effects. Laser pulse energy was selected by using a laser beam attenuator (Eksma 990-0070-800H) and measured by means of an energy meter (Coherent Fieldmax II with J-10MB-LE Energy Sensor). The laser spot diameter used during the printing experiments was around 45 μm.

The donor film was prepared by spin-coating the photo-curable prepolymer Norland NOA164 (viscosity of 120-150 mPa-s at 20 °C) on a glass slide coated with a titanium thin film (50 nm thickness). The role of the titanium was to favor absorption and reduce the direct exposure of the polymer to the laser radiation. The overall thickness of the prepolymer film was 2 μm, estimated from a weight measurement and later confirmed with AFM images. The donor film was placed on top of the receiving substrate (either glass or polydimethylsiloxane) by 25 μm spacers, and then the whole donor-receiving system was positioned on the XYZ stage to initiate the printing experiments. In general, a single shot was used to create a single microlens. Subsequent firing at different positions on the donor-receiving system resulted in customized microlens arrays. After completion of the printing process, the droplets on the receiving substrate were cured using a UV lamp.

Micro lens characterization: The morphology of the microlenses was characterized by optical microscopy (Fluoview 1000, Olympus) as well as SEM (JSM-6490LA, Jeol). Topography maps of the lens surface were obtained by AFM operating in non-contact mode (Park Systems XE-70, AppNano ACTA probes with size of 14–16 μm). Measurements of the point spread function (PSF) of the microlenses were performed by irradiating the lens with a CW laser diode (637 nm wavelength) and collecting the intensity with a 100× objective lens (0.9 numerical aperture) plus a 200 mm tube lens and a CMOS camera (Thorlabs DCC1545M). The distance between the microlens surface and the objective focal plane was controlled with a mechanical stage (minimum step size 50 nm). Imaging through the microlenses was evaluated with both reflection (Fluoview 1000, Olympus) and transmission microscopes (Nikon Eclipse N-1).

### Supplementary Material 2

The paraxial approximation cannot be typically used to describe the focusing properties of microlenses. This is mainly due to the relatively large curvature and reduced size of these lenses: in most applications the entire microlens aperture is used and marginal rays are largely deviated. As a consequence, even plano-convex microlenses with a perfectly spherical surface will suffer from spherical aberration. In these cases, though, third order aberration theory can still provide a valid analytical expression to describe the focal length of microlenses. More in detail, the overall longitudinal spherical aberration (distance between paraxial focus  $f_p$  and marginal ray focus  $f_m$ ) can be written as:

$$\frac{1}{f_m} - \frac{1}{f_p} = \frac{D^2 n^2}{8 f_p^3 (n-1)^2},$$

where  $D$  corresponds to the lens diameter,  $n$  is the lens refractive index and  $f_p = R/(n-1)$ , with  $R$  being the lens radius of curvature. Note that this equation is valid for light impinging from the lens flat surface (spherical aberration is reduced when light is incident from the curved surface). The position of best focus  $f_s$ , where intensity is the maximum, corresponds to the half point between  $f_p$  and  $f_m$ , which yields to:

$$f_s = f_p - \frac{1}{2} \left( \frac{f_p}{1 + 8 f_p^2 (n-1)^2 / D^2 n^2} \right) = \frac{R}{n-1} \left[ 1 - \frac{1}{2} \left( \frac{1}{1 + 8 R^2 / D^2 n^2} \right) \right],$$

where the position is measured from the lens principal plane (tangential to the vertex of the curved surface for a plano-convex lens). There are different methods to experimentally determine  $R$ . We used the following equation based on the geometry of the fabricated microlenses, assuming that the morphology corresponds to a spherical cap:

$$R = \frac{r^2 + h^2}{2h},$$

where  $r=D/2$  corresponding to the radius of the microlenses measured from the topography images, and  $h$  is the height of the microlenses measured from the vertex to the flat surface of the microlens.



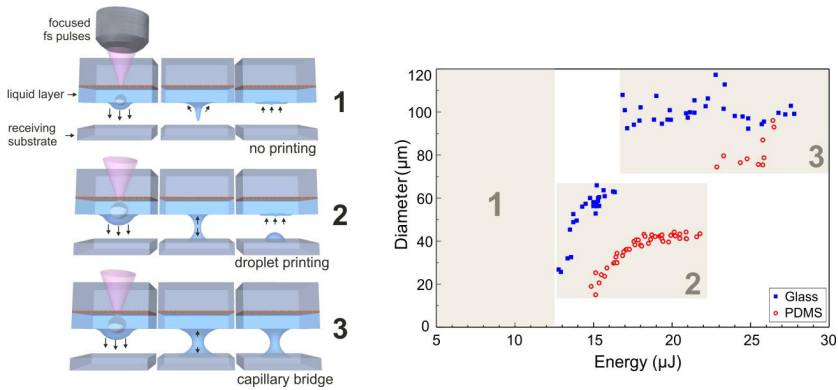


**Figure S1:** Printing mechanism of the optical glue NOA164. When the laser pulse energy is not high enough to produce the transfer of the polymer, the formed jet is contracted towards the liquid layer. Once the pulse energy is sufficiently high, the formed jet contacts the surface of the receiving substrate. For energies just above the printing threshold, the contacting jet breaks leaving behind a tiny amount of polymer that takes the shape of a circular droplet. For higher energies, the contacting jet has pulled enough liquid to enable the formation of a stable capillary bridge. The arrows in the image indicate the movement of the liquid.

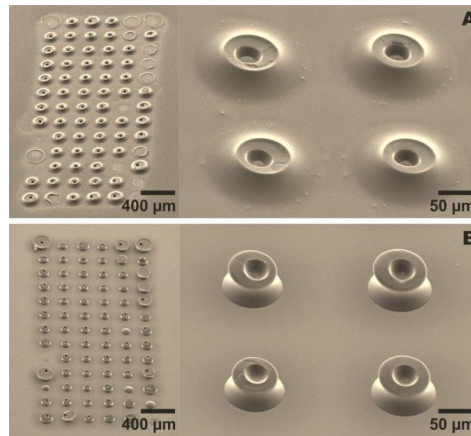


**Figure S2:** In this figure it is presented the result of a printing experiment in which the layer of NOA164 is cured before separating the donor substrate from the receiving one. The energy used during this experiment was 25  $\mu\text{J}$  (gray area Figure 1C). (A) SEM image of the donor film that presents the formation of structures that correspond to capillary bridges that were broken when the donor film was separated from the receiving

substrate. On the other side, (B) shows an SEM image of the receiving substrate. This figure shows the remaining capillary bridge that matches the ones shown in (A). In the middle of the structure, it is possible to observe the cavitation bubble that remained after the printing process. Both images were taken with a viewing angle of 60°.

**Supplementary Video:** Through focus imaging of a projection mask containing the words IIT after passing through two microlenses of different size. The formation of sharp images at different axial positions demonstrates the dependency of focal length on lens diameter.



## Combined approaches

### Paper 9

## Sub-wavelength laser nanopatterning using droplet lenses

M. Duocastella, [C. Florian](#), P. Serra, A. Diaspro.

Published at: Scientific Reports

Year: 2015

Impact factor JDR 2014: 5.578 - (Q1)

DOI: [10.1038/srep16199](https://doi.org/10.1038/srep16199)



# SCIENTIFIC REPORTS

## OPEN Sub-wavelength Laser Nanopatterning using Droplet Lenses

Received: 20 August 2015

Accepted: 12 October 2015

Published: 06 November 2015

Martí Duocastella<sup>1</sup>, Camilo Florian<sup>2</sup>, Pere Serra<sup>2</sup> & Alberto Diaspro<sup>1</sup>

When a drop of liquid falls onto a screen, e.g. a cell phone, the pixels lying underneath appear magnified. This lensing effect is a combination of the curvature and refractive index of the liquid droplet. Here, the spontaneous formation of such lenses is exploited to overcome the diffraction limit of a conventional laser direct-writing system. In particular, micro-droplets are first laser-printed at user-defined locations on a surface and they are later used as lenses to focus the same laser beam. Under conditions described herein, nanopatterns can be obtained with a reduction in spot size primarily limited by the refractive index of the liquid. This all-optics approach is demonstrated by writing arbitrary patterns with a feature size around 280 nm, about one fourth of the processing wavelength.

Optical methods are unrivaled as patterning tools thanks to the possibility to operate in ambient conditions, integration in direct-writing systems and ease of use. However, the far-field diffraction barrier limits the minimum feature size in optical systems to about half the processing wavelength, imposing a serious restriction for nanopatterning at visible or infrared wavelengths. The primary strategy to overcome diffraction has been the use of near-field effects. By focusing light through the tip of an atomic force microscope<sup>1</sup>, a microsphere<sup>2–4</sup>, or a plasmonic lens<sup>5</sup>, evanescent waves can be coupled to the material enabling deep sub-wavelength patterning. In this way, feature sizes below 100 nm can be produced, but maintaining the spacing between probe and substrate is extremely critical and difficult to perform in practice. Self-positioning systems<sup>6</sup> offer an interesting solution, although they tend to be time consuming and/or require complex setups<sup>7</sup>. In contrast, sub-wavelength feature sizes can also be fabricated by exploiting non-linearities in the interaction of light with a particular material, as in multiphoton absorption<sup>8–10</sup> or photopolymerization inspired by reversible saturable optical fluorescence transition (RESOLFT) microscopy<sup>11,12</sup>. Since these methods are based on the particular photophysics of the material to be patterned<sup>13</sup>, resolution enhancement is material-dependent and optimal results are typically constrained to a narrow range of available photoresists.

An interesting alternative for sub-wavelength optical patterning consists of using a dielectric hemispherical lens, known as a solid immersion lens (SIL), placed in contact with the surface. A SIL effectively increases the numerical aperture of a focusing optical system, producing an enhancement in lateral resolution only limited by the refractive index of the SIL material. Successful implementations of SILs include microscopy<sup>14–16</sup>, spectroscopy<sup>17</sup>, photolithography<sup>18</sup> and optical recording<sup>19</sup>, with reported feature sizes as small as 100 nm<sup>20</sup>. However, the use of SILs for surface nanopatterning presents a series of problems that prevent this approach to be widely implemented. For instance, the relative high laser energies usually required for processing a surface, especially in the case where laser ablation is to be performed, can irreversibly damage SILs. This is particularly problematic due to the challenges involved in the fabrication of SILs. In fact, conventional grinding techniques are time consuming and are limited to SILs with diameters larger than 1 mm<sup>21</sup>. Small lenses are desirable since they suffer from less aberrations and they can be easily positioned at local uniform parts of an overall uneven surface. Promising methods such as

<sup>1</sup>Nanoscopia, Istituto Italiano di Tecnologia, Via Morego 30, 16163 Genova, Italy. <sup>2</sup>Departament de Física Aplicada i Òptica, Universitat de Barcelona, C/Martí i Franqués 1, 08028 Barcelona, Spain. Correspondence and requests for materials should be addressed to M.D. (email: marti.duocastella@iit.it)

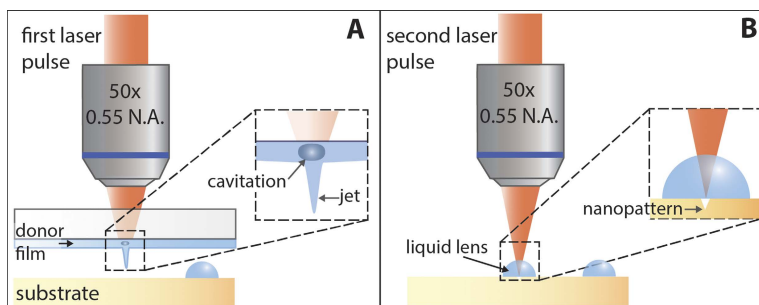


**Figure 1.** Schematic of the droplet-assisted laser processing approach. (A) A liquid droplet is printed on top of the surface to be patterned by using LIFT. (B) After removal of the donor film, the same laser source is focused through the droplet, which acts as a liquid lens. As a consequence, nanopatterns can be fabricated.

photopolymerization<sup>22</sup> or chemical etching<sup>21</sup> can produce high-quality micro-SILs, but the fabrication process remains cumbersome. In addition, to generate nanopatterns over an extended surface one needs to mechanically translate the SIL along different positions of the sample. Such stepwise approach is inherently slow and requires sophisticated feedback control systems.

Droplet-assisted laser processing (DALP) addresses the challenges encountered in current micro and nanopatterning techniques. Our approach is based on a two-step process (Fig. 1). First, we use laser-induced forward transfer (LIFT)<sup>23</sup> to print droplets with sizes ranging from 10 to 200  $\mu\text{m}$  into specific areas of interest of a surface. Next, we use the printed droplets as lenses to focus laser pulses directly below each droplet, locally modifying the surface. Notably, the same laser source used for printing can be used for surface patterning. One can consider the droplet to act as the liquid version of SILs without the constraints involved in its fabrication and placement – droplets present a flawless surface, and can be easily printed at desired locations on a surface. Thereby, this approach produces a straightforward increase in the focusing capabilities of a system by a factor that depends to first order on the liquid refractive index. In addition, contrary to immersion objectives, liquid micro-lenses can be used in a variety of optical systems, the focusing enhancement can be controlled by simply changing the liquid, and the small size of the lens minimizes possible absorption effects and even temporal dispersion in the case of irradiation by ultrafast laser pulses. Here, we investigate the optimal conditions of DALP and demonstrate the feasibility of this approach by creating nanopatterns on a polymeric surface with a feature size about one fourth of the processing wavelength.

## Results

**Principle of droplet-assisted laser processing.** The basis of our approach can be found in the lensing effect that a drop of liquid produces on a surface. This phenomenon – clearly observed when a liquid falls on a screen, with the underlying pixels appearing magnified – can be explained by the curvature and refractive index of the liquid ( $n > 1$ ), causing each drop to act as a plano-convex lens. In particular, DALP uses micrometer-size droplets whose contact angle with the surface is about  $90^\circ$  (almost perfect hemispherical shape). By placing such a droplet at the focal plane of an optical system, the effective numerical aperture of the system increases and, consequently, enhancement in lateral as well as axial resolution is achieved<sup>24</sup>. Most importantly, droplet focusing is carried out without introducing spherical or coma aberrations. This is a consequence of the hemispherical nature of the droplet – light is focused at the plane lying just underneath the flat surface, at a position corresponding to the first aplanatic point of a sphere<sup>25</sup>.

To better understand focus enhancement induced by a micro-droplet, we simulated light focusing through an optical system with and without droplet. In particular, we considered a lens doublet as the focusing element (N.A. 0.27) and solved the diffraction propagation equation for a Gaussian beam (1027 nm wavelength). The colormap intensity plot at the vicinity of the system focus without micro-droplet is presented in Fig. 2A. The beam displays the characteristic features of a focused Gaussian beam. In particular, intensity at the focal plane presents a Gaussian profile along the radial direction, with a measured full-width at half maximum (FWHM) of 1.48  $\mu\text{m}$  (Fig. 2C). Regarding beam intensity along the propagation direction (Fig. 2D), the beam presents the parabolic profile typical of Gaussian beams. The corresponding Rayleigh range, characterized by a decrease in intensity of a factor of 2, is equal to 6  $\mu\text{m}$ . Notably, the focusing characteristics of the optical system drastically change when a hemispherical micro-droplet ( $n = 1.4$ , 20  $\mu\text{m}$  in diameter) is placed at the focal plane, as shown in Fig. 2B. In

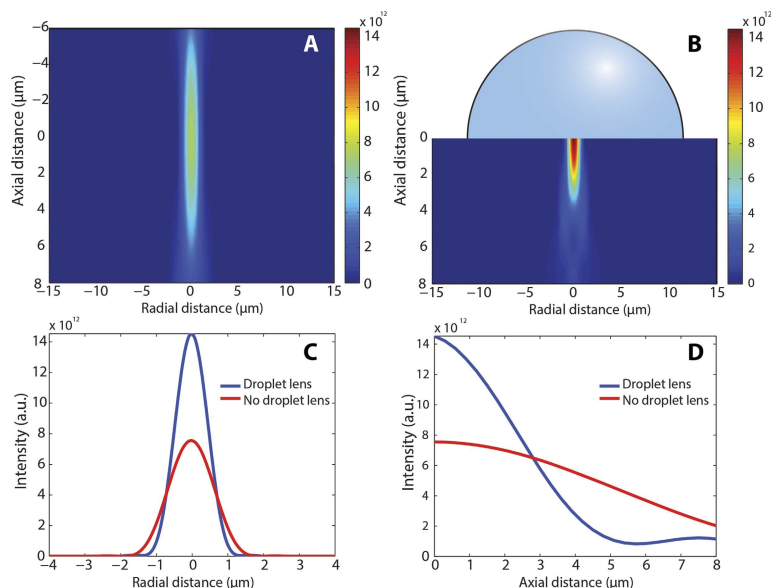


**Figure 2. Simulation of the intensity and focusing enhancement produced by droplet-assisted laser processing.** (A) Colormap plot of the intensity distribution of a Gaussian beam focused through a 0.27 N.A. objective, and (B) corresponding colormap plot after a hemispherical droplet ( $n = 1.4$ ) has been placed at the laser focus. The liquid lens results in about a factor of 2 intensity enhancement. (C) Plot of the beam intensity versus radial distance at focus. In the case of using a liquid lens, the FWHM is decreased by a factor corresponding to the lens refractive index. (D) Plot of the beam intensity versus axial distance along the optical axis. The system depth of field is reduced when using the liquid lens.

In this case, the lensing effect induced by the droplet produces stronger focusing, with an enhancement in intensity of about a factor of 2. In addition, the radial plot profile of Fig. 2C reveals a FWHM at focus of  $1.05\mu\text{m}$ , a factor of 1.4 smaller than without droplet. This value corresponds to the refractive index of the droplet, and it is in good agreement with theoretical work on SILs<sup>26</sup>. In fact, the droplet is expected to produce an increase in the effective numerical aperture of the system equal to the lens refractive index. Assuming no absorption in the droplet, the enhancement in intensity can be directly correlated to the decrease in spot size – the focusing area scales as the square of the radius, and hence the increase in intensity is  $1.4^2 \approx 2$ . The micro-droplet also constrains the focus extent along the axial direction (Fig. 2D). In this case, the Rayleigh range is  $3\mu\text{m}$ . This is also consistent with the increase in numerical aperture of the system, since the Rayleigh range scales as the inverse square of this parameter<sup>27</sup>. Simulations performed with hemispherical droplets whose diameter ranges from  $20$  to  $200\mu\text{m}$  do not present significant differences, and in all cases the droplet produces an enhancement in the system numerical aperture proportional to the liquid refractive index.

**Implementation of DALP.** The successful implementation of DALP requires a method capable of printing hemispherical droplets with controlled size at precise locations on a surface. Here, we used laser-induced forward transfer or LIFT to achieve this goal, but other methods such as inkjet printing<sup>28</sup> could be valid as well. LIFT is a laser-direct writing technique based on transferring material from a donor film to a substrate placed in close proximity to it<sup>23</sup> (Fig. 1A). In the case of using a liquid film, laser pulses induce the formation of a cavitation bubble in the liquid that evolves into a jet propelling a fraction of the material toward the substrate<sup>29,30</sup>. When the jet contacts the substrate, a droplet is formed<sup>31</sup>. Interestingly, droplets with diameters ranging from microns to sub-millimeters can be obtained by simply modifying the laser pulse energy, which renders this approach optimal for DALP. Contrary to inkjet printing<sup>28</sup>, the nozzle-free nature of LIFT makes this technique suitable for printing liquids with a wide range of rheological properties. In addition, the use of LIFT for DALP is further justified by the possibility of using the same laser source for both droplet lens printing as well as material processing.



A crucial aspect of DALP is the shape of the micro-droplet. Failing to achieve hemispherical droplets inevitably results in spherical aberrations and the consequent loss of optical performance. Therefore, it is necessary to assure an equilibrium contact angle between droplet and surface of  $90^\circ$ . Provided a hydrophobic surface, contact angle can be adjusted by adding a surfactant to the liquid. This is the approach we used in the current experiment, where the contact angle between polydimethylsiloxane (PDMS) and a mixture of water and glycerol ( $n = 1.5$ ), typically around  $110^\circ$ , was decreased to  $90^\circ$  by adding a surfactant (Supplementary Figure 1). In the case of patterning an initial hydrophilic surface, a hydrophobic coating must be first applied. By using spin-coating or other chemical deposition processes, thin films below 10 nm can be obtained<sup>32</sup>, with minimal impact on the optical performance of DALP. Besides the need for contact angle control, there is a second factor that plays a crucial role in the formation of a hemispherical droplet: the balance between gravitational and surface tension forces – gravity tends to pull the center of the droplet disrupting its spherical shape<sup>33</sup>. The ratio between these forces can be expressed using a dimensionless number, the Bond number:

$$Bo = \Delta\rho g L^2 / \gamma, \quad (1)$$

where  $\Delta\rho$  is the density difference between drop and air,  $g$  is the gravity constant,  $\gamma$  is surface tension and  $L$  is a characteristic length of the droplet (diameter, in this particular case). For  $Bo \leq 0.01$  gravitational effects can be neglected<sup>33</sup>, and the droplet retains a perfect spherical shape. When using aqueous solutions, such a value is reached for diameters below  $300\ \mu\text{m}$ , which justifies the need for printing micrometer-size droplets in order to obtain aberration-free liquid lenses.

Once micro-droplets with a hemispherical shape are deposited on a surface, sub-wavelength nano-patterning is possible by focusing laser pulses through the droplets. At this point, there are two different modes to implement DALP. The first one consists of firing a single laser pulse for each droplet. Any potential deformation or even volatilization that the droplet may suffer as a consequence of laser irradiation becomes irrelevant – each droplet/lens is used only once. In fact, for sub-picosecond pulses, volatilization would occur well after the laser pulse is over<sup>34</sup>. This approach works best when small features with large separations are required, since the minimum distance between spots is initially determined by the droplet diameter. By repeating the printing process, the separation between features can be reduced, but this process becomes cumbersome. Alternatively, it is possible to fabricate structures arbitrarily separated by using a single droplet and scanning the laser beam across it. This provides a direct approach for fabricating user-defined structures, including continuous nanopatterns, but questions remain about the performance of the lens off center, as well as the potential droplet deformation caused by multiple firing.

**Experimental characterization of DALP.** To demonstrate the feasibility of DALP, we first laser printed an array of droplets on PDMS using an energy of  $8.5\ \mu\text{J}$  (1027 nm wavelength, 450 fs pulse duration). The corresponding laser fluence was  $2.7\ \text{J}/\text{cm}^2$  (laser was defocused). Well-defined droplets with an average diameter of  $100\ \mu\text{m}$  were obtained, with a standard deviation of only  $4\ \mu\text{m}$  (Supplementary Figure 2). Such droplet control assures good reproducibility to our approach. Next, we removed the donor film used in LIFT and moved axially the planar surface of the droplet to match the objective focal plane. We then fired 10 shots at the vicinity of the droplet center, each spaced  $2\ \mu\text{m}$  from one another. We repeated this experiment for different laser pulse energies, using a different droplet for each energy (range of 2 to 30 nJ, which corresponds to fluences from 80 to  $1170\ \text{mJ}/\text{cm}^2$ ). Plots of the spot diameter and depth measured by atomic force microscopy (AFM) are presented in Fig. 3 as a function of laser pulse energy. For comparison, the results obtained with regular laser processing (no droplet) are also included. Notably, given a laser pulse energy, the spot diameter is larger and the depth is greater with DALP. This can be explained by the stronger focusing produced by the droplet and the consequent increase in the effective laser fluence. In fact, by using a moderate numerical aperture objective (N.A. 0.55 in this experiment), energies ranging from 3.5 to 10 nJ can be used to ablate PDMS. The corresponding laser fluences are 140 and  $390\ \text{mJ}/\text{cm}^2$ , below the ablation threshold for PDMS without a droplet ( $390\ \text{mJ}/\text{cm}^2$  in the current experiment, in agreement with values found in literature<sup>35</sup>). Such low energies open the door to use DALP with low power lasers or directly from laser oscillators. More importantly, at these energies (sub-threshold fluence) deep sub-wavelength patterning is possible. In this way, spot sizes as small as 280 nm were obtained for 3.5 nJ pulses, about one fourth of the processing wavelength (Fig. 4). This is almost a factor of 1.8 smaller than the minimum spot size obtained in this experiment with regular laser processing (490 nm). Such a reduction in feature size above the liquid lens refractive index (1.5), is caused by the threshold effect characteristic of laser ablation and the nonlinear relationship between beam waist and laser pulse energy<sup>36</sup>. Therefore, even if the laser beam waist is reduced by a factor equal to the lens refractive index, nonlinearities in light-matter interaction enables one to use DALP to further reduce spot size.

Figure 5A,B show the change in spot diameter and depth as the beam is focused through the droplet at different axial positions. Such characterization is of pivotal importance for the technical implementation of DALP. Indeed, accurate z-focus control is a classic problem in laser patterning: real-world surfaces are non-flat and can present warpage or texture, which typically require costly and time consuming methods capable of adjusting the focal plane relative to the surface for uniform processing to occur<sup>37</sup>. This problem is aggravated when high spatial resolution is desired, i.e. in high numerical aperture

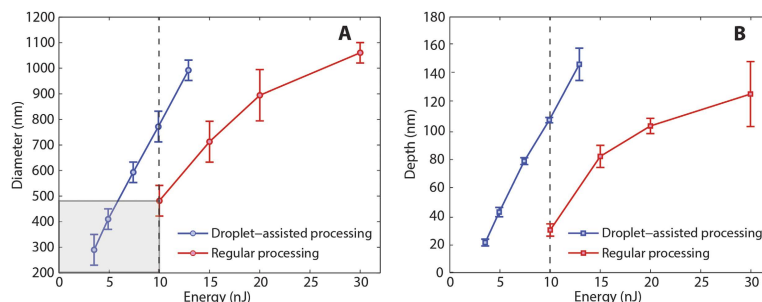


**Figure 3.** Plot of hole diameter versus energy for DALP and regular processing. The deep sub-wavelength patterning area accessible only by DALP is shown in gray. (B) Plot of hole depth versus energy. Notably, for an energy of 10 nJ, holes obtained by DALP are about 3 times deeper.

systems or near-field super-resolution techniques, where the short depth of field (DOF) inherent of these approaches constrain their use to the de facto processing of flat surfaces. In contrast, DALP tolerates an axial shift of the focal plane as high as  $5\mu\text{m}$  (Fig. 5A,B). Within this range, ablated holes at an energy of 12 nJ present a diameter and depth variation of only 10% with respect to the mean value. Such axial processing range is comparable to the DOF of the optical system without droplet (Supplementary Figure 3). Therefore, the enhancement in lateral resolution produced by DALP does not impose stronger requirements on axial focus control. In other words, DALP increases the effective numerical aperture of a focusing system without altering its original working distance or DOF. This can be understood by the theory of hemispherical SILs: as long as the planar surface of the lens is within the DOF of the focusing objective, strong focusing and deep sub-wavelength processing can be obtained without aberrations. In addition, the critical distance between lens and surface is maintained constant in DALP – the droplet is always in contact with the surface to be patterned, effectively making DALP a self-positioning approach.

The focusing performance of a liquid micro-lens off center is presented in Fig. 5C,D. An array of holes was prepared by laterally scanning the laser beam across a  $100\mu\text{m}$  droplet. The plots of the ablated hole diameter and depth versus radial position (Fig. 5C,D) show variations for these parameters of less than 5% (maximum – minimum values) up to a distance of about  $5\mu\text{m}$  off the lens center for all axial positions analyzed. This radial distance corresponds to about 10% of the initial droplet diameter. Such a value is in agreement with numerical simulations for different droplet sizes (Supplementary Figure 4), where in all cases a change of less than 2% in the FWHM of the focused beam is obtained for up to 10% of the droplet diameter – in fact, due to laser energy fluctuations the experimental values are expected to present a slightly higher variability than theory. As the beam is focused off the lens axis, the diameter values start to vary significantly while the hole depth tends to decrease, which is consistent with the presence of aberrations at these positions. Consequently, it is possible to use DALP to write nanopatterns within a single droplet, but the irradiated area must remain relatively close to the lens center. Considering the limit in droplet diameter imposed by gravity (Bond number) for most common fluids,  $\sim 100\mu\text{m}$  droplets present a suitable trade-off between preservation of hemispherical shape – absence of aberrations – and area that can be patterned ( $10 \times 10\mu\text{m}^2$ ).

Potential distortions within a droplet caused by laser firing are also an important aspect to consider. The nature of such distortions can be diverse, largely depending on laser pulse energy or laser repetition rate. In this particular experiment, we observed the formation of micrometer-size cavitation bubbles for energies exceeding 15 nJ (fluence of  $59\text{ mJ}/\text{cm}^2$ ). Such phenomenon can be caused by the use of energies above the optical breakdown in the liquid<sup>38</sup>, or by by-products of the ablative process<sup>39</sup>. Most bubbles seem to disappear after around 1 second, but the scattering induced by a bubble already imposes a limitation in the repetition rate of DALP: about 1 Hz for  $E > 15\text{ nJ}$  for this current experiment. For energies below 15 nJ and repetition rates below 5 Hz we observed no distortion in the droplet shape nor any cavitation effects. However, higher repetition rates resulted in non-circular ablated holes. We attribute this effect to the heating induced by the ablation of the polymer, and the consequent change in refractive index in the liquid that caused aberrations during droplet focusing. In particular, when firing two consecutive laser pulses (repetition rate higher than 5 Hz) at slightly different positions, the thermal effects induced by the first shot can laterally perturb the second one, breaking the circular symmetry of the focal spot and causing coma aberration. Using higher energies or higher repetition rates resulted in a significant aggravation of these effects, eventually producing a change in the droplet shape or volume, or even its total volatilization. In such instances, though, it is still possible to use DALP using a single pulse for each droplet.

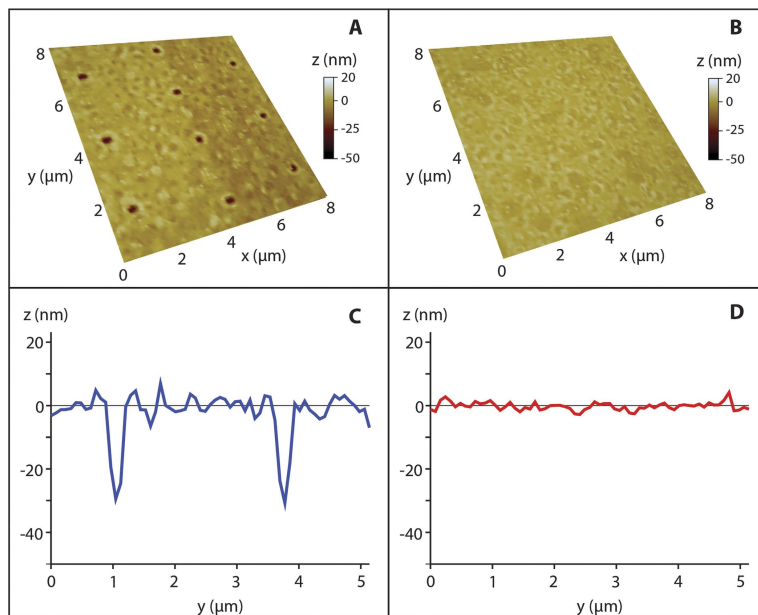


**Figure 4.** Characterization of droplet-assisted laser processing versus regular processing. (A) AFM image of 280 nm diameter holes obtained by single-shot ablation at an energy of 3.5 nJ using DALP with a droplet size of 100  $\mu\text{m}$ . (B) Morphology of the same surface irradiated using 3.5 nJ using regular processing. No modification is observed (C) Line scan corresponding to Fig. 3A, and (D) to Fig. 3B.

**Nanopatterning.** The nanopatterning capabilities of DALP are presented in Fig. 6. In this case, we prepared 3 concentric squares using a 100  $\mu\text{m}$  droplet and 5 nJ pulses. Notably, the formation of continuous features with a width of 200 nm is feasible by pulse overlapping (shot-to-shot distance of 100 nm in the current experiment). After laser irradiation and with the droplet still in place, the pattern can be clearly distinguished upon examination in an optical microscope (Fig. 6A). Washing out the droplet does not modify the pattern, which is still visible by optical microscopy (Fig. 6B). However, a simple comparison of the 2 optical micrographs reveals the lensing effects of the droplet. Indeed, the pattern imaged through the droplet appears magnified by a factor of about 1.5. This value is close to the refractive index of the liquid. In addition, the resolution is also enhanced by the droplet – nearby features are only distinguishable by droplet imaging. A statistical analysis of the pattern from AFM characterization (Fig. 6C) shows an average line width of 350 nm and depth of 50 nm, with a standard deviation of 30 nm and 5 nm, respectively. It is important to note that the lack of parallelism in the fabricated structure is not a fundamental limitation of DALP but is caused by the limited position accuracy of the mechanical stages.

### Discussion

In this paper, we have successfully demonstrated that liquid micro-droplets can be used to enhance the focusing capabilities of a laser direct-writing system, and produce features with a size down to 280 nm at sub-threshold fluences, about one fourth of the processing wavelength. We have implemented our approach by first laser-printing hemispherical droplets at user-defined positions on a surface, and subsequent firing through the droplet. Each droplet acts as a lens, whose optical performance depends on the refractive index of the liquid in a way analogous to a solid immersion lens. The axial position of the droplet with respect to the focal plane of the optical system does not significantly compromise the outcome of our approach as long as the plane surface of the droplet is within the depth of field of the focusing objective. Furthermore, continuous nanopatterns can be written within a single droplet by scanning the laser in the XY direction at low laser fluences and low repetition rates. No artifacts or aberrations are induced off the droplet center up to about 10% of the droplet diameter. In addition, droplet-assisted laser processing could further improve resolution by using high refractive index liquids, including polymers or nanoparticle-doped solutions<sup>40</sup>. DALP is easy to implement using any laser-direct writing system,

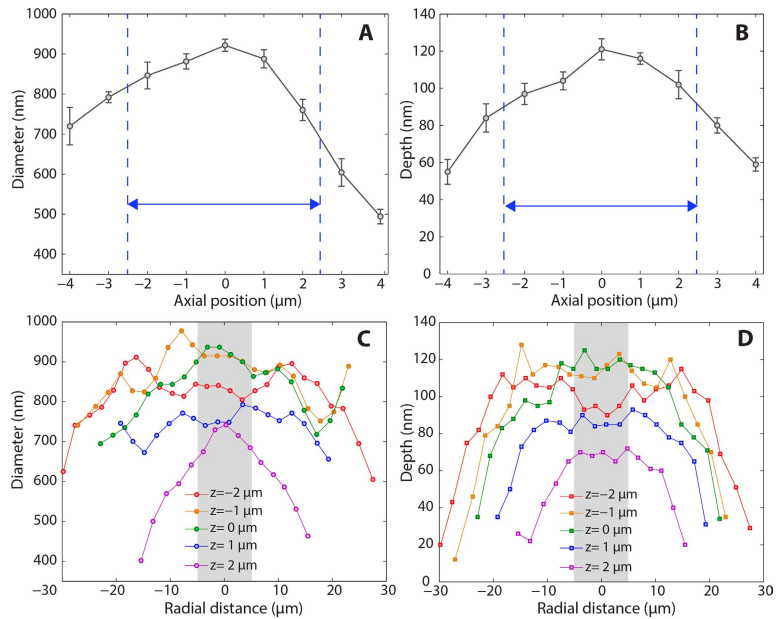


**Figure 5. Alignment tolerance of droplet assisted processing.** Plot of the diameter (A) and depth (B) of holes ablated in the center of the droplet at different axial positions. The presence of the droplet provides enhanced focusing but does not modify the axial working range suitable for uniform processing. Plot of the diameter (C) and depth (D) of holes ablated using DALP at different radial positions within a droplet. For a distance corresponding to about 10% of the droplet diameter, the hole size and depth remains constant indicating that aberration-free nanopatterning is possible.

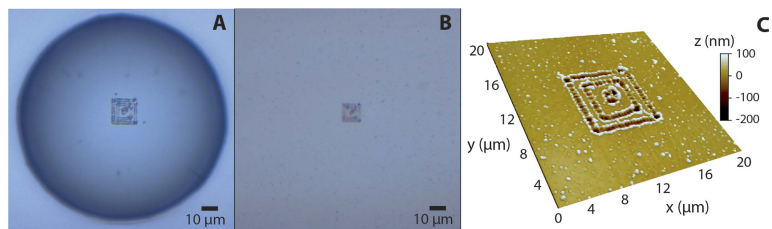


**Figure 6. Nanopatterning of concentric squares.** Optical micrograph of a pattern fabricated with a  $100 \mu\text{m}$  droplet, (A) with the droplet still in place and (B), without droplet. The drop produces a magnification of about a factor of 1.5. (C) AFM characterization of the pattern.

it can be performed in ambient conditions and it obviates the need for precision axial z-focus control or other constraints typical of current nanopatterning approaches. By combining optics and fluids, DALP provides researchers with a powerful tool capable of overcoming the traditional diffraction barrier, extending the well-known advantages of lasers to deep sub-wavelength patterning.

## Methods

**Laser direct-writing system.** A Yb:KYW femtosecond laser (Amplitude Systemes S-pulse) with a wavelength of 1027 nm and a pulse duration of 450 fs was used in single shot mode. The beam profile was Gaussian with  $M^2 = 1.35$ . The laser pulse energy was controlled by means of a variable optical density filter, and the energy of each pulse was measured by an energy meter (Ophir PD10-SH). The laser irradiation was focused onto the sample using a 50x, 0.55 NA long-working distance objective (Mitutoyo M Plan Apo 50X). The sample was positioned on a XYZ mechanical translation stage with a minimum step size of 0.5  $\mu\text{m}$  (Physik Instrumente TM M-414) aligned perpendicular to the focusing objective. Real time visualization of the ongoing process was carried out by a CMOS camera (Thorlabs DCC1645C) thanks to a dichroic mirror that reflected IR (1027 nm laser) and transmitted the visible spectrum.

**Sample preparation.** A solution of polydimethylsiloxane (PDMS) dissolved in ethyl acetate (5% v/v) was drop-casted on top of a silicon wafer. After solvent evaporation, a PDMS film with a thickness of 200 nm was obtained. Thickness control could be achieved by changing solvent concentration, but 200 nm presented the highest uniformity. It is important to note that the thickness of the polymeric layer cannot be smaller than a certain value (which depends on the optical absorption of the polymer) or otherwise ablation of the underneath surface occurs. In this case, the PDMS layer acts as a coating that provides the appropriate contact angle between droplet and surface to be patterned.

**Laser printing.** The donor film used in LIFT was prepared by blade coating a solution of water and glycerol (50% v/v) with 1% sodium dodecyl sulfate on top of a microscope slide covered with a 50 nm thick titanium film. The titanium film was used as the absorbing layer. No presence of titanium on the printed droplets was observed. However, in order to completely rule out potential contamination by the absorbing layer, it would be possible to use a volatile organic absorbing layer<sup>41</sup> or even directly print from a liquid reservoir by using high intense pulses without any absorbing layer<sup>42</sup>. The thickness of the liquid film obtained was about 10  $\mu\text{m}$  estimated from a weight measurement. The donor film was placed on top of the PDMS surface – liquid facing PDMS – at a distance of 100  $\mu\text{m}$  using spacers. The donor-PDMS substrate system was then moved to the XYZ stage to initiate the printing process. Due to the low vapor pressure of the water and glycerol solution, the donor film remained stable over a period of about 1 hour. For the same reason, the diameter of the printed droplets changed very slowly over time while its hemispherical shape was in all cases maintained (contact angle of about 90°), providing an effective processing window time for DALP of about 30 minutes.

**Optics simulation.** The physical optics propagation (POP) package from Zemax (Radiant Inc.) was used to solve the diffraction equations for an optical system consisting of a lens doublet with an estimated numerical aperture of 0.27. A Gaussian beam with a wavelength of 1027 nm was launched through the system, and the intensity distributions at different axial positions were measured. To simulate the effects of DALP, the simulations were repeated with a hemispherical lens with refractive index of 1.4 placed at the system focus.

**Sample characterization.** Optical micrographs of the fabricated patterns were captured with a commercial microscope (Carl-Zeiss Axio Imager). AFM characterization was carried out in non-contact mode using a pyramidal tip with size of 14–16  $\mu\text{m}$  (AppNano AFM probes ACTA), in an AFM system (Park Systems XE-70). Contact angle measurements were performed using a goniometer system (KSV CAM 200 Optical Tensiometer). In all cases, MATLAB was used for data analysis.

## References

- Hwang, D. J., Chimmalgi, A. & Grigoropoulos, C. P. Ablation of thin metal films by short-pulsed lasers coupled through near-field scanning optical microscopy probes. *J. Appl. Phys.* **99**, 044905 (2006).
- Piglmeier, K., Denk, R. & Bäuerle, D. Laser-induced surface patterning by means of microspheres. *Appl. Phys. Lett.* **80**, 4693–4695 (2002).
- Huang, S. M., Sun, Z., Luk'yanchuk, B. S., Hong, M. H. & Shi, L. P. Nanobump arrays fabricated by laser irradiation of polystyrene particle layers on silicon. *Appl. Phys. Lett.* **86**, 1–3 (2005).
- Pereira, A. *et al.* Laser-fabricated porous alumina membranes for the preparation of metal nanodot arrays. *Small* **4**, 572–576 (2008).
- Liu, Z. *et al.* Focusing surface plasmons with a plasmonic lens. *Nano Lett.* **5**, 1726–1729 (2005).
- McLeod, E. & Arnold, C. B. Subwavelength direct-write nanopatterning using optically trapped microspheres. *Nat. Nanotechnol.* **3**, 413–7 (2008).
- Srituravanich, W. *et al.* Flying plasmonic lens in the near field for high-speed nanolithography. *Nat. Nanotechnol.* **3**, 733–737 (2008).
- Kawata, S., Sun H. B., Tanaka T. & Takada, K. Finer features for functional microdevices. *Nature* **412**, 697–699 (2001).
- Maruo, S. & Fourkas, J. T. Recent progress in multiphoton microfabrication. *Laser Photon. Rev.* **2**, 100–111 (2008).
- Sugioka, K. & Cheng, Y. Ultrafast lasers—reliable tools for advanced materials processing. *Light Sci. Appl.* **3**, e149 (2014).
- Malinauskas, M., Farsari, M., Piskarskas, A. & Juodkazis, S. Ultrafast laser nanostructuring of photopolymers: A decade of advances. *Phys. Rep.* **533**, 1–31 (2013).
- Fischer, J. & Wegener, M. Three-dimensional optical laser lithography beyond the diffraction limit. *Laser Photon. Rev.* **7**, 22–44 (2013).

13. Andrew, T. L., Tsai, H.-Y. & Menon, R. Confining Light to Deep Subwavelength Dimensions to Enable Optical nanopatterning. *Science* **324**, 917–921 (2009).
14. Mansfield, S. M. & Kino, G. S. Solid immersion microscope. *Appl. Phys. Lett.* **57**, 2615–2616 (1990).
15. Wu, Q., Feke, G. D., Grober, R. D. & Ghislain, L. P. Realization of numerical aperture 2.0 using a gallium phosphide solid immersion lens. *Appl. Phys. Lett.* **4064**, 0–3 (2012).
16. Wildanger, D. *et al.* Solid immersion facilitates fluorescence microscopy with nanometer resolution and sub-ångström emitter localization. *Adv. Mater.* **24**, OP309–13 (2012).
17. Gerardot, B. D. *et al.* Contrast in transmission spectroscopy of a single quantum dot. *Appl. Phys. Lett.* **90**, 2005–2008 (2007).
18. Ghislain, L. & Elings, V. Near-field photolithography with a solid immersion lens. *Appl. Phys. Lett.* **74**, 1999–2001 (1999).
19. Terris, B. D., Mamin, H. J., Rugar, D., Stuedenmund, W. R. & Kino, G. S. Near-field optical data storage using a solid immersion lens. *Appl. Phys. Lett.* **65**, 388–390 (1994).
20. Agarwal, K., Chen, R., Koh, L. S., Sheppard, C. J. R. & Chen, X. Crossing the Resolution Limit in Near-Infrared Imaging of Silicon Chips: Targeting 10-nm Node Technology. *Phys. Rev. X* **5**, 1–9 (2015).
21. Fletcher, D. *et al.* Microfabricated silicon solid immersion lens. *J. Microelectromechanical Syst.* **10**, 450–459 (2001).
22. Malinauskas, M. *et al.* Femtosecond laser polymerization of hybrid/integrated micro-optical elements and their characterization. *J. Opt.* **12**, 124010 (2010).
23. Arnold, C. B., Serra, P. & Piqué, A. Laser Direct-Write Techniques for Printing of Complex Materials. *MRS Bull.* **32**, 23–32 (2007).
24. Ramsay, E. Solid immersion lens applications for nanophotonic devices. *J. Nanophotonics* **2**, 021854 (2008).
25. Born, M. & Wolf, E. Principles of optics: electromagnetic theory of propagation, interference and diffraction of light, 7th edn (Cambridge University Press, 1999).
26. Serrels, K. A. *et al.* Solid immersion lens applications for nanophotonic devices. *J. Nanophoton.* **2**, 021854 (2008).
27. Trager, F. *Springer handbook of lasers and optics* (Springer, 2012).
28. Calvert, P. Inkjet Printing for Materials and Devices. *Chem. Mater.* **13**, 3299–3305 (2001).
29. Duocastella, M., Fernández-Pradas, J. M., Morenza, J. L. & Serra, P. Time-resolved imaging of the laser forward transfer of liquids. *J. Appl. Phys.* **106**, 084907 (2009).
30. Brown, M. S., Kattamis, N. T. & Arnold, C. B. Time-resolved study of polyimide absorption layers for blister-actuated laser-induced forward transfer. *J. Appl. Phys.* **107**, 1–8 (2010).
31. Duocastella, M., Fernández-Pradas, J. M., Morenza, J. L. & Serra, P. Sessile droplet formation in the laser-induced forward transfer of liquids: A time-resolved imaging study. *Thin Solid Films* **518**, 5321–5325 (2010).
32. Ma, M. & Hill, R. M. Superhydrophobic surfaces. *Curr. Opin. Colloid Interface Sci.* **11**, 193–202 (2006).
33. Kumacheva, E. & Garstecki, P. *Microfluidic reactors for polymer particles* (Wiley, 2011).
34. Yang, G. W. Laser ablation in liquids: Applications in the synthesis of nanocrystals. *Prog. Mater. Sci.* **52**, 648–698 (2007).
35. Rubahn, K., Ihlemann, I., Jakopic, G., Simonsen, a. C. & Rubahn, H. G. UV laser-induced grating formation in PDMS thin films. *Appl. Phys. A Mater. Sci. Process.* **79**, 1715–1719 (2004).
36. Liu, J. M. Simple technique for measurements of pulsed Gaussian-beam spot sizes. *Opt. Lett.* **7**, 196–8 (1982).
37. Duocastella, M. & Arnold, C. B. Enhanced depth of field laser processing using an ultra-high-speed axial scanner. *Appl. Phys. Lett.* **102**, 061113 (2013).
38. Vogel, A., Linz, N., Freidank, S. & Palttauf, G. Femtosecond-laser-induced nanocavitation in water: Implications for optical breakdown threshold and cell surgery. *Phys. Rev. Lett.* **100**, 1–4 (2008).
39. Vogel, A. & Venugopalan, V. Mechanisms of pulsed laser ablation of biological tissues. *Chem. Rev.* **103**, 577–644 (2003).
40. Nussbaumer, R. J., Caseri, W. R., Smith, P. & Tervoort, T. Polymer-TiO<sub>2</sub> nanocomposites: A route towards visually transparent broadband UV filters and high refractive index materials. *Macromol. Mater. Eng.* **288**, 44–49 (2003).
41. Fardel, R., Nagel, M., Nüesch, E., Lippert, T. & Wokaun, A. Fabrication of organic light-emitting diode pixels by laser-assisted forward transfer. *Appl. Phys. Lett.* **91**, 061103 (2007).
42. Duocastella, M., Patrascioiu, A., Fernández-Pradas, Morenza, J. M. & Serra, J. Film-free laser forward printing of transparent and weakly absorbing liquids. *Opt. Express* **18**, 21815–21825 (2010).

### Acknowledgements

M. Duocastella and A. Diaspro thank IIT for financial support; C. Florian and P. Serra acknowledge support from MINECO of the Spanish Government (Project TEC2014-54544-C2-1-P), and Fondo Europeo de Desarrollo Regional (FEDER). In addition, we thank José Alejandro Heredia-Guerrero for help in preparing the PDMS coatings and Colin Sheppard for useful discussions on solid immersion lenses.

### Author Contributions

M.D. designed the experiments, analyzed the data and wrote the manuscript. C.F. performed the experiments. All authors contributed to the scientific discussion and revision of the article.

### Additional Information

**Supplementary information** accompanies this paper at <http://www.nature.com/srep>

**Competing financial interests:** The authors declare no competing financial interests.

**How to cite this article:** Duocastella, M.D. *et al.* Sub-wavelength Laser Nanopatterning using Droplet Lenses. *Sci. Rep.* **5**, 16199; doi: 10.1038/srep16199 (2015).



This work is licensed under a Creative Commons Attribution 4.0 International License. The images or other third party material in this article are included in the article's Creative Commons license, unless indicated otherwise in the credit line; if the material is not included under the Creative Commons license, users will need to obtain permission from the license holder to reproduce the material. To view a copy of this license, visit <http://creativecommons.org/licenses/by/4.0/>



## **Paper 10**

# Printing of silver conductive lines through laser-induced forward transfer

C. Florian, F. Caballero-Lucas, J.M. Fernández-Pradas, S. Ogier, L. Winchester, D. Karnakis, R. Artigas, P. Serra.

Published at: Applied Surface Science

Year: 2016

Impact factor JDR 2014: 2.711 - (Q1)

DOI: 10.1016/j.apsusc.2015.11.248







Contents lists available at ScienceDirect

Applied Surface Science

journal homepage: [www.elsevier.com/locate/apsusc](http://www.elsevier.com/locate/apsusc)

## Printing of silver conductive lines through laser-induced forward transfer



C. Florian<sup>a</sup>, F. Caballero-Lucas<sup>a</sup>, J.M. Fernández-Pradas<sup>a</sup>, S. Ogier<sup>b</sup>, L. Winchester<sup>b</sup>,  
D. Karnakis<sup>c</sup>, R. Geremia<sup>c</sup>, R. Artigas<sup>d</sup>, P. Serra<sup>a,\*</sup>

<sup>a</sup> Universitat de Barcelona, Departament de Física Aplicada i Òptica, IN<sup>2</sup>UB, Martí i Franquès 1, E-08028, Barcelona, Spain

<sup>b</sup> Centre for Process and Innovation Ltd, The Wilton Centre, TS10 4RF, Cleveland, United Kingdom

<sup>c</sup> Oxford Lasers Ltd, Unit 8 Moorbrook Park, OX11 7HP, Didcot, United Kingdom

<sup>d</sup> Sensofar-Tech S.L., Parc Audiovisual de Catalunya, Crta. BV1274 Km 1, E-08225, Terrassa, Spain

### ARTICLE INFO

#### Article history:

Received 23 June 2015

Received in revised form 5 November 2015

Accepted 29 November 2015

Available online 1 December 2015

#### Keywords:

Laser forward transfer

LIFT

Laser printing

Microfluidics

Conductive inks

### ABSTRACT

The generation of conductive lines from liquid inks through laser-induced forward transfer (LIFT) is achieved by printing a sequence of overlapping droplets. This procedure, however, is not free from drawbacks: the formation of continuous lines is often accompanied with undesired scalloping or bulging. In this work we present an innovative method consisting in the deposition of conductive ink through LIFT inside fluidic guides produced by laser ablation. The aim of the approach is that the guides confine the liquid within them so that the most common defects can be prevented. The production of guides through laser ablation followed by LIFT of ink inside them has proved that it is possible to find conditions in which the total confinement of liquid within the guides is achieved with good uniformity all along the line. This proves the feasibility of the proposed approach for printing continuous lines free from scalloping and bulging with excellent definition.

© 2015 Elsevier B.V. All rights reserved.

### 1. Introduction

Laser induced forward transfer (LIFT) is a direct writing technique which has been shown to be capable of printing a wide variety of materials. Though LIFT was originally applied to transfer materials from thin solid films [1,2], it was later demonstrated that the technique also allowed the transfer of materials in the liquid phase [3,4]. In fact, the LIFT of liquids operates in a similar way to inkjet printing: the material of interest is dissolved or dispersed as an ink, the ink is transferred, and following solvent removal the material remains adhered to the substrate as a pixel [5]. LIFT presents, however, remarkable advantages over inkjet printing. On one hand, it is free from clogging issues, since there is no need for a nozzle in order to print the liquid and the good spatial resolution of the technique is provided by the high focusing power of the laser beam. On the other hand, LIFT allows the user to work with a substantially broader range of inks, with few limitations concerning the viscosity or rheology of the liquid to be printed.

The principle of operation of LIFT has been described in detail previously [5]. Briefly, a pulsed laser beam is focused on a thin film of the donor ink, which itself is coated upon a substrate transparent to the laser radiation, the donor substrate. Under the action of a laser pulse, a tiny fraction of liquid is transferred from the donor ink film to the acceptor substrate, usually placed at a short distance from the donor one (between tens of microns to few millimeters). Typically, the printing outcome of a single laser pulse is a circular droplet, the size of which depends on the focusing conditions, laser pulse energy and the wetting properties of the acceptor substrate [6–9]. Using LIFT, a diverse range of materials including inorganic inks, polymers, biomolecules and living cells have been successfully printed [10–16].

The mechanisms of liquid ejection and droplet formation during LIFT have been investigated in detail [6–9,17–19] with the aim of optimizing the performance of the printing technique. The realization of patterns with geometries more complex than simple droplet arrays raise challenges greater than those associated with single droplet formation. When printing lines, for example, factors such as droplet coalescence and capillary flow within the printed line play an essential role in determining the printed line stability [20]. In practice, the formation of stable and continuous lines free from defects like scalloping or bulging is not a trivial task [20–24]. This is true not only for LIFT, but for other commonly employed

\* Corresponding author at: Universitat de Barcelona, Departament de Física Aplicada i Òptica, Martí i Franquès 1, E-08028 Barcelona, Spain. Tel.: +34 934 039 216; fax: +34 934 021 139.

E-mail address: [pserra@ub.edu](mailto:pserra@ub.edu) (P. Serra).

printing techniques such as inkjet printing [25]. In a previous work [26] we proposed a printing procedure for conductive inks which mitigated a number of the problems. However, the proposed method was time consuming and the resulting degree of definition was not as good as desired, with some residual scalloping remaining.

In this work, we present an alternative approach for printing which achieves continuous lines free from bulging and scalloping in a very reproducible and controlled way. The technique consists of printing conductive inks through LIFT inside previously patterned laser ablated fluidic guides. The obtained results demonstrate excellent definition and uniformity. Furthermore, and in spite that the feasibility of the approach is demonstrated for a silver conductive ink, it can be easily extrapolated to liquids of very different nature.

## 2. Experimental setup

The experiments were performed using an Amplitude Systems Yb:KYW laser with a wavelength of 1027 nm, a pulse duration of 450 fs and a Gaussian beam intensity profile. A microscope objective of 50 $\times$  with a working distance of 13 mm and a numerical aperture of 0.55 was used to focus the laser radiation onto the sample. A CCD camera placed coaxial to the laser beam axis allowed controlling the position of the laser beam focus on the sample. Glass substrates coated with a 1  $\mu$ m thick hydrophobic cross-linked polymer layer were used as acceptor substrates. The polymer layer was selectively removed through laser ablation in order to generate the fluidic guides and these were later filled with printed ink through LIFT. In order to achieve a good confinement of the ink inside the guides it was necessary that the polymer were substantially more hydrophobic than the glass substrate. The hydrophobicity of the polymer was achieved through the use of a fluorosurfactant additive. This combination of polymer layer/glass was chosen for convenience (the aim of the work is to prove the feasibility of the proposed printing approach), but it is anticipated that a wide range of other combinations would be possible, provided that both layer and substrate have a sufficient difference in surface energy.

The fluidic guides were produced by laser ablation using a pulse energy of 75 nJ and laser spots with a diameter of 2  $\mu$ m, which corresponded to a laser fluence of about 2.4 J/cm<sup>2</sup>. The production of a single fluidic guide was achieved by scanning the surface of the acceptor substrate at a speed of 1 mm/s and a laser repetition rate of 2 kHz. This resulted in a shift of 0.5  $\mu$ m between consecutive overlapping laser spots. The generated debris during the laser ablation process was removed by using an air flow over the treated area.

Once the fluidic guides were produced the ink was deposited into the channels by means of LIFT. The laser pulse energy during printing was 600 nJ and the laser spot diameter 12  $\mu$ m (a laser spot diameter larger than that used in the production of the fluidic guides was achieved by changing the distance between the objective and the sample); this resulted in a laser fluence of 530 mJ/cm<sup>2</sup>. In these conditions the printed droplet diameter on the glass substrate was about 180  $\mu$ m. In spite that much smaller diameters can be obtained through conventional LIFT [27], the printing conditions required to achieve such small droplets are very sensitive to non-uniformities in the thickness of the donor film. Since the purpose of this work is to prove the feasibility of the proposed approach and not yet to optimize its resolution, we chose to work in the most favorable conditions for the test: printing relatively large droplets, which does not compromise the reproducibility of the printing process.

A commercially available Ag nanoparticle ink from Sigma–Aldrich<sup>®</sup> was used in all the LIFT experiments. The particle size was smaller than 50 nm and the solid content was

around 30–35%. The donor films were prepared by blade coating thin layers of ink with a thickness between 20 and 30  $\mu$ m on glass microscope slides. The gap between the donor and acceptor substrates (160  $\mu$ m) was maintained through the use of cover slips as spacers. Although it is common that LIFT experiments use a sacrificial absorbing layer, in the presented experiments this was not needed because the Ag ink itself absorbs the laser radiation at this wavelength. The printed lines, once dried, were laser cured by means of a CW Nd:YAG laser (Baasel LBI 6000, 1064 nm wavelength, 1.2 W output power and a Gaussian intensity profile) operating at a scan speed of 2 mm/s with an irradiance of about 12 kW/cm<sup>2</sup>. At the end of the process the conductivity of the lines was measured and compared with the expected value for the ink.

## 3. Results and discussion

The common printing procedure for the generation of lines consists in depositing consecutive overlapping droplets. Fig. 1 displays the outcome of such an experiment corresponding to silver ink printed on a glass substrate. In that experiment different overlaps were tested with the aim of finding the conditions leading to the formation of stable continuous lines free from defects. The shifts between adjacent droplets ( $\Delta x$ ) in Fig. 1 corresponded to the center to center distance and ranged from 160 to 25  $\mu$ m. The first two shifts ( $\Delta x = 160$  and 120  $\mu$ m) result in non-overlapping droplets with diameters around 80  $\mu$ m. When the shift becomes equal or smaller than the droplet diameter ( $\Delta x \leq 80$   $\mu$ m), the droplets coalesce, resulting first in dashed lines ( $\Delta x = 80$ –72  $\mu$ m) and for even smaller shifts ( $\Delta x \leq 56$   $\mu$ m) continuous lines. However, in these last cases bulges are always present, mostly at the beginning of the line and occasionally in the middle. This defect can be highly detrimental in electronic circuits since it can easily lead to unwanted short-circuits between adjacent lines. It is clear, therefore, that the objective is not fulfilled: no continuous lines free from defects are obtained in such a straightforward way.

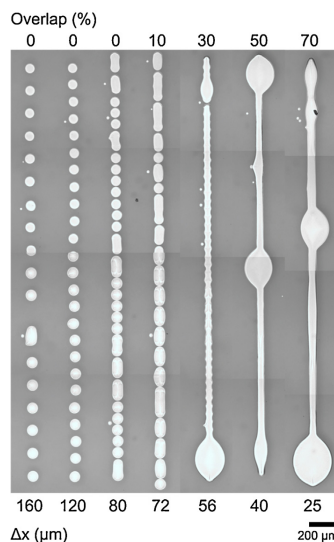
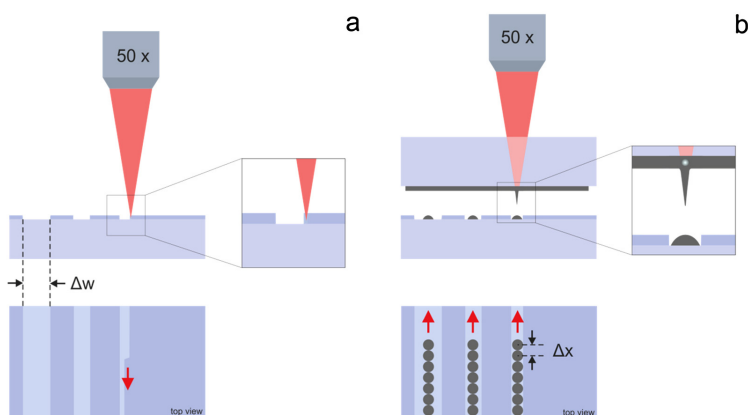


Fig. 1. Optical microscopy image of lines printed with different shifts between adjacent droplets ( $\Delta x$ , measured from center to center) decreasing from left to right.



**Fig. 2.** Sketch of the procedure used for the a) laser ablation of the fluidic guides with different widths ( $\Delta w$ ) and b) LIFT of the Ag ink inside the fluidic guides using different printing shifts between adjacent droplets ( $\Delta x$ , measured from center to center).

In a previous work [26], we proposed a printing strategy which allowed overcoming bulging and which consisted in the alternate deposition of both odd and even droplets with an intermediate drying step between them. The strategy proved successful because the dried pixels helped confining the newly deposited liquid; this spread along the adjacent dry pixels, which pinned the contact line. Unfortunately, that procedure was fairly inefficient (the drying step was time consuming) and the final result was not so good; in spite that the printed lines were free from bulging, they presented a scalloped morphology which hindered the definition of the printing outcome. Notwithstanding, the strategy provided an idea for a more efficient and flexible approach: printing ink on previously defined fluidic guides. Since bulging is a problem of liquid overflow beyond the parallel edges of the printed line due to the onset of an instability driven by capillary flow, the presence of the guide should help to confine the liquid and thus prevent the formation of bulges.

The new printing approach consists in a two-step process, as described in the Section 1. First, the fabrication of the fluidic guides through the selective laser ablation of the polymer layer coating the glass substrate (Fig. 2a). Second, the LIFT of ink inside the fluidic guides (Fig. 2b). The use of the polymer coating has advantages over the direct ablation of glass. On one hand, the removal of the polymer layer requires substantially lower fluences than those needed for the direct ablation of glass: if the laser beam is focused at the polymer–glass interface it is possible to detach the polymer coating

at a low enough fluence that does not damage the glass underneath. On the other hand, and as a consequence of that, a much cleaner ablation can be obtained: as it is observed in Fig. 3, the bottom of the crater is flat and its walls sharp and straight (the extremely small scalloping present in the edges is due to the  $0.5 \mu\text{m}$  shift between adjacent laser spots). Similar sharp edge profiles have been reported during laser ablation of PMMA on glass [28]. Since the polymer is transparent to most conventional laser radiations, femtosecond laser pulses are especially convenient here. If tightly focused, they are absorbed by essentially any material, and for that reason they can be also used for LIFT. Consequently both steps, ablation and printing, were carried out with the same laser system.

Once the fluidic guides were created, printing was carried out inside the channels. The results of a first experiment are shown in Fig. 4. In this case, fluidic guides with different widths were prepared, ranging from  $60 \mu\text{m}$  up to  $200 \mu\text{m}$ , and the shift between adjacent droplets ( $\Delta x$ ) was kept constant at  $160 \mu\text{m}$ . Initially the approach seemed promising: in three out of five widths ( $100$ ,  $80$  and  $60 \mu\text{m}$ ) continuous lines free from bulging were obtained. In all those cases the liquid covers uniformly the guide and is quite well confined within. The three lines were substantially narrower than the diameter of each individual droplet ( $\sim 180 \mu\text{m}$ ), which clearly indicates that the guiding effect is successful. However, the confinement of the ink was not totally accomplished. Indeed, there was some overflow beyond the borders of the guides. The overflow extent was surprisingly similar in the three guides, despite that

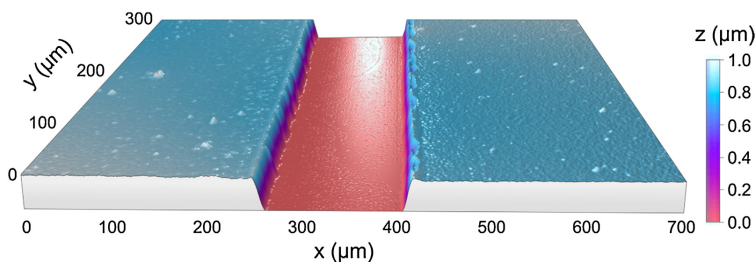


**Fig. 3.** Laser ablated fluidic guide on the acceptor substrate. The clean ablation of the  $1.0 \mu\text{m}$  thick polymer layer, which leaves the underneath glass unaltered, can be observed. The width of the guide is about  $150 \mu\text{m}$ .

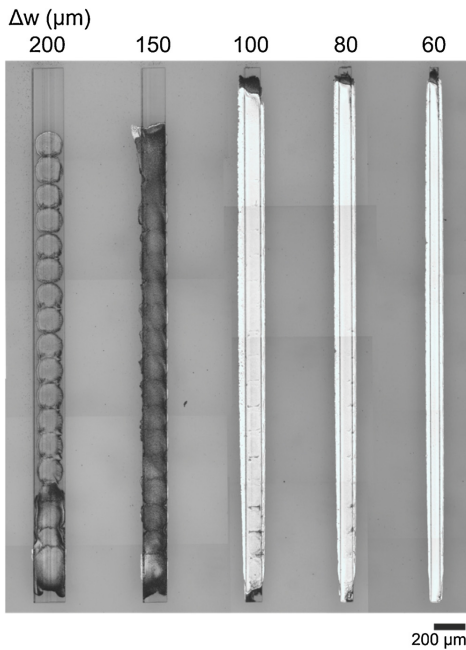


**Fig. 4.** Conductive lines generated by printing Ag ink through LIFT inside fluidic guides of different width ( $\Delta w$ ). The shift between consecutive droplets (measured from center to center) is  $160 \mu\text{m}$ .

they had different sizes and that the amount of ink was always the same. It could be expected to find the largest amount of overflow in the narrowest guides, which could not eventually contain the excess of liquid. However, in view of these results it is reasonable to assume that the overflow was not due to excess of liquid. It can be attributed to ink crawling along the polymer walls, which became hydrophilic during the ablation process (induced roughness and/or composition change). A close inspection of the borders of non-printed guides revealed the presence of some debris resulting from re-deposition of polymer ablation products. Thus, the crawling ink would then overflow beyond the edge of the guides until it meets the clean hydrophobic polymer (the debris border), which would pin the contact line of the liquid.

With the aim of achieving a better confinement of the ink within the guides, and assuming that the observed overflow is indeed due to the presence of debris, an air flow that removed the ablation products was implemented in the experimental setup. A new experiment of printing inside guides which had been ablated with the air flow on was then carried out. This time, however, instead of producing guides of different width and printing droplets at constant shift between them, the procedure was reversed: droplets separated by shifts ranging from  $240$  to  $60 \mu\text{m}$  were printed inside  $200 \mu\text{m}$  wide guides (Fig. 5a). At a distance  $\Delta x = 240 \mu\text{m}$  separated droplets were obtained, since their diameter is of about  $180 \mu\text{m}$  and there is no overlap. As the distance was decreased, the printed droplets started to coalesce, but no continuous line was generated until the distance was reduced to  $80 \mu\text{m}$ . It is observed, though, that at this distance the line is not covered uniformly, probably due to an insufficient volume of liquid, and some overflow occurred in a

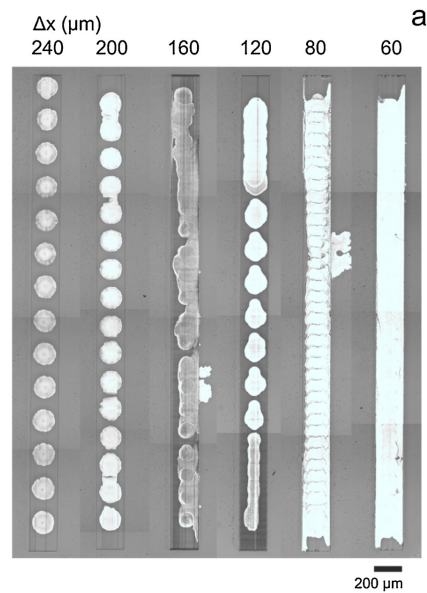


**Fig. 5.** a) Conductive lines generated by printing Ag ink through LIFT at different shifts between consecutive droplets (measured from center to center) inside fluidic guides with a constant width of  $200 \mu\text{m}$ . b) Pattern consisting in two long and connected straight lines forming an angle of  $90^\circ$  generated through LIFT of Ag ink inside previously ablated fluidic guides of  $200 \mu\text{m}$  width.

localized point, where in spite of the air flow some debris were possibly deposited. Nevertheless, a further reduction of the distance between droplets to  $60 \mu\text{m}$  finally allowed fulfilling the objective: the formation of a continuous line uniformly covered with ink perfectly confined within the guide. In fact the definition is excellent, with no bulging, scalloping or overflow at all, which proves the feasibility of the proposed approach.

Some additional discussion is required at this point. The printed lines presented in this work are substantially wider than the minimum features which can be attained through conventional LIFT [27]. The reasons for this have already been pointed out in Experimental, and according to them it is clear that the objective of the work has been fulfilled. Nevertheless, it is obvious that it would be desirable that the new approach presented resolutions close to those attainable with the conventional method. In this regard it must be stated that there is no limitation inherent to the presented approach that hinders that aim. On one hand, it is possible to print droplets through LIFT with minimum diameters close to  $10\ \mu\text{m}$ , and on the other, fluidic guides with similar widths can be easily produced through laser ablation. Therefore, it can be expected that ultimate resolutions about  $10\ \mu\text{m}$  could be achieved with the proposed approach.

As a demanding test of the degree of control and definition of the approach of LIFT printing inside fluidic guides, we proposed the realization of a challenging pattern: two long and connected straight lines forming an angle of  $90^\circ$ . The obtained result is presented in Fig. 5b. It can be observed that the finishing quality of the pattern is very high, with the most common printing defects eliminated completely: the lines have almost perfectly straight edges and the  $90^\circ$  angle shows a definition impossible to achieve without the guides, through the direct printing of overlapping droplets on glass. In spite of the length of the angle sides (about 3 mm), the liquid confinement within the guides is practically total. Only a few tiny overflow features are perceptible in the lower edge of the horizontal side, again possibly due to debris which had not been completely eliminated during the ablation step by the air flow. In any case, this realization constitutes a clear proof that the approach

of LIFT printing inside laser ablated fluidic guides allows generating complex patterns with an unprecedented degree of control and definition.

As a final test, the feasibility of the produced lines to work as interconnects in electrical circuits was proved. To that end, a pattern consisting in two  $2 \times 3\ \text{mm}$  rectangular pads connected by a  $200\ \mu\text{m}$  wide line was produced by laser ablation and finally it was filled with conductive ink through LIFT. With the two pads serving as contacts, this pattern should allow measurement of the electrical resistance of the line. After a drying time, the pattern was laser cured to improve the conductivity of the silver ink. Fig. 6a shows an image of optical microscopy of the final pattern after curing, where it can be observed that the fluidic guides again confine the liquid within their boundary without significant overflowing. With the purpose of measuring the ink level inside the fluidic guide, confocal images of the connecting line were acquired, as shown in Fig. 6b. The ink covers around 85% of the ablated volume with good uniformity along the line and has a mainly constant thickness. Finally, the conductivity was measured, resulting in a value of  $10.1 \times 10^6\ \text{S/m}$ , very close to the nominal value provided by the supplier after curing in an oven ( $9.1 \times 10^6\ \text{S/m}$ ). This indicates that the approach of LIFT printing inside laser ablated fluidic guides is suitable for the production of high definition conductive patterns.

#### 4. Conclusion

The presented approach of depositing conductive ink through LIFT inside laser ablated fluidic guides has proved feasible for printing stable and continuous lines with excellent definition and control. For a given fluidic guide width there is a range of overlaps between consecutively printed droplets that results in the perfect confinement of the ink inside the guide; the most typical defects in line printing, such as scalloping and bulging, are totally eliminated. The successful application of the described approach to the realization of such a challenging pattern as two long and connected straight lines forming an angle of  $90^\circ$  has revealed the potential of the method for the production of patterns with complex geometries with an unprecedented degree of definition. Finally, laser curing of the printed lines has demonstrated that their conductivity can be increased to values similar to those attainable through curing in an oven. This demonstrates the potential of these printed patterns as interconnects in electronic circuits.

#### Acknowledgments

This work is funded by project DigiPRINT (RDNET12-2-0002, FP7 ERA-NET OLAE+), by MINECO of the Spanish Government (Project TEC2014-54544-C2-1-P) and also by Fondo Europeo de Desarrollo Regional (FEDER).

#### References

- [1] M.L. Levene, R.D. Scott, B.W. Siry, Material transfer recording, *Appl. Opt.* 9 (1970) 2260–2265.
- [2] J. Bohandy, B.F. Kim, F.J. Adrian, Metal deposition from a supported metal film using an excimer laser, *J. Appl. Phys.* 60 (1986) 1538–1539.
- [3] A. Piqué, J. Fritz-Gerald, D.B. Chrisey, R.C.Y. Auyeung, H. Wu, S. Lakeou, R.A. McGill, Direct writing of electronic materials using a new laser assisted transfer/annealing technique, *Laser Appl. Microelectron. Optoelectron. Manuf. V* (2000) 105–112.
- [4] A. Piqué, D.B. Chrisey, J.M. Fitz-Gerald, R.A. McGill, R.C.Y. Auyeung, H.D. Wu, S. Lakeou, V. Nguyen, R. Chung, M. Duignan, Direct writing of electronic and sensor materials using a laser transfer technique, *J. Mater. Res.* 15 (2000) 1872–1875.
- [5] C.B. Arnold, P. Serra, A. Piqué, Laser direct-write techniques for printing of complex materials, *MRS Bull.* 32 (2007) 23–31.
- [6] M. Colina, M. Duocastella, J.M. Fernández-Pradas, P. Serra, J.L. Morenza, Laser-induced forward transfer of liquids: Study of the droplet ejection process, *J. Appl. Phys.* 99 (2006) 084909.

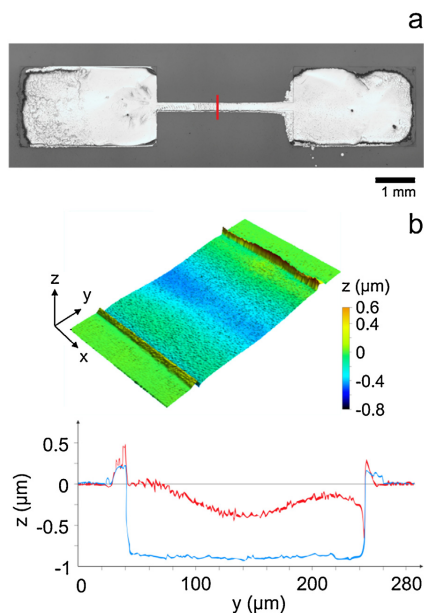


**Fig. 6.** a) Pattern consisting in two  $2 \times 3\ \text{mm}$  rectangular pads connected by a  $200\ \mu\text{m}$  wide line produced by laser ablation and subsequently filled with Ag ink printed through LIFT. b) Confocal microscopy image and transverse profile of the line indicating the correct filling of the guide with the Ag ink.

- [7] P. Serra, M. Duocastella, J.M. Fernández-Pradas, J.L. Morenza, Liquids microprinting through laser-induced forward transfer, *Appl. Surf. Sci.* 255 (2009) 5342–5345.
- [8] M. Duocastella, A. Patrascioiu, V. Dinca, J.M. Fernández-Pradas, J.L. Morenza, P. Serra, Study of liquid deposition during laser printing of liquids, *Appl. Surf. Sci.* 257 (2011) 5255–5258.
- [9] M. Duocastella, A. Patrascioiu, J.M. Fernández-Pradas, J.L. Morenza, P. Serra, On the correlation between droplet volume and irradiation conditions in the laser forward transfer of liquids, *Appl. Phys. A. Mater. Sci. Process.* 109 (2012) 5–14.
- [10] M. Colina, P. Serra, J.M. Fernández-Pradas, L. Sevilla, J.L. Morenza, DNA deposition through laser induced forward transfer, *Biosens. Bioelectron.* 20 (2005) 1638–1642.
- [11] N.T. Kattamis, P.E. Purnick, R. Weiss, C.B. Arnold, Thick film laser induced forward transfer for deposition of thermally and mechanically sensitive materials, *Appl. Phys. Lett.* 91 (2007) 171120.
- [12] C. Boutopoulos, V. Tsouti, D. Goustouridis, S. Chatzandroulis, I. Zergioti, Liquid phase direct laser printing of polymers for chemical sensing applications, *Appl. Phys. Lett.* 93 (2008) 191109.
- [13] L. Rapp, A.K. Diallo, A.P. Alloncle, C. Vidélot-Ackermann, F. Fages, P. Delaporte, Pulsed-laser printing of organic thin-film transistors, *Appl. Phys. Lett.* 95 (2009) 171109.
- [14] D. Cannatà, M. Benetti, F. Di Pietrantonio, E. Verona, A. Palla-Papavlu, V. Dinca, M. Dinescu, T. Lippert, Nerve agent simulant detection by solidly mounted resonators (SMRs) polymer coated using laser induced forward transfer (LIFT) technique, *Sens. Actuators B Chem.* 173 (2012) 32–39.
- [15] M. Duocastella, H. Kim, P. Serra, A. Piqué, Optimization of laser printing of nanoparticle suspensions for microelectronic applications, *Appl. Phys. A. Mater. Sci. Process.* 106 (2012) 471–478.
- [16] A. Palla-Papavlu, A. Patrascioiu, F. Di Pietrantonio, J.M. Fernández-Pradas, D. Cannatà, M. Benetti, S. D'Auria, E. Verona, P. Serra, Preparation of surface acoustic wave odor sensors by laser-induced forward transfer, *Sens. Actuators B Chem.* 192 (2014) 369–377.
- [17] M. Duocastella, J.M. Fernández-Pradas, J.L. Morenza, P. Serra, Time-resolved imaging of the laser forward transfer of liquids, *J. Appl. Phys.* 106 (2009) 084907.
- [18] A. Patrascioiu, J.M. Fernández-Pradas, A. Palla-Papavlu, J.L. Morenza, P. Serra, Laser-generated liquid microjets: correlation between bubble dynamics and liquid ejection, *Microfluid. Nanofluidics* 16 (2014) 55–63.
- [19] S.A. Mathews, R.C.Y. Auyeung, H. Kim, N.A. Charipar, A. Piqué, High-speed video study of laser-induced forward transfer of silver nano-suspensions, *J. Appl. Phys.* 114 (2013) 064910.
- [20] A. Palla-Papavlu, C. Córdoba, A. Patrascioiu, J.M. Fernández-Pradas, J.L. Morenza, P. Serra, Deposition and characterization of lines printed through laser-induced forward transfer, *Appl. Phys. A. Mater. Sci. Process.* 110 (2013) 751–755.
- [21] H. Kim, R.C.Y. Auyeung, S.H. Lee, A.L. Huston, A. Piqué, Laser forward transfer of silver electrodes for organic thin-film transistors, *Appl. Phys. A. Mater. Sci. Process.* 96 (2009) 441–445.
- [22] J.A. Grant-Jacob, B. Mills, M. Feinaeugle, C.L. Sones, G. Oosterhuis, M.B. Hoppenbrouwers, R.W. Eason, Micron-scale copper wires printed using femtosecond laser-induced forward transfer with automated donor replenishment, *Opt. Mater. Express.* 3 (2013) 747–754.
- [23] L. Rapp, J. Alluno, A.P. Alloncle, P. Delaporte, Pulsed-laser printing of silver nanoparticles ink: control of morphological properties, *Opt. Express.* 19 (2011) 21563–21574.
- [24] E. Biver, L. Rapp, A.P. Alloncle, P. Delaporte, Multi-jets formation using laser forward transfer, *Appl. Surf. Sci.* 302 (2014) 153–158.
- [25] P.C. Duineveld, The stability of ink-jet printed lines of liquid with zero receding contact angle on a homogeneous substrate, *J. Fluid Mech.* 477 (2003) 175–200.
- [26] C. Florian, F. Caballero-Lucas, J.M. Fernández-Pradas, R. Artigas, S. Ogier, D. Karnakis, P. Serra, Conductive silver ink printing through the laser-induced forward transfer technique, *Appl. Surf. Sci.* 336 (2015) 304–308.
- [27] M. Duocastella, M. Colina, J.M. Fernández-Pradas, P. Serra, J. Morenza, Study of the laser-induced forward transfer of liquids for laser bioprinting, *Appl. Surf. Sci.* 253 (2007) 7855–7859.
- [28] D.A. Higgins, T.A. Everett, A. Xie, S.M. Forman, T. Ito, High-resolution direct-write multiphoton photolithography in poly(methylmethacrylate) films, *Appl. Phys. Lett.* 88 (2006) 184101.

# Resum en Català

La fabricació digital de dispositius tecnològics requereix el desenvolupament de noves i millors tècniques per al microprocessament de materials que siguin al mateix temps compatibles amb mètodes de producció en sèrie a gran escala com el *roll-to-roll processing*. Aquestes tècniques han de complir certs requisits relacionats amb la possibilitat d'implementar canvis de disseny ràpids durant el procés de fabricació, l'alta velocitat de processament, i al mateix temps permetre la producció de motius de forma controlada amb altes resolucions espacials.

Els làsers són eines versàtils que compleixen els requisits de compatibilitat, velocitat i resolució espacial necessaris per a la fabricació digital. Actualment, aquests dispositius es troben presents en diferents àrees com la indústria, la medicina, les telecomunicacions i la investigació científica, entre d'altres. A causa de les propietats de la radiació làser, com l'alta monocromaticitat i direccionalitat, és possible la generació d'altres intensitats en volums molt petits, el que els fa una eina ideal per a la microfabricació de materials. En general, el microprocessament de materials amb làser es pot dur a terme de dues formes: substractiva i additiva. La primera consisteix a irradiar un determinat material amb radiació làser prou enfocada com per promoure l'ablació selectiva de l'àrea irradiada. La segona permet la transferència de petites quantitats del material d'interès sobre una gran varietat de substrats.

L'ablació amb làser és una de les tècniques de processament de materials més esteses. El seu principi d'operació consisteix en la vaporització d'una petita fracció de material just a l'àrea irradiada, produint modificacions permanents en el material. Degut a que la difusió tèrmica afecta considerablement la resolució espacial de les modificacions produïdes, en molts casos és necessari l'ús de làsers polsats amb durada d'impuls molt curta, idealment inferior als picosegons, fet que redueix dràsticament els efectes tèrmics. En aquestes condicions és possible fins i tot el processament de materials transparents a la longitud d'ona del làser. No obstant això, el processament d'aquests materials en superfície planteja nous reptes, ja que



el resultat final és extremadament sensible a la focalització del làser: lleugers canvis en la posició relativa de la mostra respecte a la cintura del feix poden produir danys no desitjats dins del material o fins i tot no generar cap modificació. Per tant, cal desenvolupar nous mètodes de focalització del feix sobre la mostra de forma controlada.

Entre les tècniques de dipòsit de materials amb làser destaca la transferència induïda per làser LIFT (per les sigles en anglès *laser-induced forward transfer*) que consisteix en la transferència de petites quantitats de material a partir d'una capa fina donadora sobre una gran varietat de substrats sota l'acció d'un impuls làser. Aquesta tècnica permet la producció de motius amb alta resolució espacial utilitzant materials funcionals, inclosos materials tan sensibles com ara proteïnes o cèl·lules. Malgrat que la tècnica LIFT ha estat àmpliament estudiada en els últims anys, hi ha encara reptes importants, com l'anàlisi de la impressió de líquids a alta velocitat o la fabricació de línies contínues amb gran resolució espacial.

D'aquesta manera, en la present tesi es proposen i implementen solucions viables a alguns dels reptes relacionats amb la microfabricació amb làser tant substractiva com additiva. D'una banda, es presenten estudis d'ablació amb mostres d'un material transparent per a la caracterització d'un mètode d'enfocament que permet posicionar la mostra amb alta precisió en posicions properes a la cintura del feix. D'aquesta manera s'aconsegueixen obtenir resolucions espacials que superen el límit de difracció a la superfície de la mostra. D'altra banda, es presenten experiments d'impressió que emulen el dipòsit de líquids a alta velocitat i permeten estudiar-ne la dinàmica subjacent mitjançant la caracterització dels píxels produïts sobre el substrat receptor i del procés d'impressió utilitzant un sistema d'adquisició ràpida d'imatges. A més, es presenten estratègies d'impressió de tintes conductores amb l'objectiu de produir línies contínues amb alta qualitat d'impressió. Finalment, s'inclouen dues propostes que són producte de la combinació de les dues tècniques, la impressió de líquids i l'ablació amb làser.

Aquesta tesi s'ha desenvolupat com un compendi de 10 articles dels quals 9 han estat publicats en diferents revistes científiques internacionals. Els resultats de la tesi s'han resumit i organitzat en capítols tal com es presenten a continuació:

## Tècniques subtractives

En aquest capítol s'inclouen els resultats d'estudis d'ablació utilitzant mostres de polimetil-metacrilat (PMMA) fent servir un làser polsat de femtosegons. L'objectiu és trobar les millors condicions per produir controladament l'ablació superficial amb alta resolució espacial utilitzant una longitud d'ona per a la qual el material és transparent. Per aconseguir-ho, s'ha desenvolupat un mètode que permet posicionar la mostra amb un alt grau de precisió en posicions properes a la cintura del feix. El mètode proposat té el mateix principi que el procediment experimental per mesurar el coeficient de refracció no lineal d'un material, conegut com a 'z-scan': l'energia transmesa es registra en un detector mentre la mostra es desplaça al llarg de l'eix de propagació de la radiació làser cap a la cintura del feix. Quan la densitat d'energia a la mostra és prou alta, l'energia és absorbida, per tant la corba de transmissió presenta una disminució dràstica quan la cintura del feix làser es troba just sobre la superfície de la mostra.

Els primers estudis es van centrar en el desenvolupament de la tècnica. En primer lloc es va avaluar com variava la transmissió durant l'aproximació de la superfície a la posició de la cintura del feix. A continuació es van realitzar experiments d'ablació per diferents posicions i amb diferents energies incidents sobre la superfície de la mostra, obtenint cràters dels quals les mides depenen de la posició al llarg de l'eix del feix i de l'energia emprada per a produir-los. De la caracterització morfològica dels cràters produïts es va poder concloure que la millor posició per controlar la posició de la mostra corresponia a les posicions intermèdies dins de la corba de transmissió. A més, les mesures de les mides dels cràters produïts indicaven que la cintura del feix es trobava en aquestes posicions. També, es va descobrir que en fer un rastreig en el pla de la mostra i coneixent la corba de transmissió és possible detectar canvis en la inclinació de la mostra respecte al pla focal, fet que resulta d'especial interès per a la producció de modificacions superficials en àrees grans.

En estudis posteriors es va refinar la tècnica del z-scan per tal d'optimitzar la resolució espacial que es pot obtenir. La simulació de la mida del feix al llarg de la direcció de propagació va permetre trobar d'una banda la relació entre la densitat d'energia a la superfície i els cràters produïts, i de l'altra, va permetre determinar amb precisió la posició de la cintura del feix dins de la corba de transmissió. Les

dades calculades teòricament presenten una bona correlació amb els resultats obtinguts experimentalment per a les posicions en que la cintura del feix es troba fora del material. Un cop la cintura del feix està situada a l'interior, les dades obtingudes teòricament es desvien lleugerament de les experimentals. Un estudi de la secció transversal dels cràters en profunditat mitjançant un feix d'ions focalitzats FIB (per les seves sigles en anglès *focused ion beam*) va confirmar la presència d'estructures poroses per sota de la superfície.

D'altra banda, es va proposar una millora addicional al mètode del z-scan en incorporar un detector extra en el muntatge experimental dedicat a registrar els canvis en l'energia reflectida per la mostra en les diferents posicions al llarg del feix làser. Aquestes mesures van permetre incrementar el control en la posició de la mostra. D'aquesta manera, va ser possible la realització de línies contínues en la seva superfície obtenint resolucions micromètriques de gran definició.

## Tècniques additives

El primer estudi correspon a la transferència de líquids mitjançant LIFT emulant la impressió a alta velocitat. El segon i tercer estudis corresponen a dues aplicacions diferents per a la impressió de líquids funcionals: una per a la impressió de línies conductores lliures de defectes d'impressió i l'altra per a la creació de microlents d'alta precisió. L'empresa Suïssa DI Projekt AG va desenvolupar una impressora industrial basada en la tècnica LIFT per a la impressió d'embolcalls en la indústria alimentària a freqüències de repetició de desenes de MHz, obtenint rendiments sense precedents de 1,3 m<sup>2</sup>/min amb 600 dpi de resolució. Un dels problemes presents en condicions d'impressió a freqüències de repetició tan altes va ser la distorsió i coalescència de píxels adjacents a distàncies de separació on el motiu esperat eren píxels separats, possiblement a causa de la interacció entre jets de líquid adjacents emesos per impulsos làser consecutius. Per trobar una solució al problema es va proposar analitzar la dinàmica d'ejecció de líquid en condicions similars. Així, es va estudiar la dinàmica d'interacció entre els jets de líquid ejectats per dos impulsos làser simultanis i adjacents (a tan elevades freqüències de repetició dos impulsos consecutius són pràcticament simultanis).

Per analitzar la dinàmica d'impressió es va realitzar un estudi d'adquisició ràpi-

da d'imatges per a spots làser simultanis generats a diferents distàncies de separació entre ells. Els resultats es van correlacionar amb les impressions obtingudes en condicions idèntiques. L'estudi va demostrar l'aparició d'una dinàmica d'emissió de líquid no reportada fins llavors, que en aquest cas era deguda a la interacció entre jets adjacents, i que tenia lloc precisament per a aquelles distàncies de separació per a les quals s'obtenia un únic píxel distorsionat on s'esperava la impressió de dos píxels circulars separats. Aquesta nova dinàmica posa de manifest l'existència d'efectes inesperats durant la impressió a alta velocitat, els quals s'han de tenir en compte en el disseny dels dispositius d'impressió, ja que poden repercutir negativament en la qualitat del resultat final.

Pel que fa a la impressió de línies conductores, es van proposar diferents alternatives d'impressió amb l'objectiu d'eliminar els defectes més comuns: discontinuïtats i 'bulging' (eixamplament espontani i no desitjat de la línia a causa del flux capil·lar al llarg d'aquesta). L'estratègia més simple correspon a la impressió seqüencial de píxels a diferents distàncies de separació; d'aquesta manera, quan la separació és inferior al diàmetre del píxel imprès, aquests s'ajunten donant lloc a la formació de línies contínues. No obstant això, tant aviat com una línia contínua es produeix, apareixen regions amb 'bulging', cosa que afecta no només la qualitat de la impressió, sinó també la seva funcionalitat ja que dues línies adjacents poden produir un curtcircuit a causa del contacte no desitjat entre elles.

Un estudi per caracteritzar la formació del 'bulge' va consistir en la impressió de diferent quantitat de gotes de tinta en ordre creixent. Els resultats van mostrar que la formació del 'bulge' passa des del principi de la impressió, fet que va suggerir la segona estratègia: la impressió alternada de píxels (primer els parells, després els imparells) amb un pas d'assecat intermedi. D'aquesta manera, els fluxos capil·lars no desitjats es redueixen, donant lloc a la formació de línies contínues totalment lliures de 'bulging'. Finalment, mesures de la conductivitat de línies produïdes després d'un tractament de sinterització amb làser van presentar valors propers a la conductivitat nominal, el que va demostrar la viabilitat de l'estratègia proposada.

Finalment, es va proposar un mètode basat en la tècnica LIFT per a la impressió d'un polímer altament viscos amb l'objectiu de fabricar microlents d'alta qualitat òptica. L'estratègia va consistir en el dipòsit de microgotes d'un pre-polímer seguit de la seva foto-polimerització induïda amb radiació ultraviolada. Ja que inicial-

ment el material dipositat és líquid, la superfície de la gota formada en el substrat receptor es conserva fins i tot després de la seva polimerització, fet que permet obtenir una lent sòlida de forma hemisfèrica gairebé perfecta. L'estudi, realitzat sobre vidre i PDMS, va permetre la fabricació de microgotes amb diferents angles de contacte segons el material del substrat, fet que es tradueix en diferents obertures numèriques per a les lents. A més, és possible controlar la distància focal de les microlents mitjançant el control de l'energia de l'impuls làser durant el procés d'impressió. Finalment, la qualitat de les microlents produïdes va ser avaluada a partir de la seva morfologia, les seves propietats d'enfocament i la seva funcionalitat per reproduir imatges. Dels resultats obtinguts es pot concloure que la LIFT pot ser utilitzada com una tècnica de fabricació de microlents d'alta qualitat.

## Tècniques mixtes

Les tècniques presentades dins d'aquesta secció són producte de la combinació de l'ablació amb làser i de la impressió de líquids mitjançant LIFT. D'una banda, es presenta una estratègia per millorar la resolució d'un sistema convencional de processament amb làser mitjançant la utilització d'una lent líquida fabricada amb LIFT. D'altra banda, s'utilitza la tècnica d'ablació de materials transparents amb làser per a la creació de guies de microfluídica en les que després s'imprimeix una tinta metàl·lica per a la fabricació de línies conductores amb alta qualitat d'impressió.

La primera proposta mixta utilitza la LIFT per a la impressió de microgotes líquides seguida de l'ablació de la superfície d'un material amb un làser de femtosegons enfocat a través de la gota líquida. En aquesta proposta, mitjançant l'elecció adequada del líquid emprat per a cada substrat receptor és possible generar microgotes hemisfèriques. D'aquesta manera s'incrementa l'obertura numèrica efectiva del sistema de marcat amb làser un factor que correspon exactament a l'índex de refracció del líquid emprat. En realitzar experiments d'ablació utilitzant la gota per enfocar la radiació làser sobre el material d'interès, les mides dels cràters van aconseguir superar el límit de difracció del sistema òptic. A més, en comparar les seves grandàries amb els del procés convencional d'ablació en superfície es va demostrar que l'estratègia proposada permet la producció de cràters nanomètrics utilitzant energies per a les quals el procés convencional d'ablació no presenta alteracions detectables sobre la mostra irradiada. Finalment, es va demostrar la viabilitat de

---

la tècnica proposada per a la producció de motius en dues dimensions amb altes resolucions espacials emprant només una microlent líquida durant el procés de fabricació.

Per últim, es va demostrar que en combinar l'ablació amb làser per a la creació de guies de microfluídica juntament amb la tècnica LIFT és possible fabricar línies conductores amb alta resolució espacial. La fabricació de guies rectangulars de microfluídica es va dur a terme mitjançant l'ablació selectiva d'una capa de polímer dipositada prèviament sobre un substrat de vidre. Les guies es van fabricar amb diferents amplades per avaluar la influència de les seves dimensions en la contenció de la tinta líquida una vegada impresa mitjançant LIFT. Després, es van dur a terme experiments d'impressió de tintes líquides utilitzant diferents distàncies d'impressió entre dos píxels consecutius. La impressió es va realitzar dins de les guies de microfluídica, aconseguint contenir el líquid al seu interior. D'aquesta manera, la tècnica mixta proposada demostra que és possible fabricar línies contínues eliminant per complet els defectes d'impressió més comuns, com el 'bulging' i les ondulacions presents en les vores, amb un nivell de definició fins i tot superior al que es pot obtenir amb l'estratègia presentada a la secció anterior. Així mateix, es va fabricar una estructura de dues guies connectades mitjançant un angle de  $90^\circ$  per contenir tinta líquida en el seu interior. El resultat d'aquest experiment demostra el potencial de l'estratègia proposada per a la creació d'estructures complexes amb qualitats d'impressió sense precedents. Finalment, les mesures de conductivitat de les línies després d'un tractament de sinteritzat amb làser van presentar conductivitats properes al valor nominal.



# Conclusions en Català

Les següents conclusions es poden extreure dels resultats obtinguts al llarg del treball de tesi:

## Tècniques substractives

- La tècnica proposada per l'enfocament denominada z-scan ha demostrat ser un mètode adequat per a la col·locació d'una mostra transparent a prop de la cintura del feix làser. La caracterització del z-scan per diferents posicions en l'eix de propagació del feix permet determinar la posició òptima per produir l'ablació a la superfície d'una mostra transparent de PMMA. Els experiments d'ablació permeten determinar la fluència llindar per a l'ablació en aquest material, així com la cintura del feix làser mínima del sistema òptic emprat.
- La concordança entre les dades experimentals i teòriques, que es van trobar amb simulacions del feix làser mitjançant la teoria de la difracció vectorial, ha permès trobar la posició de la cintura del feix làser en el rang de posicions determinat pel z-scan. Aquest és un paràmetre útil per tenir en compte en el processament de materials transparents en àrees grans i amb alta resolució espacial.
- Un altre resultat d'aquest estudi ha estat la millora en el control de la posició de la mostra en un rang de z més ample mitjançant el registre simultani de l'energia transmesa i reflectida per la mostra durant els experiments d'ablació en superfície. Això permet controlar la inclinació de la mostra en àrees grans, permetent la fabricació de línies contínues i llargues a la superfície d'una mostra transparent. A més, gràcies al bon control de la posició, el mètode d'enfocament z-scan proposat ha permès la producció de modificacions superficials amb dimensions que superen el límit de difracció al llarg de distàncies relativament llargues.



## Tècniques additives

- La transferència de líquid a través de LIFT emulant altes velocitats d'impressió ha revelat la presència d'una interacció significativa entre jets adjacents. Els estudis d'adquisició d'imatges amb resolució temporal (en anglès, *time-resolved imaging study*) han confirmat que aquesta interacció s'origina quan el làser genera bombolles que contacten entre si durant les primeres etapes de la seva expansió. La dinàmica de l'ejecció de líquids resultant de la interacció presenta nous elements, com és el cas de dos jets s'ajunten fins unir-se en un de sol, fet que pot comprometre seriosament la qualitat dels píxels en el cas de velocitats d'impressió elevades.
- És factible imprimir mitjançant LIFT línies conductores funcionals que eliminin els defectes d'impressió més comuns com les discontinuïtats i el 'bulging' mitjançant l'ús d'una estratègia d'impressió que consisteix en la transferència alternada de les gotes (les senars primer i després les parelles) amb una etapa d'assecat intermèdia. Això permet la mitigació dels fluxos capil·lars no desitjats dins les línies impreses que són, en última instància, responsables de la formació del 'bulging'.
- La tècnica LIFT ha demostrat ser efectiva per imprimir volums molt petits d'un polímer altament viscos per a la fabricació de microlents polimèriques amb propietats definides i d'alt grau de precisió. L'estratègia de fabricació proposada consisteix en només dos passos (impressió per LIFT i polimerització amb radiació UV), permetent controlar el diàmetre de les microlents simplement ajustant els paràmetres del làser, i d'aquesta manera és possible controlar la distància focal resultant de les microlents.

## Tècniques mixtes

- La combinació d'un sistema convencional làser d'escriptura directa amb microlents líquides amb geometria hemisfèrica impreses a través de LIFT ha demostrat ser adequada per generar modificacions que superen el límit de difracció en un substrat sòlid. Mitjançant l'ús d'aquesta estratègia, l'obertura numèrica eficaç del sistema òptic s'incrementa en un factor que correspon exactament a l'índex de refracció del líquid emprat. L'impacte potencial de

l'estratègia proposada per a la generació de motius nanomètrics en 2D s'ha demostrat mitjançant la fabricació de patrons geomètrics complexos utilitzant només una microgota durant tot el procés de fabricació.

- La impressió de líquids a través de LIFT dins de guies de fluídica fabricades per ablació làser s'ha fet servir exitosament per a la formació de línies conductores d'alta qualitat lliures dels defectes d'impressió més comuns, especialment el 'bulging' i les ondulacions de les vores. La fabricació de dues línies connectades que formen un angle de  $90^\circ$  demostra el potencial de l'estratègia proposada per a la fabricació de patrons de geometria complexa amb un grau de definició sense precedents.



# Curriculum Vitae



# Camilo Florian Baron

*PhD Candidate*

[\(+34\) 625554657](tel:+34625554657)

[✉ camilofb1@gmail.com](mailto:camilofb1@gmail.com)

[LinkedIn: camiloflorian](#)

## Personal Information

Identification Y1605440P.  
 Passport AS 227906.  
 Date and birthplace 18<sup>th</sup> of March, 1989, Bogotá, Colombia.

## Education

2012-2016 **PhD Student in Nanociencias**, *Universitat de Barcelona, Physics Faculty, Department of Applied Physics*, Barcelona, Spain.

2015 Research Internship: Study of the fabrication of microlenses via laser induced forward transfer. Supervised by Dr. Martí Duocastella, and Dr. Alberto Diaspro. *Istituto Italiano di Tecnologia, NanoPhysics Department*, Genoa, Italy.

- Research Internship: Line printing by laser induced forward transfer: influence of viscosity. Supervised by Dr. Philippe Delaporte and Dr. Daniel Puerto. *CNRS, Aix-Marseille University, Lasers, Plasmas et Procédés Photoniques LP3 Lab*. Marseille, France.

2011-2012 **Master in Physical Engineering**, *Universitat de Barcelona, Physics Faculty, Department of Applied Physics and Optics*, Barcelona, Spain.

Final grade: **8,6/10**.

Thesis work: Study of the ablation of poly-methylmetacrylate with a femtosecond laser.

Advisor: Juan Marcos Fernández Pradas.

2005-2010 **Bachelor in Physics**, *National Pedagogic University, Faculty of Science and Technology, Physics Department*, Bogotá, Colombia.

Final grade: **45/50**.

Thesis work: Analysis of Quantum State Teleportation with educational purposes.

Advisor: José Orlando Organista Rodríguez.

**Beginning university studies two years before the minimum required age.**

## Publications

- [C. Florian](#), S. Piazza, A. Diaspro, P. Serra, M. Duocastella.  
 Direct laser printing of tailored polymeric microlenses.  
 Submitted to: ACS Materials and Interfaces  
 Impact factor JDR 2014: 6.723 - (Q1).

- F. Caballero-Lucas, [C. Florian](#), J.M. Fernández-Pradas, J.L. Morenza, P. Serra.  
[Beam waist position study for surface modification of polymethyl-methacrylate with femtosecond laser pulses.](#)  
Applied Surface Science 374 (2016) 353-358.  
Impact factor JDR 2014: 2.711 - (Q1).
- [C. Florian](#), F. Caballero-Lucas, J.M. Fernández-Pradas, S. Ogier, L. Winchester, D. Karnakis, R. Artigas, P. Serra.  
[Printing of silver conductive lines through laser-induced forward transfer.](#)  
Applied Surface Science 374 (2016) 265-270.  
Impact factor JDR 2014: 2.711 - (Q1).
- M. Duocastella, [C. Florian](#), P. Serra, A. Diaspro.  
[Sub-wavelength laser nanopatterning using droplet lenses.](#)  
Scientific Reports 5 (2015) 16199.  
Impact factor JDR 2014: 5.578 - (Q1).
- [C. Florian](#), F. Caballero-Lucas, J.M. Fernández-Pradas, S. Bosch, J.L. Morenza, P. Serra.  
[Femtosecond laser surface ablation of polymethyl-methacrylate with position control through z-scan.](#)  
Journal of Physics D: Applied Physics, 48 (2015) 335302.  
Impact factor JDR 2014: 2.721 - (Q1).
- [C. Florian](#), F. Caballero-Lucas, J.M. Fernández-Pradas, R. Artigas, S. Ogier, D. Karnakis, P. Serra.  
[Conductive silver ink printing through the laser-induced forward transfer technique.](#)  
Applied Surface Science, 336 (2015) 304-308.  
Impact factor JDR 2014: 2.711 - (Q1).
- F. Caballero-Lucas, [C. Florian](#), J.M. Fernández-Pradas, J.L. Morenza, P. Serra.  
[Precise surface modification of polymethyl-methacrylate with near-infrared femtosecond laser.](#)  
Applied Surface Science, 336 (2015) 170-175.  
Impact factor JDR 2014: 2.711 - (Q1).
- A. Patrascioiu, [C. Florian](#), J.M. Fernández-Pradas, J.L. Morenza, G. Hennig, P. Delaporte, P. Serra.  
[Interaction between jets during laser-induced forward transfer.](#)  
Applied Physics Letters, 105 (2014) 014101.  
Impact factor JDR 2014: 3.302 - (Q1).
- [C. Florian](#), F. Caballero-Lucas, J.M. Fernández-Pradas, J.L. Morenza, P. Serra.  
[Surface ablation of transparent polymers with femtosecond laser pulses.](#)

Applied Surface Science, 302 (2014) 226-230.

Impact factor JDR 2014: 2.711 - (Q1).

- J.M. Fernández-Pradas, C. Florian, F. Caballero-Lucas, J.L. Morenza, P. Serra.  
[Femtosecond laser ablation of polymethyl-methacrylate with high focusing control.](#)  
Applied Surface Science, 278 (2013) 185-189.  
Impact factor JDR 2013: 2.538 - (Q1).

## Scholarships and Recognition

- 2015 Young Scientist Award at the European Materials Research Society (E-MRS) Spring Meeting. Lille, France.
- 2013 Best poster presentation at the 14th International Symposium on Laser Precision Microfabrication (LAMP). Niigata, Japan.
  - Scholarship FI of the Agència de Gestió d'Ajuts Universitaris i de Recerca (AGAUR). Barcelona, Spain.
  - Scholarship AAD for teaching assistantship of the Agència de Gestió d'Ajuts Universitaris i de Recerca (AGAUR). Barcelona, Spain.
- 2012 Best poster presentation at the European Materials Research Society (E-MRS) Spring Meeting. Strasbourg, France.
- 2011 Scholarship APIF of the Universitat de Barcelona. Barcelona, Spain.
- 2008 Honours registration, by academic excellence. Full year. National Pedagogic University. Bogotá, Colombia.

## Conferences, Meetings and Workshops

- 2016 C. Florian, F. Caballero, P. Sopeña, A. Patrascioiu, J. M. Fernández-Pradas, J. L. Morenza, P. Serra.  
Laser-induced forward transfer: propelling liquids with light.  
European Materials Research Society (E-MRS) Spring Meeting, Lille, France.  
Contribution: Oral presentation.
  - F. Caballero-Lucas, C. Florian, J.M. Fernández-Pradas, S. Ogier, L. Winchester, D. Karnakis, R. Geremia, R. Artigas, P. Serra.  
Laser printing in fluidic guides: production of high-resolution conductive lines through capillary flow along the guide  
European Materials Research Society (E-MRS) Spring Meeting, Lille, France.  
Contribution: Póster presentation.
- 2015 P. Serra, A. Patrascioiu, C. Florian, J.M. Fernández-Pradas, J.L. Morenza.  
High-speed laser induced forward transfer of inks.  
The 23th Annual International Conference on Advanced Laser Technologies(ALT15), Faro, Portugal.  
Contribution: Oral presentation.
  - C. Florian, F. Caballero-Lucas, J.M. Fernández-Pradas, S. Ogier, L. Winchester, D. Karnakis, R. Geremia, R. Artigas, P. Serra.  
Printing of silver conductive lines through laser-induced forward transfer.



- European Materials Research Society (E-MRS) Spring Meeting, Lille, France.  
Contribution: Oral presentation. **Young Scientist Award.**
- A. Patrascioiu, C. Florian, J.M. Fernández-Pradas, J.L. Morenza, G. Hening, P. Delaporte P. Serra.  
Interaction between liquid jets in high-speed laser printing.  
European Materials Research Society (E-MRS) Spring Meeting, Lille, France.  
Contribution: Oral presentation.
  - F. Caballero-Lucas, C. Florian, J.M. Fernández-Pradas, J.L. Morenza, P. Serra.  
Control of beam waist position for surface modification of transparent materials with femtosecond laser pulses.  
European Materials Research Society (E-MRS) Spring Meeting, Lille, France.  
Contribution: Poster presentation.
  - D. Karnakis, R. Geremia, L. Winchester, S. Ogier, R. Artigas, C. Florian, F. Caballero-Lucas, J.M. Fernández-Pradas, P. Serra.  
Laser-assisted conductive silver ink printing with inkjet and laser-induced forward transfer techniques for organic transistor fabrication.  
SPIE Photonics West, San Francisco, United States.  
Contribution: Oral presentation.
- 2014 P. Serra, A. Patrascioiu, C. Florian, J.M. Fernández-Pradas, J.L. Morenza.  
Laser induced forward transfer of liquids: Time-resolved imaging analysis of the jetting dynamics.  
8th International Conference on Photo-excited Processes and Applications (ICPEPA-9), Matsue, Japan.  
Contribution: Oral presentation.
- C. Florian, F. Caballero-Lucas, J.M. Fernández-Pradas, J.L. Morenza, P. Serra.  
Ag conductive ink printing through LIFT technique.  
12th International Conference on Laser Ablation (COLA), Lille, France.  
Contribution: Oral presentation.
  - F. Caballero-Lucas, C. Florian, J.M. Fernández-Pradas, J.L. Morenza, P. Serra.  
Precise surface modification of polymethyl-methacrylate with near-infrared femtosecond laser.  
European Materials Research Society (E-MRS) Spring Meeting, Lille, France.  
Contribution: Poster presentation.
  - A. Patrascioiu, C. Florian, J.M. Fernández-Pradas, J.L. Morenza, G. Hennig, P. Delaporte, P. Serra.  
Time-resolved imaging of multi-jet interaction during LIFT.  
European Materials Research Society (E-MRS) Spring Meeting, Lille, France.  
Contribution: Poster presentation.
  - J.M. Fernández-Pradas, A. Patrascioiu, C. Florian, F. Caballero-Lucas, J.L. Morenza, P. Serra  
Laser transfer methods for the printing of complex materials from liquid suspensions.  
The 7th World Congress on Particle Technology (WCPT7), Beijing, China.  
Contribution: Oral presentation.

- 2013 C. Florian, F. Caballero-Lucas, J.M. Fernández-Pradas, J.L. Morenza, P. Serra.  
Femtosecond laser ablation of transparent polymer materials.  
12th International Conference on Laser Ablation (COLA), Ischia, Italy.  
Contribution: Poster presentation.
- C. Florian, F. Caballero-Lucas, J.M. Fernández-Pradas, J.L. Morenza, P. Serra.  
Surface laser ablation of polymethyl-methacrylate using 1027 nm femtosecond laser.  
14th International Symposium on Laser Precision Microfabrication (LAMP), Niigata, Japan.  
Contribution: Poster presentation. **Best student poster presentation award.**
  - F. Caballero-Lucas, C. Florian, J.M. Fernández-Pradas, J.L. Morenza, P. Serra.  
Study of the ablation of transparent materials with near-infrared femtosecond laser.  
14th International Symposium on Laser Precision Microfabrication (LAMP), Niigata, Japan.  
Contribution: Poster presentation.
  - J.M. Fernández-Pradas, C. Florian, F. Caballero-Lucas, J.L. Morenza, P. Serra.  
Surface ablation of transparent polymers with femtosecond laser pulses.  
European Materials Research Society (E-MRS) Spring Meeting, Strasbourg, France.  
Contribution: Oral presentation.
- 2012 C. Florian, J.M. Fernández-Pradas, J.L. Morenza, P. Serra.  
Femtosecond laser ablation of polymethyl-methacrylate with high focusing control.  
European Materials Research Society (E-MRS) Spring Meeting, Strasbourg, France.  
Contribution: Poster presentation. **Best student poster presentation award.**
- 2011 Summer School, Nanomaterials: Science and Applications.  
Faculty of Science, Utrecht University, Utrecht, The Netherlands.  
Contribution: Oral presentation.
- 2009 C. Florian, M. Linares and O. Organista.  
Analysing a beam splitter, a key to understand quantum states teleportation.  
XXXIII Congreso Nacional de Física, Santa Marta, Colombia.  
Contribution: Oral presentation.
- M. Linares, C. Florian and O. Organista.  
Some concepts of modern physics and its implications in the formation of physics teachers.  
X Conferencia Interamericana de Educación en Física, Medellín, Colombia.  
Contribution: Oral Presentation.

## Professional Experience

- 2013 **Teaching Assistance**, *Electromagnetism Laboratory and Physics Laboratory for Engineering, Applied Physics and Optics Department, Universitat de Barcelona, Barcelona, Spain.*
- 2009 **Teaching Assistance**, *Mechanics II and Differential Calculus, Physics Department, National Pedagogic University, Bogotá, Colombia.*

**Administrative Monitoring**, *Physics Department, National Pedagogic University, Bogotá, Colombia.*

2008 **Interinstitutional Relations Office (ORI). Member of the Support Group**, *National Pedagogic University, Bogotá, Colombia.*

---

## Languages

Spanish Native Speaker.  
English TOEFL iBT 92 points. S:23, L:24, W:25 and R:20.  
Catalan Level B2.  
German Level A2.

---

## Computer Skills

Languages C++, Python.  
OS Linux and Windows.  
Tools LabView, Office Package, Corel Draw, AutoCAD, ImageJ.  
TEX Editors  $\LaTeX$ ,  $\text{BIB}\TeX$ , PSTricks, Beamer.  
Others Google Sketchup, PovRay, Gnuplot, Derive, Mathematica, Origin.